

AN EVALUATION OF A CURRENT REAR IMPACT DUMMY AGAINST HUMAN RESPONSE CORRIDORS IN BOTH PURE AND OBLIQUE REAR IMPACT

Claire Willis, Jolyon Carroll, Adrian Roberts

ABSTRACT

Much recent research has been conducted on Whiplash Injury, however little has focussed on oblique or non-symmetrical rear impact loading and the attributes that a test device should have to detect injury risk, including responses to asymmetrical loading, which will be needed in a regulatory test device. A series of low speed, oblique rear tests have been conducted with volunteers and the RID^{3D} dummy. Pure rear impact tests were also conducted with the RID^{3D} to replicate previous tests using volunteers as well as the BioRIDIIb and THOR α dummies. The paper also reviews further issues that must be addressed for regulatory application.

This research evaluated:

- Volunteer responses with respect to impact orientation and muscle activity
- The RID^{3D}'s response against volunteer response corridors for oblique rear impact.
- The RID^{3D} for repeatability and reproducibility.
- The RID^{3D}, BioRIDIIb and THOR α dummy responses against human response corridors for pure rear impact.
- The interaction of the dummy with the test seat compared to human subjects.

The main findings were:

- Muscle activity should be considered in rear impact events.
- Both RID^{3D} and BioRIDIIb had aspects of their responses which fitted the human response corridors generated.
- The THOR α 's response was less human-like than the other two dummies.
- Both RID^{3D} and BioRIDIIb had aspects of their motion which could be improved.
- There were issues of concern with the RID^{3D} in terms of reproducibility.
- The BioRIDIIb was the only dummy that interacted with the test seat in a human like way
- The BioRIDIIb appeared to be the more biofidelic dummy based on the testing conducted but further study of the reproducibility of its response is required.

INTRODUCTION

Extensive research has been carried out during the last 10 years in the area of rear impact and whiplash injury research, resulting in the development of two dummies designed specifically for rear impact testing. The first, the BioRID II, was developed by Davidsson (2000) [1] with a fully articulated spine, designed to be representative of a human seated in a typical vehicle seat. The RID^{3D} started life as the RID (Svensson and Lovsund, 1993 [2]) and then the TRID neck (Thunnissen et al, 1996 [3]), designed as an adaptation for the Hybrid III dummy. However, as a result of the EC 4th Framework project – ‘Whiplash I’ project the neck was applied to a modified THOR torso, which also included a modified pelvis and abdominal flesh, creating the RID2. The neck was then modified in the Whiplash II project to detect whiplash injuries from all impact directions to create the RID^{3D}.

The BioRID has been evaluated against the RID2 by Zellmer et al (2002) [4], who concluded that in terms of seat ranking ability using injury criteria such as NIC, the two dummies were comparable. The authors used a recently designed dynamic sled-based test procedure, a range of different car seats and NIC and Nkm for injury criteria to compare the two dummies. The designs of the two dummies were discussed in detail. Zellmer et al noted that although the results were comparable the kinematics of the two devices were different. The authors recommended that the kinematics of each dummy should be compared with those of human volunteers to determine whether particular aspects of human motion are important and to show which dummy was the most “human-like”. The authors do not appear to have evaluated the repeatability or reproducibility of either dummy during their test series.

A wide variety of volunteer and PMHS tests have been conducted by different research groups to generate biofidelity data for the evaluation of rear impact test devices and in order to gain an understanding of the mechanisms and subtleties of Whiplash injury. However, to date, all biofidelity data against which dummies have been evaluated has been generated from pure rear impacts. Golinski and Gentle (2002) [5] used a model of the Hybrid III dummy with a human neck to show that a scenario where the occupant had their head turned at an angle just prior to impact could significantly increase the stress on the neck. As part of the

Whiplash II project, TRL set out to generate high quality oblique-rear impact volunteer response data, as reported by Willis et al (2004) [6]. These tests followed on from work conducted by Roberts et al (2002) [7] to generate high-quality pure rear volunteer response data. Both test series used identical test set-ups and evaluation techniques so that the two sets of data would be comparable and any significant differences in volunteer response could be identified. The only difference between the two test series was that the volunteers used for the oblique-rear tests were blindfolded and given mental tasks to complete which were played through headphones to ensure that the volunteers were unaware of the impending impact and were therefore unbraced.

In order to make best use of these response corridors, a variety of dummies were evaluated against the pure rear response corridors (Roberts et al, 2002 [7]). Subsequently the RID^{3D} was evaluated against both sets of response corridors. In order to make the evaluation more thorough, two identical prototype RID^{3D}s were tested under identical impact conditions, in order to assess the reproducibility and repeatability of the dummy as well as its biofidelity. The results of the pure rear tests with the RID^{3D} may be compared to those of other dummies and provide a basic comparison between the RID^{3D} and BioRIDIIb. (It should be noted that the BioRID is at revision IIg at time of writing.)

METHOD

The test procedure used for the volunteers was documented by Willis et al (2004) [6]. The testing was conducted under strict ethical guidelines and approval was obtained from the relevant medical ethics committee before testing commenced. A group of eight male volunteers, approximately 50th percentile, were tested in an oblique rear impact scenario, using a dual sled system to give an impact of 2g and a ΔV of 7kph (1.9m/s). The seat used was angled at 15° to the direction of impact as it was thought that having the volunteers' heads turned at an angle would have carried too great a risk of injury and could not have been replicated with a dummy. The angle of 15° was based on a study of drivers in a range of vehicles and the angle through which they turned their heads to monitor the mirrors etc. The volunteers were blindfolded and given a series of mental and oral tasks so that they were unaware of the impending impact. The

volunteers were instrumented with accelerometers, visual targets and electromyography (EMG) sensors.

The dummy tests were designed to apply identical impact conditions to the dummy as had been used for the volunteers. The oblique rear set-up is illustrated in Figure 1 (the pure rear set-up was identical but with the seat facing forwards). Two identical prototype RID^{3D}s were tested under both pure and oblique rear impact conditions, using two impact pulses as illustrated in Figure 2, the first was used for the volunteers, the second was a more severe pulse to assess the dummy's sensitivity. The test seat was based on an UN/ECE Regulation 44 (1998) Test Bench but the seat back was padded with 70mm polyethylene foam and increased to a height of 590mm above the CR line. An adjustable head restraint was also added. The seat back and head restraint were instrumented with load cells and inertial compensation accelerometers, as illustrated in Figure 3. A pressure mat was positioned 50mm from the base of the seat back to record the pressure distribution formed by each subject's back against the seat during the test. The dummy was instrumented with a variety of internal sensors; tri-axial accelerometers at the head centre of gravity, T1, T12 and Pelvis; 6-axis upper and lower neck load cells and tilt sensors as illustrated in Figure 5. In addition the dummy was instrumented with external tri-axial accelerometers on the left and right of the head, at T1 and on the chest to mimic the positions used for the volunteer instrumentation.

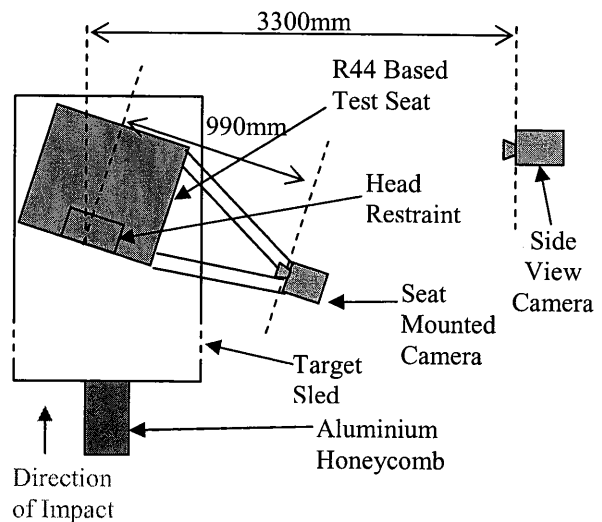


Figure 1: Oblique-Rear Impact Test Set-up as viewed from above

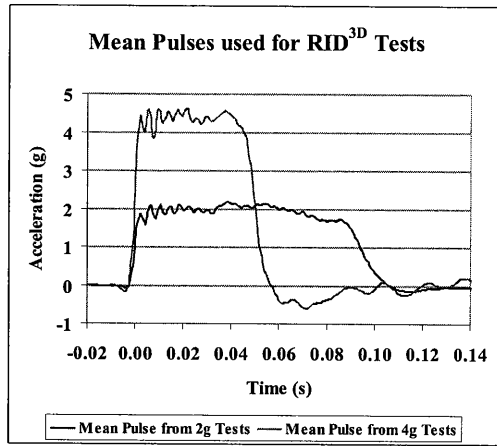


Figure 2: Acceleration Pulses used for RID^{3D} Testing

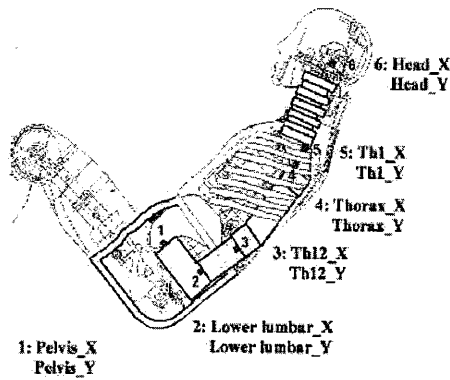


Figure 4: RID^{3D} Tilt Sensor Positions

A standard procedure was followed for dummy positioning to try to ensure repeatability. Although, initially, the procedure demonstrated in training (for the RID^{3D}) was followed to set the lumbar bracket and T1 bracket correctly, these settings were not altered for a given dummy during testing, to try to ensure that the dummy was set up as repeatably as possible. The dummy positioning procedure (once lumbar and T1 brackets were set) was as follows:

- External sensors and tracking targets were put in place.
- The dummy back flesh was put in place
- The neck cable tension was checked qualitatively (no quantitative method was available)
- The dummy was positioned such that the back-set¹ was 75mm (a spacer was used for this) and all tilt sensors were reading within the set-up range as far as this was possible.
- Stills photographs were taken and the position of visual targets on the dummy were noted, relative to the sled.

¹ Back-set – the distance between the rear of the head and the front of the head restraint.

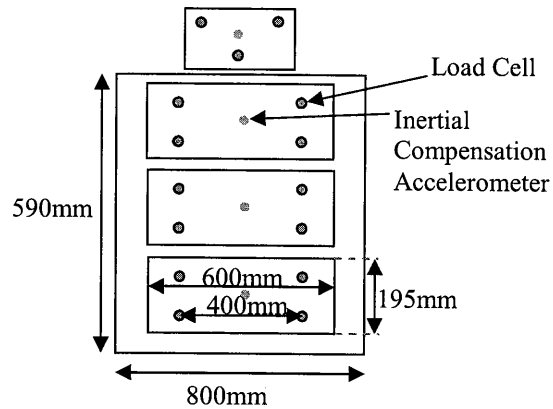


Figure 3: Seat Back Instrumentation

Position of Sensor	Set-up Angle Target and Tolerance	
	x-axis	y-axis
Head	$0^\circ \pm 1^\circ$	$0^\circ + 0^\circ/-1^\circ$
T1	None	$0^\circ \pm 1^\circ$
Thorax	None	None
T12	None	None
Pelvis	$0^\circ \pm 1^\circ$	$22.5^\circ \pm 5^\circ$
Lumbar Spine	None	$0^\circ \pm 1^\circ$

Figure 5: RID^{3D} Settings for Tilt Sensors

- Post-test, more photographs were taken. The dummy back flesh was removed to ensure that it did not become compressed between tests. The dummy was also inspected for damage.

RESULTS

Oblique Rear Volunteer Tests

High quality response corridors were generated from the volunteer testing and these have been previously presented by Willis et al 2004 [6]. It was noted that although the amount of displacement and acceleration recorded varied between different volunteers, their responses usually had similar characteristics, for a given parameter. Thus the displacement and acceleration corridors represented the characteristics of the volunteer responses well.

When the oblique rear volunteer results were compared to the results of the pure rear tests conducted by Roberts et al 2002, it was found that:

- The oblique rear volunteers were much less aware of the timing of the impending impact and therefore were unprepared for the impact,

whilst the pure rear volunteers were aware and to some extent “braced” themselves.

- The oblique rear volunteers experienced head rotation about the z-axis and some lateral motion. This was not recorded for the pure rear volunteers since none was expected.
- The pure rear volunteers exhibited less vertical motion at T1 than the oblique rear volunteers, possibly because they were braced and therefore had straighter, ‘stiffer’ spines prior to impact. All T1 vertical motion was caused by the volunteers’ spines flattening against the seat back in both series of tests.
- The oblique rear volunteers loaded the seat back asymmetrically.
- Both sets of volunteers loaded the top and bottom of the seat back more than the middle (shoulders and pelvis) and the bottom of the head restraint.
- Both sets of volunteers showed muscle activation sufficiently early after the impact for their muscles to have affected their motion during impact.

RID^{3D} General Set-up and Use

The procedure for setting the neck cable tension on the RID^{3D} at present requires the dummy to be dismantled which can be very time-consuming. Unfortunately, the dummy cannot be set up prior to shipment. Once the cable tension has been set correctly, it can only be verified using a qualitative method as no quantitative method exists.

As the dummy is designed specifically for use in shaped car seats it is extremely difficult to position in a seat with a flat or abnormal shaped seat back as its back has been given a fixed, curved profile. The rigid thoracic spine and non-human-like back flesh made it impossible to put the dummy in the same seated position as the volunteers as they were able to configure themselves to the nuances of the particular seat. This is a feature that may be considered advisable in a human surrogate. The back flesh also prevented any shoulder interaction with the seat back and made the dummy unable to detect any asymmetric loading from the seat back. The difficulties in positioning the dummy also extended to setting the lumbar and T1 brackets correctly. Small differences in the settings used for these brackets ($\pm 2^\circ$) can, according to manufacturers, have a significant effect on the dummy’s response.

Although the tilt sensors were set and recorded as accurately as possible, it was found that it was impossible to have all sensors reading within the specified tolerance range with the dummy positioned in a flat backed seat. It was also found that without the moulded back of a car seat to support it, the dummy’s own movement after

positioning was sufficient to move the tilt sensor readings outside of the setting up tolerance.

RID^{3D} Repeatability

The repeatability of internal sensor readings was monitored during testing to ensure that a sufficient number of tests had been conducted to identify any possible anomalies. In general, the repeatability of response was found to be good according to both internal and external sensors (Figure 6). However, there were anomalous readings recorded by both the upper and lower neck load cells as illustrated in Figure 7.

The kinematic responses indicated that the RID^{3D} responses were repeatable at 2g but there was some variation in the response at 4g (Figure 8).

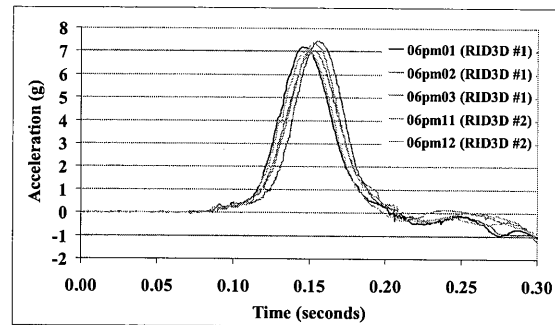


Figure 6: Head Centre of Gravity Fore-Aft Acceleration (pure rear tests at 2g)

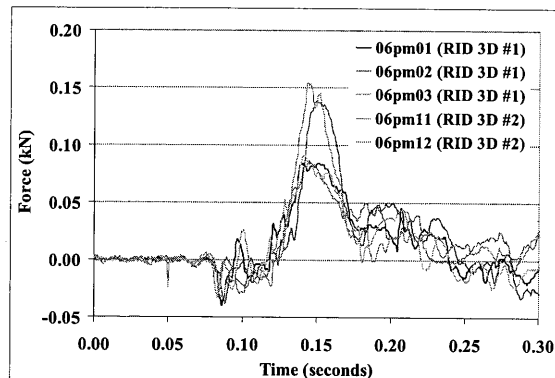


Figure 7: Upper Neck Load Cell Axial Force (pure rear tests, both dummies, at 2g)

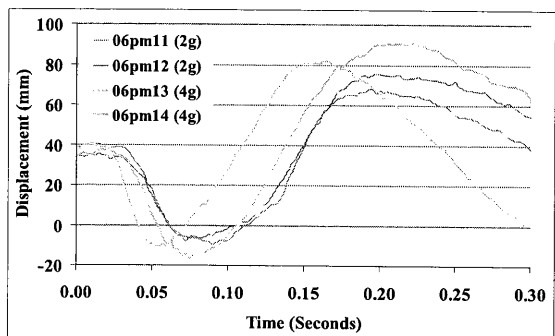


Figure 8: Head Centre of Gravity Displacement relative to T1 (pure rear, 2g and 4g tests)

RID^{3D} Reproducibility

When the internal sensor readings were compared during testing, little difference was found between the responses of the two dummies (Figure 6), although some sensor readings showed small differences in the response characteristics. However, when the kinematic responses were compared, distinct differences were found for every parameter (Figure 9 and Figure 10). These differences have been attributed to the lumbar spines of the two dummies not having been certified dynamically prior to testing. Subsequent testing has revealed differences between the two spines in terms of stiffness.

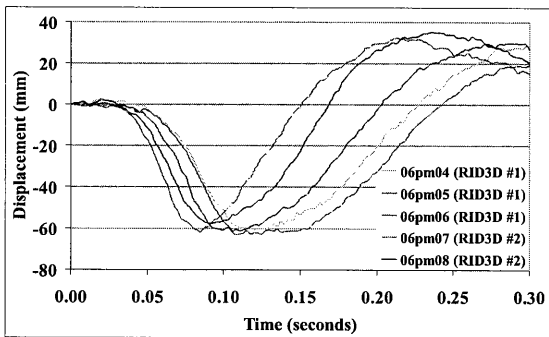


Figure 9: Head Fore-Aft Displacement relative to T1 (oblique rear tests, at 2g)

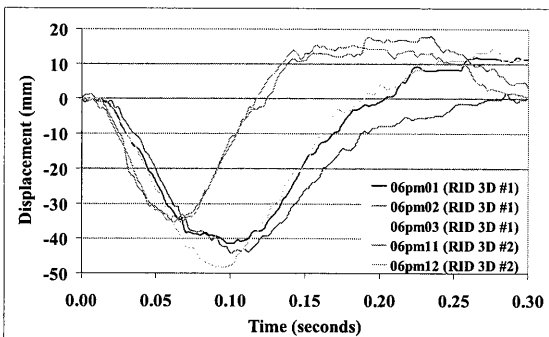


Figure 10: Chest Fore-Aft Displacement (pure rear tests, at 2g)

RID^{3D} Biofidelity

The two dummies produced very similar amounts of head and T1 fore-aft displacement as compared with the volunteers. However, the differences between the responses from the two dummies were a problem in this respect. Figure 11 shows that the response from the RID^{3D} #1 fits within the corridor, whilst the response from the RID^{3D} #2 was quite different.

The main differences between the RID^{3D} responses and those of the volunteers were in the amount of vertical motion (Figure 12) and head rotation about the z-axis (Figure 13). The RID^{3D}'s spine is too

rigid to allow much head rotation about the z-axis and although it showed some ability to mimic the human vertical motion relative to the seat back this was insufficient, particularly in oblique impact where the asymmetric loading appeared to reduce the spine's flexibility.

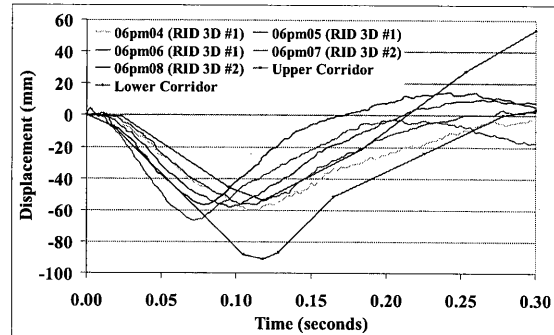


Figure 11: T1 Fore Aft Displacement relative to seat back (oblique rear tests, at 2g)

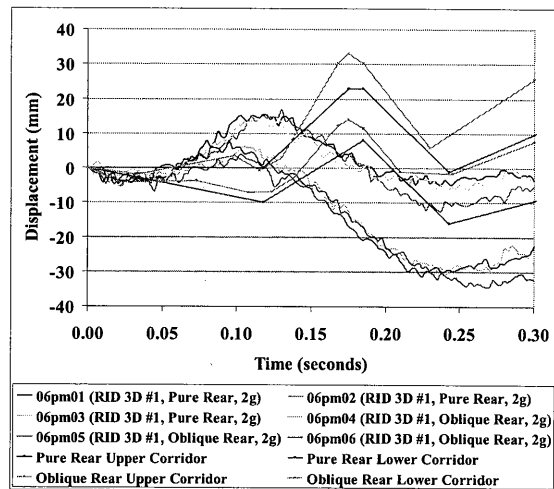


Figure 12: T1 Vertical Displacement relative to seat back (pure and oblique rear tests, at 2g)

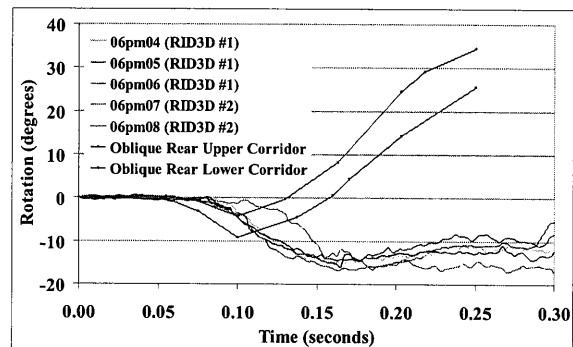


Figure 13: Head Rotation about the z-axis (oblique rear tests, at 2g)

Pressure profiles

The pressure profile readings taken during testing were compared to those taken during volunteer testing and showed that the dummies' interaction with the seat back were very different to those of the volunteers (Figure 14 and Figure 15). When the

force distribution from a typical dummy test was compared to the load cell readings from the volunteer tests there were also noticeable differences in the way the dummy loaded the seat back.

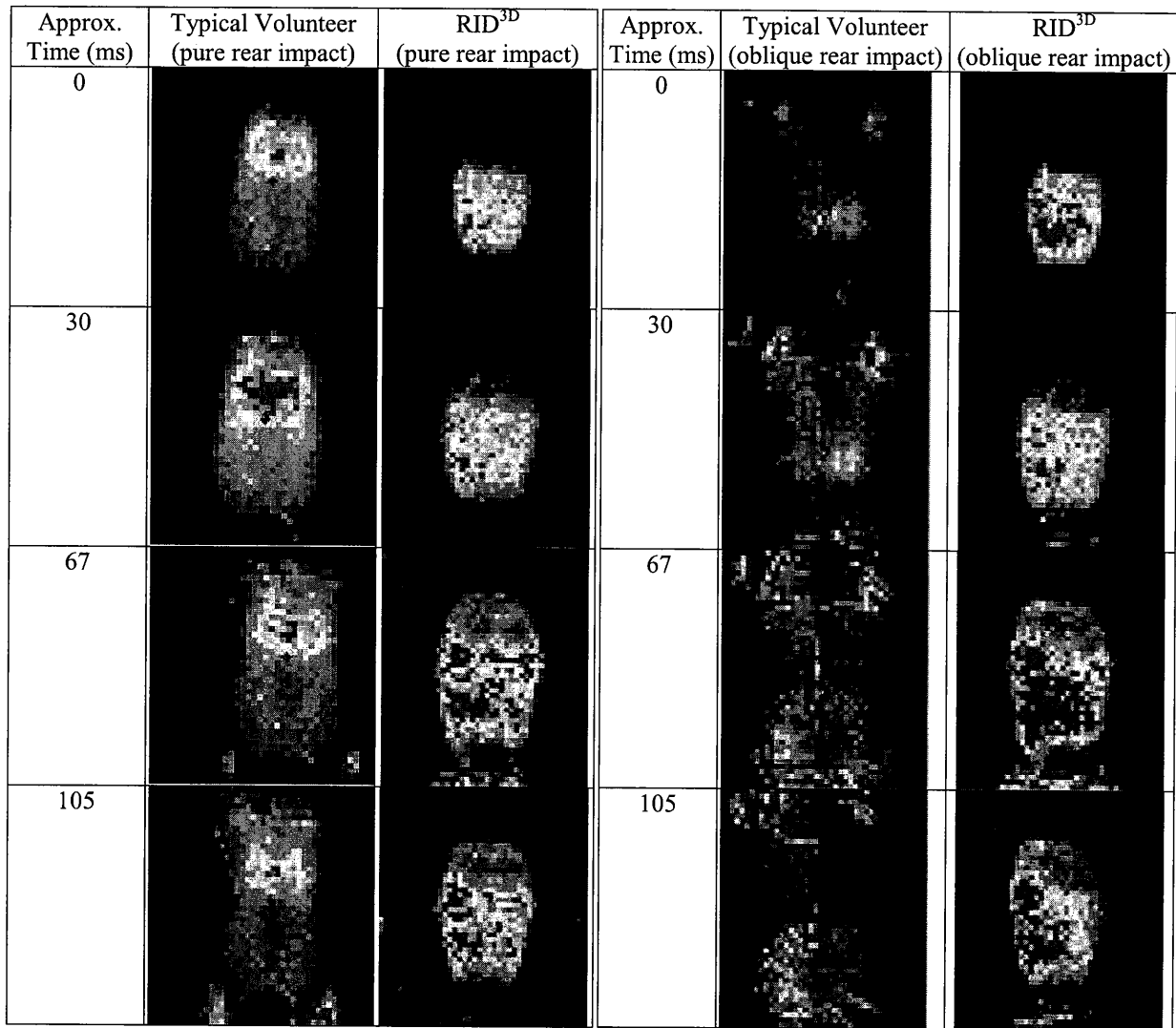


Figure 14: Comparison of pressure profiles from a typical volunteer and the RID^{3D} (pure rear tests)

Figure 15: Comparison of pressure profiles from a typical volunteer and the RID^{3D} (oblique rear tests)

Comparison of RID^{3D} Response with Other Dummies in Pure Rear Impact

The BioRIDIIb, THOR α and THOR α with a EuroSID neck were all tested under the same pure rear impact conditions as the RID^{3D} and volunteers. (BioRID is now at version 2g and the THOR α has since been developed further as the THOR-NT and the THOR-FT has also been created. Each dummy was tested at least twice under the same impact conditions. The repeatability of response was good for every dummy except the THOR with the EuroSID neck. There appeared to be a problem with the impact point (T_0) timing of the RID^{3D} results and hence they were adjusted to fit with the other dummy responses.

Considering the acceleration responses, both the BioRID and RID^{3D} produced fore-aft head and T1 responses that were very close to the volunteer responses (Figure 16). Similarly the fore-aft displacement responses for both dummies were close to or within the volunteer corridors and very similar to each other. The main differences between the dummy responses were apparent in the vertical accelerations and displacements. For the head and T1 accelerations, both the RID^{3D} and BioRID had the correct characteristics to their responses but the BioRID response was closer to the corridors (Figure 17 and Figure 18). The relative timing of the BioRID head fore-aft and vertical accelerations was also closer to that of the human volunteers than the other dummies. The THOR responses were very different to the corridors (not surprising since THOR was designed for high severity frontal impact). When head vertical displacement is considered (Figure 19) the BioRID had the best response but was still not close to the corridor; however, the RID^{3D} and THOR with EuroSID neck had much better T1 vertical displacement responses (Figure 20) with the correct characteristics compared to the corridor, although again, they were not close to the corridor in the time domain.

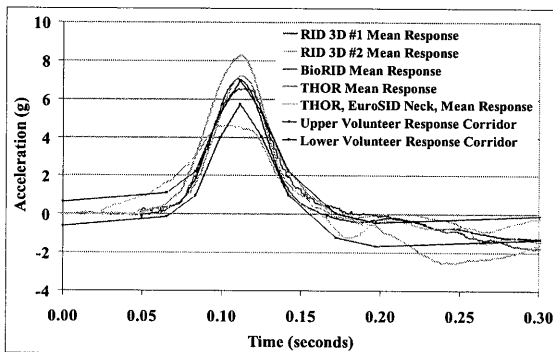


Figure 16: Head Fore-Aft Acceleration

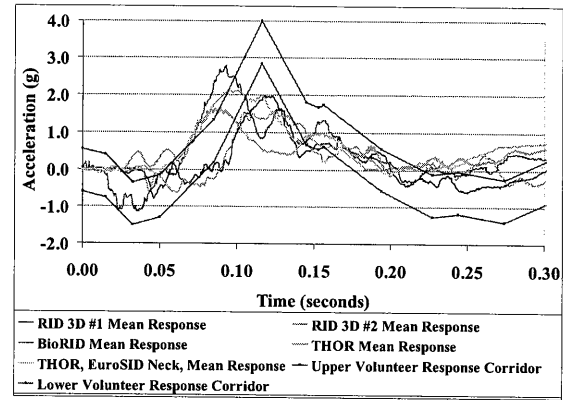


Figure 17: Head Vertical Acceleration

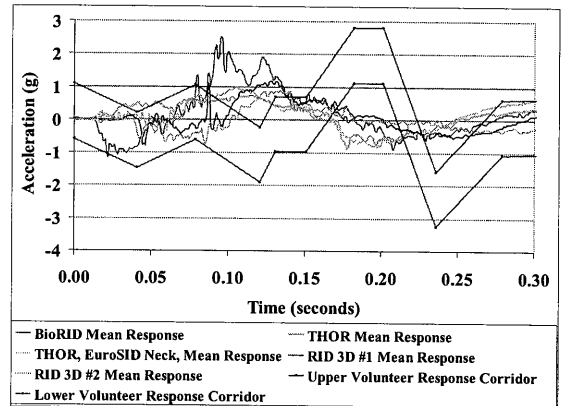


Figure 18: T1 Vertical Acceleration

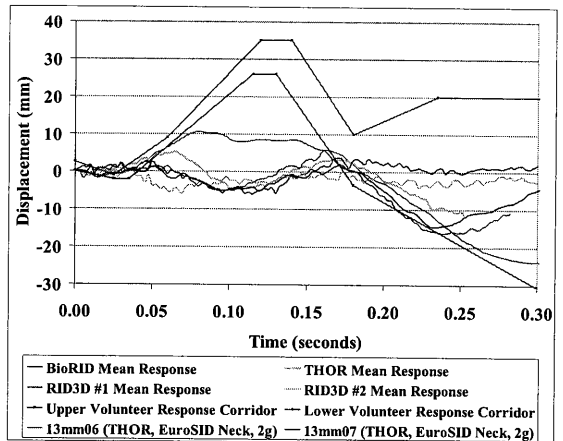


Figure 19: Head Vertical Displacement

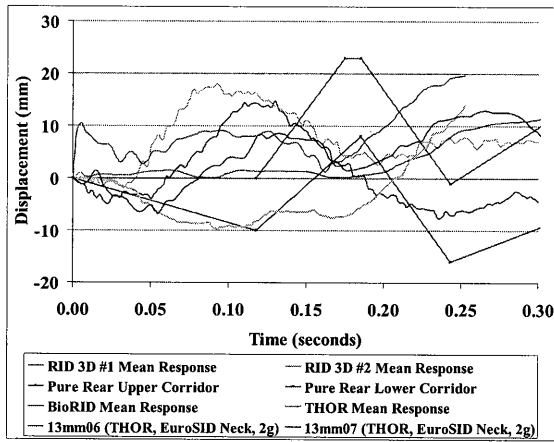


Figure 20: T1 Vertical Displacement

An unusual effect was observed when the recorded axial neck loads for each dummy were compared; the BioRID neck load cell recorded a compression peak, whilst the other dummies recorded neck tension during the same part of the impact (Figure 21). When the relative accelerations of the human head and T1 are compared from the volunteer tests, the head is accelerated upwards initially and then downwards relative to T1, causing compression in the neck itself (Figure 22); thus the BioRID response would appear to be most representative of the effects experienced by a human.

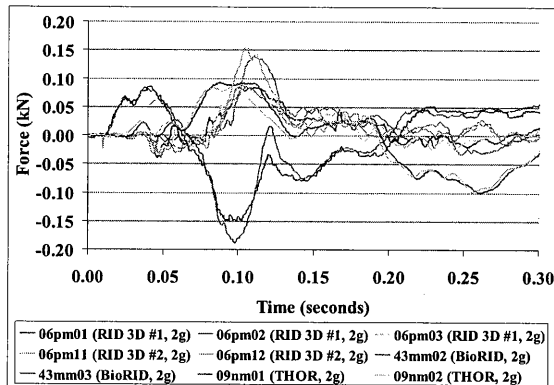


Figure 21: Comparison of Neck Axial Force recorded by each dummy

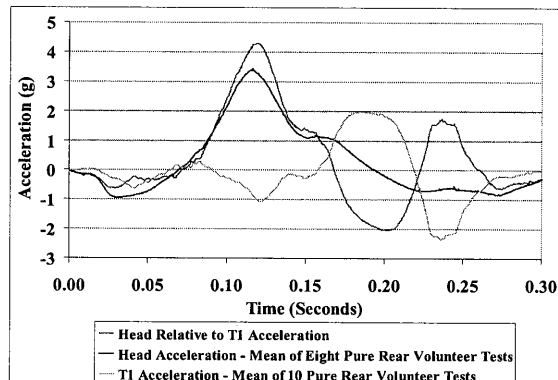


Figure 22: Relative Acceleration of Head and T1

ANALYSIS

RID^{3D} Reproducibility

The differences between the responses from the two dummies were investigated thoroughly. One of the dummies had kinematic responses closer to the volunteer corridors than the other. However, it was not known whether the RID^{3D} showing the least biofidelity was the one functioning incorrectly or correctly. To determine which response was from the faulty RID^{3D}, the tilt sensor readings and visual images for each test were compared to identify any differences in the initial positioning or set-up of the dummies that might have caused the differences in response but no explanation was found. The RID^{3D} spine consists of a flexible, straight lumbar element, two solid steel sections and a small flexible thoracic element connecting the two steel sections as illustrated in Figure 23. The lumbar elements are identical to those used in a EuroSID dummy; however, in this instance these units were not certified dynamically prior to testing. Subsequent certification tests revealed significant differences in the stiffness properties of the two elements. Unfortunately, the element which produced the most human-like kinematic response was the one which failed the certification tests because it was too stiff. It is recommended that the effects of the lumbar spine properties on RID^{3D} kinematic response be investigated further.

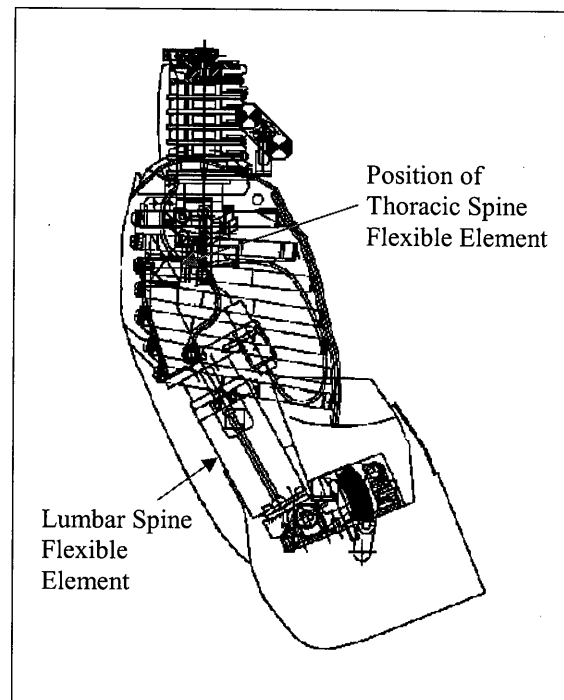


Figure 23: Schematic of the RID^{3D} Torso illustrating the position of the Lumbar and Thoracic Spine Flexible Elements

Dynamic certification criteria do not exist for the thoracic spine element. It is suggested that some of the problems identified may be attributed to this uncertified part. The interaction of the lumbar and thoracic elements, each having potentially different material properties for each dummy, could possibly explain the differences observed between the kinematic responses of the two dummies.

RID^{3D} Biofidelity

The design of the RID^{3D} spine and back flesh can also explain the lack of vertical motion in its response and the differences between the way the dummies and humans interacted with the seat back. The human volunteers initially had some degree of natural curvature in their spines prior to impact (depending on their posture and the amount of pre-impact bracing). They were then pushed backwards into the seat back by the impact. This had the effect of causing their spines to flatten against the seat back, adapting to the shape of the seat, and hence for their thoracic spines, necks and heads to move upwards. The dummies started with most sections of their spines straight prior to impact and hence any vertical head and neck motion was minimised. However, the motion recorded at T1 showed that the RID^{3D} has the correct form in its response but the response is too rapid. The amount of vertical motion is also reduced in the oblique impact – implying the RID^{3D} design is less able to produce the correct vertical motion when loaded obliquely. The head vertical motion shows that the neck design does not allow the correct relative vertical motion between T1 and head. In contrast, the BioRID shows almost no vertical motion at T1 but excellent relative motion between head and T1, including the timing of the response. It is suggested that this is due the fact that the BioRID neck starts with a natural curvature, representative of human posture. Its poor T1 vertical motion is caused by the fact that its flexible spine is designed to start with the lumbar spine straight and a natural curve in the thoracic area; this initial starting posture may have prevented there from being much spine straightening during the impact. It is possible that the thoracic spine was flattened against the seat back in its initial starting position as the resistance to bending/straightening at this section of the spine is limited.

The BioRID has the advantage of engaging with the seat back in a more human-like manner compared with the RID^{3D}. The problem with the RID^{3D}'s engagement with the seat back is that all of the load is transmitted to the seat through the back flesh, which is designed for a specific in-car posture. This prevents the dummy's shoulders and pelvis from engaging with flatter seats than the back flesh was designed for. This would prevent the dummy from

“seeing” asymmetric loading or yielding caused by the seat in a test environment.

Both RID^{3D} and BioRID dummies have some limitations with regard to the biofidelity of their response and their suitability for use in a regulatory impact test procedure. However, it would seem that the most human-like dummy in terms of kinematics and forces detected would be the most suitable candidate. Currently, the BioRID's response is closer to that of a human in terms of relative head and neck motion and the forces recorded by the neck load cells. The BioRID also appears to have better seat back interaction capabilities. However, the reproducibility of the BioRID response was not determined in this test series, neither has its response been evaluated under oblique loading conditions to assess its suitability for detecting asymmetric loading. It is not known how suitable either dummy would be for detecting lumbar injuries which are also prevalent in low severity rear impacts.

DISCUSSION

At the current time, rear impact dummies are only being used in consumer type evaluations. It is suggested that for regulatory application they should be more robust and able to assess injury risk with biomechanical foundations since approval thresholds should be related to the risk of injury, rather than comparative seat performance.

In a regulatory framework it will not be known what the structure of seats will be, that the dummy will be required to assess and whether the seat will yield to absorb energy. In addition one can not guarantee that a vehicle seat would yield symmetrically or load the dummy symmetrically thus the regulatory test device must be able to ‘adapt itself’ to many different types of loading structure. It is also suggested that any dummy should be able to assess injury risk for ‘all rear impact injuries’, not only ones to a particular body segment. If all areas are not simultaneously assessed, it could be possible to transfer injury risk from one body area to another by protecting one area and not another. A holistic approach to rear impact safety is essential.

It is acknowledged that the test seat used in this study was one that would not be seen in a vehicle but was used as it was easy to define and build and can be replicated easily by other research groups. The test also attempted to evaluate whole body behaviour and not just head and neck kinematics. It is suggested that a dummy that could be used for regulatory evaluations should be able to adapt to any seat design, as did the human volunteers, and be able to assess all types of loading to ensure that whole body injury risk is reduced and not just transferred. Therefore, this ‘non-car’ seat test

configuration is a valid assessment of dummy behaviour.

The oblique tests loaded the humans asymmetrically thus any dummy should be able to respond in like manner, since one should not expect all vehicle seats to fail symmetrically, even in a pure rear impact test. This asymmetrical loading was most evident in the shape of the pulse detected by the left and right accelerometers, externally mounted on the head of the volunteer or dummy. This indicates that for any type of regulation testing, a dummy should be fitted with a 6 or 9-axis array of head accelerometers, rather than a centrally mounted tri-axial array to allow any lateral or rotational components of the motion to be detected.

Both the RID^{3D} and BioRID dummies showed attributes that would be beneficial for a regulatory fit test dummy. It is not possible to indicate the overall importance of the results presented in this paper since the test severities were sub-injury. Therefore it is not known whether dummies that did not comply would be more or less appropriate at higher impact severities. Even so it is suggested that if a dummy could match both the pure rear and oblique rear requirements then it would be a very good candidate dummy for injury risk assessment.

Neither dummy met fully the defined requirements but both had positive and negative features. It is suggested that a hybrid of the two dummies may be the best for regulatory use.

CONCLUSIONS

RID^{3D} Repeatability and Reproducibility

When each RID^{3D} dummy response is considered in isolation, most of the acceleration and displacement responses appear to be repeatable for the tests conducted at 2g, except for the outputs from the neck load cells, which showed anomalous readings.

A significant doubt concerning reproducibility was determined in that the motion of the two dummies varied significantly for the same test set-up. The problem affected the response of the entire dummy and not just the motion of the head and neck. It is hypothesised that this could be explained by the properties of the lumbar spine elements which were subsequently found to be different, as these parts were not certified dynamically prior to testing. The set-up was sufficiently tightly controlled to be ruled out as a possible cause of the differences seen.

A comparison of the responses from the two RID^{3D} dummies, that were tested in this programme, in pure and oblique rear impact, suggests that the RID^{3D} spine may be less flexible when loaded obliquely and hence less human-like.

RID^{3D} Biofidelity

Many of the responses from RID^{3D} #1 fitted within or were close to the volunteer response corridors; the exceptions were the head and T1 vertical accelerations and displacements and the head rotation about the z-axis.

The RID^{3D}s produced less head and T1 vertical motion, particularly for oblique impact, probably due to the inability of the spine to adapt to the profile of the seat back in the same way as a human.

The z-axis rotation of the RID^{3D} spine under low severity oblique rear impact conditions is very different to that of a human; the results imply that the neck is much too stiff to allow the correct rotational response.

The RID^{3D} seat back profile is fixed completely differently to that of a human being. Currently there would be no way for the RID^{3D} to detect localised or asymmetric loading from the seat-back due to the design of the back flesh and rigidity of the spine (compared to the BioRID).

Since the RID^{3D} thoracic spine is not able to adapt to the profile of the seat back in the same way that a human would, it has implications for proper activation of active head restraints in car seats and the assessment of other spinal injury.

Comparison of RID^{3D} Responses with BioRIDIIb and THOR α in Pure Rear Impact

The BioRID head and neck motion is more human-like in terms of the characteristics of the response compared with any of the other dummies tested, even though the timing is not always correct.

The RID^{3D} T1 displacement response has the most potential in terms of human-like motion characteristics compared to the other dummies tested, although some further development is suggested as the amount of vertical motion is noticeably less than that of a human.

The responses for the RID^{3D} and BioRID are similarly close to the fore-aft volunteer response corridors generated for pure rear impact. However, neither dummy fully complies with the defined corridors. It is not known which responses are most significant in terms of injury generation. Hence, it must be assumed that neither dummy is currently adequate to assess injury risk.

The THOR dummy responses were seldom as close to the corridors as those of the BioRID and the RID^{3D}, which was as expected since the THOR was not designed for rear impact.

Differences are noted between pure rear impact and oblique rear impact conditions. Since it is not known how the dummies would be loaded in a

regulatory test, even if it was only a pure rear impact test, it is recommended that any dummy should comply with both the pure rear and oblique rear requirements.

FUTURE DIRECTIONS

This whole research program has developed a set of quality dummy design and assessment targets that should be used for the assessment of test dummies to be used in low severity rear impact testing, taking a holistic approach to dummy behaviour (Willis et al, 2004 [6] and Roberts et al, 2002 [7]). The different candidate dummies that could be used in a regulatory test have been evaluated, but not in all the equivalent or comparative test conditions. It would be advantageous to be able to complete the test matrix so that equivalent comparative comments could be made regarding the latest version of the dummies in the comparative tests.

Both the RID^{3D} and BioRID dummies have positive and negative features. It is suggested that dummy designs should be encouraged to merge the best features of the dummies into a single advanced test device that could be used in a regulatory test procedure.

ACKNOWLEDGEMENTS

The authors are grateful to Mr. C. Walker and Mr. C. Geddes for their help in conducting the various test series reported in this paper. Special thanks are extended to Dr. A. Whitfield (Healthnet), Mrs. S. Burton and Miss. S. Bygrave for their contribution to the volunteer testing.

All work reported was funded partly or fully by the UK Department for Transport. The oblique rear volunteer tests and RID^{3D} testing was also jointly funded by the EC project Whiplash II.

The opinions expressed are those of the authors and not necessarily those of the UK Department for Transport or the EC Whiplash II Consortium.

REFERENCES

- [1] **Davidsson J, 2000.** *Development of a Mechanical Model for Rear Impacts: Evaluation of Volunteer Responses and Validation of the Model.* Doctoral Thesis, Chalmers University of Technology, Gothenburg, Sweden, 2000.
- [2] **Svensson M Y and Lovsund P (1992).** *A Dummy for Rear-End Collisions – Development and Validation of a New Dummy Neck.* Proceedings of the 1992 IRCOB Conference (299-310).
- [3] **Thunnissen J G M, van Ratingen M R, Beusenburg M C and Janssen E G (1996).** *A Dummy Neck for Low Severity Impacts.* Proceedings of the 15th International Conference on the Enhanced Safety of Vehicles, 1996, Paper 96-S10-O-12.
- [4] **Zellmer H, Muser M, Vetter D and Walz F, 2002.** *Performance Criteria of Rear Impact Dummies: Hybrid III (TRID), BioRID and RID2.* Proceedings of the 2002 IRCOB Conference, Munich, 18-20 September 2002.
- [5] **Golinski W Z, Gentle C R, 2002.** *The influence of initial head rotation (non-sagittal plane positioning) on Whiplash injury.* Proceedings of the Vehicle Safety Conference 2002, London, UK.
- [6] **Willis C, Bygrave S, Carroll J, Roberts A K, 2004.** *Kinematics of the Human Spine in Rear Oblique Impact: a Volunteer Study.* Proceedings of the Vehicle Safety Conference 2004, London, UK.
- [7] **Roberts A K, Hynd D, Dixon P R, Murphy O, Magnusson M & Pope M H, 2002.** *Kinematics of the Human Spine in Rear Impact and the Biofidelity of Current Dummies.* Proceedings of the Vehicle Safety Conference 2002, London, UK.

DEVELOPMENT OF THE NUMERICAL MODEL OF THE NEW-BORN CHILD DUMMY Q0

Christian Gehre

Volker Schindler

Technical University of Berlin

Germany

Paper Number 05-0074

ABSTRACT

The European research project "CHILD" (Child Injury Led Design) is working on the improvement of passive safety of children as occupants in cars. One of the objectives is to develop new child dummy models. This paper focuses on the development of the finite element model of the new-born child dummy Q0 for the use with LS-Dyna.

The Q0 model was created by using the CAD models of the hardware-Q0. All non-rigid body segments such as head, neck and torso were validated by using results of component tests. Optimisation tools were used to identify the adequate material models for the body segments and to define the parameters of these materials.

The response of the dummy database in these calibration test procedures correlates well with the physical Q0 dummy. Furthermore, all parts would pass the certification requirements.

INTRODUCTION

The new-born child dummy Q0 (Figure 1), developed by TNO and FTSS was one of the first results of the CHILD project. The numerical model is based on this first series of Q0 dummies.



Figure 1. Child dummy Q0.

The Q0 represents a six week old infant with a mass of 3,400 grams and a sitting height of 355 mm. It

was designed for the use with child restraint systems (CRS) for this age group in frontal, lateral, rear and roll-over crash configurations. Compared to the P0 and the CAMI dummy, it offers the opportunity to measure head, chest and pelvis accelerations as well as the upper neck forces and torques. So it is now possible to assess the protection level of child restraints of this age group by using physical measurements on the dummy.

METHOD

The dummy model was designed and validated for the use with the finite element solver LS-Dyna 970, release 3858.

Those parts of the dummy, which are designed to be non-deformable in a crash test, are made as rigid bodies in the model to reduce the total computing time. All other parts of the model, such as skin of the head, rubber of the neck or torso foam are using non-rigid materials to describe the material behaviour of these dummy parts.

All non-rigid parts were validated by using results of component tests with these parts or an assembly with these parts involved. Furthermore results of a thorax impact test of the complete dummy were used to validate the model.

The choice of the material models of every dummy part was proven by comparison with the corresponding parts of other existing numerical dummy models, designed for the use with LS-Dyna. However, no material model or its material parameters of other dummies were transferred directly to the Q0 dummy model.

STRUCTURE OF THE DUMMY MODEL

Figure 2 shows the Q0 dummy model. It has a skull, a neck, a rigid thoracic spine, a lumbar spine, which is identical to the neck and a rigid pelvis. The torso part made of foam covers the internal structure of the dummy from the pelvis up to the shoulders. The bent arms and legs are directly screwed to the upper thoracic spine and the pelvis, respectively. Their only

degree of freedom is the rotation around the transverse axis.

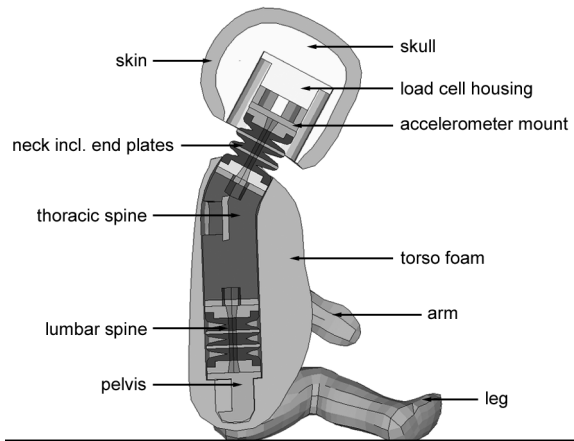


Figure 2. Structure of the Q0 dummy model.

The FEA mesh of all parts is made of solid elements, mainly of six-node hexagon and five-node pentagon elements. The surface of some parts is covered with a thin layer of shell elements. It is used as interface for contacts to other parts of the dummy and the surrounding areas. In total 7,500 nodes, 2,000 rigid elements and 11,000 deformable elements were used for the dummy besides the suit.

The total computing time of the dummy without any environment, such as CRS, is approximately 13 seconds for every millisecond of simulation time on a Pentium 4 3.0 GHz machine.

Head

The head assembly is made of skull including skin layer, upper neck load cell and accelerometer mount. A visco-elastic material model was used for the skin and an elastic model for the beam of the load cell. This beam connects the skull with the load cell housing. Skull, load cell housing and accelerometer mount are made of rigid material.

A version with a non-rigid skull was also simulated, but the non-rigid material had no advantage over the rigid version. The computing time was longer and the numerical stability was less than for the rigid version.

The head is equipped with two sensors, a six-axial load cell to measure forces and torques in the upper neck of the dummy and a tri-axial accelerometer.

Neck and lumbar spine

The structure of the neck (Figure 3) is similar to the neck of Hybrid III dummies. The main part, the neck

mould, is made of rubber and includes two metal end plates and two metal intermediate disks. A non-pre-tensioned steel cable, fixed between the two end plates, restricts the neck tension. Three slits at the front side of the neck mould are reducing the stiffness in rearward bending conditions.

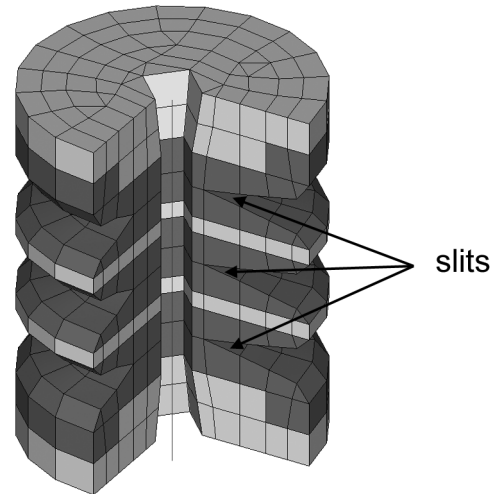


Figure 3. Model of the neck.

The comparatively small and soft neck is very sensitive against the density of the used mesh. Some important geometrical details, such as the geometry of the slits, are lost by using a wider FEA mesh. The used fine mesh is a compromise of computing time, numerical stability and response of the upper neck load cell in the validation tests.

A second model of the neck with an increased computing time efficiency was validated in parallel.

The lumbar spine joint is identical to the neck assembly. It is mounted in upside down position with slits to the back of the dummy.

Thoracic spine and pelvis

The thoracic spine is made of rigid material. A tri-axial accelerometer measures the chest acceleration. The arms are connected to the spine top plate.

The pelvis of the dummy is made of steel. So rigid material has been used in the model. Furthermore the pelvis is equipped with a tri-axial accelerometer.

Torso and rubber suit

The torso flesh foam covers the skeleton of the dummy from the shoulders to the pelvis. It has a cut on the rear side from the upper pelvis to the lower neck to allow the assembly of the dummy. The cut is closed by the suit of the dummy.

Solid elements are also used for the torso part, but compared to the others, the solid mesh consists only of tetrahedron elements.

The Q0 dummy is provided with a suit, which covers torso, upper arms and uppers legs. Until now it is not included in the numerical model. It will be provided with a later version of the model. The suit is not only necessary because of the additional soft layer on the dummy's surface, it also covers the gaps between extremities and torso.

The torso foam is fixed to the dummy's skeleton only by using contacts. No node or element is attached to another part of the dummy.

Extremities

Arms and legs are made of the same PVC-based material. They are attached with bolts to the top spine plate and the pelvis, respectively.

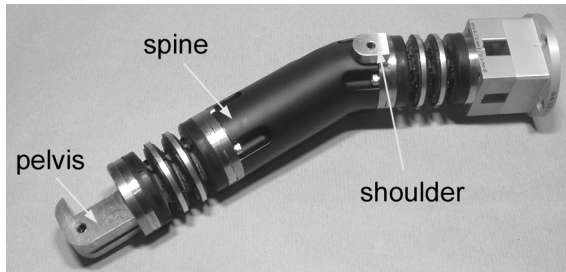


Figure 4. Skeleton of the Q0.

Figure 4 shows the skeleton of the Q0 including the top plate of the thoracic spine with the simplified rigid shoulder and the pelvis. Arms and legs are made of the same material.

VALIDATION PROCEDURES

Head and neck have to pass several certification tests [4] to show the biofidelity and to get the approval for the use in crash tests. Results of these tests were used to validate the model. Furthermore, some additional component tests with neck, torso and extremities, and thorax impact tests with the complete dummy were performed to obtain more data for the validation.

The software tool Altair Hyperstudy was used to vary the material parameters and to get an optimised model.

Head

The head assembly was validated by using three different set-ups of head drop tests (Table 1). Both tests with drop height of 130 mm are part of the certification procedures. The third one, a 45° frontal impact

test with a drop height of 376 mm, is taken from the certification procedures of CRABI 12 month old child dummy [1].

Table 1. Set-up of head validation tests.

Impact direction	Drop height	Angle
frontal	130 mm	28°
lateral	130 mm	35°
frontal	376 mm	45°

Not only the maximum head acceleration was used to validate the model of the head assembly. Also the shape of the acceleration curve should correlate with the experiment. The width of the signal is also described by the a_{3ms} value. So it was used as secondary parameter for the validation.

The maximum resultant head acceleration has to be between 91 g and 157 g in frontal and 94 g and 162 g in lateral direction to pass the certification requirements [4].

Neck

Two different test set-ups were used to validate the head-neck assembly in flexion, extension and lateral bending. In all lateral bending tests the head was mounted on the neck rotated by 90° around the vertical axis (rearward position) in order to have symmetrical neck loading.

In the first configuration the neck was mounted on a sled, which was accelerated by a pneumatic catapult. Figure 5 shows the set-up of the flexion bending test. In all tests there was no contact between chin and mounting device.

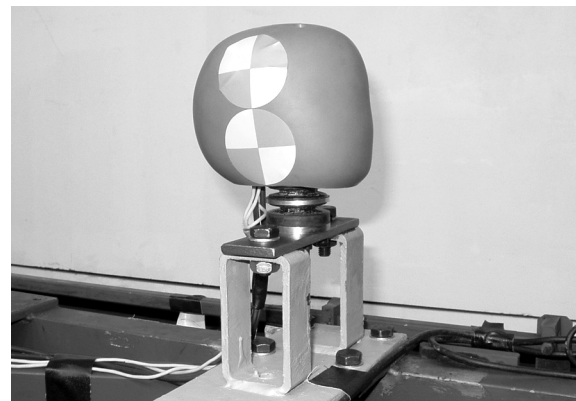


Figure 5. Set-up of sled test.

The second configuration, a pendulum test, is part of the certification procedures. The pendulum is described in Part 572 subpart E [2].

Figure 6 shows the average crash pulses of the pendulum and the sled tests. The average impact velocity was about 3.37 m/s in the pendulum tests and 4.12 m/s in the sled tests.

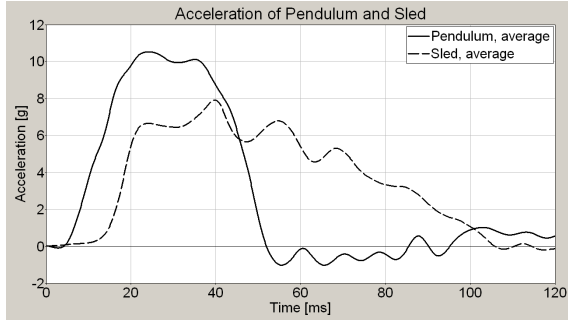


Figure 6. Acceleration in sled and pendulum tests.

The head rotation angle, the upper neck forces and torques were used as main target values to validate the model. Additionally the neck moment at the occipital condyles (OC-joint), a combination of neck moment and shear force, was used. The calculation of these moments is shown in (1), (2) and (3).

$$M_{xOC} = M_x + 0.033 \text{ m} \cdot F_y \quad (1)$$

$$M_{yOC} = M_y - 0.033 \text{ m} \cdot F_x \quad (2)$$

$$M_{zOC} = M_z \quad (3)$$

The moment at the OC-joint was used as simplified indicator of a correct time dependent course of neck forces and moments.

Torso foam

The torso part was validated by using results of two different test set-ups. Firstly, a simple drop test with the torso foam was used to pre-validate the model and secondly, a thorax impactor test with the complete dummy for the final validation (Figure 7).

The computing time of a single thorax impact test by using the complete dummy is comparably long. So the drop test was used to make a quick pre-selection of the material model and the range of variation of material parameters. Thus it was possible to reduce the total time of validation of the torso foam. The final validation of the foam was done with the complete dummy including all functions such as internal contacts and

the fixation of the extremities to the skeleton with joints.

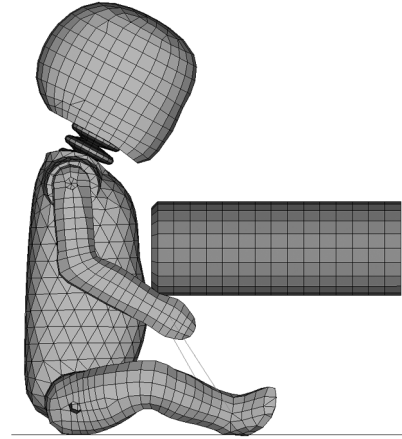


Figure 7. Set-up of thorax impactor test.

The arms of the dummy in the thorax impactor test were fixed at the legs with tape material. The mass of the impactor was about 2.6 kg and the impact velocity was 2.2, 3.2 and 4.3 m/s. The torso drop test were performed with the same velocities.

Based on the longitudinal accelerations of chest and impactor the maximum chest deflection and impact force were calculated. Both parameters were used for the validation of the torso foam.

Extremities

The extremities are not included in the certification procedures of the Q0. Therefore simple drop tests with different impact velocities, taken from the torso tests, were performed to get data to validate arms and legs of the model. Arm and leg were fixed with tape with their inner side under a steel plate (Figure 8). So load was applied to the parts in lateral direction.



Figure 8. Set-up of arm drop test.

Following the validation of the head, peak and a_{3ms} value of the vertical impactor acceleration were used as main parameters of the validation.

RESULTS

The sign conventions of the SAE J211 standard are used in the experiments and simulations for all measured values. Also all plots of these measures follow this standard.

Head

The head assembly was validated by varying the material model and the material properties of the skin layer of the head. All used material models have a visco-elastic characteristic. Finally MAT_062, a non-linear viscous foam, originally made for the rib padding of the EuroSID [3], was selected for the skin. The response of a linear material model cannot be as exact as a non-linear model at different impact velocities in this application.

The ratio between head acceleration in the frontal and in the lateral impact test with a drop height of 130 mm was the main problem in the validation. It has to be approximately 1.05, but finally 0.94 was achieved with MAT_062, the best compromise of all tested materials.

Table 2. Maximum head acceleration.

Set-up	Experiment	Simulation
frontal, 28°, 130 mm	116.6 g - 122.8 g av. 120.0 g	107.3 g
frontal, 45°, 376 mm	237.0 g - 276.3 g av. 254.9 g	273.9 g
lateral, 35°, 130 mm	110.6 g - 116.7 g av. 114.1 g	113.7 g

However, the maximum head acceleration as well as the a_{3ms} value correlate well with the experiment. Table 2 shows the maximum head acceleration of the finally selected and optimised viscous foam MAT_062. So the model fulfils the requirements of the certification tests.

The main influence parameters on the maximum head acceleration are the initial Young's modulus (E_1) and the exponent in power law for Young's modulus (n_1) [3]. A declining E_1 or n_1 reduces the maximum head acceleration and the width of the acceleration curve. In this case the a_{3ms} value increases. The influence of E_1 and n_1 increases with the impact velocity.

Except for the Poisson's ratio, which has only a slight influence on the head response, all other parameters of MAT_062 have in principle the same behaviour as E_1 and n_1 .

Figure 9 shows the acceleration curves of experiments and simulation in the 28° frontal impact configuration. The gradient of the acceleration in the model is lower than in the test. Additional simulations using MAT_062 and a mesh of smaller elements improved the shape of the curve, especially between 1.5 and 3.0 ms. At the same time the gradient of the declining edge gets slightly too high. A fine mesh generally stiffens the material, and the maximum acceleration increases.

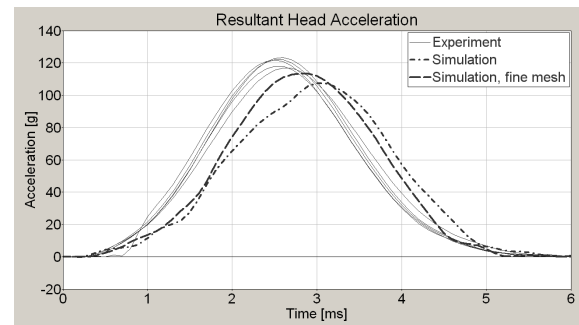


Figure 9. Head response in the 28° frontal impact.

The effect of stiffening the material to improve the shape of the curve affects also the other tested configurations. The shape of the head acceleration curve in the 45° frontal impact and the 35° lateral impact (Figure 10) correlates better with results of the experiments than in the 28° frontal impact.

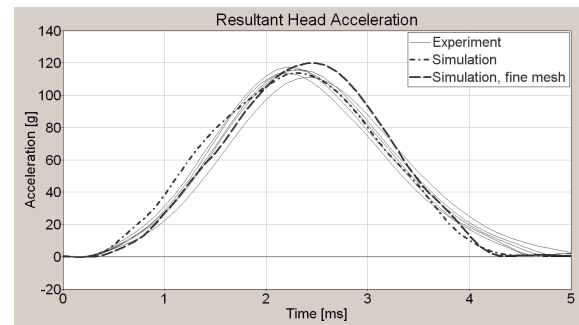


Figure 10. Head response in the 35° lateral impact.

However, the achieved results already show a good agreement with target values of the experiments. Modifications of the skin's mesh could improve the shape of the acceleration curves. Therefore in a next step the mesh of the skin will be modified and the material parameters will be adapted to this new mesh.

Neck

The model was validated by varying the type of visco-elastic material, the material properties, the thickness of the contact between the neck segments and level of detail of the FEA-mesh. MAT_006, a simple linear visco-elastic material model, was finally selected for the rubber parts of the neck. Other, more detailed visco-elastic materials of LS-Dyna offer more parameters to adapt the material in detail, but they had no advantage in this application. Furthermore the computing time of the neck was rather high when using these materials.

There are four parameters available in MAT_006, the elastic bulk modulus (BULK), a short-time (G0) and a long time (GI) shear modulus and finally the decay constant (BETA). Not all of them have the same effect on upper neck shear force, bending moment and head rotation angle.

The angle in all three loading configurations is mainly affected by the long-time shear modulus. An increasing GI reduces the head angle. The shear force is mainly influenced by G0 and BETA. They have opposite influence. An increasing G0 or a decreasing BETA are increasing the absolute shear force. The bending moment is mainly influenced by G0 and GI in extension bending and by BULK in flexion and lateral bending. Increasing BULK and G0 reduce and an increasing GI rises the measured torque.

A thick contact area reduces the bending angle of the neck, but it also has an influence on the moments. The torque is increasing under flexion bending and decreasing under extension bending with a thicker contact area.

MAT_001, an elastic material was chosen for the steel cable of the neck. The only varied influence parameter was Young's modulus E. Modifications of the cable stiffness affects mainly the rotation angle of the head, especially in the pendulum tests. A stiffer cable material reduces the angle.

The Young's modulus of the cable was only varied in the neck pendulum test set-up.

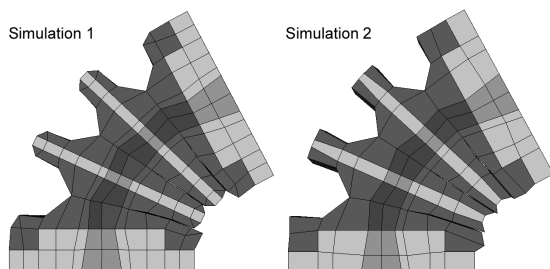


Figure 11. Different models of the neck in flexion test at 90 ms.

The structure of the FEA mesh of the neck is an important parameter for the overall performance of the neck model. Figure 11 shows the two different detailed neck models used. The fine mesh (Simulation 1) was firstly created and validated. Based on these experiences a less detailed mesh (Simulation 2) was created with the focus on computing time. So it was possible to reduce the computing time by 25% while keeping the same response characteristic.

Neck sled tests

First of all the neck was validated by using the results of the sled tests. Afterwards the material properties were slightly adapted to also fit to the pendulum tests. All diagrams with results of the sled tests show the response of the neck with material, validated only for this configuration. The results differ slightly, when the final material, resulting from the sled and pendulum tests is used.

The model of the neck was validated by using the same priority of flexion, extension and lateral bending. So the validated model is a well balanced compromise.

Figure 12 shows the neck moment at the OC-joint versus the head rotation angle in the flexion bending test. The neck is slightly too stiff, but there already is a good correlation of simulation and experiment. The peak at an angle of 7° in the rebound phase of the neck is coming from the shear force signal and is probably caused by contact problems of the neck and the stiff neck cable. This phenomenon also occurred in simulations with a higher pulse, but disappears when using a softer cable. However, in none of the simulations any element of the neck collapsed.

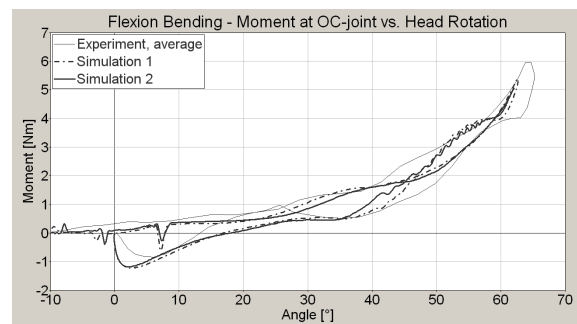


Figure 12. Neck flexion performance in sled test.

The response of the neck in the flexion bending test is shown in detail in Figure 13. While shear force F_x , head rotation angle are well correlated to the experiment, the moment M_y , the base of the OC-moment, is approximately 50% less than required. A change of the position of the sensor element within the load cell or a change of the centre of gravity of the head could

change this problem easily, because of the different length of the internal lever arm. However, both information are directly taken from the dummy and should not be modified. Furthermore, the extension and the lateral bending tests point out the correct position of both factors. So the only remaining option, is the modification of the material properties to increase M_y . All trials to increase the moment had too negative effects on the results of the extension and lateral bending response of the neck. The relevant deviation of M_y between experiment and simulation starts at 70 ms. At this time the head rotation angle reaches 50°. The contact between chin and chest limits the head rotation in the assembled dummy to this angle. So the problem of the missing moment is less critical and the deviation can be accepted.

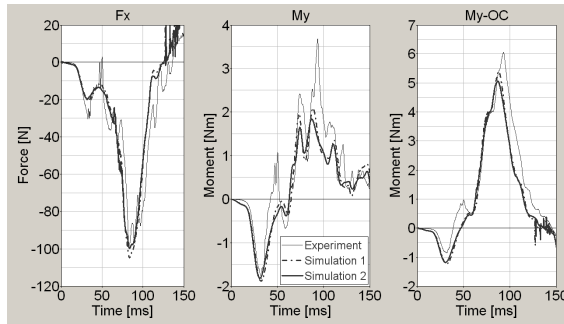


Figure 13. Neck response in flexion bending test.

The response of the neck in extension bending (Figure 14) and lateral bending (Figure 15) correlates well to the experiments up to a head angle of approximately 40°. The moment at the OC-joint is slightly too high in both load cases. The deviations of the single signals from the experiments are clearly smaller than in the flexion bending test.

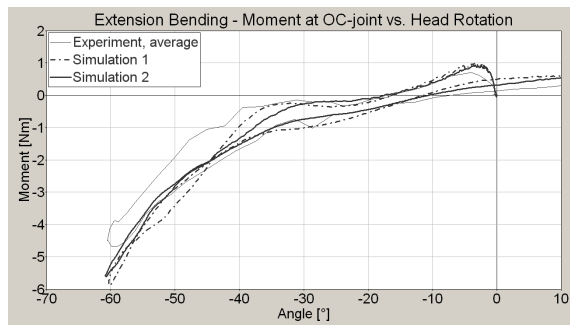


Figure 14. Neck extension performance in sled test.

The achieved correlation of the response of both neck models in all tested configurations is a good base

for the second step, the validation by using the neck pendulum test set-up.

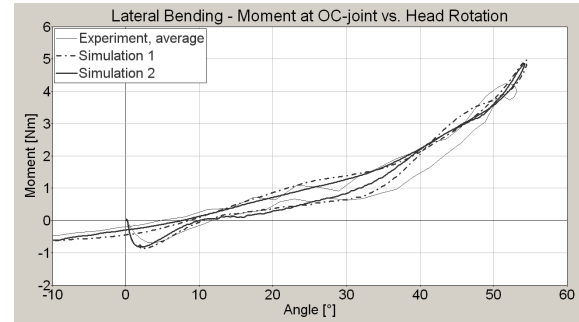


Figure 15. Neck lateral flexion performance in sled test.

Pendulum tests

The response of the neck models, validated only by using the sled tests, is already close to the results of the neck pendulum tests. Solely the head rotation differs significantly from the requirements. The validation started by varying the stiffness of the neck cable. These modifications have only limited influence on the upper neck shear force and bending moment. So the global response of the neck is not changed.

Figure 16 shows the response of the neck in the flexion test set-up. The results of both neck models are very close to the experimental data and within the biomechanical corridor of the neck flexion of a newborn child [4]. Furthermore the certification corridor at 50° is met by the numerical model.

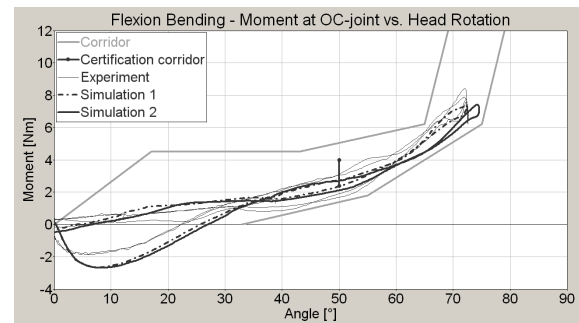


Figure 16. Neck flexion performance in pendulum test.

The model of the neck complies with the experimental data under extension loading up to 40° (Figure 17). Above this bending angle the model as well as the dummy leaves the biomechanical corridor. However, both models of the neck meet the certification requirements. The less detailed model

(Simulation 2) correlates slightly better to the experimental data than the more detailed one.

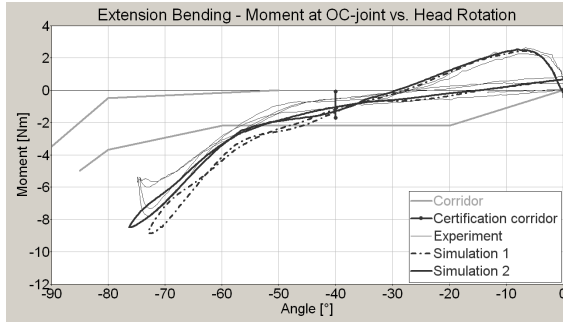


Figure 17. Neck extension performance in pendulum test.

The quality of the neck's response in lateral bending is similar to the extension test. Above an angle of approximately 40° the model tends to be too stiff (Figure 18). The results of the detailed neck model are again slightly worse than the results of the less detailed one. However, both models fulfil the requirements of the certification test.

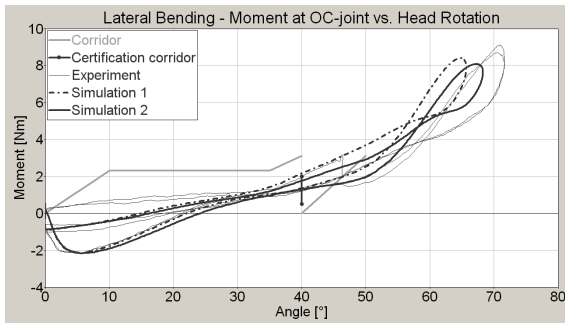


Figure 18. Neck lateral flexion performance in pendulum test.

The differences of the neck rubber material, validated for sled tests and for pendulum, are very little. Therefore the rubber material validated by using the neck sled tests was finally chosen. A softer neck cable, used in the pendulum simulations, also improves the neck response in the neck sled test configuration.

Both current versions of neck models were not validated to correlate also to the neck tension force F_Z . First simulations showed an acceptable correlation between simulation and experiment. In a next step the material properties of the neck's steel cable and the neck rubber will be slightly modified to get a better response of F_Z .

A decision, what neck model will finally be used for the dummy model has not been made yet. The final selection depends on the results of additional tests to

check the numerical robustness of the model and the head and neck response in full-dummy simulations.

Thorax

The torso foam was pre-validated by using data of drop tests. Different types of foam models were tested. Finally material MAT_083, a Fu-Chang foam [3], was chosen. This material model is also used for the abdominal block of the LS-Dyna model of the EuroSID.

Most of the material parameters of the EuroSID foam were transferred to the Q0 model. Only the Young's modulus E , the viscous coefficient to model damping effects (DAMP) and two stress-strain functions were varied. Both curves are based on a simple baseline stress-strain curve (Figure 19). They differ only due to scaling the magnitude of stress.

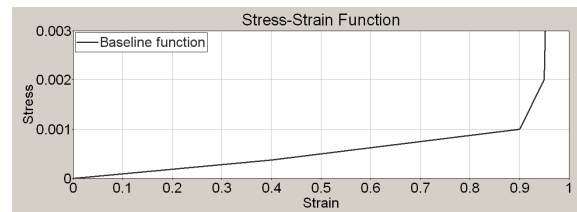


Figure 19. Baseline stress versus strain function.

Figure 20 shows exemplarily the Q0 model in the thorax validation test at 11 ms with an impact velocity of 4.3 m/s. All parts of the model are working well together and the kinematics of head, neck and spine is realistic.

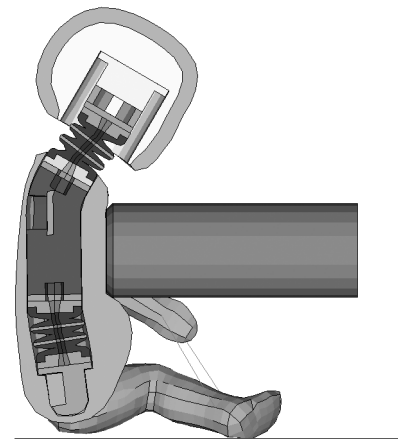


Figure 20. Section cut of the Q0 in impactor test.

The chest deflection, calculated from chest and pendulum acceleration, is mainly influenced by the amplitude of the stress-strain functions and the material damping. Stiffer functions and higher damping reduces the chest deflection. At the same time the

impactor force, calculated from the impactor acceleration and the impactor mass, increases. However, the force is mainly affected by the amplitude of the first stress-strain curve. DAMP and E have only a very small influence on the force.

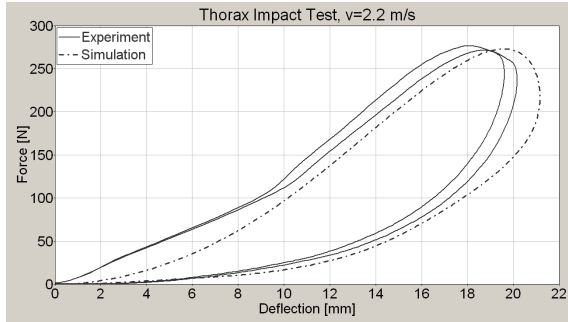


Figure 21. Force versus deflection curve at 2.2 m/s.

Figure 21 shows the force-deflection characteristic of the torso foam at an impact speed of 2.2 m/s. The foam is slightly too soft in this test. Especially the force during the first 10 mm of chest deflection is too low. However, the simulation is still very close to the experiment.

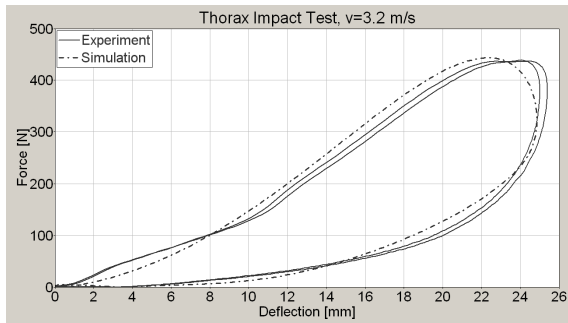


Figure 22. Force versus deflection curve at 3.2 m/s.

At an impact speed of 3.2 m/s the chest-deflection characteristic in the model is clearly closer to the experimental data (Figure 22). MAT_083 is obviously not able to reproduce the velocity dependent effects of the torso foam in the used configuration with only two material-describing stress-strain functions.

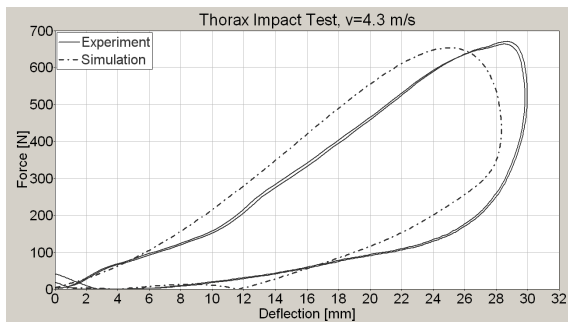


Figure 23. Force versus deflection curve at 4.3 m/s.

The results of the impact test at 4.3 m/s supports this assumption (Figure 23). The foam is too stiff under these conditions. In a next step one or two functions will be added to the material model to get a better response of the foam in the three load cases.

Extremities

Arms and legs of the Q0 dummy are made of the same material. So the same material model with the same properties was chosen for arms and legs.

The linear visco-elastic material MAT_006 was chosen for the extremities. The maximum acceleration of the impactor is mainly influenced by GI and BETA. An increasing GI and a decreasing BETA stiffen the material and the acceleration declines.

Figure 24 shows exemplarily the results of the arm drop test with a velocity of 3.2 m/s. The simulation correlates to the experiment in this configuration as well as in the other two with different impact speeds. The maximum acceleration of the impactor with a leg mounted is too low at all three velocities tested. The deviation varies from 14% at 2.2 m/s to 5% at 4.3 m/s. It was almost impossible to validate the model for the leg impactor test. Simulations, using non-linear material models to get a better velocity-dependent response, had no drastic advantage over MAT_006. The ratio between improvement of the response of the model and worsening of computing time was not acceptable.

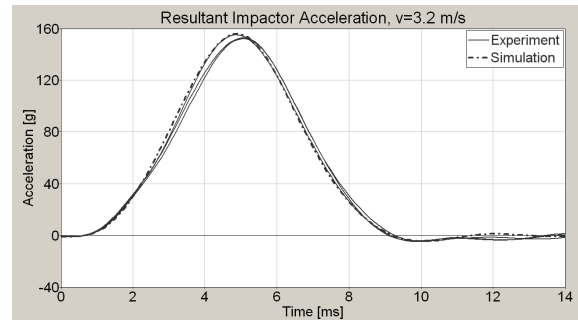


Figure 24. Acceleration in arm drop test at 3.2 m/s.

Figure 25 shows the resultant impactor acceleration of the leg impact test at 3.2 m/s. The increasing and the declining edge of the curve are close to the experimental data. Solely the peak value is not met.

One of the difficulties to validate the leg by using the results of drop tests could be the set-up of the tests. While the arm could easily be fixed with tape on the impactor plate and a large area of the arm had an initial contact to this plate, the fixation of the leg was difficult. Only spots at ankle, knee and thigh had an initial contact to the impactor plate. Therefore the position of

the leg was less fixed than the arm's. So the leg was able to move during the impact and its deformation. Since there were no high speed video recordings of the tests available, the kinematics of the parts could not be compared to the simulation. It was decided to validate the extremities in first priority with respect of the response of the arm and in second priority to the leg. However, the achieved results are acceptable.

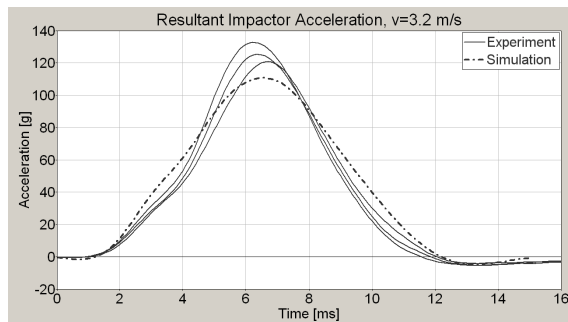


Figure 25. Acceleration in leg drop test at 3.2 m/s.

Application of the Q0

Some frontal impact simulations were done with a generic Group 0+ child restraint system and a 3-point harness to tests functionality of the dummy model (Figure 26).

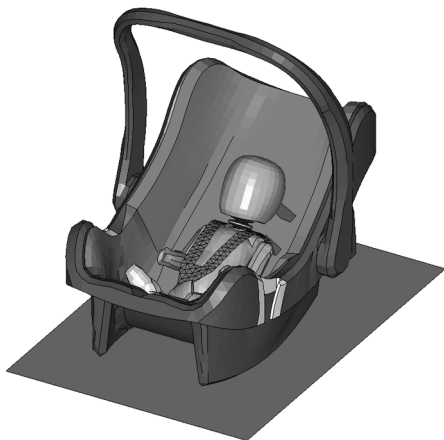


Figure 26. Q0 dummy model in a infant carrier.

It was difficult to place the dummy in the CRS because of the differences in clothing of babies and dummy. Certainly, in the current version of the model the suit is missing but it is very thin compared to diapers. A thick diaper changes the initial seating position and thus, the dummy's initial position to the harness changes as well. These differences may have an influence on the kinematics and the measured loads. In general it is easier to put a diaper on the dummy than on the dummy model.

LIMITATIONS

Until now the dummy is made of validated sub-parts. The thorax impactor test was the only test with all assembled body segments and their interior contacts. All achieved results are promising and the remaining problems seem to be solvable. However, the Q0 dummy model was so far not tested in a validated CRS environment and numerical stability limits of the model are unknown at the moment. So it may be possible that some parts have to be modified in the next phase of the dummy development.

FURTHER DEVELOPMENT

There is some work left to complete the development of the LS-Dyna Q0. Firstly, the response of the head will be improved by modification of the skin's FEA mesh. Secondly, the neck needs to be validated to the neck tension force F_z . Finally the response of the thorax could be improved. Therefore it is necessary to create a model of the dummy's suit.

Afterwards the dummy model will be used within CHILD for in-depth investigations of the dummy kinematics by using a CRS environment and data coming from full-scale accident reconstructions.

In parallel the model will be tested to get the limitations of the model in terms of numerical stability and the validation process.

The work on a MADYMO FEA-version of the Q0 dummy has already begun. It will be completed by end of 2005.

CONCLUSION

The current state of the Q0 LS-Dyna model already shows a good correlation to the Q0 hardware version. All non-deformable body segments were validated by using different test set-ups or different levels of loading. So the response of the dummy segments is not only valid for a single type of loading or impact.

The resultant peak acceleration of the head is within the range of the results of two of three head drop tests. It deviates from the minimum required level by 8% in the third drop test. In a next step the FEA mesh of the head's skin layer will be modified to improve the results.

The neck response in flexion, extension and lateral bending is already close to the results of experiments using a pendulum and a sled test set-up, respectively. Furthermore a more computing time efficient version was developed. It has a lower level of detail, but the results are partly better than of the more detailed model. Until now the neck was validated in terms of

shear force, bending moment and head rotation, but it also needs to be validated in the future for a good response of the neck tension force F_z .

The extremities were validated by again using a drop test configuration. The correlation of the model's response to the experiment is acceptable as there are no requirements in the certification procedures of the dummy. There is no intention to modify the achieved level of validation.

The torso foam was validated by using results of impactor tests with the complete dummy. The overall performance of the model in terms of kinematics and response of the dummy sensors is more than acceptable. In a next step the material of the torso foam will be slightly modified to get better results at different impact velocities. Furthermore the model will be equipped with a model of the dummy's suit.

The current version of the Q0 dummy model is ready for the use within the CHILD project. It is needed for some in-depth studies of dummy kinematics and some parametric studies to support the experimental task of the project.

ACKNOWLEDGEMENTS

The development of the Q0 dummy model is embedded in the CHILD project (G3RD-CT-2002-00791) and is founded by the European Commission. More information is available on the website <http://www.childincarsafety.com>.

The authors would like to thank TNO Automotive and FTSS Europe for supporting the work with the provision of CAD data, results of component tests and a Q0 prototype.

REFERENCES

- [1] American Code of Federal Regulations 49, Part 572 Subpart R,
- [2] American Code of Federal Regulations 49, Part 572E
- [3] "LS-Dyna - Keyword User's Manual",
Livermore Software Technology Corporation,
April 2003, Version 970
- [4] Waagmeester, C. D.
"Q0 Dummy User's Guide",
TNO Automotive, January 23rd, 2003

COMPARISON OF THE INERTIAL RESPONSE OF THE THOR-NT, HYBRID III, AND UNEMBALMED CADAVER TO SIMULATED KNEE-TO-KNEE-BOLSTER IMPACTS

Jonathan D. Rupp, Matthew P. Reed,

Nathaniel H. Madura, Carl S. Miller

University of Michigan Transportation Research
Institute, USA

Shashi Kuppa

National Highway Traffic Safety Administration,
USA

Lawrence W. Schneider

University of Michigan Transportation Research
Institute, USA

Paper Number 05-0086

ABSTRACT

The inertial responses of five seated unembalmed midsize cadavers to sub-injury knee impact loading were characterized and compared to the inertial responses of the Hybrid III midsize male and THOR-NT ATDs collected under similar knee loading conditions. All impacts were performed using a 275-kg padded impactor to symmetrically load the left and right knees at velocities of either 1.2 or 3.5 m/s. At both knee impact velocities, the Hybrid III and THOR-NT produced peak knee impact forces that were substantially higher than those of the cadaver. At the 1.2 m/s impact velocity, the peak knee impact forces produced by the cadavers varied from 0.9 to 1.0 kN while the peak knee impact forces produced by the THOR and Hybrid III were 1.4 and 1.6 kN, respectively. The two cadavers tested at the 3.5 m/s impact velocity produced peak applied forces of 3.5 and 3.8 kN, while the THOR and Hybrid III produced peak applied forces averaging 5.5 and 6.1 kN, respectively.

For both knee impact velocities, femur and pelvis accelerations produced by both ATDs and the cadavers were similar in magnitude. However, peaks in cadaver femur and pelvis accelerations occurred substantially earlier than peaks in cadaver knee impact force, while peak Hybrid III and THOR femur and pelvis accelerations occurred at the time of peak force. These differences are most likely due to loosely coupled mass in the cadaver that is not represented in either ATD.

INTRODUCTION

Fractures and dislocations of the knee-thigh-hip (KTH) complex in frontal crashes are of substantial concern to automotive safety engineers and clinicians because of the frequency at which these injuries occur and the associated potential for long-term disability (Kuppa et al. 2001, Read et al. 2002, Burgess et al. 1999). Of all AIS 2+ KTH injuries, hip injuries, and in particular acetabular fractures, are the most frequent, occurring at a rate of almost 14,000 per year (Rupp et al. 2001).

A research program is underway at the University of Michigan Transportation Research Institute to develop new KTH injury criteria that can assess the risk of hip injury in frontal crashes. To date, this program has demonstrated that under dynamic knee loading, the hip has a tolerance of 6.1 kN and is the weakest component of the KTH complex with the pelvis and femurs oriented in a seated automotive posture (Rupp et al. 2002, 2003a). The 6.1-kN hip tolerance was determined using a fixed pelvis boundary condition and is therefore representative of the fracture tolerance of the hip in terms of force applied to the hip. However, under real-world knee-to-knee-bolster loading, the force at the knee is greater than the force at the hip because there is mass proximal and distal to the hip that is decelerated by knee-bolster impact. To determine the risk of hip injury associated with a force applied to the knee, it is therefore necessary to know the decrease in force between the knee and the hip, which is governed by the inertial response of the knee-thigh-hip complex. In addition, to develop improved KTH injury criteria it is necessary to know how forces measured by ATD load cells relate to force at the human hip under similar knee impact conditions.

Horsch and Patrick (1976) attempted to characterize the inertial response of the cadaver to knee impact loading by measuring force applied to the knees of unembalmed cadavers and the resulting femur accelerations under high-rate sub-fracture impact loading by a flat-faced rigid ballistic pendulum. Inertial response of the cadaver to knee impact loading was reported as an effective mass, which was calculated by dividing the force applied to the knee by the acceleration of the femur. For the four cadavers tested, the effective mass of each side of the

body was approximately 2.0 kg immediately prior to the time of peak force, after which femur acceleration rapidly approaches zero and the effective mass calculation fails.

Because Horsch and Patrick used a rigid impactor, peak forces occurred approximately 2 ms after the onset of knee loading. Stalnaker et al. (1977) have shown that it takes 2-5 ms after the start of force application for a reaction force to be developed at the pelvis. In other words, 2-5 ms are needed for the femur to displace a sufficient amount to start recruiting the mass of the pelvis. Thus, the 2.0 kg effective mass value reported by Horsch and Patrick is likely representative of the effective mass of the skeletal knee/femur complex and does not accurately represent effective mass of one side of the body under longer-duration knee impacts, such as those observed in FMVSS 208 and NCAP.

Horsch and Patrick also characterized the inertial response of the Hybrid II ATD in the same manner that cadaver inertial response was characterized. The effective mass of the Hybrid II under impact of one knee was approximately 11.5 kg. The Hybrid II also produced peak knee impact forces that were 1.5 to 3.7 times greater than those produced in the cadaver knee impacts. The hypothesized reasons for the differences between Hybrid II and cadaver response were that the Hybrid II KTH complex is stiffer and has more tightly coupled mass than the cadaver.

The current study expands on the data collected by Horsch and Patrick by characterizing the inertial response of unembalmed cadavers under longer duration knee loading conditions and comparing these inertial responses to those of the Hybrid III and THOR-NT ATDs.

METHODS

Cadaver Tests¹

The characteristics of the five unembalmed cadavers used in this study are listed in Table 1. All subjects were males that were close to the 176 cm midsize male stature. Subject masses varied from 66 to 89 kg and averaged 77 kg.

Figure 1 shows the apparatus used to determine the inertial response of the cadavers under knee impact loading. Simultaneous loads are applied to the left and right knees of a seated cadaver by pneumatically accelerating a 275-kg platform to a velocity of 1.2 m/s or 3.5 m/s prior to knee impact. Load cells on the forward surface of the platform were used to independently measure the force applied to the left and right cadaver knees. The acceleration of the mass on the forward surface of each load cell was measured and used to inertially compensate all force measurements. As shown on the right-hand side of Figure 1, the left and right knee impact surfaces were padded. For the 1.2 m/s knee impacts, each knee was padded with 38-mm thick 50-durometer (Shore OO scale) Sorbethane padding. As indicated in Table 1, this combination of padding and impact velocity was used in tests of all five cadavers.

Because the 1.2 m/s knee impact condition produced peak forces and loading rates that were substantially less than those produced in FMVSS 208 and NCAP compliance tests, a second set of impacts was performed to determine how the inertial response of the cadaver changes when the knee is loaded with forces and loading rates that are more representative of those produced in FMVSS 208 and NCAP tests. The higher loading rates and higher knee impact forces in this second test condition were generated by increasing impactor velocity to 3.5 m/s and padding the knee impact surface with 25 mm 70-durometer Sorbethane and 25-mm thick 50-durometer Sorbethane.

Cadavers were instrumented by rigidly attaching triaxial accelerometer blocks to the midshaft femur and sacrum. Each cadaver was dressed in a Lycra leotard. Prior to each test, the cadaver was seated on a force platform that was covered with a low friction surface to ensure that friction on the pelvis and thighs did not substantially affect the force applied to the knee. Shear forces measured by the force platform were used to verify that friction forces were low in all tests (< 50 N in the 1.2 m/s tests and less than < 150 N for the 3.5 m/s tests). The fore-aft position of the cadaver on the force platform was adjusted to ensure that the cadaver was able to slide 15-20 cm rearward on the platform prior to contact between the posterior leg and the forward surface of the force platform.

¹ The rights, welfare, and informed consent of the subjects who participated in this study were observed under guidelines established by the U.S. Department of Health and Human Services on Protection of Human Subjects and accomplished under medical research design protocol standards approved by the Committee to Review Grants for Clinical Research and Investigation Involving Human Beings, Medical School, The University of Michigan.

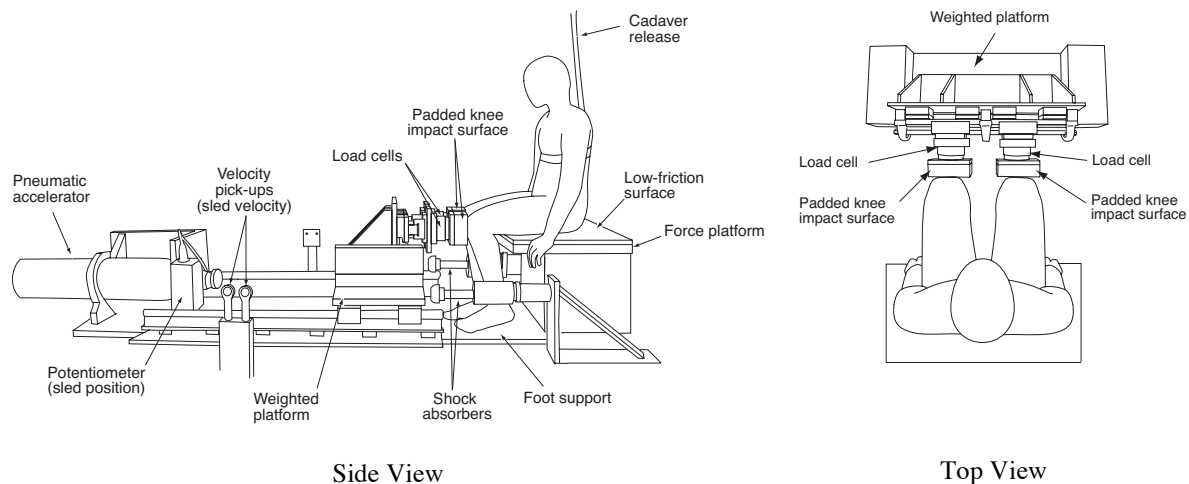


Figure 1. Apparatus used for dynamic femur response assessment.

The cadaver's feet were supported by a second force platform. The heights of the foot support and the cadaver-seating platform were adjusted so that the long axis of the femur was horizontal. The fore-aft positions of the cadaver's feet were adjusted so that the included angle between the tibia and the femur was approximately 90°. The lateral spacing between the centers of the knee impact surfaces was adjusted so that, in an overhead view, the shaft of the femur was aligned with the direction of impact.

Table 1. Cadaver Characteristics and Test Conditions

Subject Number	Gender	Age	Stature (cm)	Mass (kg)	Knee Impact Velocity	
					1.2 m/s	3.5 m/s
1	M	66	179	89	X	
2	M	64	178	82	X	
3	M	66	178	73	X	
4	M	76	178	70	X	X
5	M	82	180	66	X	X
	<i>Mean</i>	70.8	178.6	76.0		
	<i>sd</i>	7.8	0.9	9.4		

The cadaver's torso was held in an upright position by a strap that was looped under the cadaver's arms and around the cadaver's chest and connected to a release mechanism. About 20 ms prior to knee impact, the release mechanism was actuated, thereby allowing the cadaver to move rearward with minimal constraint during impact loading.

Because any asymmetry in cadaver knee positions could result in differences in the magnitudes and the phasing of the forces applied to the knees, a repetitive test protocol was used. The knees of each cadaver were impacted multiple times until three to five impacts had been performed on each cadaver for

which the magnitudes and phasing of the applied forces were very close. Overhead and side view high-speed videos of the impact event were recorded and used to ensure that the cadaver knees were symmetrically contacted, that the cadaver was released prior to impact, and that the kinematics of the left and right sides of the body were similar.

As shown in the Appendix, forces applied to the left and right knees and the left and right resultant femur accelerations from each test on the same subject were similar and were therefore averaged at each point in time to determine an average resultant femur acceleration and average applied force. The average applied forces, average femur accelerations, and pelvis accelerations in repeated tests on the same subject were also similar and were averaged to determine a representative applied force and femur and pelvis accelerations for each subject.

For each test performed on a subject, the inertial resistance to motion of the left and right sides of the body were calculated as described by Equation 1, where the forces applied to the left and right knees are divided by the resultant pelvis acceleration to determine effective masses. Left- and right-sided effective mass histories calculated using pelvis acceleration were similar and were therefore averaged to determine a single pelvis-acceleration-based effective-mass response for each test.

Effective mass histories from each subject were also calculated, as described in Equation 2, by dividing the left and right applied force by the left and right resultant femur accelerations, respectively. An average femur-acceleration-based effective-mass history for each test was calculated by averaging the

left and right effective mass histories calculated using femur acceleration.

Each set of femur- and pelvis-acceleration-based effective-mass histories from repeated tests on single subject were similar and were therefore averaged to determine a single femur-acceleration-based effective mass history and a single pelvis-acceleration-based effective-mass history for each subject.

$$M_{eff} = \frac{F_{\text{applied to knee}}}{a_{\text{pelvis resultant}}} \quad [1]$$

$$M_{eff} = \frac{F_{\text{applied to knee}}}{a_{\text{femur resultant}}} \quad [2]$$

To provide a reference point for comparing effective mass histories, the effective mass at the time of peak force was determined from each of the average left and right-sided effective mass curves. The range associated with each peak effective mass value was also determined using the average of the left and right effective mass values from each of the repeated tests on a single subject.

Hybrid III and THOR-NT Response Tests

The inertial responses of the Hybrid III and THOR-NT were determined using the same test apparatus and test procedures described for the cadaver tests. Repeated tests were performed at impact velocities of 1.2 m/s and 3.5 m/s until five tests had been performed where the timing of the left and right knee contacts was similar. Force applied to the ATD knees and accelerations of the femur and pelvis were measured.

Each ATD was equipped with tri-axial pelvis accelerometer blocks and left and right six-channel femur load cells. The THOR-NT was also equipped with the standard 3-axis acetabular load cells. Tri-axial accelerometer blocks were mounted to the mid shaft of the Hybrid III femur and to the THOR femur proximal to the compliant element. Prior to testing, the knee-thigh-hip response of the THOR and the knee response of the Hybrid III were calibrated using standard procedures (Society of Automotive Engineers 1998, Shams 2004).

ATD positioning for all tests was similar to the cadaver positioning. Both ATDs sit upright with minimal assistance, so the release mechanism was not needed in the ATD tests.

RESULTS

Cadaver Responses

1.2 m/s Knee Impacts

Figure 2 compares the applied force histories from each of the five cadavers. Applied force histories from all tests were similar with peak applied forces varying between 900 and 1000 N. Figures 3 and 4 compare the average pelvis and femur acceleration histories. Acceleration at the time of peak force is indicated in Figures 3 and 4 by a filled circle. Both femur and pelvis accelerations peak at between 6 and 8 g. In addition, both femur and pelvis accelerations peak approximately 6-8 ms earlier than the time of peak applied force. Figure 5 illustrates that, until the time of peak acceleration, femur acceleration leads pelvis acceleration.

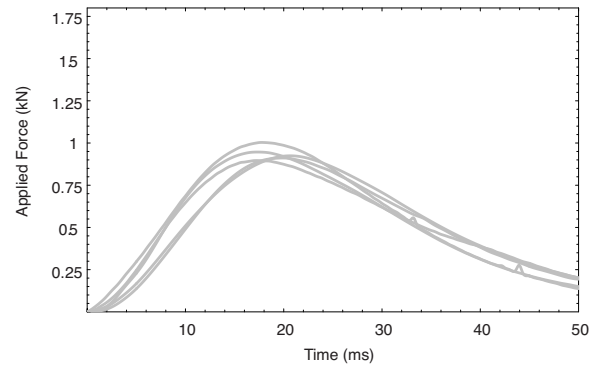


Figure 2. Applied force histories from cadaver tests at the 1.2 m/s impact velocity.

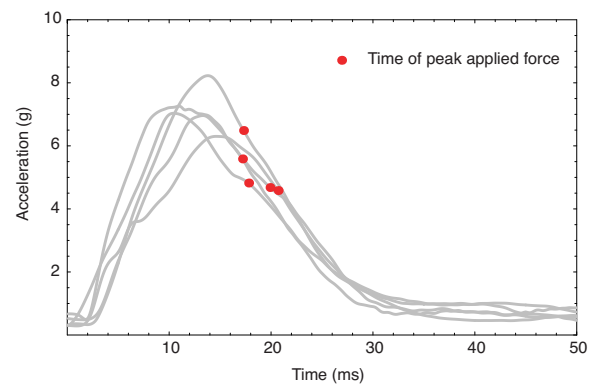


Figure 3. Resultant pelvis accelerations from cadaver tests at the 1.2 m/s impact velocity.

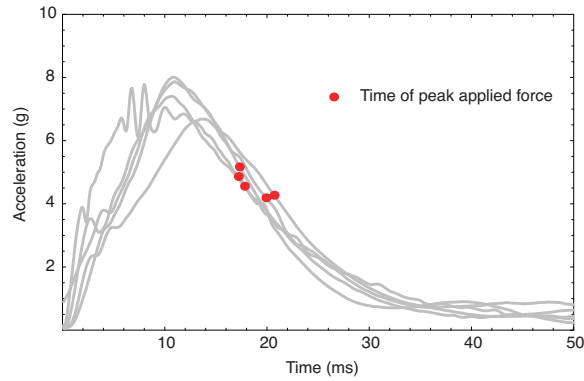


Figure 4. Resultant pelvis accelerations from cadaver tests at the 1.2 m/s impact velocity.

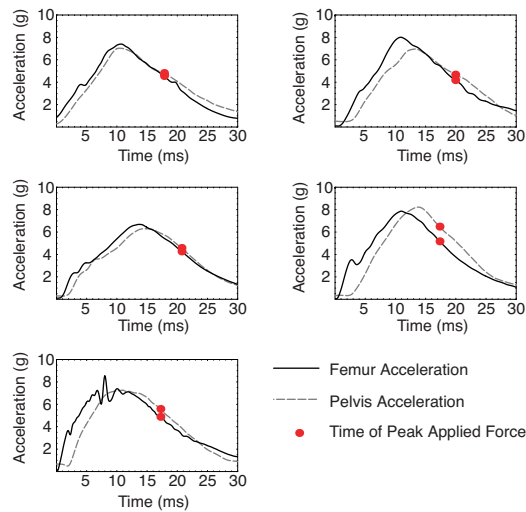


Figure 5. Femur and pelvis accelerations from all cadaver tests at the 1.2 m/s impact velocity.

Figures 6 and 7 show the effective mass histories from each cadaver calculated using the resultant pelvis and femur accelerations, respectively. The shaded regions in Figures 6 and 7 are where the effective mass calculation fails because femur and pelvis accelerations are low, and consequently, small variations in acceleration result in large changes in effective mass values. Figures 6 and 7 both show that the effective mass of the cadaver is initially low and then steadily rises over the course of the loading event. The effective mass history calculated using pelvis acceleration is initially higher than the effective mass history calculated using femur acceleration because pelvis acceleration is initially lower than femur acceleration and consequently, when the same applied force is divided by pelvis acceleration, a higher effective mass is produced.

Table 2 lists the effective masses at the time of peak force calculated using femur and pelvis accelerations for each of the five cadavers. The overall average effective mass at the time of peak force calculated using pelvis acceleration is 20.4 kg (Range: 17.2-26.1 kg). The overall average effective mass at the time of peak force calculated using resultant femur acceleration is 21.4 kg (Range: 14.9-23.3).

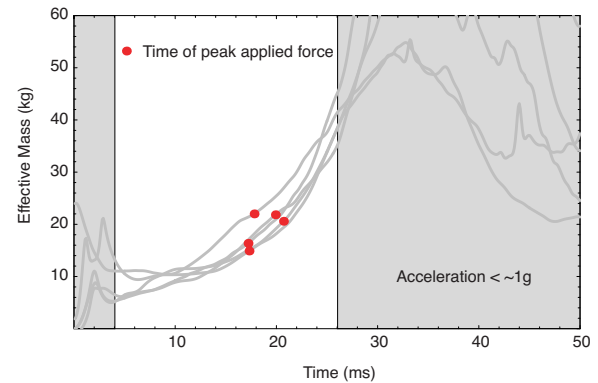


Figure 6. Pelvis-accleration-based-effective-mass histories from cadaver tests at the 1.2 m/s impact velocity.

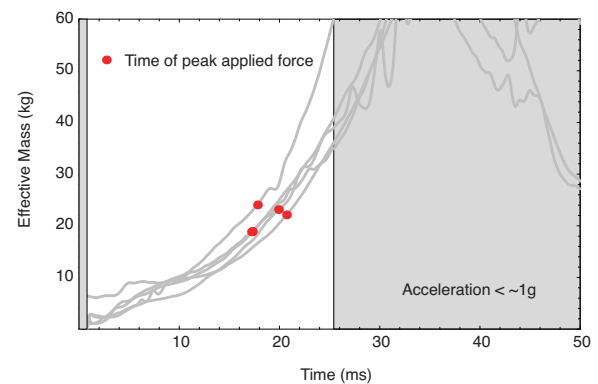


Figure 7. Femur-accleration-based-effective-mass histories from cadaver tests at the 1.2 m/s impact velocity.

Table 2. Cadaver Effective Mass at the Time of Peak Applied Force at the 1.2 m/s Impact Velocity

Subject	Calculated with Pelvis Acceleration, kg (Min-Max)	Calculated with Femur Acceleration, kg (Min-Max)
1	22.0 (21.3-23.3)	24.1 (21.2-26.1)
2	21.8 (19.1-22.7)	23.1 (19.0-23.1)
3	20.6 (20.1-21.0)	22.1 (21.2-22.6)
4	14.9 (14.9-15.5)	18.9 (17.2-20.0)
5	16.4 (16.2-16.6)	18.8 (18.7-19.0)
Overall Average (Range)	20.4 (17.2-26.1)	21.4 (14.9-23.3)

3.5 m/s Knee Impacts

Figure 8 shows the force histories from the two sets of sub-injury effective mass tests that were performed at the 3.5 m/s knee impact velocity. Peak forces for these tests are 3.5 and 3.8 kN.

Figure 9 shows the resultant pelvis acceleration from one of the two sets of cadaver tests that were performed at the 3.5 m/s knee impact velocity. Instrumentation problems preventing the collection of pelvis accelerations from the other set of tests at the same impact velocity, and pelvis accelerations from this subject were therefore excluded from Figure 9. Figure 10 shows the average resultant femur accelerations from the two cadavers that were tested at the 3.5 m/s impact velocity. Figures 9 and 10 also illustrate the pelvis and femur accelerations at the time of peak applied force. As was the case at the lower impact velocity, both the cadaver femur and pelvis accelerations peak earlier than applied force peaks.

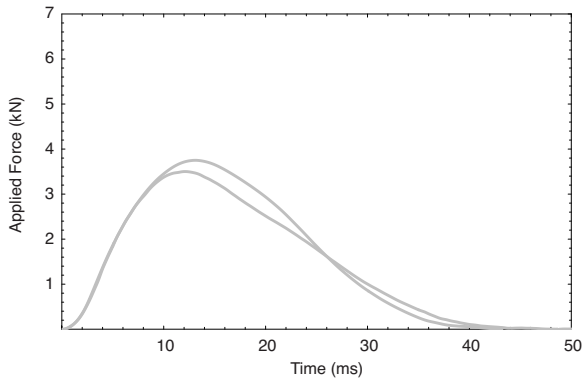


Figure 8. Applied force histories from cadaver tests at the 3.5 m/s impact velocity.

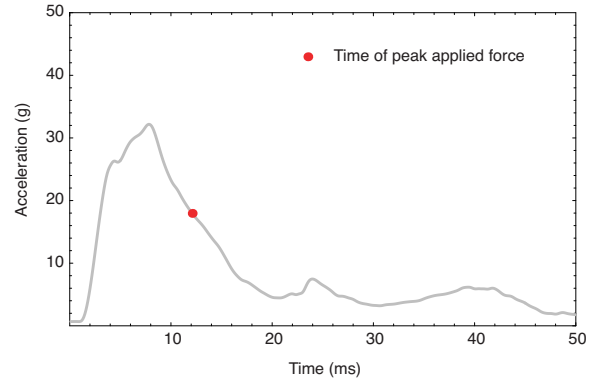


Figure 9. Resultant pelvis acceleration from the single cadaver test at the 3.5 m/s impact velocity.

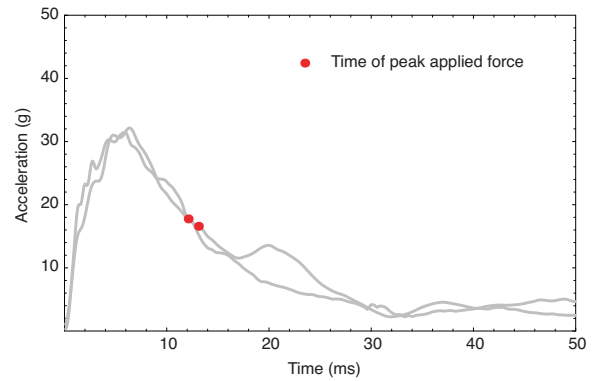


Figure 10. Resultant femur accelerations from cadaver tests at the 3.5 m/s impact velocity.

Figures 11 and 12 show the effective mass histories calculated from pelvis and femur accelerations, respectively. Both of these effective mass histories are similar to their lower speed counterparts. That is, Figures 11 and 12 show that cadaver effective mass increases until slightly after the time of peak force. The effective mass history calculated using pelvis acceleration is initially higher than the effective mass history calculated using femur acceleration because pelvis acceleration is initially lower than femur acceleration and consequently, when the same applied force is divided by pelvis acceleration, a higher effective mass is produced.

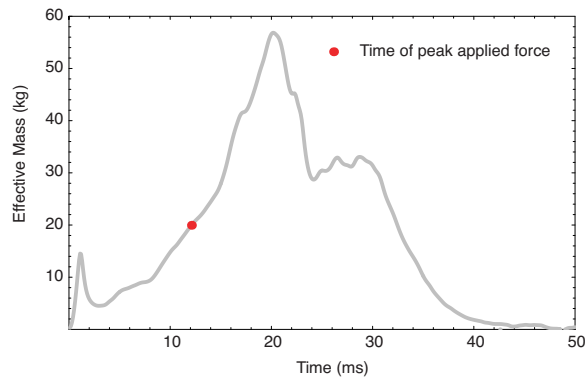


Figure 11. Pelvis-acceleration-based effective mass history from the 3.5 m/s impact velocity.

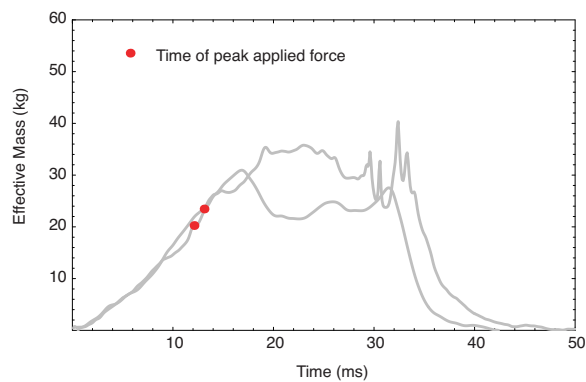


Figure 12. Femur-acceleration-based effective mass histories from cadaver tests at the 3.5 m/s impact velocity.

Table 3 lists the effective masses at the time of peak force calculated using femur and pelvis accelerations. The effective mass at the time of peak force calculated using pelvis acceleration is 20.0 kg (Range: 19.2-21.3 kg) for the single subject where pelvis accelerations were successfully measured. The effective masses at the time of peak force calculated using resultant femur acceleration are 23.5 kg (Range: 22.5-24.4 kg) and 20.3 kg (Range: 19.8-22.2 kg). These values and the ranges of these values are greater than the effective mass values and associated ranges from Subjects 4 and 5 calculated from the 1.2 m/s impact data.

Table 3. Effective Mass From Cadaver Tests at the Time of Peak Force at the 3.5 m/s Impact Velocity

Subject	Calculated with Pelvis Acceleration, kg (Min-Max)	Calculated with Femur Acceleration, kg (Min-Max)
4		23.5 (22.5-24.4)
5	20.0 (19.2-21.3)	20.3 (19.8-22.2)

THOR-NT, Hybrid III and Cadaver Responses

1.2 m/s Knee Impacts

Figure 13 compares the knee impact forces from 1.2 m/s cadaver tests to similar impacts to the knees of the Hybrid III and THOR-NT ATDs. The knee impact forces produced by the THOR-NT averaged to approximately 1.4 kN, while the knee impact forces produced in tests with the Hybrid III averaged to approximately 1.6 kN. These values are both substantially greater than the 940 N average peak knee impact force produced in cadaver tests.

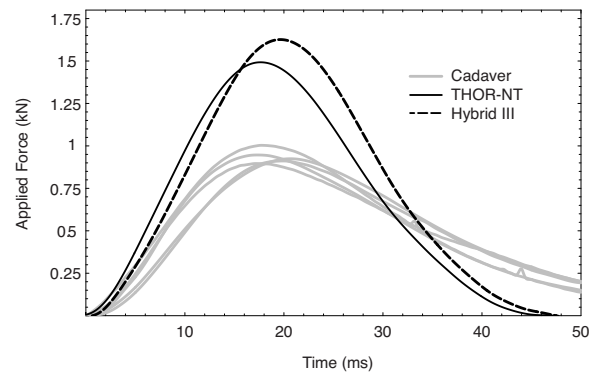


Figure 13. Comparison of cadaver applied force histories with applied force histories applied to THOR-NT and Hybrid III at the 1.2 m/s impact velocity.

Figure 14 compares pelvis accelerations from the cadaver tests to tests with the THOR-NT and Hybrid III. Figure 15 compares femur accelerations from the tests with cadavers and the two ATDs. The magnitudes of the femur and pelvis accelerations measured from both ATDs are similar to those measured in similar cadaver tests. However, peak ATD femur and pelvis accelerations occur later than peak cadaver femur and pelvis accelerations. In addition, both the THOR and Hybrid III femur and pelvis accelerations peak at the same time applied force peaks, while applied force peaks after femur and pelvis accelerations in all cadaver tests.

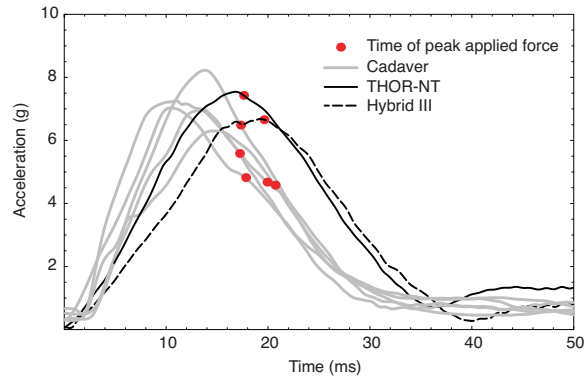


Figure 14. Comparison of cadaver pelvis accelerations with pelvis accelerations histories from THOR-NT and Hybrid III at the 1.2 m/s impact velocity.

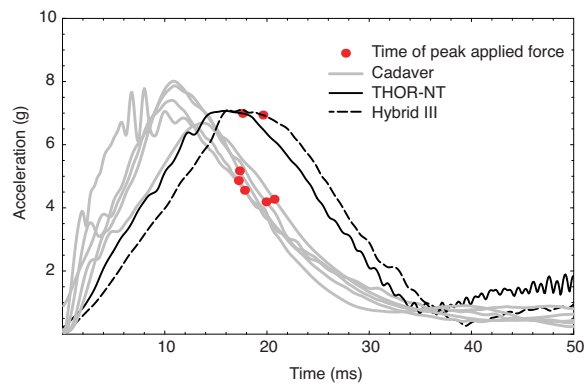


Figure 15. Comparison of cadaver femur accelerations with femur accelerations histories from THOR-NT and Hybrid III at the 1.2 m/s impact velocity.

Figure 16 compares the effective mass histories calculated using the pelvis accelerations from the THOR, Hybrid III and cadavers, while Figure 17 compares the effective mass histories calculated using femur acceleration. Effective mass calculated using femur and pelvis accelerations from ATDs increases rapidly during the early part of the effective mass history and then gradually increased for the remainder of impact loading.

Table 4 compares the Hybrid III and THOR effective masses at the time of peak applied force calculated using femur and pelvis accelerations. The Hybrid III effective masses at the time of peak force calculated using pelvis and femur accelerations are 24.9 kg (Range: 24.6-25.3 kg) and 24.0 kg (Range: 23.5-24.5 kg), respectively. The THOR effective masses at the time of peak force calculated using pelvis and femur accelerations are 20.5 kg (Range: 20.1-21.2 kg) and 22.0 kg (Range: 21.7-22.7 kg), respectively. These values are similar to the overall average cadaver effective mass calculated using similar methods.

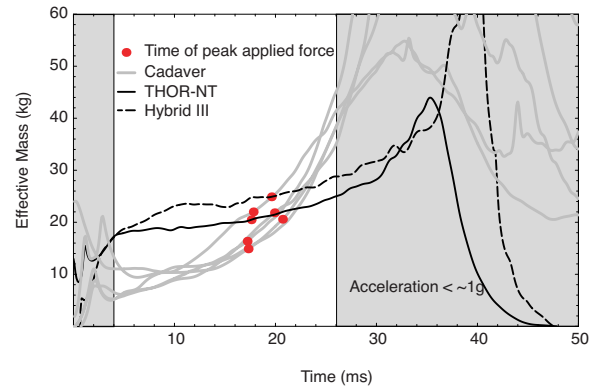


Figure 16. Pelvis-acceleration-based effective-mass histories from THOR-NT and Hybrid III compared to cadaver effective mass histories at the 1.2 m/s impact velocity.

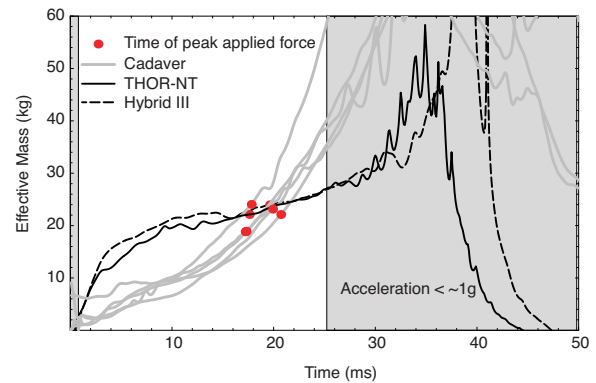


Figure 17. Femur-acceleration-based effective-mass histories from THOR-NT and Hybrid III compared to cadaver effective mass histories at the 1.2 m/s impact velocity.

Table 4. Effective Mass From Cadaver and ATD Tests at the Time of Peak Force at the 1.2 m/s Impact Velocity

Subject	Calculated with Pelvis Acceleration kg (Min-Max)	Calculated with Femur Acceleration, kg (Min-Max)
Overall Average Cadaver	20.4 (17.2-26.1)	21.4 (14.9-23.3)
Hybrid III	24.9 (25.3-24.6)	24.0 (23.5-24.5)
THOR-NT	20.5 (20.1-21.2)	22.1 (21.7-22.7)

3.5 m/s Knee Impacts

Figure 18 compares the applied force histories from the THOR-NT and Hybrid III to the applied force histories from the cadavers for tests at the 3.5 m/s knee impact velocity. Peak applied forces produced by impacts to the THOR and Hybrid III knees were 5.5 kN, and 6.1 kN, respectively. In comparison,

peak forces produced in the cadaver tests were 3.5 and 3.8 kN.

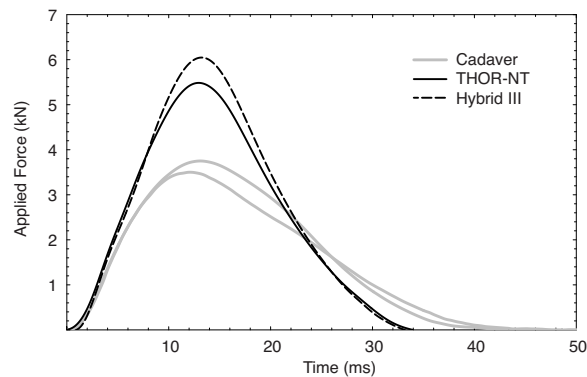


Figure 18. Comparison of applied force histories from cadaver, THOR-NT and Hybrid III at the 3.5 m/s impact velocity.

Figure 19 compares pelvis accelerations from the Hybrid III and THOR-NT with pelvis acceleration from the single cadaver that produced usable pelvis acceleration data at the 3.5 m/s knee impact velocity. Figure 20 compares the femur accelerations from the THOR and Hybrid III with similar quantities from the cadaver tests. Similar to the 1.2 m/s responses, the peak ATD femur and pelvis accelerations are similar in magnitude to the peak cadaver femur and pelvis accelerations. Also like the 1.2 m/s knee impacts, the peak ATD femur and pelvis accelerations occur at the same times as peak applied force while the peak cadaver femur and pelvis accelerations occur approximately 6 ms earlier in the impact event than peak applied force.

Figures 21 and 22 compare effective mass histories from cadavers and ATDs calculated using pelvis and femur accelerations, respectively. Similar to the results from 1.2 m/s testing, effective mass calculated using femur and pelvis accelerations from ATDs increased rapidly during the early part of the effective mass history followed by a gradual increase in effective mass until after the time of peak force. Table 5 lists ATD and cadaver effective masses at the time of peak force calculated using femur and pelvis accelerations from the 3.5 m/s tests. The effective masses at the time of peak force calculated using Hybrid III and THOR pelvis accelerations are 23.0 kg (Range: 20.1-20.5 kg) and 17.0 kg (Range: 16.4-17.4 kg). These values and the ranges of these values are similar to the effective mass from Subject 4 calculated under similar loading conditions.

The effective masses at the time of peak force calculated using Hybrid III and THOR femur

accelerations are 21.3 (Range 20.7-21.8) and 17.0 kg 19.0 (Range 18.4-19.2). These values and the ranges of these values are similar to the effective mass from Subjects 4 and 5 calculated under similar loading conditions.

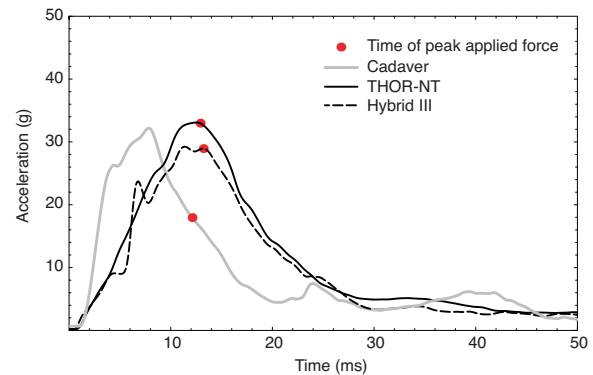


Figure 19. Comparison of cadaver pelvis accelerations with pelvis accelerations histories from THOR-NT and Hybrid III at the 3.5 m/s impact velocity.

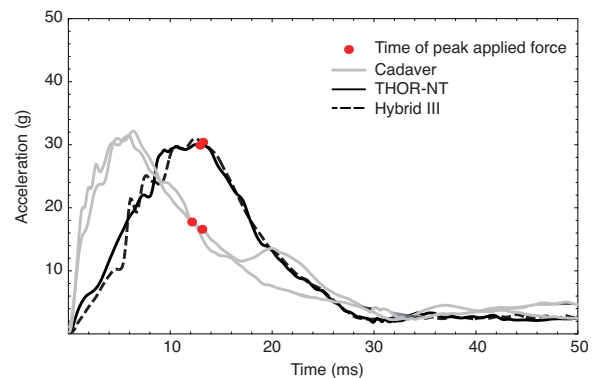


Figure 20. Comparison of cadaver femur accelerations with femur accelerations histories from THOR-NT and Hybrid III at the 3.5 m/s impact velocity.

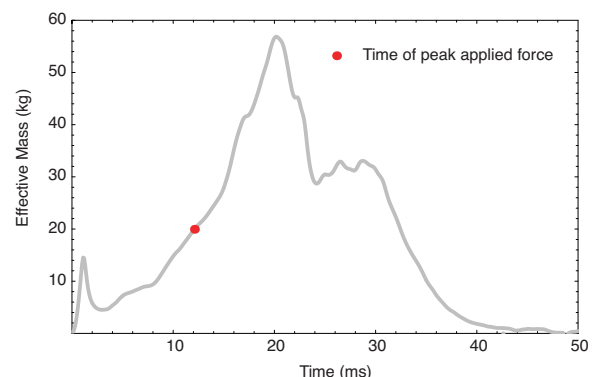


Figure 21. Pelvis-acceleration-based effective-mass histories from THOR-NT and Hybrid III compared to cadaver effective mass histories at the 3.5 m/s impact velocity.

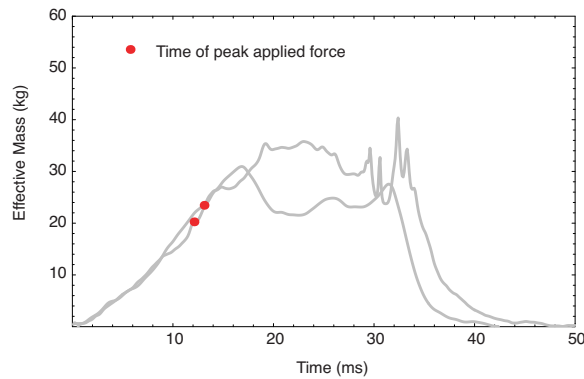


Figure 22. Femur-acceleration-based effective-mass histories from THOR-NT and Hybrid III compared to cadaver effective mass histories at the 3.5 m/s impact velocity.

Table 5. Effective Mass From Cadaver and ATD Tests at the Time of Peak Force at the 3.5 m/s Impact Velocity

Subject	Calculated with Pelvis Acceleration, kg (Max-Min)	Calculated with Femur Acceleration, kg (Max-Min)
4		23.5 (22.5-24.4)
5	20.0 (19.2-21.3)	20.3 (19.8-22.2)
Hybrid III	20.3 (20.1-20.5)	21.3 (20.7-21.8)
THOR-NT	17.0 (16.7-17.4)	19.0 (18.4-19.2)

DISCUSSION

The inertial responses of five midsize male cadavers and the Hybrid III and THOR-NT midsize male ATDs were characterized and compared using symmetric knee impacts with 275-kg flat-faced-padded impactor at velocities of 1.2 m/s and 3.5 m/s. The combination of impactor velocity and the padding on the knee impact surfaces in the 1.2 m/s tests were selected to ensure that no KTH injuries would be produced. However, this loading condition was associated with Hybrid III peak femur load cell forces and loading rates of 1.3 kN and 85 N/ms, which are substantially lower than the 3-6 kN range of peak forces and the 200-600 N/ms range of loading rates in FMVSS 208 and NCAP tests. Because these less severe 1.2 m/s impacts produced a different inertial response, two of the five cadavers used in this study were also tested at a 3.5 m/s knee impact velocity, which resulted in peak Hybrid III femur forces and loading rates of 5 kN and 500 N/ms, which are in the range of femur forces and loading rates that are typically found in FMVSS 208 and NCAP tests.

Because none of the knee impacts resulted in knee, thigh, or hip fractures, it was possible to repeatedly impact each cadaver to obtain a set of three to five knee impacts where the phasing of the forces applied to the left and right knees was similar. Data from each pair of symmetric left and right knee impacts on the same cadaver were similar and were therefore averaged to obtain an single set of applied force, femur and pelvis accelerations, and effective mass histories calculated using the applied force and femur and pelvis accelerations.

All of the cadavers used in this study were midsize United States males in stature and within 12 kg of midsize United States male mass. Because the inertial response of the cadavers to knee impact is expected to vary substantially with subject mass, an effort was made to normalize subject response data using equal-stress equal velocity techniques. However, this normalization increased the scatter in the 1.2 m/s response data and was therefore not used to scale either the 1.2 m/s or 3.5 m/s cadaver responses.

For the 1.2 m/s tests, cadavers produced peak forces of approximately 940 N while the THOR-NT and Hybrid III produced peak knee impact forces of approximately 1.4 kN and 1.6 kN, respectively. Peak femur and peak pelvis accelerations for all cadavers and the ATDs were between 6 and 8 g. In the two cadaver tests at the 3.5 m/s impact velocity, the cadaver peak knee impact forces were 3.5 and 3.8 kN. In comparison, the peak forces produced in the 3.5 m/s impacts to the THOR and Hybrid III knees were 5.5 and 6.1 kN, respectively. Peak femur and pelvis accelerations for the cadaver and both ATDs were between 29 g and 32 g.

In both the 1.2 and the 3.5 m/s impacts, peak force applied to the cadaver knees occurred after peak femur and pelvis acceleration while in the ATDs, peak force and peak accelerations occurred at the same time. The similarity in the timing of peak applied forces and accelerations in the ATDs indicates that most of the mass in the ATDs is tightly coupled to the skeletal knee-thigh-hip. The difference in timing between femur and pelvis accelerations and applied force in the cadaver is likely because there is mass in the cadaver that is initially loosely coupled to the skeleton and that becomes more tightly coupled to the skeleton as it moves.

The shapes of the cadaver effective mass histories were similar for both the 1.2 m/s and 3.5 m/s tests.

Early in the impact event, effective mass calculated using both cadaver pelvis and femur acceleration was low and then increased until after the time of peak force. Because cadaver femur acceleration leads pelvis acceleration by approximately 2 ms during the loading portion of all tests, the low initial effective mass is due to coupling of the femur to the impactor. The subsequent increase in effective mass is likely from coupling of the pelvis to the displacing femur. In addition, coupling of flesh mass to the thigh and pelvis, coupling of torso mass to the pelvis, and coupling of the leg to the knee likely account for some of the increase in effective mass that occurs following the initial portion of the effective mass history.

ATD effective mass histories at both impact velocities are different than cadaver effective mass histories. During the early part of the knee impact event, ATD effective mass is much higher than cadaver effective mass. As the impact event progresses, ATD effective mass gradually increases until, at the time of peak force, ATD and cadaver effective masses are within approximately 20% of each other.

The initial rapid increase in ATD effective mass is because most mass in the ATD KTH is rigidly coupled to the skeletal femur and pelvis, which under knee impact, immediately couple to the impactor. High-speed video suggests that the subsequent gradual increase in ATD effective mass is from the leg and torso coupling to the skeletal femur and pelvis, respectively.

Comparisons of effective mass histories from tests at 1.2 m/s and 3.5 m/s performed on the same two subjects indicate that more severe knee loading conditions result in larger effective mass values at the time of peak force. This likely occurs because more severe knee loading conditions result in higher skeletal KTH displacements at the time of peak force, which likely couple additional mass to the KTH. The differences in KTH effective mass response with knee impact severity suggest that comparisons between ATD and cadaver knee impact response should be made using loading conditions that are representative of the knee loading conditions that occur in the real world, such as the 3.5 m/s knee impacts. To make comparisons between the cadaver and ATDs, it is necessary to develop corridors that characterize the variability of cadaver responses. However, because only two subjects were tested at the 3.5 m/s impact velocity, more data are needed before corridors can be developed.

Comparisons between ATD and cadaver responses suggest that ATDs can be made to respond more like cadavers by decreasing the mass that is tightly coupled to the femur and pelvis. However, the knee/femur stiffness of the Hybrid III is 8-12 times greater than the knee stiffness of the cadaver and the knee/femur stiffness of the THOR- α /THOR-NT is 2-3 times greater (Rupp et al. 2003b) than that of the cadaver. Therefore, decreasing the coupling between skeletal and flesh mass in ATD may not alone be sufficient to make ATD knee impact forces similar to cadaver knee impact forces.

The effective mass response of the cadaver may be substantially different from the effective mass response of a living human because of muscle tension, which would tend to increase the coupling of the thigh and pelvis flesh to the skeletal KTH. It may therefore be advisable to develop computational models of the lower extremities that can simulate the effect of muscle tension on response of the KTH to knee impact loading. These models could then be used to suggest how to redesign ATDs to better mimic living humans rather than cadavers.

Although cadaver femur force was not measured in this study, the peak cadaver femur force at the 3.5 m/s impact velocity will be less than the peak cadaver applied force of 3.5 kN to 3.8 kN. Because peak femur load cell forces measured by the Hybrid III and THOR under similar loading conditions were substantially greater than 3.8 kN, it can be inferred that ATDs and cadavers produce different forces at the femur load cell location. Therefore, either femur force measurements from the Hybrid III and THOR-NT will need to be scaled to be used with force-based injury criteria developed from cadaver tests or the Hybrid III and THOR will need to be modified to respond more like a living human.

The cadaver data collected in this study can be used to develop models that predict the distribution of forces at any location along the knee-thigh-hip complex for knee impacts that are representative of real-world knee-to-knee bolster impacts. Such models can be also be used with the hip injury tolerance data measured by Rupp et al. (2003a) to predict the risk of hip fracture for knee loading by a knee-bolster-like surface. These models can also be used to optimize knee bolster design to reduce the risk of disabling hip injuries in frontal crashes.

CONCLUSIONS

The inertial responses of five midsize male cadavers, the Hybrid III midsize male, and the THOR-NT were

characterized and compared using symmetric padded knee impacts at a 1.2 m/s impact velocity. Two of these five cadavers were also impacted at a 3.5 m/s impact velocity using a similar impactor. Using applied force and femur and pelvis acceleration data from these impacts, the following observations and conclusions can be made:

- Knee impact forces produced by the cadaver were substantially less than those produced by the THOR and Hybrid III.
- Femur and pelvis accelerations produced by both dummies and the cadavers were similar in magnitude, but different in phasing. The peak cadaver femur and pelvis accelerations occurred substantially earlier than the time of peak force, while the peak ATD femur and pelvis accelerations occurred at the time of peak force. This behavior suggests that there is loosely coupled mass in the cadaver, but not in either ATD.

ACKNOWLEDGEMENTS

This research was supported by the National Highway Traffic Safety Administration under contract number DTNH22-99-H-1700.

The authors are grateful to Thomas Jeffreys for his assistance in cadaver preparation and testing. The authors would also like to acknowledge the contributions of Charles Bradley, Brian Eby, Stewart Simonett, and James Whitley who assisted in the data collection and test preparation. The assistance of Kathy Klinich in the review of this manuscript is gratefully acknowledged.

REFERENCES

- Burgess, A.R., Dischenger P.C., O'Quinn, T.D., and Schmidhauser, C.B. (1995). Lower extremity injuries in drivers of airbag-equipped automobiles: clinical and crash reconstruction correlations. *Journal of Trauma* 38(4): pp 509-516.
- Eppinger, R.H. (1978). Prediction of thoracic injury using measurable parameters. *Proceedings of the 6th International Technical Conference on Experimental Safety Vehicles*, pp. 770-780. National Highway Traffic Safety Association, Washington D.C.
- Horsch, J.D. and Partick, L.M. (1976). Cadaver and dummy knee impact response. SAE Paper No. 760799. Society of Automotive Engineers, Warrendale, PA.
- Kuppa, S., Wang, J., Haffner, M., and Eppinger, R. (2001). Lower extremity injuries and associated injury criteria. *Proceedings of the 17th International Technical Conference on the Enhanced Safety of Vehicles*, Paper No. 457. National Highway Traffic Safety Administration, Washington, D.C.
- Kuppa, S. and Fessahaie, O. (2003). An overview of knee-thigh-hip injuries in frontal crashes in the United States. *Proceedings of the 18th International Technical Conference on Experimental Safety Vehicles*. National Highway Traffic Safety Association, Washington D.C.
- Read, K. M., Burgess, A. R., Dischinger, P. C., Kufera, J. A., Kerns, T. J., Ho, S. M., and Burch, C. (2002). Psychosocial and physical factors associated with lower extremity injury. *Proceedings of the 46th Annual Conference of the Association for the Advancement of Automotive Medicine*, pp. 289-303. Association for the Advancement of Automotive Medicine. Des Plaines, IL
- Rupp, J.D., Reed, M.P., Van Ee, C.A., Kuppa, S., Wang, S.C., Goulet, J.A., and Schneider, L.W. (2002). The tolerance of the human hip to dynamic knee loading. *Stapp Car Crash Journal* 46, 211-228.
- Rupp, J.D. Reed M.P., Jeffreys T.J., and Schneider L.W (2003a). Effects of Hip Posture on the Frontal Impact Tolerance of the Human Hip Joint. *Stapp Car Crash Journal* 47. pp 21-33.
- Rupp, J.D., Reed, M.P., Madura, N.H., Kuppa, S., and Schneider L.W. (2003b) Comparison of knee/femur force-deflection response of the Thor, Hybrid III, and human cadaver to dynamic frontal-impact knee loading. *Proceedings of the 18th International Conference of Experimental Safety Vehicles*. National Highway Traffic Safety Administration, Washington DC.
- Shams, T. (2004) Personal communication on force-deflection response of the THOR-NT femur puck.
- Society of Automotive Engineers Dummy Testing Equipment Subcommittee (1998). User's manual for the midsize Hybrid III test dummy, Engineering Aid 23. Society of Automotive Engineers, Warrendale, PA.

APPENDIX

The following plots illustrate the variation in cadaver applied force, femur and pelvis acceleration, and effective mass responses from a single subject.

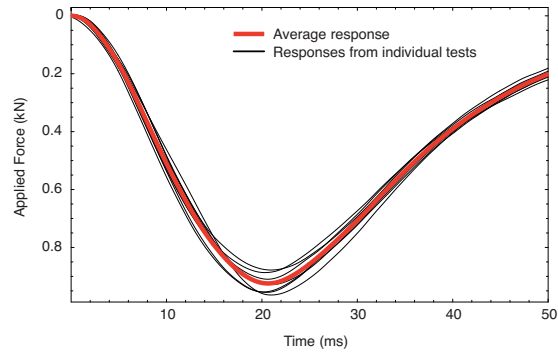


Figure A1. Left and Right knee impact forces from all tests performed on Subject 3 relative to the associated average knee impact force.

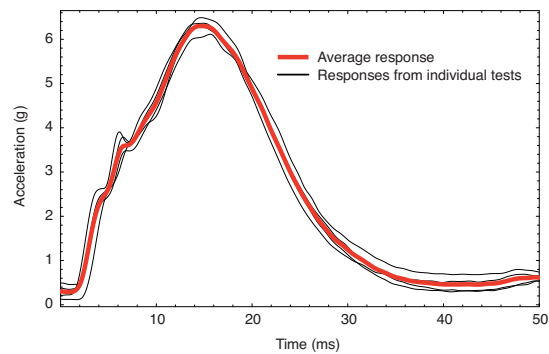


Figure A2. Pelvis accelerations from all tests performed on Subject 3 relative to the associated average pelvis acceleration.

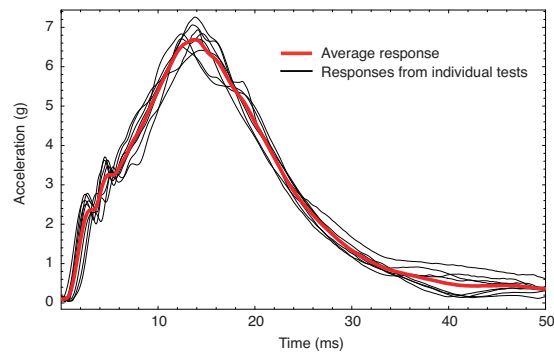


Figure A3. Left and Right femur accelerations from all tests performed on Subject 3 relative to the associated average femur acceleration.

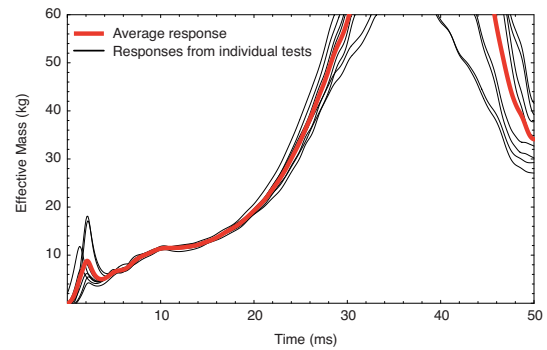


Figure A4. Left and Right pelvis-acceleration-based effective-mass histories from all tests performed on Subject 3 relative to the associated average pelvis-acceleration-based effective-mass history.

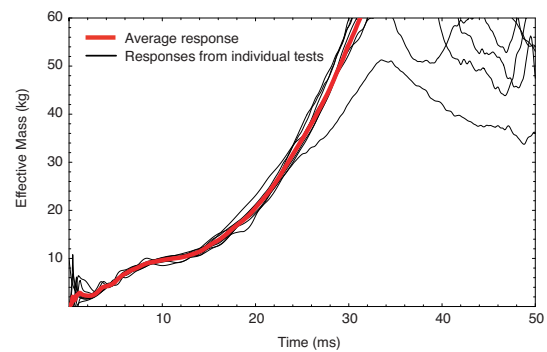


Figure A5. Left and Right femur-acceleration-based effective-mass histories from all tests performed on Subject 3 relative to the associated average femur-acceleration-based effective-mass history.

DEVELOPMENT OF CORRELATION METHODOLOGY USING OPTIMIZATION TECHNIQUE

Soongu Hong

Jeoungkeun Lee

Hyundai MOBIS

Korea

Paper Number 05-0120

ABSTRACT

Recently, the applications of optimization technique for occupant simulation are increasing to achieve a good correlated model, simulation reliability with actual test condition and design improvement. However, when the simulation model becomes complicated, the number of unknown parameters increases. Currently, point (one dimension) parsing has been used in optimization technique. Therefore, it takes longer time to parse all design parameters and to control the input parameters after parsing design parameters. Also, a longer time is required to run all input parameters.

To overcome this problem and achieve a good correlated model with test, this study introduces the new developed process, curve parsing method (two dimension parsing) and applications for correlation methodology with test and simulation using optimization technique. Particularly, the component and system level of occupant simulation are applied to the program developed with Engineous. Thus, simple parsing with the design parameters can be achieved for the optimization technique application.

From the result, the convergence accuracy of new approach was better than the old approach with specific optimization techniques. And the simulation run numbers and time had dramatically reduced compared to the ones in the previous approach.

INTRODUCTION

Traditionally, the trial and error method for correlation of occupant simulation has been used. The correlation quality and reliability of

simulation depended on engineer's experience, comparison of results and deviation of acceleration shape. Currently, the correlation methodology that can numerically express the correlation level has been developed by some company. Deren Ma, Jennifer Matlack, et al.,⁽¹⁾ presents the paper that the correlation quality of overall kinematics and dynamic response is scored and color-coded from weak, marginal, adequate, good to excellent. And Jack Van Hoof, et al.,⁽²⁾ introduced a commercial software package "ADVISOR" which contains a model quality-rating module with its own measurement criteria. In this manner, the correlation methodology is very critical and most sensitive in simulation area.

Recently, the usage of optimization technique at occupant simulation are increasing to obtain good correlation with actual test⁽¹⁾⁻⁽⁶⁾. Especially, Yan Fu, Eung Lee, et al.⁽³⁾ attempted to solve the problem systematically by using a genetic algorithm which is a valuable optimization tool to obtain a high quality simulation model.

Also the multi-body dynamic model has many uncertain parameters. For the example, in case of ellipsoid modeling, the geometry of actual shape can not be exactly represented and can not be modeled with exact material damping and moment of inertia, joint stiffness, etc. Also, it requires tremendous time to correlate with actual test, although the model has exact input shape, moment of inertia and so on. However, the optimization technique can be easily applied at multi-body dynamic model because it does not take a long time to run.

In case of frontal MADYMO simulation model, it requires more than 25 force-displacement curve data including loading and unloading curves. And it takes a long time (about 2months) to obtain those curve data from proto component tests. Also, even after gathering all F-D curve data, we usually spend a long time to correlate with component test results. Nevertheless, many assumptions for correlation are required to give a reliable occupant simulation before conducting the component test. Also, assumptions are required when there are only sled and barrier test results without component test results.

Currently, the optimization program is deficiency since it parses the input parameters using 1dimesional point. For example, a lot of time is spent to parse the input parameters when a

certain curve to object function needs parsing.

To overcome this problem and achieve the good correlated model with test, this study introduces the new developed process, curve

parsing method (two dimensional parsing) and applications for correlation methodology with test and simulation using optimization technique.

CURRENT SIMULATION METHOD

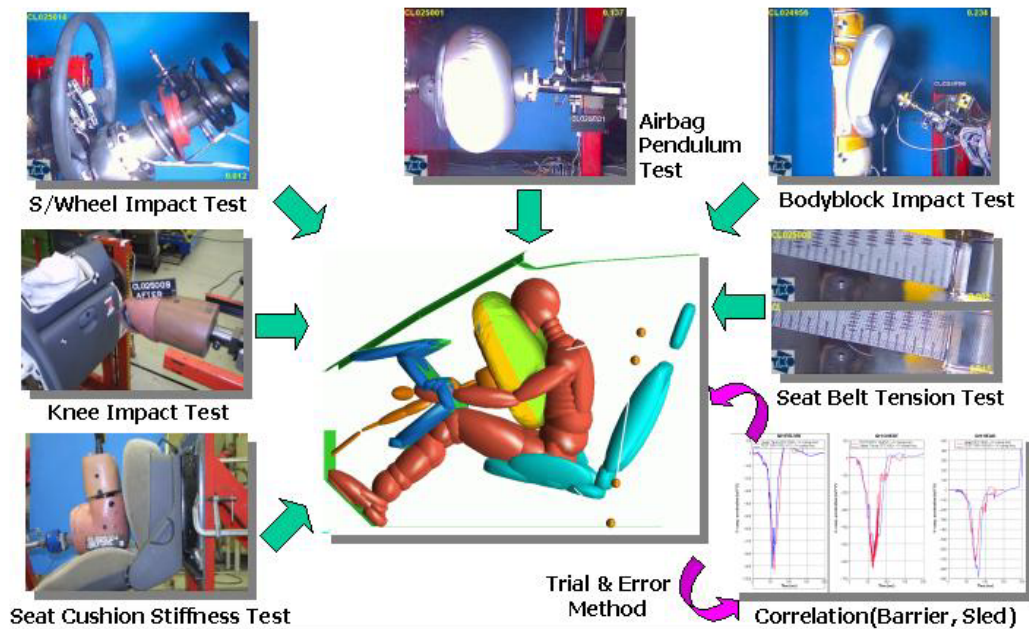


Figure 1. Current process of occupant simulation

Currently, MADYMO (Mathematical Dynamic Modeling) program prevails in the occupant simulation, but we need a lot of component test results (F-D curve) to build the frontal occupant

simulation. Previously, the trial and error method to correlate with actual test and tune the F-D curve and uncertain parameter has been used in occupant simulation. (see Figure 1.)

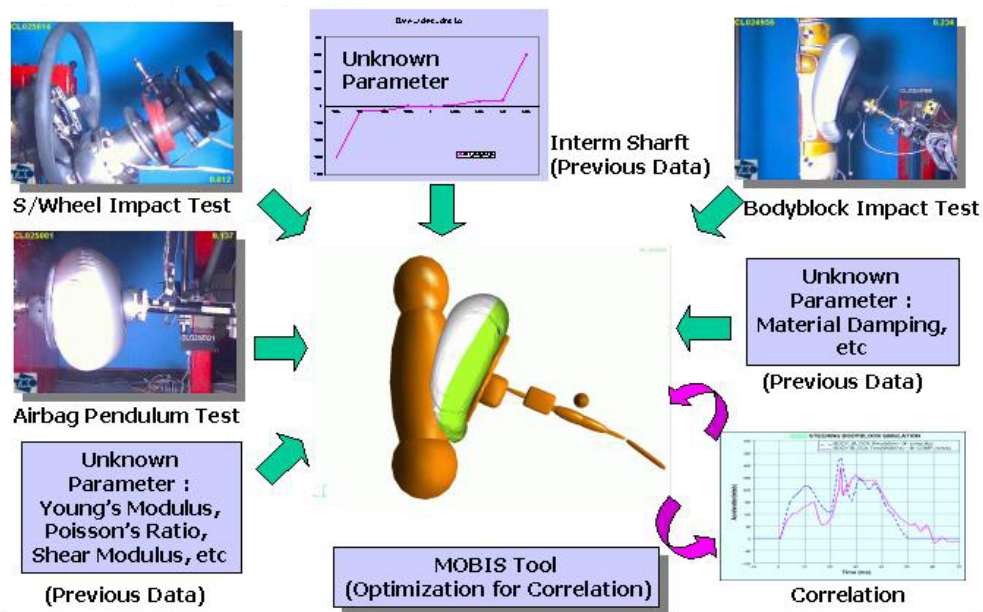


Figure 2. Example of correlation optimization

Therefore, a centralized correlation optimization can help to solve the problem using commercial software, i-SIGHT.

Also, the centralized correlation optimization program was developed to match test and

simulated curves automatically when using the old data (previous vehicle data) without the new vehicle component test results or the unknown parameter in components model.(see Figure 2.)

CURRENT OPTIMIZATION PROBLEMS

Currently, the optimization program supports just 1 dimensional point value for objective and input parameter parsing. Therefore, a user confronts difficulty to input the curve for objective and input parameters. And the automation job is needed when comparing test

and simulation curves in every simulation. Also, it require a long time to parse the objective function (test and simulation), specially when input parameter have many curves. And even after finishing parsing of all curves to object, the total run number is increased and it requires a long time to run the simulation.

PROGRAM DEVELOPMENT

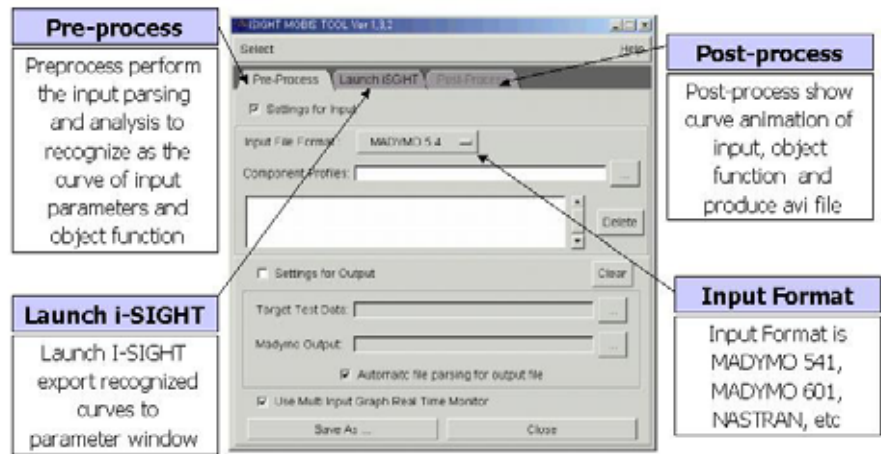


Figure 3. Pre-processor description

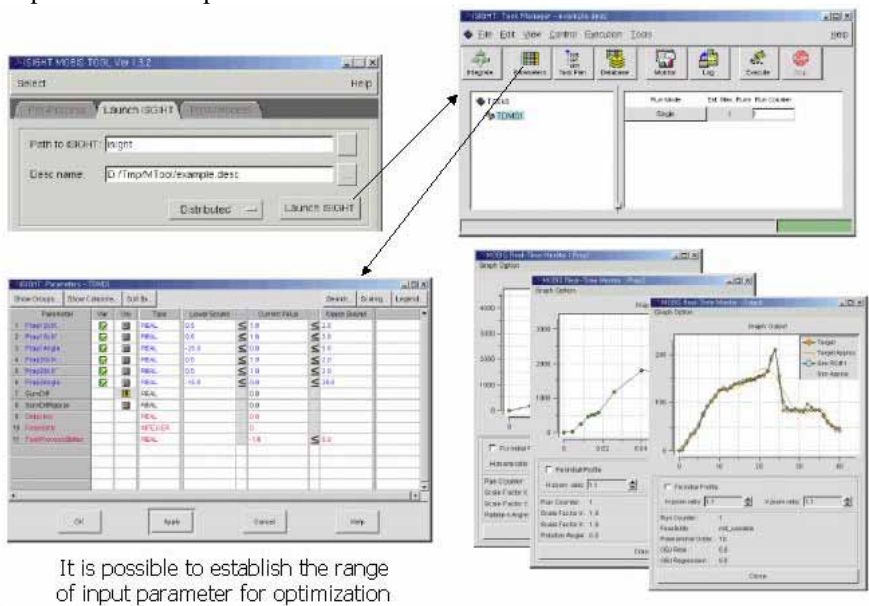


Figure 4. Launch I-SIGHT description

The program consists of three parts : pre-processor, launching i-SIGHT and post processing. The pre-processor includes a process that parses input parameters for curves through the curve

fitting or exponential to parse physical means of the acceleration curve shape. Then, this can be compared with the simulation and test acceleration result. (see Figure 3.)

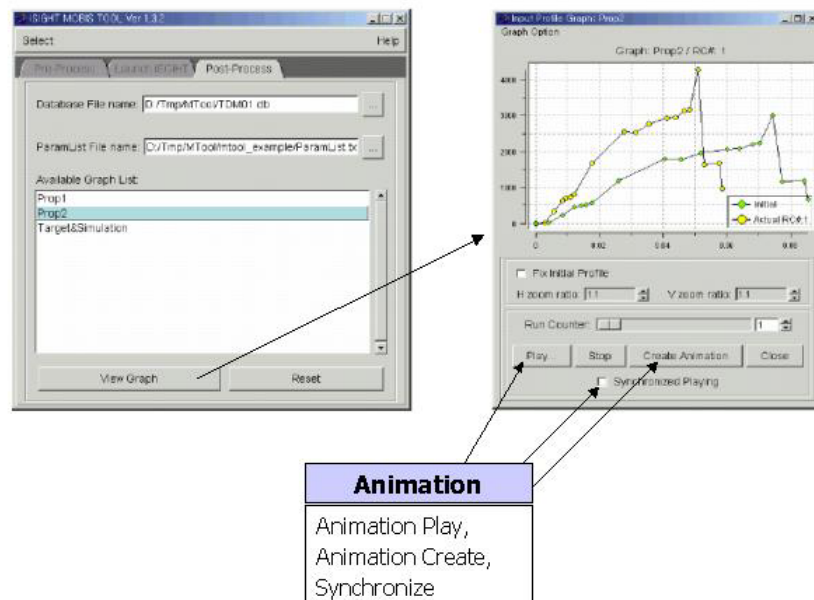


Figure 5. Post Processor description

The launching of i-SIGHT brings the parsed input parameter or objective function (curves) from the pre-processor into i-SIGHT program. (see Figure 4.)

Then, the post-processor shows the simulated results and optimized results, and the convergence process of simulation can be animated and exported to the animation files. (see Figure 5.)

PROGRAM EVALUATION

To evaluate the developed program, the deflection example of a simply supported beam (cantilever beam) solved by NASTRAN has been applied. As a result (see Table 1.), the number

of parameters reduced considerably than the ones in old method. The accuracy of convergence is higher than the one in old method. And only 20%~34% of simulation run time of the old method was taken.

Method	Parsing Method	Number of Parameter	Accuracy of Convergence	Run Time(Run Number)
Old Method	1Dimension (Value,Point)	A lot	-LHC+MMFD : 59.7% -SA+HJ : 92.8%	100%
MOBIS Tool	2Dimension (Curve)	Few	-LHC+MMFD : 99.1% -SA+HJ : 89.6%	20%~34%

LHC : Latin Hyper Cube
MMFD : Modified Method of Feasible Directions
SA : Simulated Annealing
HJ : Hooks-Jeeves Pattern Search

Table 1. Evaluation results of MOBIS tool

PROGRAM APPLICATIONS

Droptower Test and Simulation

The droptower example with objective function curve and input parameter of point value is shown in Figure 6.

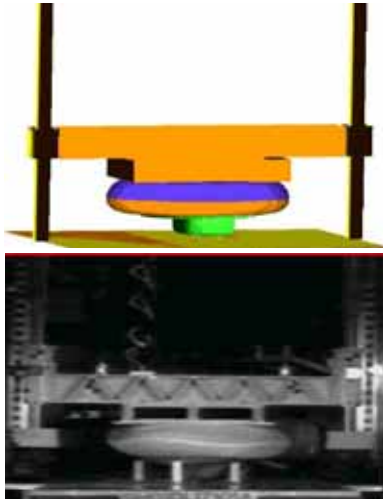


Figure 6. Droptower test and simulation

Also, the acceleration pulse before correlation optimization is shown in Figure 7 and the comparison results of acceleration after correlation optimization is shown in Figure 8.

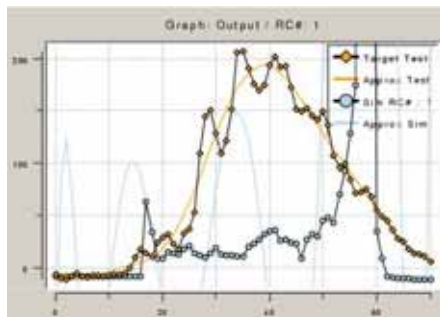


Figure 7. Before the correlation optimization

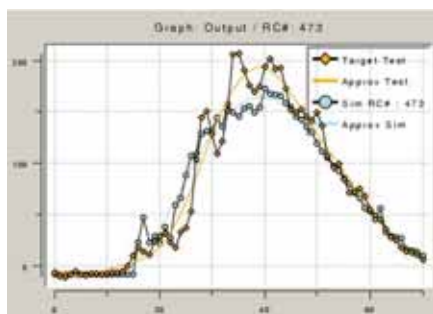


Figure 8. After the correlation optimization

Knee Impact Test and Simulation

The knee impact example with objective function curve and input parameter curves is shown in Figure 7.



Figure 9. Knee impact test and simulation

The tolerance can be found even though the F-D curve has been extracted from component test results since mostly the kneebolster surface is a plane and it requires modification of F-D curve obtained from component test result using the FE model for kneebolster. Therefore, correlation optimization or trial and error method are needed in order to compare with component result.

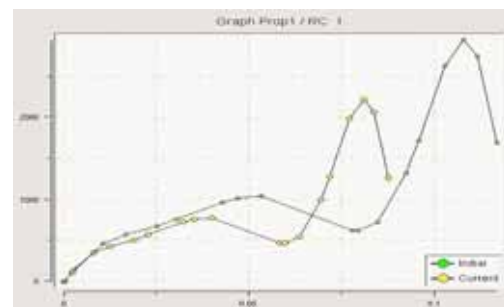


Figure10. Before the correlation optimization (1)

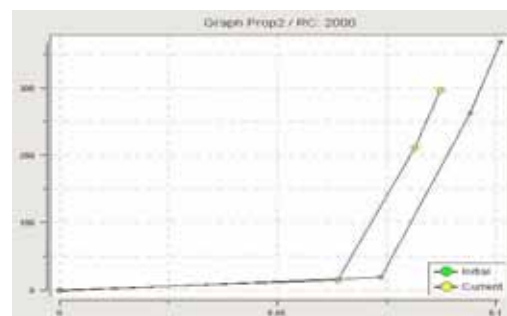


Figure11. Before the correlation optimization (2)

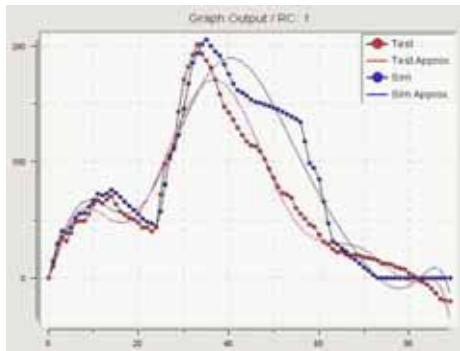


Figure12. Acceleration pulse before correlation optimization

Figure 10 shows the kneebolster loading curve before correlation optimization, Figure 11 shows the kneebolster unloading curve before correlation optimization, and Figure12. show the comparison of results of knee impact test and simulation acceleration before correlation optimization.

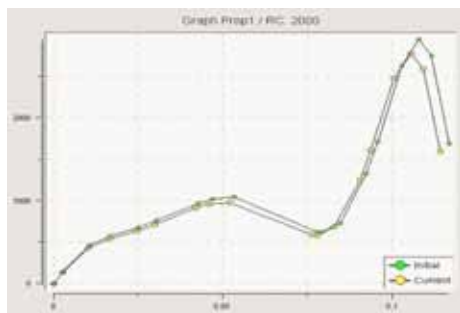


Figure 13. Input parameter of K/Bolster-loading curve after correlation optimization

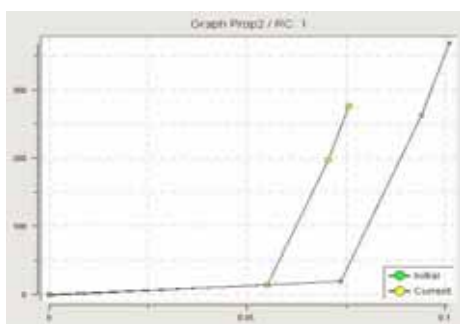


Figure 14. Input parameter of K/Bolster-unloading curve after correlation optimization

Figure 13 and 14 show the kneebolster loading and unloading curve after correlation optimization, and Figure 14 shows the comparison of results of knee impact acceleration curve between simulation and test.

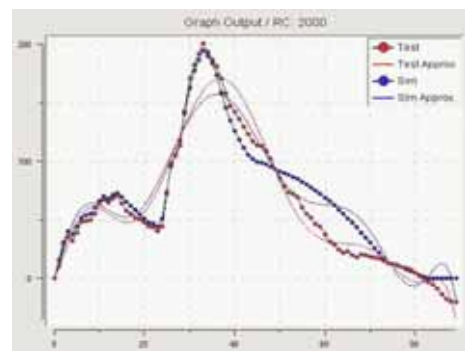


Figure 15. Acceleration pulse after correlation optimization

Steering Wheel Impact Test and Simulation



Figure 16. Steering wheel stiffness test setup and simulation model

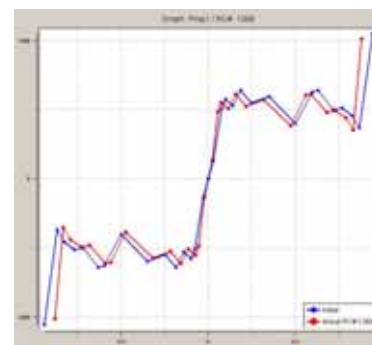
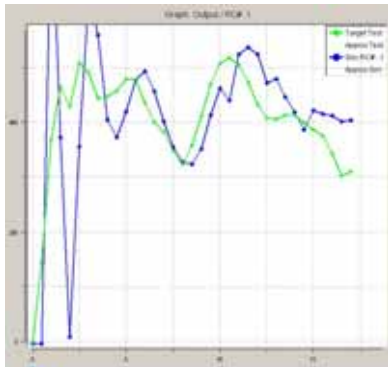
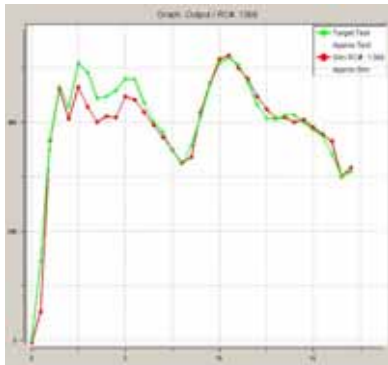


Figure 17. Rim joint stiffness curves with correlated model and original model



(a) Head form acceleration of initial model



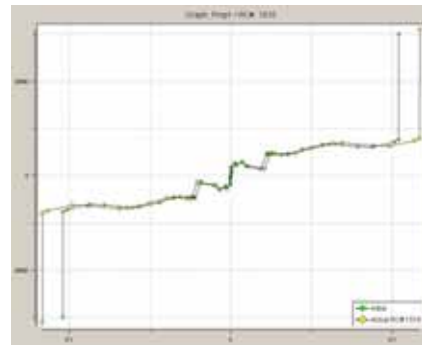
(b) Head form acceleration of correlated model

Figure 18. Correlation of the head form acceleration in simulation model with the component test

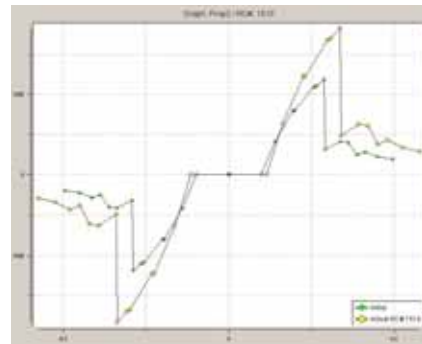
Bodyblock Impact Test and Simulation



Figure 19. Bodyblock test and simulation

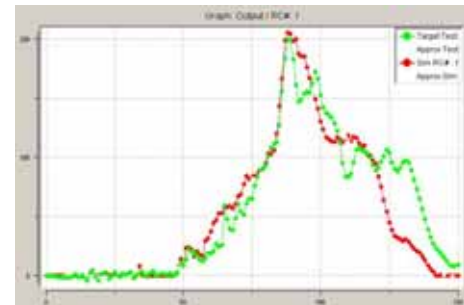


(a) Steering column axial stiffness

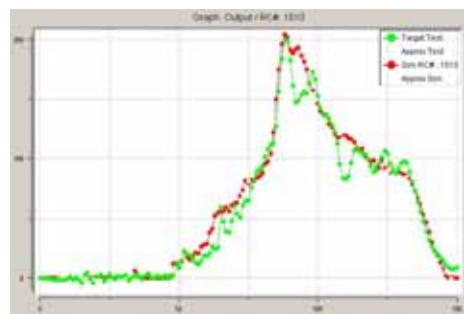


(b) Steering column tangential stiffness

Figure 20. Comparison of initial and optimal F-D curves of joints



(a) Body block acceleration of the initial model



(b) Body block acceleration of the correlated model

Figure 21. Comparison of bodyblock acceleration in test and simulation

CONCLUSION

In order to overcome the old correlation optimization with many problems (i.e. parsing difficulty, numerous input parameters, long run time) and to achieve good correlated model with test, this study introduced the new developed process, curve parsing method (two dimensional parsing method) and applications for correlation methodology with test and simulation using optimization technique. And the conclusion remarks are as follows.

1. It was possible to reduce the run time and number of run because the curve was recognized as one parameter.
2. It was possible to predict the unknown parameters (Specific Curve, Damping, Friction, etc) using optimization technique.
3. It was possible to construct the validated simulation model and simulation procedure.
4. The optimization technique used in this study was very suitable for the correlation of the occupant simulation model that has 2-dimensional test input data (F-D curve). It will be a powerful tool for correlation problem between test and simulation using optimization technique.

REFERENCE

- [1] Deren Ma, Jannifer Matlack, Honglu Zhang and John Sparkman, "Correlation Grading Methodology for Occupant protection system model", SAE paper 2004-1-1631.
- [2] Jack Van Hoof, et al., "ADVISOR : A software Tool for Evaluation and Numerical Models in Crash Safety Analysis", 18 ESV 483,
- [3] Yan Fu, Eung Lee and Stephan Kang, "Occupant Model Correlation using Genetic Algorithm", SAE paper 2004-1-1624.
- [4] Jungkeun Lee, Soongu Hong, et al., "A Correlation Methodology of Airbag Body Block Test and Simulation Using Optimization Technique", SAE 2004-01-1630.
- [5] Soongu Hong, Wonjin Park and Jungkeun Lee, "The correlation optimization between test and simulation result at the occupant simulation", KSAE, 2003
- [6] Soongu Hong, Wonjin Park and Yasuhiro Tanaka, "Customization of iSIGHT for correlation on safety", The 2003 International i-SIGHT Automotive conference, 2003.
- [7] iSIGHT 7.0 user's guide, 2002.

[8] MADYMO Reference Manual version 5.4.1, 1999.

[9] MADYMO Theory Manual version 5.4.1, 1999.

FINITE ELEMENT MODELING OF THOR-LX AND ITS APPLICATION

Hyung Yun Choi

Joong Yub Shin

Hongik University

Korea

Inhyeok Lee

Hankook ESI

Korea

Chang Nam Ahn

Han Il Bae

Hyundai Motor Co. & KIA Motors Corp

Korea

Paper No. 05-0125

ABSTRACT

The first part of this paper introduces a FE modeling effort of the lower extremity of Thor dummy, Thor-Lx Hybrid III retrofit. The FE model consists of 9,800 nodes and 8,300 elements, of which 2,900 are deformable solid elements. Three kinematic ankle joint elements are respectively used to represent dorsiflexion, inversion/eversion, and internal/external rotation of the foot. In addition to kinematic joint elements which represent the initial linear resistance developed by continuous joint stop, sliding contact interfaces are also defined between neoprene rubber and rotating center blocks for the subsequent non-linear stage. This two-stage joint definition then provides the precise description of ankle joint characteristics both in loading and unloading phases. The simulated outcomes of FE model have been validated for the performance of the ankle under different rotation motions and showed good agreement with both quasi-static and dynamic test results.

The second part of the paper deals with a practical application of the FE Thor-Lx model. Numerical simulations of a NCAP frontal 40% offset crash with a small size sedan are performed. A sub-structuring scheme for isolating the occupant compartment from the full car crash simulation is then adopted in order to facilitate the parametric study in which the various levels of structural deformations are attempted. The FE model of Hybrid III 50th percentile male upper body including knees and femurs is utilized to mount Thor-Lx and Hybrid III leg for the quantitative and comparative analyses of both legs. The Hybrid III leg mostly produces higher tibia index values than Thor-Lx due to its simple ankle joint structure which might result in steep increase of moments at the end of the range of motion. The paper concludes with the improved capabilities of Thor-Lx for the injury risk assessment compared with Hybrid III leg.

INTRODUCTION

Crash injuries of the lower extremities are usually not fatal, but may result in long-term impairment and immobility. It has been estimated that annually about 110,000 occupants sustain lower limb injuries with a severity rating of 2 or 3 on the Abbreviated Injury Scale (AIS).[1] Almost half of these injuries occur below the knee and, of those, ankle and foot injuries are the most frequent and can be responsible for long-term impairment.[2,3] Accordingly, in 2002, NHTSA announced an ANPRM (Advanced Notice of Proposed Rulemaking, 49 CFR Part 572, Docket No. NHTSA 2002-11838) for including the instrumented lower legs in vehicle crash tests to assess the risk of injuries occur below the knee. In the NHTSA proposal, two kinds of dummy lower legs for addressing lower leg injuries in frontally-oriented impacts are proposed: (1) The Hybrid III/Denton (HIII/Denton) instrumented leg and (2) the more recently designed Thor-Lx Hybrid III Retrofit (Thor-Lx/HIIIr) leg. Only one of these two available lower leg designs would be incorporated into the safety standard after some comparative evaluation period. The Thor-Lx appears to have substantially improved ankle and tibia biofidelity and a broader set of instruments while the Denton leg has been used over many years by the automotive industry for vehicle development. Since its formal release in December of 2000, the design of Thor-Lx has been kept nearly unchanged and incorporated in Thor NT which is the latest version of Thor dummy.[4]

The objective of this study is to build a finite element model of Thor-Lx. The detail modeling procedures such as geometry construction, FE meshing, and material characterizations are introduced as well as the results of model validation. A practical application with the developed FE model, the assessment of lower leg injury due to toepan intrusion, is also presented in this paper.

FINITE ELEMENT MODELING OF THOR-LX

The geometry of the Thor-Lx FE model is based on the AutoCAD drawing package (version 3.2, downloaded from NHTSA website: http://www-nrd.nhtsa.dot.gov/departments/nrd-51/thor_LX/Thorlxweb.html). The 3D solid model in CATIA[5] format was then built by utilizing the drawing package. After the 3D solid modeling work had been completed, the finite element meshing was performed with HyperMesh[6] and converted into Pam-Crash[7] input format. Fig. 1 shows the CATIA solid model and the FE mesh of Thor-Lx model.

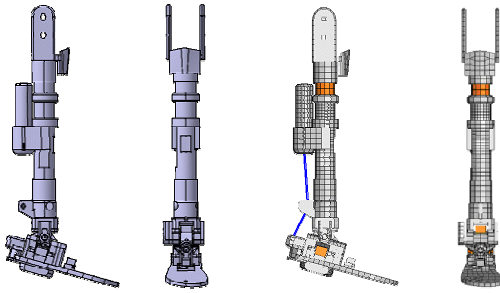
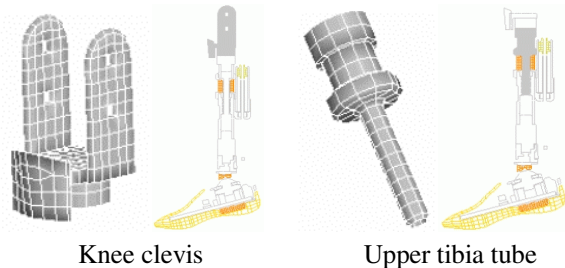


Fig. 1 Solid model (left 2) and FE mesh (right 2) of Thor-Lx model

Rigid Body Definition

Most metal parts in the Thor-Lx model are rigidly modeled while the rubbers and urethanes are modeled as deformable materials. These rigid bodies are modeled by null shell elements (material type 100 in PAM-SAFE[7]). Dynamic properties such as mass and principle moments of inertia for each rigid body definition were calculated from the 3D solid model in CATIA. Fig. 2 shows the rigid bodies in the Thor-Lx model which are connected to each other by either deformable parts, kinematic joints for the ankle joint, or springs for the load cells.



Knee clevis

Upper tibia tube

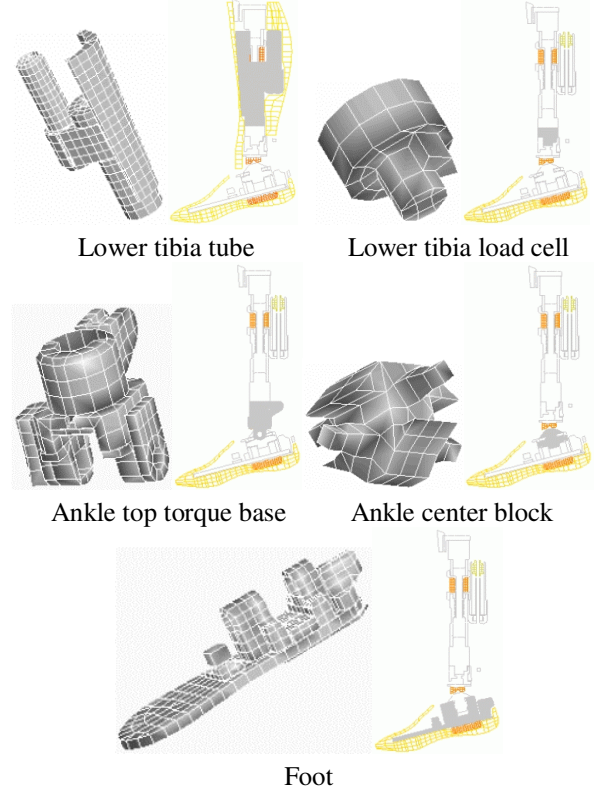


Fig. 2 Rigid body definitions in FE model

Deformable Part Definition

The rubber and urethane parts such as joint stops, tibia flesh, and heel pad were modeled by linear visco-elastic materials in which the characteristics were determined through the tuning processes with various component tests. The visco-elastic parameters of various deformable parts are listed in Table 1 and the corresponding figures are in Fig. 3.

Table 1 Visco-elastic parameters of various deformable materials in Thor-Lx model

Components	$K^{1)}$	$G_0^{2)}$	$G_\infty^{3)}$	$\beta^{4)}$
Tibia Compliant Bushing	0.28	4	1.4	0.5
Z-Rotation Stop	0.28	3.5	1.75	0.525
Dorsi-Plantar Flexion Soft Stop	0.09	20	4	0.085
Inversion-Eversion Soft Stop	0.079	3.5	0.7	0.85
Heel Pad	0.16	3.5	1.75	0.525
Foot Flesh	0.16	3.5	1.75	0.525

1) Bulk modulus (kN/mm^2)

2) Short time shear modulus (N/mm^2)

3) Long time shear modulus (N/mm^2)

4) Decay constant (sec^{-1})

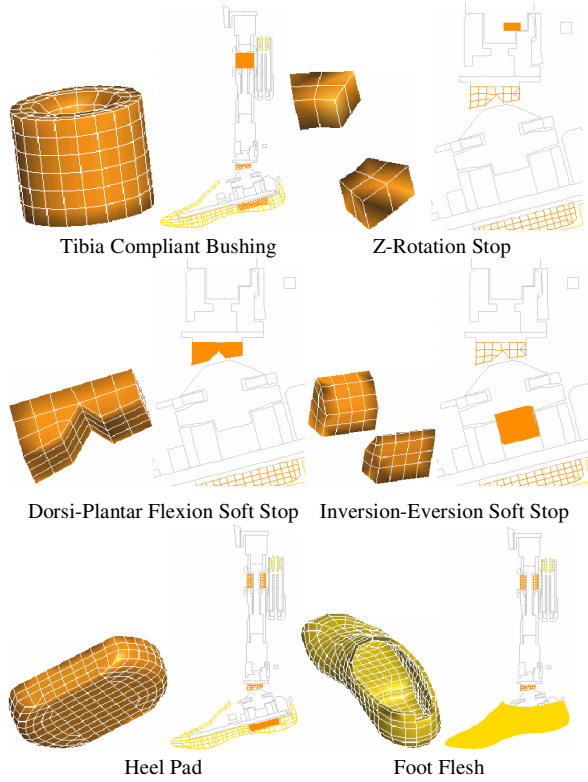


Fig. 3 Deformable parts in FE model

One of improved biofidelic characteristics of Thor-Lx compared with Hybrid III is the introduction of Achilles spring tube shown in Fig. 4 which consists of coil spring in parallel with elastomer spring element. In the model, nonlinear bar element was employed, and its loading/unloading characteristics are shown in Fig 5.

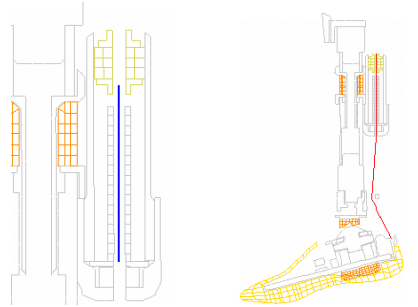


Fig. 4 Achilles spring tube and cable

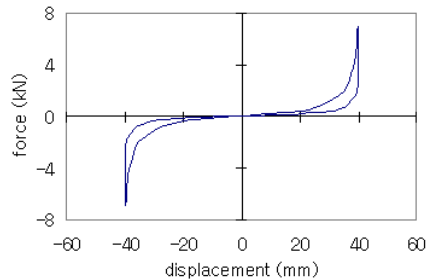


Fig. 5 Loading/unloading curve for Achilles spring

Kinematic Joint Definition

Ankle joint rotations about all three axes in Thor-Lx are independent of each other as shown Fig 6, and inversion/eversion (xversion) and dorsiflexion/plantarflexion (flexion) have separate, anatomically located centers of rotation. Flexion occurs primarily at the talar joint in the human, and xversion occurs at the subtalar joint. This is replicated in the Thor-Lx by placing the xversion joint 17 mm distal to the flexion joint. The first resistance of xversion and flexion is generated by the continuous joint stop (CJS) which increased its resistive torque in a linear fashion as the joint rotates. This first stage of linear joint resistance is modeled by a revolute joint element. Secondary resistance develops when the stopper begins to engage the rotating center block. In the modeling, the realistic geometry and characteristics of rubber block has been kept and a sliding interface definition between the center block and rubber element is applied to represent the second stage resistance in the joint. Fig. 7 shows a schematic of the joint features producing the two-stage resistance.

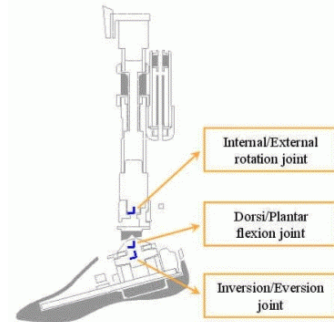


Fig. 6 Locations of ankle joints

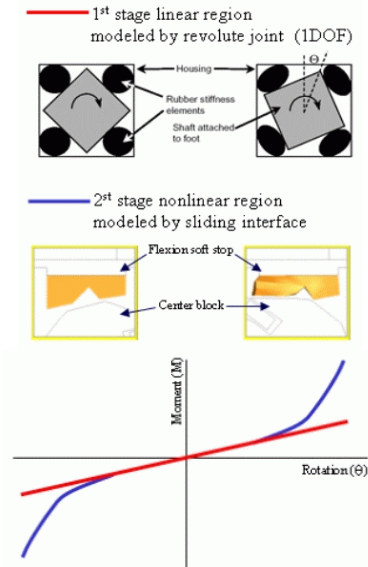


Fig. 7 Schematic joint characteristics representing two-stage resistance

Load Cell Definition

Load cells are defined in the model by using nonlinear 6 DOF spring elements. Each load cell is modeled by a single spring with zero length and is located at the intersection of the load cell's neutral axes. Fig. 8 shows the locations of load cells. They act stiff translational and rotational springs just for an accurate representation of reality. Although the physical load cells may be single, five or six axis transducers, load cells in the model provide all six output channels (i.e., three forces and three moments).

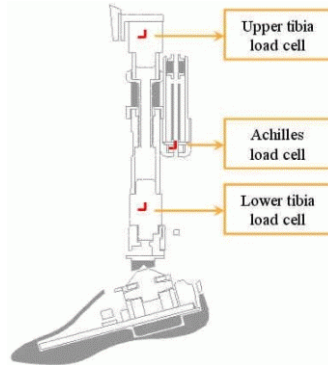


Fig. 8 Locations of load cells

VERIFICATION OF THE MODEL

In order to ensure the quality of the FE model, two kinds of validation were performed against the certification requirements and the design reference guidelines presented in NHTSA documents [8, 9].

Quasi-static ankle motion tests

The quasi-static ankle motion tests to examine the range of motion and resistance of the ankle joint soft stops in dorsiflexion/plantarflexion, inversion/eversion, and internal/external rotations were simulated according to the same test procedures as used in NHTSA certification procedures [9]. The simulated responses of the model were then compared with the test results.

Fig. 9 shows the set-up for the dorsiflexion test with and without Achilles. The detailed test and measurement procedures can be found in NHTSA certification procedures [9]. Simulation results with and without the Achilles cable are shown in Fig. 10 and 11, respectively. The simulated moment-angle curves in both cases coincide quite well with a typical response from the tests.

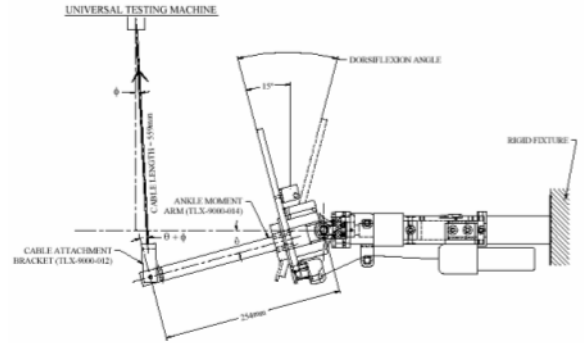


Fig. 9 Test set-up for quasi-static dorsiflexion test

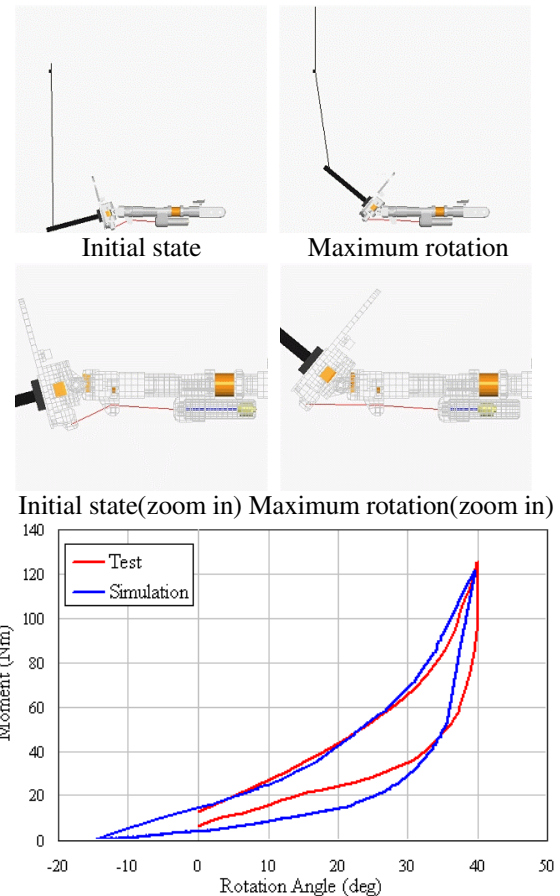
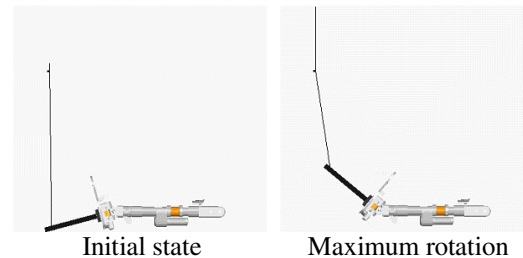
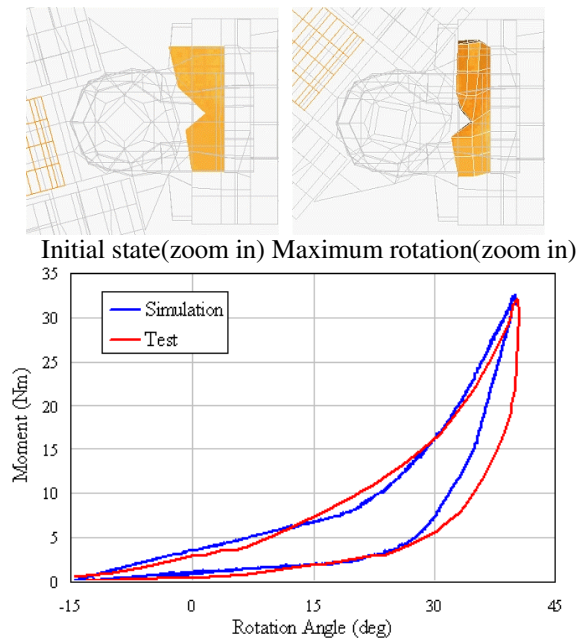


Fig. 10 Simulation of quasi-static dorsiflexion (with Achilles cable)





The test set-up and procedure for plantarflexion are similar to those for the dorsiflexion and the simulated moment-angle curve is presented in Fig. 12.

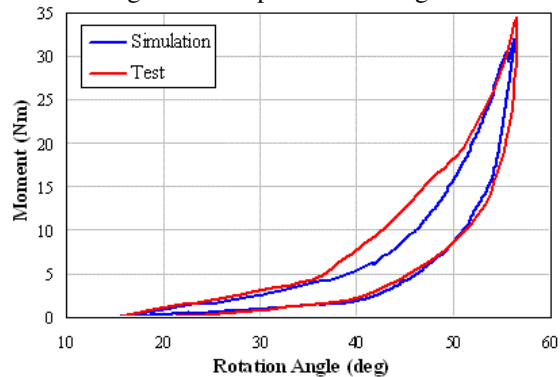


Fig. 13 shows a comparison between test and simulation results for inversion. Since the predicted unloading path of simulation is little higher than that of the test, the energy dissipation is also underestimated. Due to the symmetric design of the xversion joint, the validation for eversion had been skipped. The results of the simulation for the internal rotation compared with a test are shown in Fig. 14. The internal/external joint in the Thor-Lx was designed to provide approximate biofidelity within the range of $\pm 15^\circ$ and the considerable discrepancy in unloading path between simulation and test might have been caused by excessive rotation in the test and could be neglected.

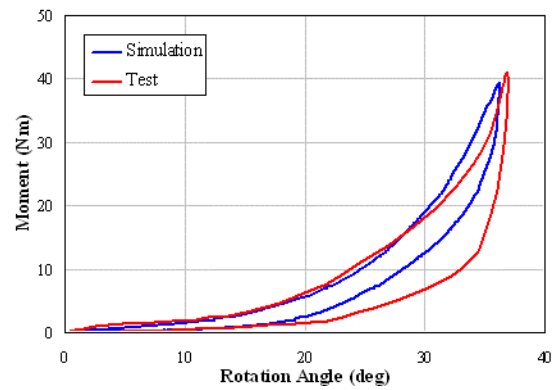
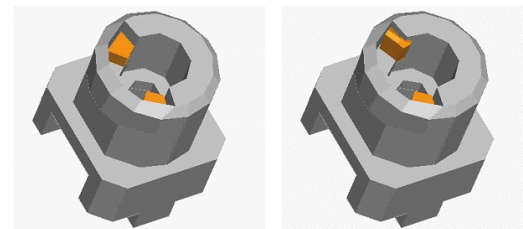


Fig. 13 Simulation of quasi-static inversion



Initial state

Maximum rotation

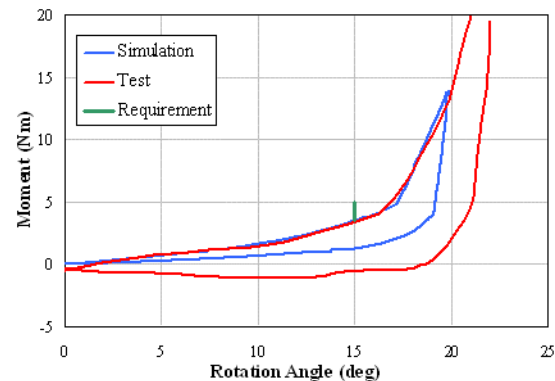


Fig. 14 Simulation of quasi-static internal rotation

Dynamic impact tests

To validate the dynamic performance of the ankle joint and the compliant elements in the foot and tibia, two pendulum impacts were simulated. The anatomical areas of pendulum impact are the ball of the foot and the heel of the foot. Test setups and the simulation results for impact simulations are presented from Fig. 15 to Fig. 18.

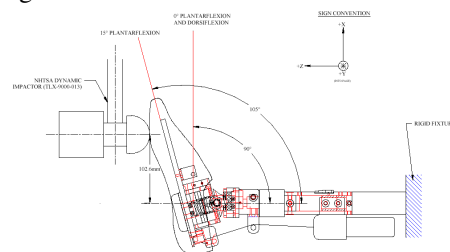


Fig. 15 Ball of foot impact set-up

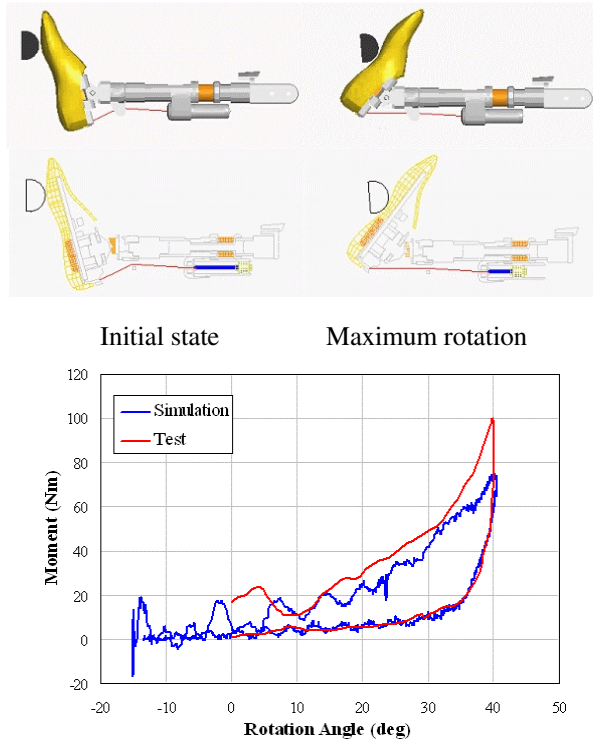


Fig. 16 Simulation result of ball of foot impact

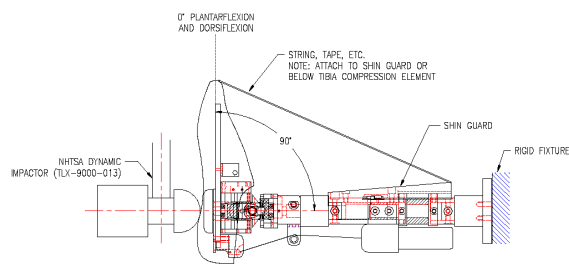


Fig. 17 Heel of foot impact set-up

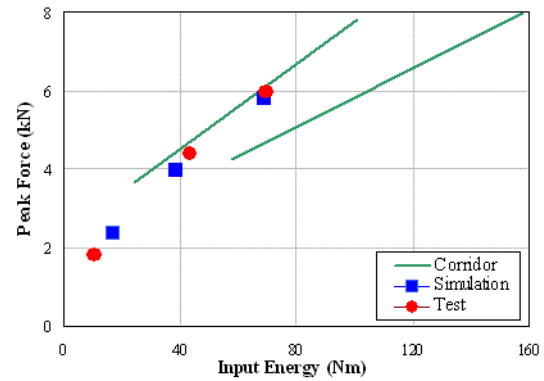
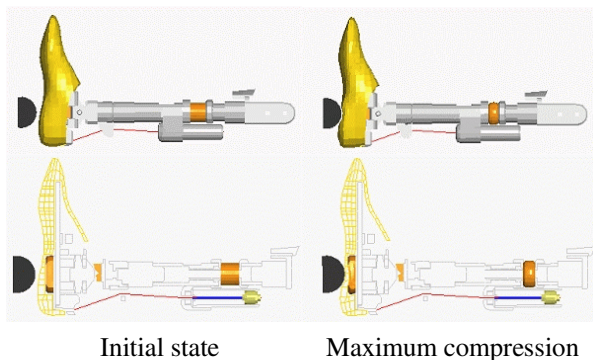


Fig. 18 Simulation result of heel of foot impact

ASSESSMENT OF LOWER EXTREMITY INJURY WITH THOR-LX

In order to examine the FE model of Thor-Lx for practical use, a series of crash simulations, NCAP 40% offset crash for a small size sedan have been performed using the Thor-Lx model. Translational and rotational vehicular deceleration pulses, and the deformation profile of occupant compartment computed from the full car simulation shown in Fig. 19, were applied to create an isolated offset sled model shown in Fig. 20. Applying a sub-structuring scheme to this offset sled model, a parametric study for various levels of structural deformation has been performed.

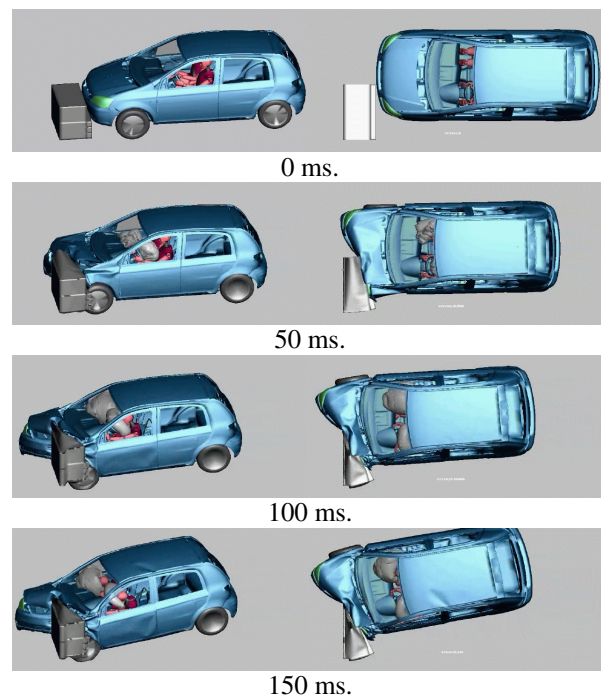


Fig. 19 Simulation of full car offset crash (Left: side view, Right: top view)

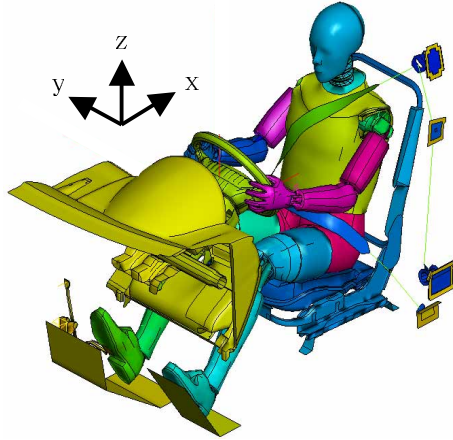


Fig. 20 Offset sled model

A finite element Hybrid III 50% dummy model developed by FTSS was adopted for an occupant surrogate in this study. The Thor-Lx model introduced in first part of this paper was also retrofitted to the Hybrid III thigh.

The intrusion profiles of the pedal and toe pan in the offset sled model were selected as design variables in parameter study. Three levels of severity for toe pan intrusion were fabricated and used for the quantitative investigation of their effects on lower extremity injury risk. The amount of intrusion of the toe pan and the floor in case #1 were adopted from the base NCAP 40% offset car crash simulation in Fig. 19. The overall amounts of intrusions were then raised for cases #2 and #3 as shown in Fig. 21 to mimic more excessive structural deformations. The intrusions in case #1 were from the deformation of the dash panel only while cases #2 and #3 were intended to represent the decreasing gap between the dash and the occupant due to floor collapse.

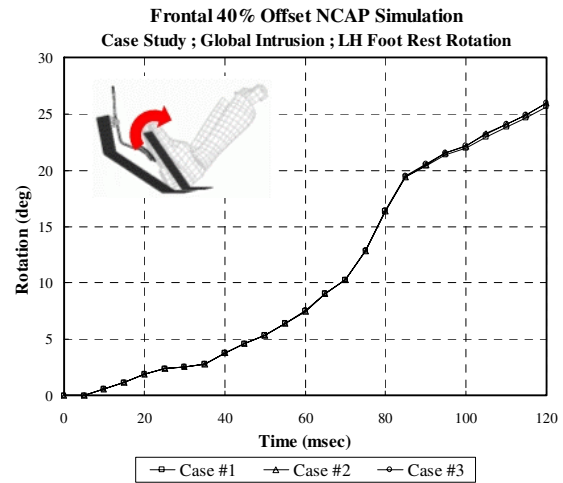
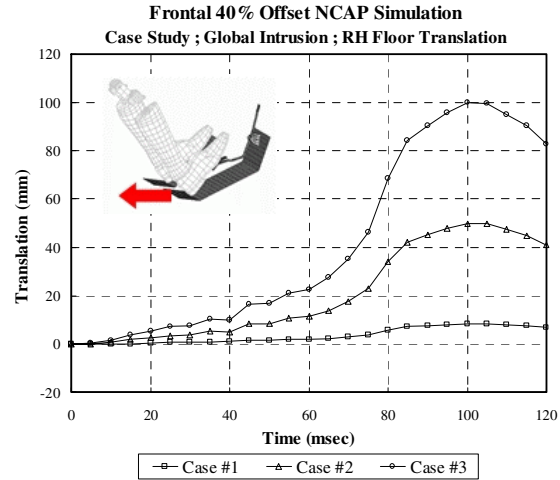
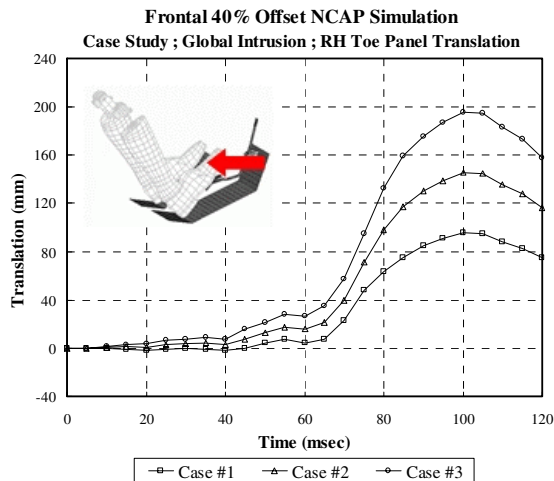


Fig. 21 Intrusion profiles in parametric study

Table 2 shows the injury predictions of the three cases in the parametric study. The amount of left dorsiflexion in the Thor-Lx showed small changes with increasing intrusion, which means the dorsiflexion had reached its maximum range due to the forward excursion of the body at an early stage. Therefore, RTI (Revised Tibia Index) and tibia F_z (axial force in tibia) for the Thor-Lx increased gradually with the intrusion due to the rise of ankle joint force and moment after the dorsiflexion had saturated. The Thor-Lx predicted more than a 50% risk of left side ankle joint injury for all three levels of intrusion severity. The highest severe tibia and fibula fracture risk predicted by the Thor-Lx was a 50% probability of fracture on the right hand side for case #3. The TI (Tibia Index) values of the Hybrid III exceeded the injury threshold for both sides in cases #2 and #3. The Hybrid III ankle tended to develop a very steep increase in the moment at its limit of rotation as shown in Fig. 22 because of its joint stop design, and thus the Hybrid III predicted relatively high risks of injury. The amounts of xversion (inversion and

eversion) for the Thor-Lx did not show a strong dependence on intrusion severity.

Table 2 Injury predictions from parametric study

Thor-Lx	Injury Limits		Case #1		Case #2		Case #3	
	25% Prob.	50% Prob.	Left	Right	Left	Right	Left	Right
Femur Fz	9.04 kN	11.15 kN	-1.46	2.82	-1.62	2.94	-2.09	5.76
Knee Shear	-	15 mm	0.12	1.14	0.42	0.94	1.18	0.26
RTI ¹⁾	0.91	1.16	0.55	0.70	0.79	0.95	1.10	1.23
Tibia Fz	5.2 kN	6.8 kN	3.14	3.97	3.40	5.94	3.75	7.00
Xversion	-	35 deg	-11.07	36.44	-12.74	24.72	-19.16	26.75
Dorsiflexion	-	35 deg	-42.11	-5.85	-42.02	-7.40	-50.39	-21.31

H III	Injury Limits	Case #1		Case #2		Case #3	
		Left	Right	Left	Right	Left	Right
Femur Fz	9.07 kN	-1.22	2.37	-1.34	2.84	-1.66	3.21
Knee Shear	15 mm	-0.12	0.14	1.31	0.19	0.29	0.27
TI ²⁾	1	0.42	0.73	1.23	1.99	1.77	3.13
Tibia Fz	8 kN	1.77	3.19	2.79	5.70	2.96	8.56

1) RTI: Revised Tibia Index, 2) TI: Tibia Index

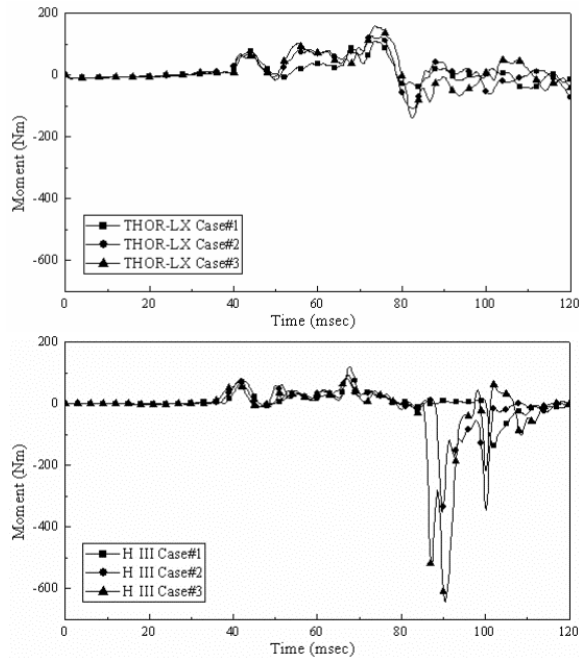


Fig. 22 Comparison of lower tibia dorsiflexion bending moments between Thor-Lx and Hybrid III

The behavior of the lower extremities of Thor-Lx, and Hybrid III for case #3 in the parameter study is depicted in Fig. 23.

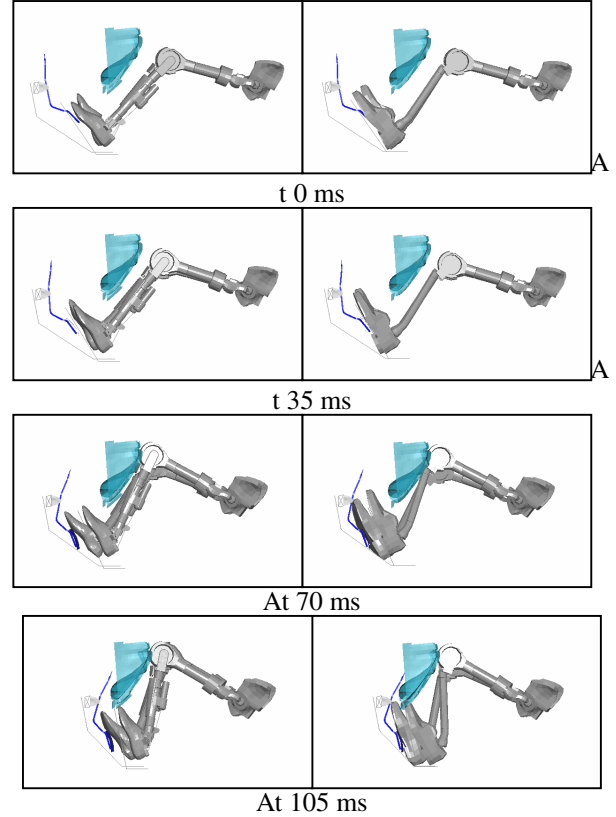


Fig. 23 Simulated lower extremity behaviors (Flesh has been made invisible, Left: Thor-Lx, Right: Hybrid III)

CONCLUSIONS

A finite element model of Thor-Lx has been completed. The model is computationally efficient since most non-deformable parts are modeled as rigid bodies, but it still successfully exhibited a good performance in the validation process. The modeling effort for the unique design of the ankle joints, which have two stages of moment-rotation characteristics, was made by employing kinematic joint elements together with definitions of sliding contact interface between the deformable rubber stoppers and rotating center blocks. This attempted to reproduce the hysteretic energy loss even for the multiple loading and unloading cycles.

In order to demonstrate the practical use of the model, a numerical investigation of lower leg injury risk from 40% offset crashes was performed. The comparative analysis with a Hybrid III dummy model showed that the use of Thor-Lx appears to be more favorable when assessing the lower leg injury risks due to its improved biofidelic design.

ACKNOWLEDGMENT

The authors would like to thank the NTBRC of NHTSA for providing the information of Thor dummy through their internet website. The authors also would like to thank Dr. Rodney Rudd at Center for Applied Biomechanics of UVA for reviewing the manuscript and providing a constructive commentary.

REFERENCES

- [1] National Automotive Sampling System-Crashworthiness Data System, 1994–1996, U.S. Department of Transportation, National Highway Traffic Safety Administration.
- [2] Morgan, R., et al. 1991. “Ankle Joint Injury Mechanism for Adults in Frontal Automotive Impact,” Proceedings of the 35th Stapp Conference
- [3] Kuppala, S., et al., “Lower Extremity Injuries and Associated Injury Criteria,” Seventeenth International Technical Conference on the Enhanced Safety of Vehicles, Amsterdam, June, 2001.
- [4] Tariq Shams. 2004. Presentation of Thor-NT: Features and Performance, SAE Thor Evaluation Task Group, Nashville, November 3rd
- [5] CATIA, VERSION 5, RELEASE 7, DASSAULT, FRANCE
- [6] HYPER-MESH, TRAINING MANUAL, VERSION 7.0, ALTAIR ENGINEERING. INC, USA
- [7] PAM-CRASH/SAFE USERS AND THEORY MANUAL, VERSION 2004, ESI GROUP, FRANCE
- [8] GESAC, “BIOMECHANICAL RESPONSE REQUIREMENTS OF THE THOR NHTSA ADVANCED FRONTAL DUMMY (Revision 2001.02)”
- [9] NHTSA VRTC, “CERTIFICATION PROCEDURE FOR THE THOR-LX/HYBRID III RETROFIT VERSION 3.2 October 2001”

DEVELOPMENT OF A SET OF NUMERICAL HUMAN MODELS FOR SAFETY

Philippe Vezin

Jean Pierre Verriest*

*HUMOS2 project coordinator, on behalf of HUMOS2 consortium

INRETS, Biomechanics and Human Modeling Laboratory

France

ID (05-0163)

ABSTRACT

The objective of the EC funded HUMOS2 project is to develop Finite Element (FE) human models representing a large range of the European population and allowing an accurate injury risk prediction for victims involved in road accidents. A human model of a male in a driving position close to the 50th percentile – HUMOS model – resulting of the previous HUMOS project was presented (Robin [1]) at the ESV conference in 2001. The present paper focuses on the new developments that have been made in the still running HUMOS2 project.

Firstly, methods allowing the personalization (anthropometry, geometry and position) of human numerical models have been developed. They include a scaling tool enabling to derive any individual model from the original one through mesh control points and statistical relationships between external and internal dimensions. These were established from geometric data collected on standing and sitting human volunteers with a low dose bi-plane X ray system but also directly measured on isolated bone parts. A positioning tool has also been developed, based on a set of reference postures including seated car occupant, out of positions (OOPs) and pedestrian postures, in order to adjust and test the models for different sitting and standing postures.

Secondly, experimental work has been conducted on human volunteers in order to identify the influence of muscular tensing on body response to moderate impacts. A data base of biomechanical test results, appropriate for model validation, has been set up. It includes new biomaterial laws for ligament and skeletal muscles, as well as existing cadaver tests results coming from former EC projects and Heidelberg University. It and will be further completed by specific tests performed by consortium members. On-going work includes injury prediction rules introduction in the models then, extensive testing of the model in various conditions defined for validation.

INTRODUCTION

The European Union is the largest car producing area in the world and the largest car market. Research and Technological Development is essential for improving

the impact motor vehicles have on our society. Safety is one of the key issues in this respect.

In 2001, there were approximately 40,000 reported deaths and 1.6 millions casualties as a result of road traffic accidents in the European Union. The annual cost to the European Society due to these accidents was more than 160 billion Euro which was about twice the entire budget of the European Union. This situation increases with the integration of new state members. Injuries due to road accidents are a problem that can be controlled considerably if adequate attention is given to accident and injury prevention strategies. Injury control measures, i.e. passive safety, have been proven a very effective method for the reduction of the trauma problem.

The development of safety devices needs tools capable of predicting the injury risk and of evaluating the protection of road users (car occupants, pedestrians, two wheels users). For a long time, these tools have been only represented by mechanical crash test dummies. They were used for car safety research, development, and regulatory testing as well. These anthropometric crash dummies are limited in their biofidelity and in their application type. Moreover, the existing mechanical dummies represent only the population through 3 sizes (50th percentile male, 5th percentile female and 95th percentile male). Therefore, the crash test dummies produce important shortcomings with respect to a real crash situation.

Increasing computational capabilities have allowed designers to efficiently integrate simulation techniques into the conception cycle of their prototypes. This is also true for numerical models of crash test dummies, nowadays fully integrated into the crash simulation procedures. Unfortunately, these models inherit the deficiencies of their mechanical counterparts (i.e. biofidelity).

Moreover, there is an increasing interest on the possibility to use and introduce the “Virtual Testing” concept in the regulation and in the design process of safety devices, car or other transportation modes. This advanced approach requires more efficient, complex and biofidelic human substitutes. A global human body model capable to simulate the response of a human being and capable to predict the injuries in case of an omni-directional impact is one of the main keys of this new challenge.

The basic assumption of the project is that a biofidelic model shall be structurally close to the real human body. This assumption means that a correct representation of the human structures is needed, not only the bony parts but also the organs and muscles. Afterward, an up-to-date knowledge is also needed in order to provide the model with a satisfactory mechanical behavior in a car crash situation.

The second assumption of the HUMOS2 project is that all road users need to be correctly protected by the safety devices during a collision and consequently it is necessary to develop personalized models able to represent all the population. That means that, in parallel with the development of a biofidelic finite element human model, tools need to be developed for the “scaling”, i.e. personalization of the internal and external geometry, and for the “positioning” to obtain easily specific models for car occupants, pedestrian, motorcyclist, etc... from a reference model.

METHODS

The HUMOS2 program was organized around different tasks. *The two first tasks* aimed at providing meshes representative of the 5th percentile female and the 50th and 95th percentile male in sitting and standing positions. European databases of anthropometry measurements were therefore analyzed in order to define the external geometry of the human body corresponding to these percentiles. For the internal geometry, relationships between external dimensions and internal organ dimensions were established. The paired acquisition of internal dimensions (skeletal parts and some soft organs) and of external (anthropometric) measurements was performed on 64 volunteers by means of a low dose bi-plane X Ray imaging system [2] and on PMHS (Post Mortem Human Subject) by direct measurements. The collected data were analyzed by statistical methods in order to establish a scaling law for the prediction of internal organ dimensions from external ones. Thus, internal dimension of the 5th percentile female and the 50th and 95th percentile male derives from external geometry. Based on these statistical relations, a specific software was developed. This tool allows the scaling of the existing HUMOS mesh (close to the 50th percentile) towards any other percentile from a set of external main dimensions. It was used to produce the 5th, 50th and 95th percentiles in sitting positions. Before being scaled, the existing mesh (HUMOS) was improved in order to ensure its quality, especially after the scaling and positioning processes. This work was based on:

- identification of mesh defects during crash simulation (done by end users of the original model),
- needs identified by biomechanical experts for injury mechanisms simulation,

- needs identified for scaling and positioning purposes.

Specific road user postures were also defined for car occupants and pedestrians, using ergonomic and/or accident study data. Automatic methods were defined as positioning tool for small and for large displacements. From the meshes corresponding to the driving position (5th, 50th, 95th percentiles), other meshes were built for the pedestrian positions.

The third task deals with the improvement of biomechanical behavior knowledge specifically concerning the mechanical properties of biological tissues, the effect of muscle tone and the whole body response to realistic impact conditions. This knowledge is fundamental for the improvement and validation of the FE models.

Firstly, the effects of muscle tonicity on the global body response of volunteers subjected to impact and on local deformation of muscle were analyzed, as well as the effect of the muscular pre-activation. Secondly, mechanical characterization of soft tissues (muscles, tendons and ligaments) was performed. The mechanical properties of skeletal muscles during (impact) loading, up to failure were determined. Existing sled tests on PMHS were reanalyzed and new tests are being performed in more realistic impact conditions to validate the developed models. Effects of organs interaction during impact were determined thanks to the analysis of clinical records of visceral injuries, dissections and drop tests on trunks. Finally, all these biomechanical data will be stored in a biomechanical database necessary for the task dedicated to the models validation.

Task 4 deals firstly with the improvement of the developed models by simulating the injury mechanisms, the pressurization and the effect of muscle tone. For the simulation of injury occurrence, injury mechanisms were identified for each body parts. Behavioral laws for the tissue up to failure will be implemented and validated. The experimental data obtained on volunteers concerning the effect of muscle tone will be used for the development and the validation of active muscle models. Secondly, after the improvement of the whole body models, their biofidelity and injury prediction capabilities will be assessed by referring to the PMHS sled tests performed in the biomechanical study.

The last task is dedicated to an extensive use of the HUMOS validated models in different impact conditions in order to assess their capacity in predicting injuries. The simulation of car crash or other transport accident situations and of body response in case of out of position will be carried on. Another objective of this work is to compare these capabilities with dummies in view to complete the current regulations by numerical simulations.

GEOMETRY DEFINITON

Geometry Acquisition

In the field of product design, it is important to be able to represent the user population from the 5th percentile female to the 95th percentile male. Three dimensional data allowing geometrical reconstruction of any individual are therefore necessary. The “geometrical acquisition” work performed aimed at providing a database of external and internal measurements of the human body.

The external measurements concern more than 50 anthropometric lengths of body segment (on volunteers and PMHS in both standing and sitting positions). Data collected (Appendix 1) includes age, sex, weight, lengths, heights and circumferences.

Three-dimensional measurements of anatomical landmarks (acromions, trochanters, iliac crests, etc...) identifiable on the skin were performed in order to define the orientation of body segment in a sitting position. Their anatomical identification was simply done by palpation with the help of anatomists. Their 3D coordinates are expressed in a global frame attached to the subject. Other anatomical points were also acquired on volunteers in both standing and sitting position.

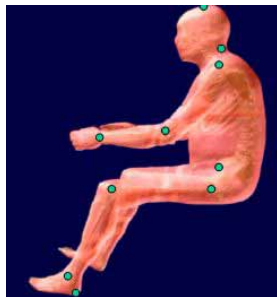


Figure 1. Palpable points (Doc. Univ. of Méditerranée).

The internal measurements related to anatomical points, which allow the description of the geometry of the organs. That concerned the head, the spine, the ribs and the sternum, the pelvis, the bones of the upper and lower limbs and the liver. For each organ, “control” points, dimensions based on these points and a local frame attached to the organ were defined. With the symmetry hypothesis, more than 1000 control points and 400 dimensions have been defined.

In order to define the relative position of each organ in the sitting position, all local anatomical frames were expressed in the global frame attached to the subject. Data were acquired on 64 volunteers (mean 30 ± 9 years old) distributed as 16 female, 33 and 15 male subjects representative of respectively the 5th, 50th and 95th percentile, (Table 1.). Data were also collected on 24 PMHS.

Table 1.
The 5th, 50th and 95th percentile definition

Percentile	Weight (Kg)	Standing height (cm)	Erect sitting height (cm)
5 th female	47	154	83
50 th male	77	178	94
95 th male	103	190	100

A common protocol was used to perform external measurements on volunteers and PMHS but different protocols were set up for internal data. The “*volunteer protocol*” is based on an X-ray acquisition using the low dose stereo X-rays system EOS[®] and on a 3D reconstruction procedure (Figure 2). Internal data concern the 3D points of the trunk skeleton (C3-L5 vertebrae, pelvis, 1st to 10th right and left ribs, sternum).

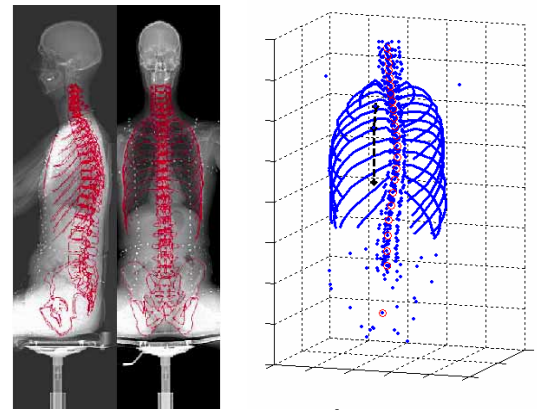


Figure 2. X-ray picture of a 50th male subject in sitting position and 3D control points obtained on a seated volunteer. Ribs are represented with lines joining 3D points (Doc. SERAM).

The “*PMHS protocol*” is based on 3D measurements of anatomical points on bones removed from PMHS. The study focused on limbs bones, head and sternum. In order to have some data on soft tissue organs, a specific protocol based on dual X-ray images was set-up to acquire data on the liver. An example of 3D control points is given in Figure 3.

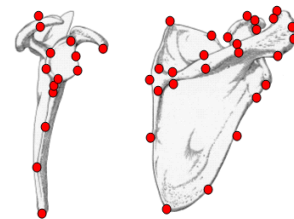


Figure 3. 3D control points measured on the scapula (Doc. INRETS).

These data were used to find statistical links between dimensions, inter or intra organ, and to give an approximate geometry of any percentile. The samples contained in the database are described in Table 2.

Table 2.
Description of the samples contained in the HUMOS2 Geometrical Database

Internal control points	Subjects	Samples
Head	11	21
Clavicle	14	18
Scapula	14	50
Humerus	23	32
Radius	14	24
Ulna	14	29
Femur	23	38
Tibia	23	30
Fibula	13	19
Sternum	73	3
Thorax	64	100
Pelvis	64	401
Liver	9	9
External dimensions	88	54
External control points	Samples	
Sitting position	64 trunks, 10 limbs	
Standing position	15 trunks	

Parameters Defining External/Internal Human Body Geometry

The European 5th, 50th and 95th percentile definitions given in Table 1 were determined from existing database analysis. For a p^{th} percentile, an arbitrary function δp , depending on weight (W_i), height (H_i), and erect sitting height (ESH_i) of a subject S_i was defined as follows (Eq. 1.):

$$\delta_p(S_i) = \frac{|W_p - W_i|}{W_p} + \frac{|H_p - H_i|}{H_p} + \frac{|ESH_p - ESH_i|}{ESH_p} \quad (1.)$$

The δp function was applied to all the subjects (volunteers and PMHS) in order to select among all of them the 3 subjects S_p with the smallest $\delta p(S_p)$. These subjects will be the target for the building of the different HUMOS2 percentile meshes.

Table 3 shows the subjects of the geometrical database whose anthropometry was the nearest (according to the δp criteria) to the percentile definitions.

The methodology chosen for the personalization of a numerical model, based on a “*scaling method*”, needs the definition of the links between external/external, external/internal or internal/internal dimensions. These correlations are the key data of the “*statistical tool*”, which provides from a small number of main

(external) parameters (input data) all the parameters (external and internal) defining the geometry of the considered person.

Table 3.
Subjects with the smallest δp value

Percentiles p		H_p (cm)	ESH_p (cm)	W_p (kg)
5 th female	PMHS	159.5	85.0	47.5
	Volunteers	155.9	83.0	46.9
50 th male	PMHS	179.0	82.0	72
	Volunteers	182.5	93.0	76.3
95 th male	PMHS	-	-	-
	Volunteers	189.4	97.1	98.5

The method comprised three steps which provide the three following output (Figure 4.):

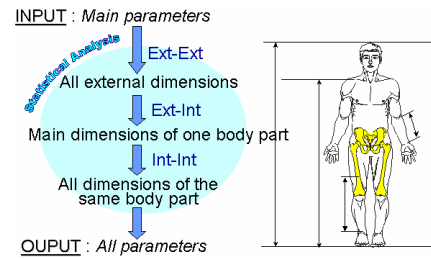


Figure 4. Regressive methodology (Doc. SERAM)

1. All external dimensions determined from main parameters by using external/external links;
2. The main dimensions of body parts from all external dimensions by the mean of external/internal links;
3. All dimensions of a body part from the main dimensions of the same body part by using internal/internal links.

Many correlations were found in the literature but the existing relationships do not meet to the HUMOS2 objective. Hence, the HUMOS2 geometrical database was analyzed by statistical methods in order to establish relationships between external anthropometric dimensions and internal organs dimensions. This work is based on:

1. The definition of MPE (Main External Parameters for the whole body or one body segment, MSE (Secondary External Measurement for one body segment), MPI (Main Internal Parameters for one body segment), and MSI (Secondary Internal Measurement for one body segment);
2. The definition of anthropometrical links: external/external (MPE/MPE, MPE/MSE), external/internal (MPE/MPI, MSE/MPI), and internal/internal (MPI/MPI, MPI/MSI);
3. The determination of correlation coefficient;
4. The determination of linear regressions.

Thanks to the statistical procedure, 285 linear regressions were assessed in order to model 285/411 (69%) parameters. Figure 5 describes the diagram of the statistical analysis which provides internal and external anthropometrical dimensions from 10 of the external measurements. It consists in 3 steps: 1) all the MSE are modeled thanks to 10 MPE; 2) 81 MPI and 30 MII (Isolated Internal Measurements) are modeled thanks to the MPE and the MSE; 3) 134 MSI are modeled thanks to the 81 MPI.

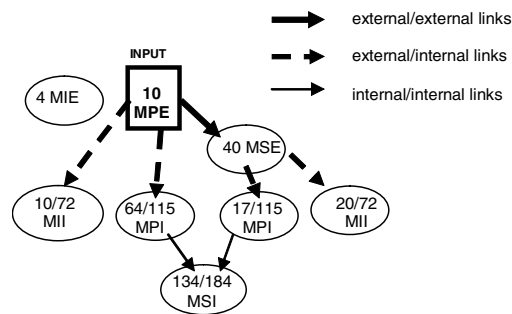


Figure 5. Statistical analysis summary (Doc. SERAM).

Given the small size of samples used to determine some regressions, some body part dimensions modeled by simple linear equations are less effective than others. Some internal parameters were not modeled by the statistical analysis as shown. This is due to the selection criteria used for the regressions ($R^2 > 0.5$) but it seems essential to get accurate predictions.

Methodology for Scaling

A specific tool was built allowing the “scaling” of the reference mesh (previous HUMOS 50th percentile) toward any other p -percentile and to validate it with the 3 common used percentiles (5th female, 50th and 95th male). These different HUMOS2 meshes are generated by the HUMOS2 “scaling tool” (Figure 6).

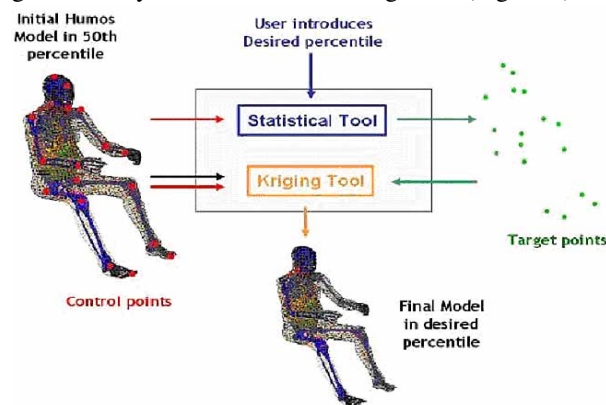


Figure 6. Main structure of HUMOS2 scaling tool. (Doc. Mecalog).

This tool uses the above-mentioned anthropometrical links and the “control points” defined on the initial HUMOS mesh (the “control points” have the same location as those measured on the volunteers and PMHS). From the 10 main parameters of a desired p -percentile, the “statistical” part of the tool determines the “target points” of this p -percentile. Then, using a method based on the kriging method the mesh of this desired p -percentile is created.

Consequently, the scaling of HUMOS2 mesh into any percentile in driving position is realized through a single step and requires only 10 anthropometrical dimensions. An example of the 5th female, 50th and 95th percentile male obtained from HUMOS mesh with this scaling tool is given in Figure 7.

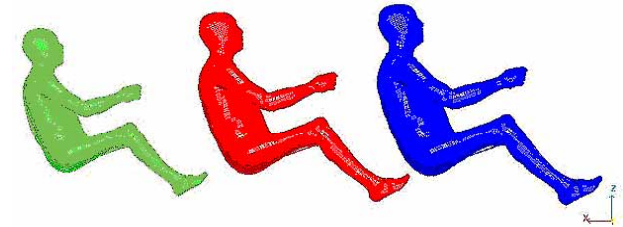


Figure 7. Example of the different HUMOS2 percentile (Doc. Mecalog).

MESHES UPDATE

Before proceeding to the scaling, the HUMOS model was exhaustively analyzed in order to define and select model which segments have to be improved via mesh improvements conditioned by 3 elements:

- Identification of HUMOS mesh defects during crash simulation conducted by end-users,
- Requirements for injury mechanisms simulation,
- Requirements for the scaling and positioning of the initial model.

The following improvements have been made:

Head and Brain Meshes

Brain Modeling: In order to predict the brain movement and brain vessel failure, the skull needed first to be separated from the brain. The skull is meshed using shell elements, which means that there is no physical thickness of the skull bone structure. For that reason the intracranial space was directly connected to the skull by sharing the same (joined) nodes. After the separation, the positions of the nodes are still the same but the nodes are no longer attached.

Bridging Veins Implementation: Because of the bridging veins introduction in the head model, the brain was repositioned and scaled such that the veins are more realistically positioned and orientated..

Anatomy handbooks show that the average distance between skull and brain is 1.4 mm and this space is filled with fluid (CSF). The intracranial space of the model was scaled to get this correct average distance. A layer between the brain and bone skull inner "surface" is also needed to get a better prediction of the bridging vein failure during crash. Rupture of these veins results in Subdural Hematomas, which are one of the most important causes of fatal head injuries. Figure 8 shows the skin shell (light brown), the head flesh solid (brown transparent), the bone skull shell layers (blue) and the intracranial space (red) with in between the veins (yellow).

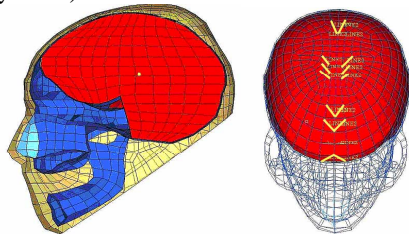


Figure 8. New head model with intracranial space and bridging veins (Doc. TNO).

Neck Improvement

Neck Geometry Modification: The geometry and corresponding mesh of the neck of the HUMOS model needed some modifications to achieve a more biofidelic performance. The relative angle between C3 and C4 was found to be out of range for normal values, 23.8° instead of 6.6°, Harrison et al. 0[3], and needed correction. The relative angle between C2-C7 for HUMOS is larger than an average neck but was kept to avoid important changes at this stage. The global curvature of the neck was adjusted to a better distribution of the vertebrae and cervical discs, C3-C6 were individually rotated around a local transverse axis, at the rear lower part of the vertebra body. The relative angles between the adjacent vertebrae were also defined within the range given by Harrison.

Neck Mesh Modification: After rotation of the vertebrae, the mesh of the pedicles and the spinous processes were modified to give the global neck model a smoother curvature. The facets also follow the new orientation of the pedicles. The comparison of the old and new neck is shown in Figure 9. The meshes of spine disc and nucleus pulposus were modified for a better size distribution within the solid elements and are modeled with two elements over the height and adjusted by placing the mid-layer-nodes at half distance between the upper and lower surface nodes.

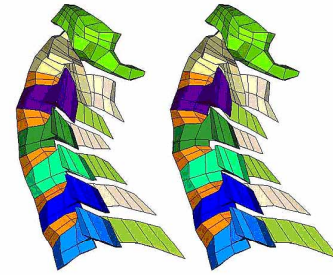


Figure 9. (left) Old geometry, (right) modified model with smoother curvature (Doc. Volvo).

Upper Limb

Elbow Mesh Refinement: In order to get a good contact description between the components of the elbow, refinement of the bones was needed. The meshes of the attached components were adapted as shown in Figure 10. From the available surfaces it was not possible to re-mesh the components to make them more realistic (smooth surface rounding instead of the edge formed surfaces). The number of shell elements was increased from 225 to 877 to have a denser mesh.

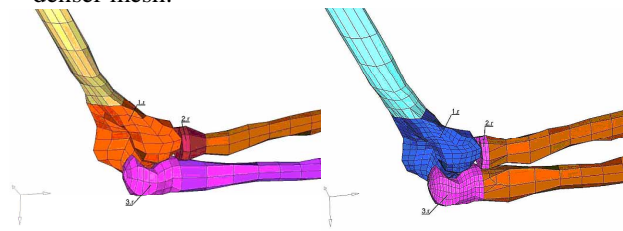


Figure 10. Elbow mesh refinement, left) old; right) new (Doc. TNO).

Elbow Ligaments Implementation: In order to be able to predict the movement of upper and lower arm through contact descriptions in the elbow, ligaments are necessary to keep the different components positioned correctly with respect to each other. Four ligaments, CollUlnar, AnnuRadial, CollRadial and Quadrate-R, were added in the refined mesh and therefore were adapted to the new mesh density. Figure 11 shows an example of two of the four added ligaments on right elbow with the denser mesh.

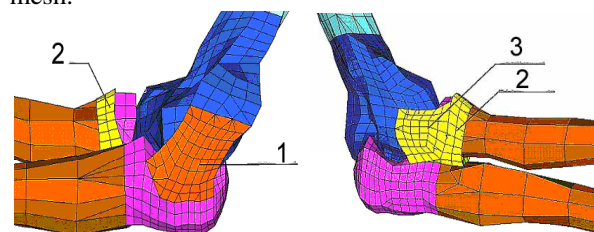


Figure 11. Elbow mesh with ligament CollUlnar 1), AnnuRadial 2) and CollRadial 3) (Doc. TNO).

Thorax, Abdomen, Pelvis

Ribs Mesh Improvement: To predict the rib injury with greater accuracy, the ribs mesh has been refined. Figure 12 shows the ribcage before (left) and after (right) refinement of the cortical (shells) and the trabecular (solids) bones. Each element has been divided into two elements along the curvature of the rib. The refined rib cage is now composed of 5518 shells and 2796 solids.

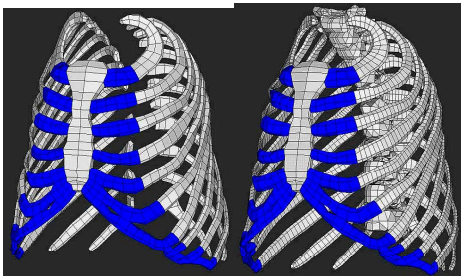


Figure 12. (left) Old, (right) new ribs mesh (Doc. ESI).

Aorta Insertion: The aorta rupture is an important injury of the thorax. The mesh of this organ has been added in the model. The geometry of the aorta came from unused data of the previous HUMOS project. It has been transformed to obtain an adequate position with respect to the heart, the spine and the diaphragm mesh. Figure 13 shows the mesh with shell elements of the aorta between the heart and the diaphragm.

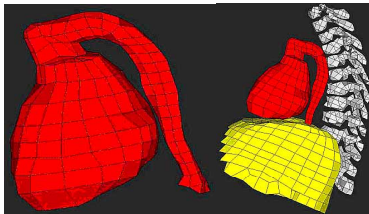


Figure 13. Aorta mesh (Doc. ESI).

The mesh of the aorta is composed of 191 shells and is connected to the heart and to the diaphragm by a continuous mesh. It is superimposed to the flesh for connection between organs. Thus, no interaction between the aorta and the flesh is possible through the mesh. An attachment between the aorta and the spine and a contact between the aorta and the lungs, the heart, and the spine has still to be modeled.

Thoracic and Abdominal Organs Mesh Improvements: The mesh quality of the thoracic and abdominal organs has been checked and corrected. The liver, the stomach and the intestines mesh have been corrected, but the maximum angle criteria (mesh quality criteria) were partially respected because of the specific geometry of those organs. In the first HUMOS model, the mesh of the heart, the lungs and the flesh were continuous. In the updated version, the heart mesh has been separated from the flesh and from the

lungs to allow the relative motion of the heart with respect to the lungs. This part of the model needs further development concerning the description of the organs and soft tissues, especially in the abdomen

Lower Limb

Lower Limbs Bones Improvements: The femur and tibia cortical bones were refined to improve the response of lower limbs and to predict bone fracture. Each element has been divided into two elements along the bone long axis. The refined femur and tibia bones are respectively composed of 220 and 176 shells. The capsular hip joint, composed of 16 1D elements, has been added between the femoral head and the Glena (Figure 14) to improve the hip model.

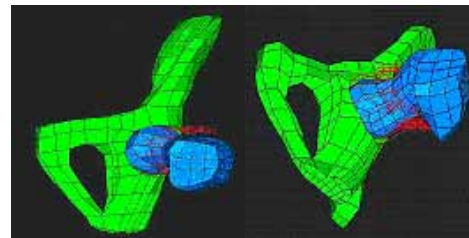


Figure 14. Capsular hip joint (Doc. Mecalog).

Lower Limbs Flesh Modifications: To improve the response of the model in terms of soft tissue/bone contact and to reproduce more precisely the behavior of pedestrian, refinements were performed on the flesh and skin of lower limbs.

Figure 15 shows the new mesh of the knee. For the limbs, the meshes are composed respectively of 1559 solids and 914 shells elements (787 solids and 573 shells elements for the old flesh and skin version).

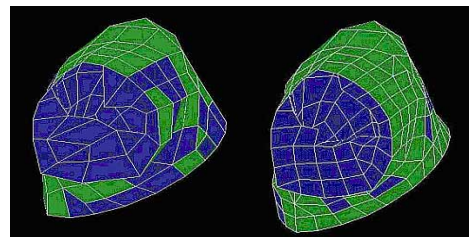
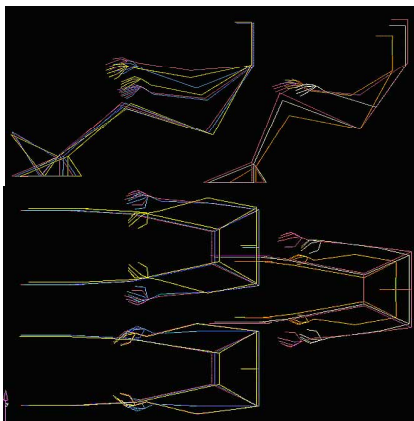


Figure 15. Upper leg and knee flesh (blue) & skin (green), left) old; right) new (Doc. Mecalog).
POSTURE DEFINITION

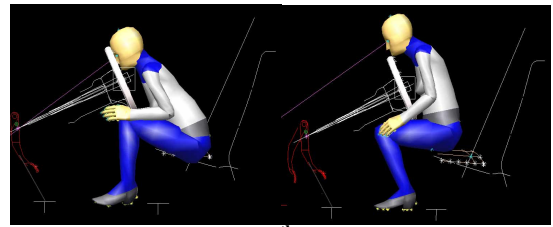
Standard Occupant Position

The occupant of a car involved in an accident can be a driver, a passenger front seat or a passenger rear seat. Defining correctly these various occupants' positions is a need for an accurate injury prediction. The occupant morphology was also taken into account. For each case the best ergonomic posture was studied. It was proposed to use DSPM [Driver

Among all the available posture, 3 random postures were chosen for 2 types of cars and for each occupant. Figure 17 shows an example of the 3D postures for the 95th percentile (passenger front seat, rear seat and driver) in the car #2:



The second part of the task was addressing *Out Of Position (OOP)* postures of the 5th female model to get an idea of the relative change of body joint angles of two OOP postures compared to a normal driving position. The result obtained will be an input for the positioning tool. The study was performed using a RAMSIS 5th dummy; the outcome is expected to be very similar for the HUMOS2 model. OOP1 is chin on airbag module; OOP2 is chin on the rim of the steering wheel, both according to the FMVSS 208 (Figure 18).



Standard Pedestrian Position

(1) Analysis of accident regarding walking, running, and jumping postures. The impact directions were from pedestrian lateral side, pedestrian facing to car or impacted from backside.

- The study was carried out in several steps : 1) review of published literature dealing with pedestrian initial posture; 2) accident statistics analysis with available data; 3) accident reconstructions; 4) analysis of simulations of pedestrian impacts; and 5) analysis of normal gait cycle.

- In 80-90% of the cases the pedestrians were hit from the side by the front structure of a vehicle when crossing a street;
- In the EU countries, the number of pedestrians struck by passenger cars is around 60% to 80% of the reported vehicle-pedestrian accidents;
- The initial postures of the pedestrians at the impacts could be in a standing position, normal walking or running movement.

VEZIN - 8

- In about 85% of the cases the pedestrians were hit laterally (37% at the right side, 48% left);
- 15% of the pedestrians are struck on their front;
- 79% of the pedestrian were in motion;

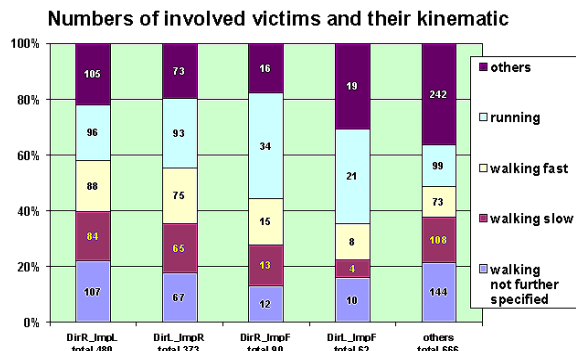


Figure 19. The numbers of involved victims and their initial moving postures (Doc. VW).

Then, an investigation was performed with 35 well-documented fatal cases of pedestrian/vehicle accidents which were reconstructed. The typical positions in real accidents with location of the first contact interaction and the produced injury by this contact were analyzed. The analysis pointed out that:

- for most of the pedestrian/car accident cases, the pedestrian was hit while crossing the road in an upright position;
- the 1st contact interaction of an adult is most frequently located at the lower extremity especially the shank, according to the bumper height of the involved car;
- there is a correlation of normal gait cycle with pedestrian initial posture.

The pedestrian postures in front of the vehicle before the impact were analyzed based on accident data:

- For the walking position, it was proposed to take into account the leg orientation. During the pedestrian impact, the kinematics and dynamic loading of pedestrian are not the same if the left leg is forward or if the right leg is forward;
- Concerning the running position, it is difficult to validate a pedestrian model due to the lack of physical test data available in this configuration;

Based on the results from this study, it was concluded that the impact responses and injury outcomes are significantly affected by the initial postures and the orientation of body segments. The consortium agreed to develop two pedestrian models. One model is in normal standing posture and another in normal walking posture. The positioning of the pedestrian model is defined based on the anatomical position of human body (Figure 20).

The postures of the pedestrian models are to be adjusted according to the configuration of the needs in specific modeling of vehicle/pedestrian impact.

The normal walking and running postures with left leg forward are specified with related rotation of joints from the baseline model within the range of physiological movement (Figure 20).

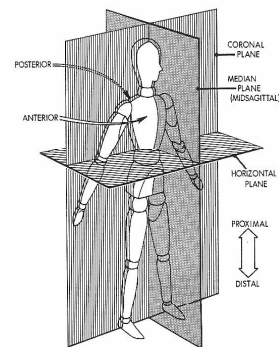


Figure 20. Anatomical position of the human body, baseline model.

Table 4.
Rotation from normal standing to walking and running posture

Body segment	Walking	Running
Left hip flexion	6°	6°
Right hip extension	6°	5°
Left knee flexion	3°	8°
Right knee flexion	5°	35°
Left elbow flexion	6°	80°
Right elbow flexion	4°	69°
Left shoulder joint	8°	23.5°
Right shoulder joint	8°	15°
Left ankle extension	3°	-
Right ankle flexion	2°	-

Positioning Tool

The meshes of 5th, 50th and 95th percentiles in the pedestrian and car occupant positions will be created from the corresponding meshes in sitting position. To achieve these objectives a positioning tool is under development. Preliminary simulations were performed to study HUMOS capability to be in standing position and shown satisfactory results even if a re-mesh of pelvis flesh in standing position are necessary.

Each software developer involved in the development of the HUMOS2 models builds its own positioning tool based on different approaches.

For example the positioning tool developed by ESI uses interactive real-time background calculations provided by a simplified finite element solver (SFE solver). The main feature of this positioning tool is to model the physics needed during user imposed articulation movements. It does this by:

- performing real time simulation,
- using rigid body dynamics and joint physics in the simulation,
- imposing user requested rotations and translations,
- using other physics based options such as elastic structures and contact interfaces,
- using geometry based options such as geometrical interpolation.

An example of results from the positioning tool developed by ESI is shown in the following Figure 21 and compared with the position of a car occupant as defined in “car occupant definition” work.

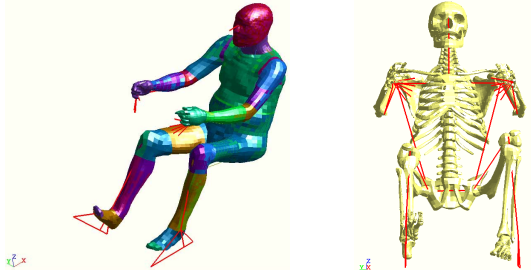


Figure 21. HUMOS2 model in posture of 50th percentile driver compared with the standard car occupant position (Doc. ESI).

The method used by Mecalog in its positioning tool software allows setting any percentile model in any position without calculation. By using a pre-calculated position database, a new position can be computed by using only linear interpolations. The specification of the wanted position by the input of 28 angles allows a quick, easy and reliable use of the software. Figure 22 shows an example of the different leg position obtained from the software.

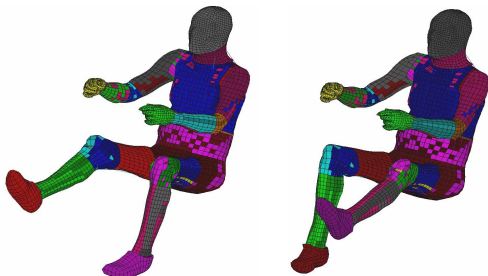


Figure 22: Different leg positions for a 50th percentile obtained from the Mecalog positioning tool (Doc. Mecalog).

TISSUE MECHANICAL PROPERTIES

Biological Material Laws

The assessment of injury risks and the prediction of injuries need the implementation in the model of up-to-date material properties. Soft tissues, in particular muscle material properties at high loading rate are poorly described in the literature. Consequently, some experimental static and dynamic tests were achieved

within the project on different biological materials such as ligaments and skeletal muscle.

Dynamic Behavior of Ligaments: The goal of this research was to characterize the mechanical behavior of soft tissues under a wide range of loadings (from quasi-static to dynamic). A protocol was designed for performing tensile tests on knee ligaments placed in a *physiological* position. The experiments deal with cyclic and failure tests, under quasi-static and dynamic loadings of the PCL (Posterior Cruciate Ligament) and LCL (Lateral Collateral Ligament). The same protocol was used for the two types of loading. (Figure 23.)



Figure 23. Pictures of the sample placed on the tensile device (Univ. of Méditerranée).

Cyclic tests were performed with prescribed displacement at the frequencies: 10, 20 and 30 Hz, and amplitudes of displacement: 1, 2 and 3 mm, and with sinus or triangle displacements. Speed range was then from 20 mm/s to 180 mm/s. The knees were first cyclically tested with the 2 ligaments, then one of them was removed. Finally, the other ligament was tested up to failure. Tests were beside performed for 2 angles of knee flexion (180° and 120°).

The comparison of ligaments behavior shows that:

- The dissipation during cyclic tests is independent on the frequency, that is to say on the velocity,
- The ranges of load for the cyclic tests are not very different in quasi-static and in dynamic,
- For the failure tests, the stiffness of the PCL in flexion and of the PCL in extension are only a bit higher in dynamic than is quasi-static, whereas the failure loads and failure displacements are clearly higher in dynamic than in quasi-static,
- The failure occurs mainly at the insertion sites, and it is deeper in dynamic than in quasi-static. In dynamic, there is always a loss of cohesion in the ligament, whereas this was not observed for the quasi-static tests, at least at the macroscopic level.

Finally, from the results, numerical laws are proposed for the behavior of the ligaments and will be implemented in the HUMOS2 models.

Dynamic Muscle Properties: There is only few data available on the behavior of skeletal muscle under dynamic conditions. A study was then dedicated to improve this knowledge. The aim is to

determine the transverse mechanical (stiffness) properties of skeletal muscle at quasi-static loading and for dynamic loads up to high frequencies. A second objective is to find damage thresholds of the skeletal muscle, which can be used in crash tests.

The quasi-static properties were determined using in a non-invasive set-up that allows *in-vivo* determination of the properties of skeletal muscle in Brown Norway rats using a MRI-facility. Conceptually, the best way to determine properties is to do that *in-vivo*, because problems with making test-samples and keeping tissues in the proper conditions during *ex-vivo* testing can be avoided. Moreover, properties found are more representative for the real tissue than *ex-vivo* properties. Immediately after a load is applied and removed it is also possible to detect damage at the cell level by means of T2-weighted imaging (Figure 24).

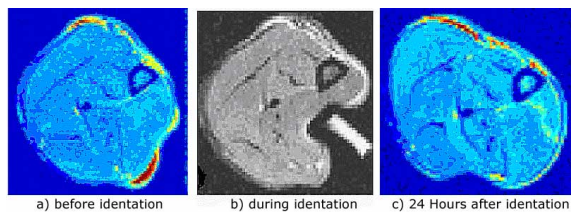


Figure 24. T2-maps of the rat hind limb. (Doc. TU Eindhoven).

The dynamics tests were performed *ex-vivo* with standard DMTA testing on a rheometer. In this case the disadvantages of *ex-vivo* testing were accepted, because of the possibility to use time-temperature superposition. By cooling down the samples and measuring at low temperatures, the properties change according to a specific time/temperature rule. Then, a master curve at the relevant temperature can be constructed for a broad range of frequencies. This procedure has been already performed for brain tissue with success (Brands et al. [8]) and could be used for skeletal muscle for frequencies < 16Hz.

From a comparison from quasi-static and dynamic experiments the following conclusions can be drawn:

- It appears that the shear stiffness increases to reach a plateau value of 40 kPa at high frequencies. Visco-elastic effects become very small at high frequencies.
- The muscle tissue behaves linear for shear strains up to $3 \cdot 10^{-3}$. The loss modulus decreases from with the frequencies. At high frequencies the material starts to behave as an elastic material.
- For small deformations the Neo-Hookean model is a suitable model for muscle. For large deformation the Ogden model has to be used. For details on the implementation of the Ogden model in a finite element code see Simo [9].
- It is acceptable to use elastic properties for skeletal muscles for impact studies with the HUMOS2 model.

Effect of Muscle Tonicity

The main limitation of current human models is the lack of data included about the effect of the muscle activities. Moreover, the models are often validated with data coming from cadaver tests without muscle tonicity. A tentative work was started in the project in order to obtain information on the effect of muscle tone on the global kinematics and on materials properties and to assess the influence of the muscle pre-activation on the response to a moderate impact.

Effects of Muscle Tone on the Kinematics: The first objective was to determine the effect of muscle tone on the response of the human body in lateral, dorsal and frontal thoracic impact by subjected volunteers to pendulum impact (Figure 25).



Figure 25. Impact locations lateral, dorsal and frontal (Doc. LMU).

The influence of muscle state was investigated by performing “unexpected” (relaxed muscles) and “expected” (pre-activated muscles) pendulum tests. Quantitative analysis of displacements (amplitude, time of beginning and maximum) and muscle activities (time of onset) resulted in mean values that can be used for validation of the HUMOS2 models.

The test setup fulfilled the following requirements:

- Used of volunteers with minimal risks of injuries;
- Application of experimental results for simulation;
- “Simple” modeling of test setup for simulation.

The kinematics were recorded by a motion analysis system using reflecting markers, the muscle activity was recorded by surface electrodes. The following parameters were quantified and used for the validation of the human models by comparing the experimental results with results from the simulation:

- Displacement in the impact direction for head-top and C7 markers;
- Angle of the head relative to the trunk;
- Onset times for left and right different muscles.

Measurements with different “height of deflection” and “weight of pendulum” were performed. An example of some results is given hereafter:

- Head-top and C7 displacements are less for tensed muscles than for relaxed muscles. Due to inertia the head shows a small displacement in opposite impact direction before the head is accelerated together with the trunk in impact direction.
- For higher energies, larger displacements and angles can be observed.

- High impact energy causes higher and faster muscle responses. Trunk muscles are activated later than neck muscles for side and rear impact..
- Displacements and angles show a higher variance for tests with relaxed muscles than for those with activated muscles. However, displacement curves for both muscle states appear similar for each volunteer (individual characteristics).
- For similar impulses in side impact, but twice the energy, similar displacements were found. Most likely, the impulse mainly influences the reaction or kinematics of the body.
- In rear impact, EMG onsets show a high variance and no correlation for the lowest energy. For higher impact energies the displacement is better correlated. In frontal impact, a good correlation is found for all impact intensities.

Effects of Muscle Tone on the Material

Properties: The second objective was to determine the effect of muscle activation on the transverse material properties of the arm and femur soft tissue. Only few articles could be found investigating transversal material properties of muscle tissue. A test setup was therefore developed for the dynamic study of these properties in dependence of the muscle activation state. An impactor falls through a Plexiglas tube and impacts the volunteer's muscle (Figure 26).

Three impact locations were tested: 1) upper arm ventral, m. biceps brachii ; 2) upper leg ventral, m. quadriceps femoris, pars rectus femoris ; 3) upper leg dorsal, m. biceps femoris.



Figure 26. Experimental setup (Doc. LMU).

Peak accelerations, rebound heights, indentations and velocities were obtained. EMG signals of the muscle were recorded in order to get the muscle activity during the impact. The main results are:

- 1) Acceleration peak values for different activation states at a constant falling height nearly coincide.
- 2) Acceleration peak values vary between volunteers for relaxed muscles, but remain nearly constant for repeated tests with the same volunteer.
- 3) An increasing height of fall causes higher acceleration peak values.
- 4) First acceleration peak exhibits a distinct shape for relaxed and tensed arm muscles. This phenomenon could only be observed for the arm muscle, not for the leg. This might be caused by the difficult impact location definition.

- 5) For relaxed muscles no impactor rebounds were observed. The whole impact energy is transformed into flesh deformation. For tensed muscles several impactor rebounds are observed. The time between the first and the second acceleration peak (rebound peak) can be used for calculating the amount of energy transformed into deformation of the flesh.

Influence of Muscle Pre-activation: The third objective was to define the influence of muscular activation prior to impact (pre-activation) on the overall stiffness of the lower limb and to establish the relationships between this muscular activation prior to impact and impact loading associated with shock wave transmission from the shank to the thigh.

To establish these relationships, experiments were carried out using volunteers and a sledge ergometer (Figure 27). Such device allows to impact to the lower extremity of the seated subject while controlling the level of pre-activation. The evolution of the reaction force developed at impact, the corresponding variation of loading rates, the muscular force around the impact time (at and after), the associated kinematics of the lower limb and the impact cushioning provided by them were assessed.



Figure 27. Sledge ergometer (Doc. Univ. of Méditerranée).

The positive relationship between, on the one hand, the level of pre-activation and the impact peak force and, on the other hand, the associated loading and unloading rates were demonstrated. In others words, the increase of pre-activation generates the increase of the force-related parameters (impact peak force and associated loading and unloading rates).

It was tried to show the existence of differentiated reflex mechanisms with the increase of voluntary muscular pre-activation for the lower limb muscles controlling the thigh and leg dynamics.

On a functional point of view, it is evident that the driver tends to increase the overall stiffness of the lower extremity via muscular activation when a frontal collision is imminent and visible. The consequences of the increased pre-activation are:

- increase of the amplitude of the impact peak force with a higher loading rate,
- increase of reflex facilitation,

- the knee is the most controlled joint due to the predominant action of the Vastus medialis muscle compared to Triceps surae.
- massive attenuation of highest frequency components.

These results strengthen the point that it is necessary to include in human numerical models the muscle behavior to better evaluate the overall stiffness of the body before and at impact. The improvement of the biofidelity of the numerical models will allow the development of passive and especially active security devices in the automotive domain.

Global Validation Data

Finally, the whole human body models need to be globally validated in a situation representative of a real car crash. First validation data from sled tests were obtained in the first HUMOS project (Vezin et al. [10]). In HUMOS2 the acquisition of validation data is pursued through the re-analysis of existing data and by performing new test in frontal and oblique directions with up-to-date restraint systems. All these data and the information coming from the human material properties research will be gathered in a “Biomechanical Experiment Database” that allows the exchange of information between data suppliers and end-users of these information.

Existing sled tests analysis: The first objective was to re-analyze 46 frontal impact cadaver sled tests, performed at Univ. of Heidelberg, with belt and/or airbag protected subjects.

The tests were distributed in 4 test groups:

- 1st: 30kph, medium sled deceleration 20G, 11 tests
- 2nd: 40kph, medium sled deceleration 20G, 11 tests
- 3rd: 50kph, medium sled deceleration 20G, 12 tests
- 4th: 60kph, medium sled deceleration 15G, 12 tests

The analysis concerned: test conditions, anthropometric data for each case, time-histories of single and resultant signals, corridors, photographs prior to and after the test, medical findings in word protocol and schematic with classification according to AIS and digitized high-speed films.

Moreover acceptable correlations were found between mechanical parameters and injury severity:

- max. shoulder belt force vs. weight;
- max. shoulder belt force vs. weight x seating height;
- max. shoulder belt force vs. seating height;
- max. shoulder belt force vs. chest circumference;
- area below force-deflection curve vs. impact velocity.

Complementary sled tests: To further extend the validation database of the HUMOS2 models, new sled tests with PMHS are performed at INRETS. The goal of these experiments is to provide detailed information

on the global behavior of a body submitted to frontal and oblique impacts. Different impact conditions (50kph and 20G, 30kph and 15 G) and different restraint systems including load limited belt and airbag are being tested. A specific protocol was prepared by the Consortium and mainly focuses on the thorax behavior, but data about head, neck pelvis and lower legs will be provided.

Biomechanical Experiment Database

The objective is to develop a biomechanical experiment database which can gather the impact biomechanics results from experimental studies conducted with human subjects, either cadavers (donated to Science) or live volunteers. This research brings valuable results but is facing numerous difficulties due to various reasons: scientific, practical, technical and ethical. In some countries, this kind of research is very difficult to organize and sometimes is not possible at all. It is important to ensure the dissemination of these results as far as possible towards the scientific community in a way their use is facilitated. The european biomechanical experiment database will be established by the INRETS-LBMH Laboratory in order to properly disseminate and safeguard this data. The content includes data from biomechanical impact tests conducted in different laboratories involved in the project, as well as information on the associated test facilities and test subjects. The possibility to extend the content to the biomechanical experiments conducted within all EC funded RTD projects in the field of passive safety has been considered.

In the perspective of achieving this task, a list of specifications was drawn in order to establish the database. The opportunity was given to potential users of these data to express their needs (crash simulation code developers, dummy manufacturers, automobile manufacturers). Fruitful discussions conducted to several resolutions, among them the definition of guidelines for biomechanical testing depending on the use of the results (numerical model or dummy development). The database has been included into the activities of the European Advanced Passive Safety Network of Excellence, APSN, in order to guarantee its viability after the end of the project. This will provide at European level similar information as the existing NHTSA database in the US. The accessibility to the scientific community at large is also considered.

DISCUSSION AND CONCLUSIONS

In the view of designing widely accepted human body models, a joint effort between some European

car manufacturers, suppliers, software developers, public research institute and universities was undertaken since 1997 within the HUMOS project. The same participants and new partners, who provided expertise and knowledge in the field of biomechanics have decided to continue and increase this effort in the HUMOS2 project started at the end of 2002. This program led to the definition of a set of refined FE models of the human body in driving and pedestrian postures. These models were implemented with three main dynamic FE codes: Madymo®, Radioss® and Pam-Crash®. This collaboration at a pre-competitive stage is very important to reach the common objective of designing a widely accepted model.

A large validation database was build and will be used to validate the models in different impact configurations. The injury predictive capabilities implementation and the validation of the model still have to be done in the final step of the project. This validation will comprise the simulation of injury mechanisms mainly for the thorax, knee and lower legs. The simulation of influence of muscle tonicity based on the experimental work performed in the project will be performed. Some attempts will be done to simulate the effect of the inner pressure. Finally the models will be validated thanks to the data included in the biomechanical experiments database.

In parallel with this validation effort, the HUMOS2 models will be extensively used in different impact conditions in order to assess their capacity in predicting injuries in real accident scenario via simulated reconstructions. The simulation of car crash or other transport accident situations and of body response in case of out of position will be carried on. Another objective is to compare these capabilities with those of the dummies in view to address the issue of introducing virtual testing with human models in the regulatory process.

Unfortunately, it is currently still difficult to account for the properties of living subjects, and as far as the mechanical behavior in car crash conditions is concerned, mainly cadaver results are available in the literature. In HUMOS2, a new step forward was done through the investigations on the muscle tone contribution and muscle pre-activation using volunteers tests. This research field is of great interest, especially for the low speed impact conditions that can be encountered in real field accident analysis. Furthermore, some limitations are due to the lack of knowledge of the injury mechanisms. The currently used criteria were implemented in the model, but its injury prediction capabilities are limited with regard to its complexity.

From the beginning of this research work, it was foreseen that some major limitations would remain. First of all, the geometrical definition of the model

despite its refinement, comes from a unique specimen, with some particularities. However, thanks to the geometrical acquisition work performed and scaling techniques, the HUMOS2 partners were able to define 1) a 50th percentile model from the current reference mesh and, 2) a 5th and a 95th percentile occupant models. They also derived from these models some pedestrian models. To achieve these innovations, two specific softwares were developed, one for the personalization of the model, i.e. “the scaling tool” one for the positioning of the models, “the positioning tool”. Obviously, these tools need further development, but within a very short term, they can provide the possibility to derive models of any living people in any postures possible during an accident occurring in any kind of transport mode.

It was also identified during this work that some knowledge is still missing as far as the soft tissues behavior is concerned, especially the abdomen needs a great attention in the future, and also the muscle tone contribution in some crash conditions. It is expected that the model itself, which is accounting for the main muscular structures and the main soft tissues will enable to carry out parametric studies aiming at evaluating the muscle contribution and aiming at the assessment of some injury mechanisms. In the future, Human models are called to play an important role in the development and validation of safety solutions through the use of virtual testing. Standardization and regulation bodies (ISO, EEVC) are presently looking at the potential for virtual testing to be used in a regulatory context. HUMOS2 is willing to support this process and may bring interesting tools besides those developed within other EC funded projects like VITES and ADVANCE. A lot of efforts is still needed for the development of the FE global human models; a new phase is about to start within the European funded Integrated Project “Advanced Protective Systems Project “APROSYS.

CONTRIBUTING PARTNERS

The development of the HUMOS2 models is a joint effort of many partners. The coordination of the work was done by INRETS which was also involved in different parts of it. Univ. of Méditerranée coordinated the geometrical acquisition task and in collaboration with SERAM and INRETS performed an innovative work on the paired acquisition and analysis of internal and external dimensions of the human body. This was a very difficult and crucial work and the data obtained are of great interest for the research in biomechanics. Mecalog, with Univ. of Méditerranée developed the scaling tool for the personalization of the models.

Software developers were strongly involved in this research program. Mecalog (Radioss software) coordinated the meshing activities and insured the assembly of the final model with Radioss. ESI (Pam-Crash software) participated to meshing activities and was responsible of the validation task of the models. ESI also insured the assembly of the final model with Pam-Crash. TNO carried out the meshing and modeling work under the Madymo software and coordinated the human mechanical properties work. These three software companies have developed their own positioning tool during the project.

The car manufacturers involved were Volvo (neck re-meshing, validation and evaluation activities), PSA, Renault (evaluation work) and VW (definition of the positions, validation and evaluation tasks). The supplier Faurecia carried out the investigation of car occupant and pedestrian positions and participated to the evaluation and validation effort.

Chalmers University achieved a wide bibliographical study on the knowledge about injury mechanisms and contributed to the validation and evaluation of the models. Univ. of Heidelberg provided a deep re-analysis of full-scale sled tests with human substitutes including injury mechanism and contributed to the extension of the validation database. INRETS carried out complementary sled tests with human substitutes and contributed to the creation and the extension of the validation database. TU Eindhoven, and Univ. of Méditerranée carried out a research work aiming at defining of physical material laws under loading conditions for the different human soft tissues. The effect of muscle tonicity and pre-crash activities were studied through an innovative program of volunteer tests by Univ. of Méditerranée and LMU Muenchen. LMU participated also to the thoracic injury mechanism study, pedestrian position definition and to the validation and evaluation of the models. All these partners delivered a wide set of new experiments and contributed to the extension of the validation database.

ACKNOWLEDGEMENT

This project is funded by the European Commission under the 'Competitive and Sustainable Growth' Programme (1998-2002). The authors would like to thank to Ms. Liliane Pereira-Bahia and Mr. Loic Courtot for their essential help and contribution to the day-to-day management of this project.

REFERENCES

[1] Robin (2001). HUMOS: Human model for safety – A joint effort towards the development of refined human-like car occupant models. Proc. of the 17th Int.

Tech. Conf. on the Enhanced Safety of Vehicles, Paper Number 297.

[2] Kalifa G., Charpak Y., Maccia C., Fery-Lemonnier E., Bloch J., Boussard J.M., Attal M., Dubousset J., Adamsbaum C. (1998), Evaluation of a new low-dose digital x-ray device: first dosimetric and clinical results in children. *Pediatr Radiol* 28, 1998, pp 557-561.

[3] Harrison D.D. et al (1996). Comparisons of lordotic cervical spine curvatures to a theoretical ideal model of the static sagittal cervical spine, *SPINE*, 21 (6) 667-67.

[4] Appel, H., Stürtz, G. and Gotzen, L. (1975) Influence of impact speed & vehicle parameter on injuries of children and adults in pedestrian accidents. Proc. of the 2nd Int. Conf. on Biomechanics of Serious Trauma. Birmingham, England. pp. 83-110.

[5] EEVC (1982) Pedestrian injury accidents. Proc. of the 9th Int. Tech. Conf. on Experimental Safety Vehicles, pp. 638 – 671.

[6] EEVC (1998) Improved test methods to evaluate pedestrian protection afforded by passenger cars, Report, EEVC, WG17.

[7] Mizuno, (2003) Summary of IHRA pedestrian safety WG Activities (2003) - Proposed test methods to evaluate pedestrian protection afforded by passenger cars, Proc. 18th Int. Technical Conf. on Enhanced Safety Vehicle, pp.1-17.

[8] Brands D.W.A., Bovendeerd P.H.M., Peters G.W.M., Wismans J.S.H.M., (2000). The large shear strain dynamic behavior of in-vitro porcine brain tissue and a silicone gel model material, *Stapp Car Crash Journal*, Vol. 44, pp. 249-260.

[9] Simo J.C., (1987). On a fully three-dimensional finite-strain viscoelastic damage model: Formulation and computational aspects, *Computer Methods in Applied Mechanics and Engineering*, 60 pp. 153-173.

[10] Vezin P., Bermond F., Bouquet R., Bruyere K., Ramet M., Verriest J.P., Voiglio E. (2001). Comparison of head and thorax cadaver and Hybrid III response to a frontal sled deceleration for the validation of a car occupant mathematical model. Proc. of the 17th Int. Tech. Conf. on the Enhanced Safety of Vehicles, Paper No 114.

APPENDIX A

Table A1.
List of anthropometric measurements

1	Height (vertex - ground height)	26 c	Head maximum width
2	Eyes - ground height (Frankfort's plane parallel to the ground)	27	Head circumference passing over the glabella and through the occiput
3	Acromion (superior border) - ground height	28	Chin - occipital circumference (with lower jaw closed)
4	Elbow - ground height	29	Neck circumference under the thyroid cartilage
5	Anterior-superior iliac crest - ground height	30	Abdominal width (navel) (in sitting position)
6	Greater trochanter top - ground height	31	Abdominal circumference (navel) (in sitting position)
7	Knee articular interline spacing - ground height	32	Oblic circumference of the pelvis (going through the pubis cranial edge and EIPS, in sitting pos.)
8	Iliac bi-crest width	32bis	Thickness of buttock (pubis level, in sitting and standing pos.)
9	Bi-trochanter width	33	Abdominal thickness (navel) (in sitting pos.)
10	Sitting height (vertex - seat)	34	Buttock - heel length (tense leg)
11	Eyes - seat height (Frankfort's plane parallel to the ground)	35	Low pelvic circumference (going through the trochanters) (in standing pos.)
12	Acromion - seat height	36	Thigh upper circumference (superior third of 6-7 length)
13	Elbow - seat height	37	Thigh bottom circumference (inferior third of 6-7 length)
14	Cervical (C7) - seat height	38	Knee circumference (interline spacing level)
15	Bi-acromial width (between the 2 lateral borders)	39	Greatest calf circumference
16	Knee - ground height	40	Smallest ankle circumference
17	Buttock (backrest)- Knee length	41	Greatest foot width
18	Forearm length (olecranon - ulnar styloid with zero rotation of the hand)	42	Greatest foot length
19	Arm length (acromion (superior border) - 90°-flexed elbow) = middle of (12-13, 3-4) (calculated)	43	Lateral maleolus top (point the most lateral) - ground height
20	Thoracic axillary width (end of the exhalation) (in sitting pos.)	44	Arm upper circumference (superior third of 19 length)
21	Thoracic axillary thickness (end of the exhalation) for female subject without bosom (in sitting position)	46	Sternum length (without the xiphoid)
22	Thoracic axillary circumference (end of the exhalation) (sitting pos.)	47	Xiphoid angle (a, b, c) (tangent with the cartilage)
23	Thoracic sub-sternal width (end of the exhalation) (sitting pos.)	48	Longest hand length
24	Thoracic sub-sternal thickness (end of the exhalation) (sitting pos.)	49	Arm bottom circumference (inferior third of 19 length)
25	Thoracic sub-sternal circumference (end of the exhalation) (sitting pos.)	50	Greatest forearm circumference
26 a	Head length = glabella - occiput distance	51	Smallest forearm circumference
26 b	Skull height = auricular height (porion - vertex)		

DETERMINING ACCURATE CONTACT DEFINITIONS IN MULTI-BODY SIMULATIONS FOR DOE-TYPE RECONSTRUCTION OF HEAD IMPACTS IN PEDESTRIAN ACCIDENTS

Robert Anderson

Jack McLean

Centre for Automotive Safety Research, University of Adelaide
Australia

Yasuhiro Dokko

Honda R&D Co.,Ltd

Japan

Paper Number 05-0175

ABSTRACT

Crash reconstruction is sometimes used to study injury mechanisms and thresholds, but is often difficult because crash and model parameters are not known precisely. If simulation is used as part of the reconstruction process, then various Design-of-Experiment (DOE) tools may be easily applied to estimate response surfaces of the dependent variable (e.g. head acceleration), to a range of possible crash factors, subject to the validity of the model. This approach relies on the validity of the model's characteristics over the range of likely crash conditions, meaning that non-linear aspects of the system will often need to be included. The contact between the head of a pedestrian and the hood of a car is an example of a non-linear contact that is critical to the estimation of the variable of interest: the head impact severity (as measured by linear and angular acceleration or HIC, for example). This paper describes the reconstruction of four pedestrian collisions in which the effects of uncertainties in posture and impact speed on the estimation of a head impact severity were quantified. For each case, physical tests were conducted at lower, middle and upper estimates of head impact speed on a vehicle of the same make and model as the striking vehicle in the collision. The results of these tests were used to define a single non-linear contact characteristic in MADYMO that could reproduce the results of all three impact tests. This contact characteristic was then used in the simulation of the collision to estimate a likely range for the head impact severity.

INTRODUCTION

The reconstruction of crashes is one method that has been used to investigate the tolerance of the body to impact and the biomechanics of injury. Anderson et al. (2003) used the reconstruction of pedestrian crashes in the laboratory to test whether headform impact tests could discriminate the injury potential of vehicle structures in pedestrian crashes. We have also previously presented attempts to examine the ability of a finite element model of the head to predict axonal injury in fatal pedestrian collisions (Dokko et al., 2003). There are also other examples in the crash injury literature.

A shortcoming of using reconstructions to study the biomechanics of head injury is that many input parameters used in the reconstruction process are estimates. Uncertainties arising from the investigation process (for example the impact speed of the vehicle) may lead to point estimates of head impact conditions that may be significantly in error. Ideally, any uncertainty should be taken into account.

If computer simulation is used to reconstruct the crash, it is relatively straightforward to create many simulations that encompass, for example, a range of impact speeds. There are tools available that can be used in conjunction with computer simulations to perform simulations according to design-of-experiment principles. The large number of simulations required using such a design mean that it is advantageous to retain as much numerical simplicity as possible: for example, multi-body simulations are more efficient than finite-element methods. However, maintaining the validity of a multi-body model over a range of different conditions is not guaranteed if a simple (linear) multi-body contact model is used, when in reality, contact interactions are non-linear. Ideally, the head-to-vehicle interaction (and other interactions as well) should be valid over the range of likely crash conditions, so that estimates of head impact severity can be made more accurately.

One obvious solution would be to replace critical parts of the multi-body model with finite element structures. However, this may take too long to do. The size of the computation may also limit the number of scenarios that can be simulated, and when several crashes are being analysed these limitations are multiplied.

This paper describes the use of multi-body techniques to reconstruct several fatal pedestrian crashes. In each case, uncertainties about the crash were incorporated by performing variants of the simulation according to what was known about the collision. Subsequently, a contact characteristic between the head and the vehicle has been devised to be valid over the range of head impact speeds predicted by the modelling, and this allowed estimates to be made of the range of the head impact severity to be made, rather than a point estimate of the severity.

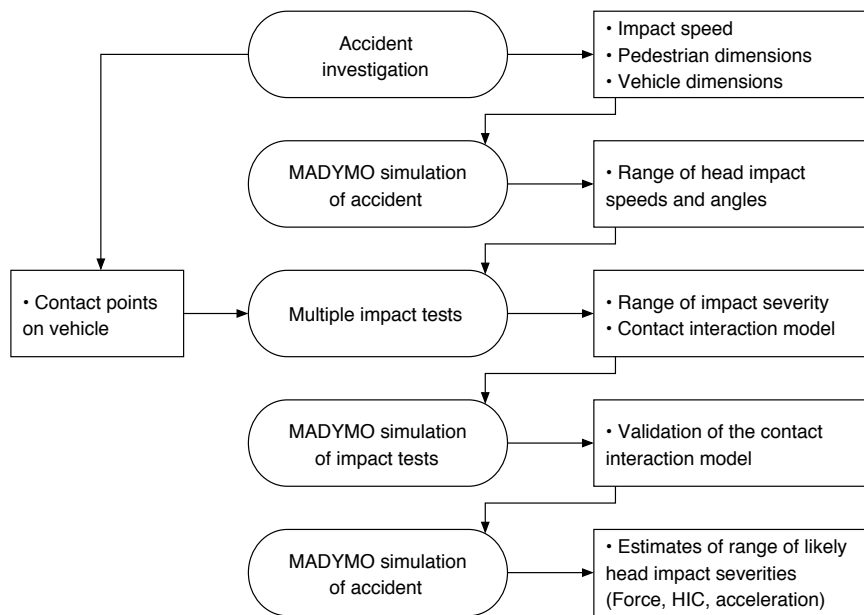


Figure 1. Methodology used in this study

METHOD

The methodology used for this study is illustrated in Figure 1. As explained in the introduction, the methods used in this study attempt to minimise the effects of uncertainties in the reconstruction process by estimating a range of the head impact condition that is likely to encompass that experienced in the actual collision. This means that many collision scenarios have been simulated, covering a range of plausible vehicle speeds and pedestrian postures. For each case, three speeds and six pedestrian postures are considered in 18 simulations. Note that the procedure would be equally applicable where there are other uncertainties in the reconstruction of a crash.

The simulations are analysed to choose three combinations of impact speed and angle (upper, middle and lower) that represent the range of the head impact velocity that was experienced in the accident (as predicted by the modelling). These three impact speeds and angles are used to do sub-system impact tests, on the same make and model of vehicle that was involved in the crash. These tests provide upper, middle and lower estimates of the head impact severity and, enable us to characterise the contact between the head and the car: the tests are used to generate a contact interaction model that can adequately describe the interaction of the headform and the vehicle over the range of test velocities.

The resulting contact interaction model is validated by reproducing the headform acceleration in a MADYMO model of each sub-system test. If the contact interaction model can reproduce the head impact acceleration over the range of impact speeds in the tests, by extension it can be considered suitable to describe the contact between the head and vehicle in the simulations of the pedestrian-vehicle collision. We then estimate a range of values for the head impact severity: the range should encompass that experienced in the crash. The impact severity is reported using HIC values, and linear

and angular acceleration. Furthermore, the definition of this characteristic will make improvements in the estimate of head acceleration possible, should we improve the models.

Cases

The Centre for Automotive Safety Research has investigated over 200 fatal pedestrian crashes. Investigations include site surveys, vehicle examinations and photography, determining impact and travel speeds, and attending the autopsy of the victim. At the autopsy, injuries are noted with the aid of the forensic pathologist, and photographs and body dimensions are taken.

In South Australia, the Coroner investigates the cause of death of every road mortality, and as part of his investigation, he requires the examination of the brain by a neuropathologist. This examination has usually taken place at the Institute of Medical and Veterinary Science, located in Adelaide. The combination of this routinely collected neuropathological data, and the accident investigation, provides a rare source of data on human brain injury and the circumstances of its causation.

This study set out to find cases in which the brain injuries were suitable for further analysis by the finite element method. Some results from the FE analysis have been presented previously (Dokko et al., 2003).

The cases reconstructed for this study are summarised in Table 1.

Computer simulation

The model that was used for the simulation part of this study was developed specifically to simulate pedestrians in car-pedestrian collisions. The model has been presented previously (Garrett, 1996; Garrett, 1998) and used for accident simulation purposes (Anderson et al., 2002; Anderson et al., 2003). The model consists of 17 rigid segments linked by kinematic joints that are

Table 1.
Details of cases used for the reconstruction

Case	Pedestrian	Vehicle	Throw distance	Impact speed	Head contact structure	Head and C0 injuries (may not be the fatal injury)
H021-86	87 y.o. male, 66 kg, 186 cm	1976 Large 4-door sedan	22-25 m	50 - 64 km/h	bonnet	Fracture of right temporal base of skull and patchy subarachnoid haemorrhage
H032-86	81 y.o. male, 75 kg, 175 cm	1974 Small 4-door sedan	22-25 m	50 - 64 km/h	base of windscreen and dash	Subarachnoid haemorrhage
H029-89	87 y.o. male, 44 kg, 158 cm	1976 Mid-size 4 door sedan	28-33 m	57 - 74 km/h	bonnet	Fracture/dislocation of the atlanto-occipital joint with spinal cord laceration and lacerations to the head
H070-85	14 y.o. female, 64 kg, 163 cm	1970 Small 4-door sedan	24 m	53 - 64 km/h	base of windscreen and dash	Fractured skull base, subdural haematoma, contusion to left frontal lobe, cerebral laceration cerebral oedema

largely based on the model proposed by Ishikawa et al. (1993) although some joints have been added while others have been modified (see Garrett, 1996).

Before the simulations could be made, the model was checked to see that it satisfied validation corridors that were constructed from post-mortem human subject (PMHS) tests, carried out in Hannover (Ishikawa et al., 1993). These corridors specify the trajectory of different body components as well as the time history of the head velocity. The biofidelity of the model was tested using two car profiles used in the PMHS experiments. 'Car A' was simulated with the pedestrian model at three speeds, while 'Car B' was simulated at two speeds. The initial stance of the model was chosen to match the general stance of the PMHS in the experiments.

The model's behaviour is in generally in accordance with the corridors drawn from the PHMS tests. The results of the simulation of the collision between the PMHS and Car B are particularly close. The characteristics of the model in a collision with the profile of Car A still produce results that mostly fit the corridors of the tests, but the behaviour seems to diverge slightly from experimental results in some parts of the simulation. The profile of Car A has a higher leading edge than Car B. The results of pedestrian collision models appear to become more variable with higher leading edges (Anderson and McLean, 2001). However, we judged that these discrepancies were not important for the current study.

Implementation of the model in the simulation of the accidents

The cases that were modelled in this study involved pedestrians of varying ages and statures. The model was based on and validated against the behaviour of a fiftieth percentile adult male. Therefore, the model was scaled to the dimensions of each pedestrian in each case. The pedestrians' weights and heights were used to generate anthropometric data (segment dimensions, masses and moments of inertia) using GEBOD (Baughman, 1983), a program which generates anthropometric segment data using regression equations derived from a database of human body measurements. The resulting dimensions were checked against the

actual body dimensions of the pedestrians that were measured at autopsy. In cases where the dimensions could be cross referenced, the dimensions were adjusted as the opportunity arose and used to generate a revised GEBOD data-set.

The next step in the simulation process was to model the posture of the pedestrian prior to impact. Body postures representative of the human gait cycle were used to generate separate simulations. Six postures were used in all and represented evenly spaced positions in one gait cycle. Combined with the three speeds, these postures meant 18 simulations were carried out in each case. The gait positions are illustrated in Figure 2.

Vehicle modelling

Vehicles that corresponded to the make, model and series of those involved in the cases were obtained for the physical reconstruction process. We also measured the geometry of the cars for the simulation. A Geodimeter (usually used in surveying) was used to measure the main geometrical features of the car. A prism was held at various points and the Geodimeter was used to record the position of the prism in Cartesian coordinates. These were used as a basis of the geometry created in MADYMO. The geometry was imported into Easi-CrashMAD (a MADYMO pre-processor) in IGES format. The vehicle geometry was then approximated by defining planes, elliptical cylinders and ellipsoids. An example is shown in Figure 3. Where the vehicle in the case braked heavily, the front of the vehicle was lowered by 100 mm and then rotated by 3°, to take account of the dip in cars produced by braking (Figure 4). Sections of the vehicle were assigned contact characteristics based on published values.

Because the speeds of the vehicle were only estimated as a range, three sets of simulations were made to cover the range of possible vehicle velocities. These were at the upper and lower limits of the estimate of impact speed, and the third at the median speed of the range.

RESULTS

Each simulation provided estimates of the head impact velocity and impact angle. The head impact speed and angle were averaged over each gait position at

each vehicle impact speed to provide test conditions for the impact reconstruction. The results of this are shown for each case in Figure 5 to Figure 16.

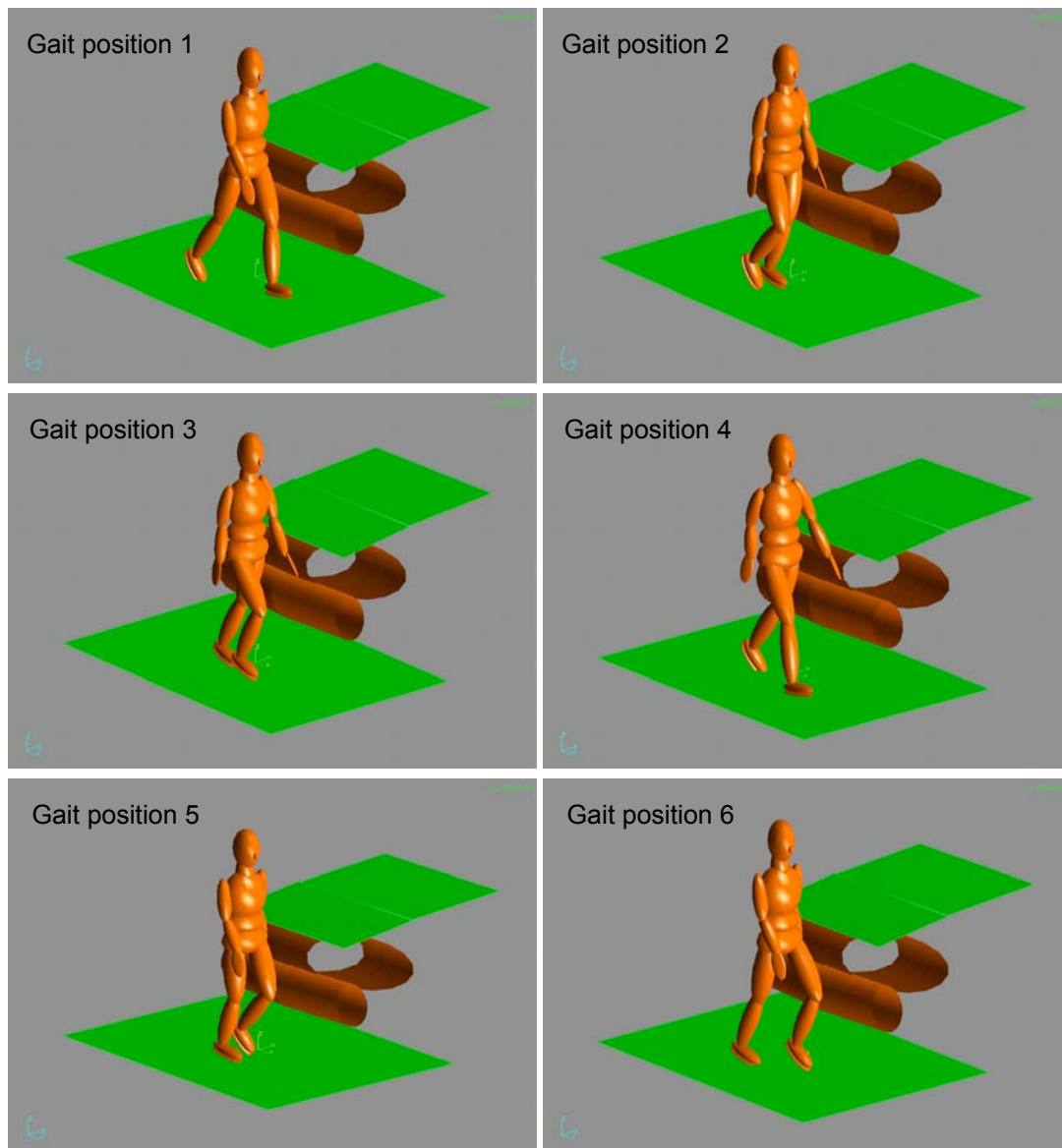


Figure 2. Gait positions used in the simulation.

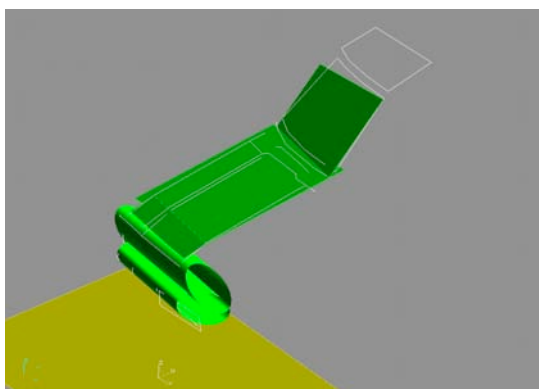


Figure 3. Geometry of one of the vehicles, and the entities used to approximate its shape in MADYMO.

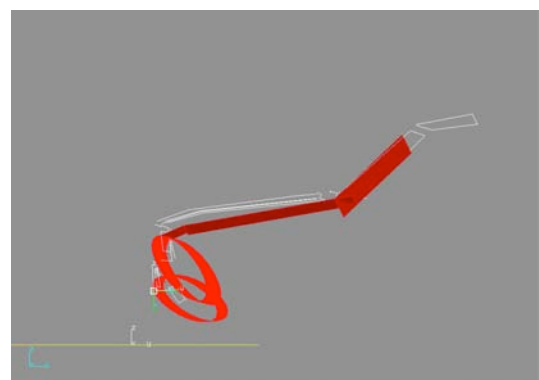


Figure 4. Dip introduced for vehicles that were braking.

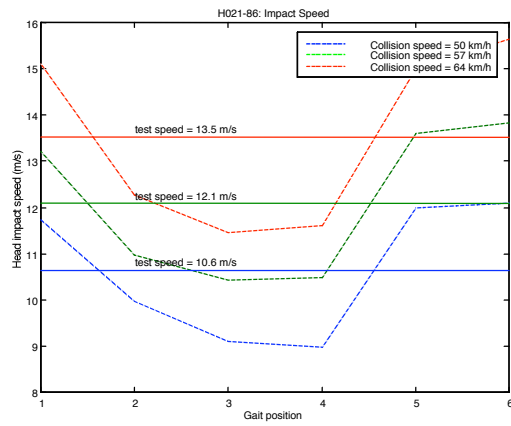


Figure 5. Head impact speed in the simulations of Case H021-86

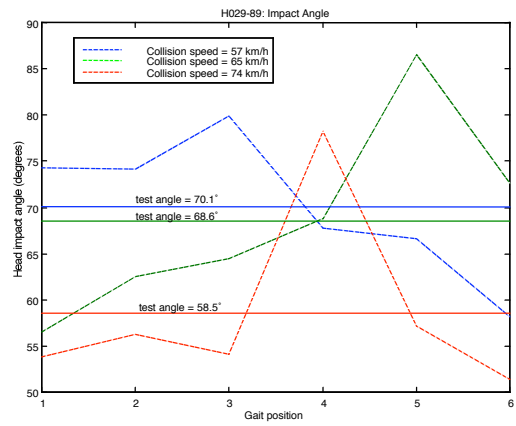


Figure 8. Head impact angle in the simulations of Case H029-89

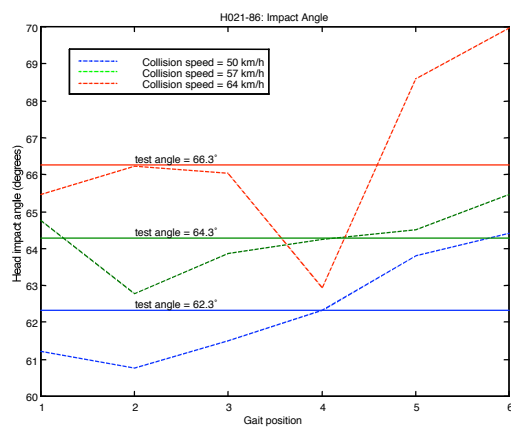


Figure 6. Head impact angle in the simulations of Case H021-86

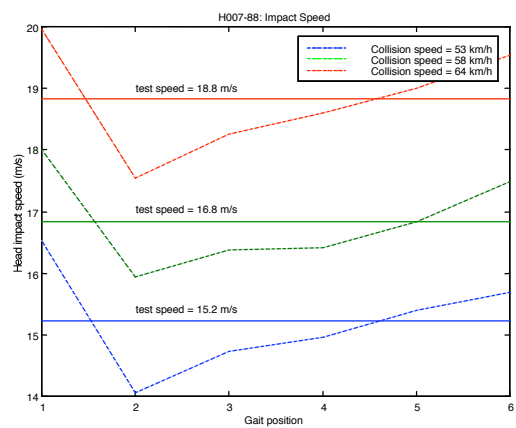


Figure 9. Head impact speed in the simulations of Case H007-88

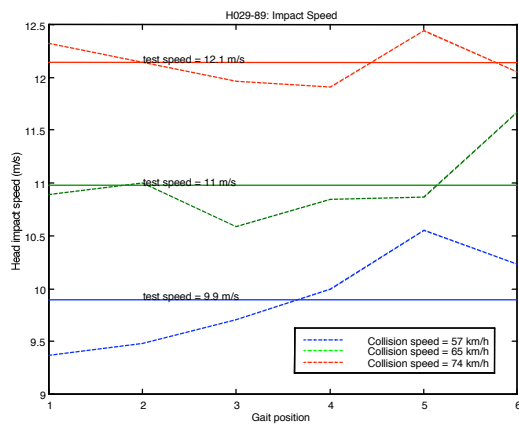


Figure 7. Head impact speed in the simulations of Case H029-89

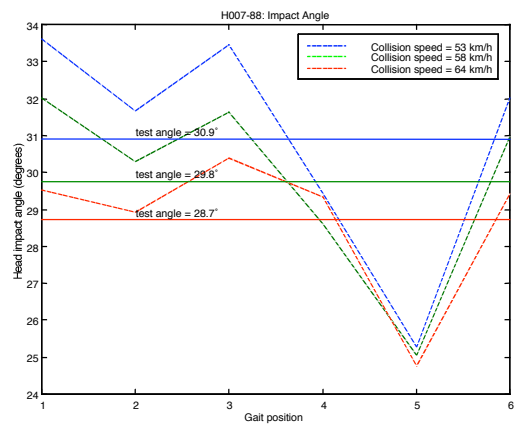


Figure 10. Head impact angle in the simulations of Case H007-88

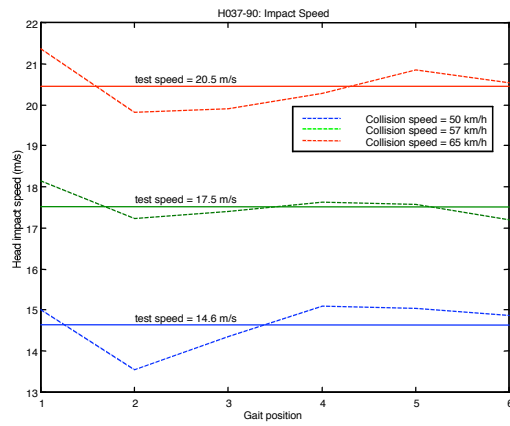


Figure 11. Head impact speed in the simulations of Case H037-90

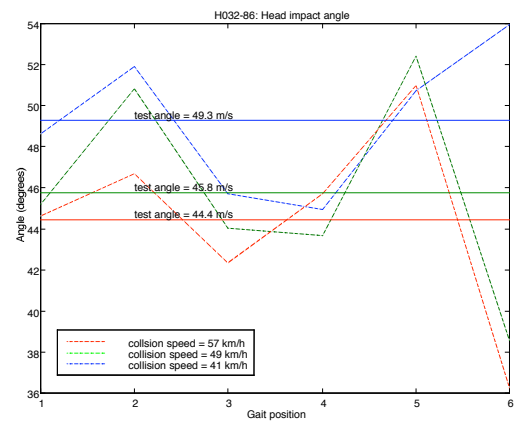


Figure 14. Head impact angles in the simulations of Case H032-86

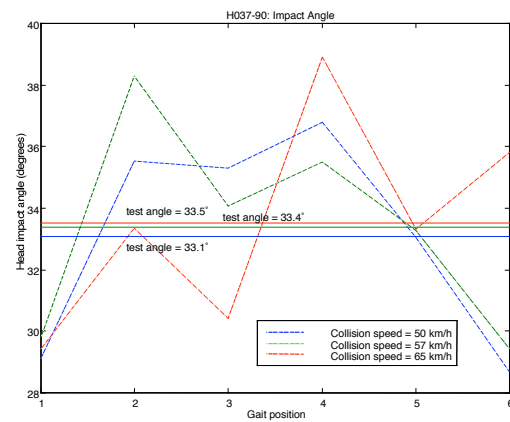


Figure 12. Head impact angle in the simulations of Case H037-90

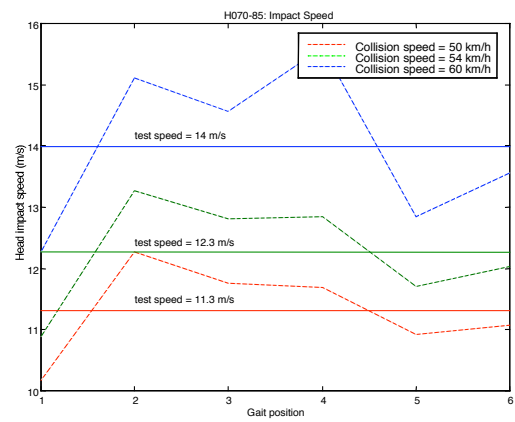


Figure 15. Head impact speeds in the simulations of Case H070-85

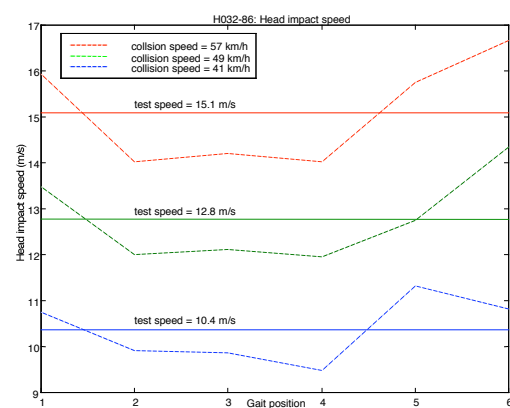


Figure 13. Head impact speeds in the simulations of Case H032-86

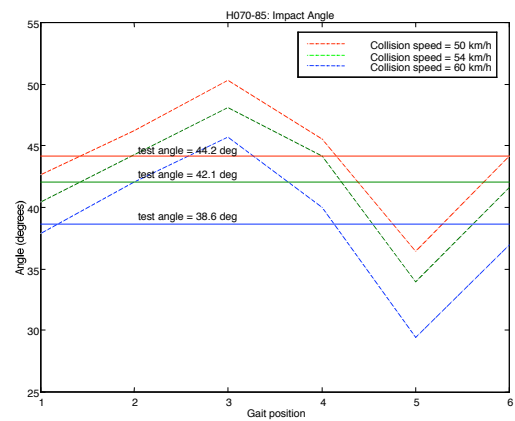


Figure 16. Head impact angles in the simulations of Case H070-85

HEADFORM IMPACT TESTS

The aim of the headform impact tests was to characterise the contact interaction between the head and the vehicle. The impact was reconstructed using a free flight headform, using the angle and speed estimated from the MADYMO simulations of the accident.

Methods

The impact tests were undertaken at the Pedestrian Impact Laboratory at the Centre for Automotive Safety Research. The laboratory includes a free-flight headform launcher that is capable of propelling a headform of 4.8 kg at speeds up to 70 km/h.

The headform used for this study was one conforming to the specifications of EEVC WG10. The head impact speed and angle were set according to the results of the simulations (discussed previously). Three tests were conducted for each case. Where necessary, a separate vehicle was obtained for each test. This was necessary where the structure of the car was altered by the impact.

The results of the impact tests were used to derive contact interaction models that were valid over the range of speeds used in the impact tests. This is discussed in the next section of the paper.

SIMULATION OF HEADFORM IMPACT TESTS

The aim of this part of the study was to determine a suitable contact characteristic that could be used to describe and reproduce the impact of the headform and the vehicle in MADYMO, over the range of velocities used in the testing. The derived contact characteristic should reproduce, in a simulation of the impact test, the acceleration history of the headform test at each test speed. Such a contact characteristic was then considered a valid approximation of the contact characteristic over the range of estimates that the modelling predicts for the head impact speed in the collision. Therefore, the contact characteristic enabled further simulation of the accident to provide justifiable estimates of HIC, and the linear and angular acceleration experienced by the head of the pedestrian.

The contact between headform and vehicle is non-linear. There are rate effects, as well as the presence of other non-linearities in the structure, which means that simple linear stiffness is rarely a satisfactory description of contact over any range of impact speeds. An approximation of the non-linearities arising from rate-effects (such as damping), can be made using a dynamic amplification factor. In MADYMO, dynamic amplification applies a scaling factor that depends on the rate of penetration, to a “base” stiffness. This factor may include stiffening or softening effects.

The use of dynamic amplification factors is not new, and has been used to estimate the dynamic response of structures from quasi-static tests (Prasad and Padgaonkar, 1981).

Determination of contact interaction parameters from test results

The procedure used to determine the contact interaction between headform and vehicle will be explained by way of an example. Figure 17 shows the acceleration time histories from three impact tests. These tests were conducted at upper, lower, and middle estimates of the head impact speed, as determined from the initial simulations of the pedestrian-car collision in Case H021-86. These results can be used to approximate the force-displacement characteristic of each impact by converting the acceleration to force (by multiplying by the mass of the headform) and by integrating the acceleration to derive the displacement of the headform throughout the impact. The three force-displacement characteristics that result from this process are shown in Figure 18.

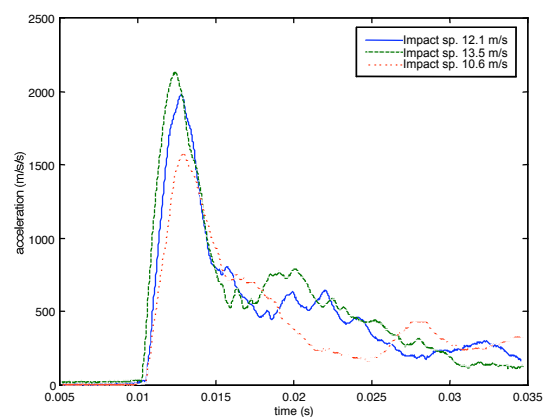


Figure 17. Head acceleration measurements made in the reconstruction of Case H021-86

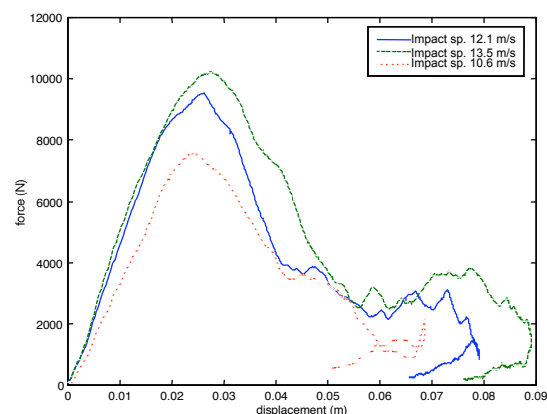


Figure 18. Dynamic force-displacement curves estimated from the impact tests for Case H021-86

What is notable here is that the three curves are essentially scaled versions of one another. (In other cases, the relationship between results and different speeds may be more complex.) In this example it would seem reasonable to try approximating the contact

behaviour as a stiffness that is scaled linearly according to the impact velocity. For example, a dynamic amplification factor may be chosen that is of the following form:

$$c_1 + c_2|v|$$

where v is the rate of deformation and c_1 and c_2 are constants.

To get an idea of how well such a dynamic amplification factor could approximate the contact interaction, we can scale each of the force-displacement curves by the above factor, using the initial impact speed as a proxy for the rate of deformation. (In reality, the velocity of the headform will rapidly drop throughout the impact, but the assumption is that the velocity profiles of each test are roughly proportional to one another.) The result of this is shown in Figure 19. The similarity between the three resulting curves indicates that the contact interaction model that includes the dynamic amplification factor should be a reasonable description of the contact interaction over the speed range of the testing. To use the model in MADYMO, we defined a “base” stiffness. This base stiffness will be amplified according to the velocity of the headform. The base stiffness for the example is shown in Figure 20, for $c_1 = 1$ and $c_2 = 0.25$. The unloading is approximated by a null curve, and the hysteresis slope is set to 800000 N/m.

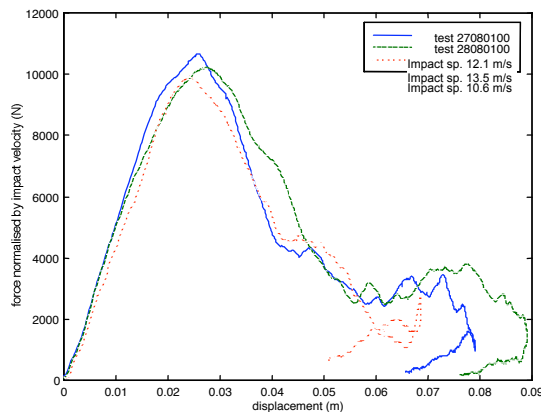


Figure 19. Force-deflection curves from impact tests associated with Case H021-86, normalised by the impact velocity

The next step is to model the three impact tests in MADYMO, to see how well the contact interaction model can reproduce the results of the impact tests. The model set-up is shown in Figure 21. The headform model is taken from the MADYMO dummy database. The bonnet of the car is modelled as a single plane, and the contact interaction with the headform is modelled with the base stiffness and the dynamic amplification model ABSEXP, with $c_1 = 1$ and $c_2 = 0.25$.

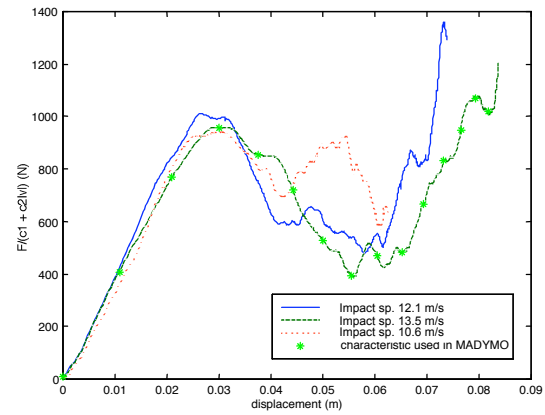


Figure 20. The force-displacement curves of each test, divided by the proposed dynamic amplification factor, and the discrete curve used in the MADYMO simulation of the impact tests.

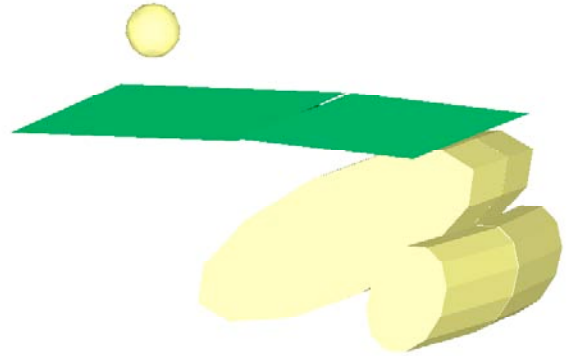


Figure 21. Illustration of the simulation of the headform test

The results of the simulations, and the results of the actual impact tests are shown in Figure 22 through Figure 24.

These figures show that the headform acceleration predicted by the simulation is very close to that measured experimentally. The important feature of this result is that the model can predict the acceleration of the headform over the range of velocities used in the testing. Therefore, collision scenarios with different velocities can be modelled, and over the range of resulting head impact velocities, better estimates of head impact severity can be made than had a simple linear contact characteristic been used. The accuracy of the acceleration measurement is now dependent on modelling parameters other than the contact characteristic, such as the behaviour of the neck and the geometrical and inertial properties of the head. Changes can be made to the model to improve biofidelity, and the definition of the contact interaction should remain valid (as long as the head velocity is not grossly affected by modelling changes).

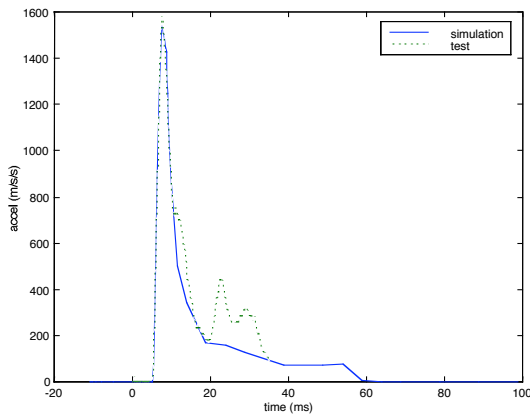


Figure 22. Headform acceleration estimated from the simulation, and the acceleration recorded in the impact test (Case H021-86, impact velocity = 10.6 m/s)

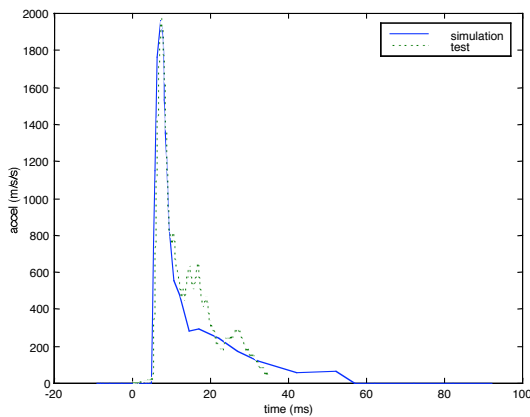


Figure 23. Headform acceleration estimated from the simulation, and the acceleration recorded in the impact test (Case H021-86, impact velocity = 12.2 m/s)

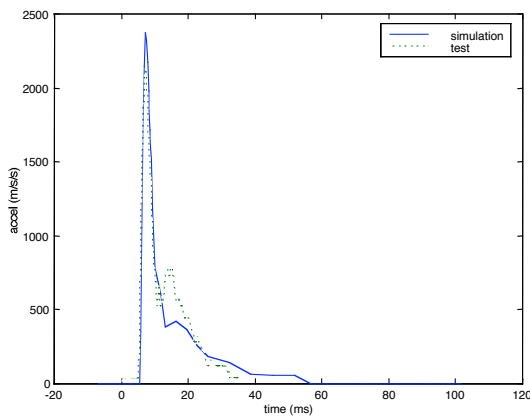


Figure 24. Headform acceleration estimated from the simulation, and the acceleration recorded in the impact test (Case H021-86, impact velocity = 13.7 m/s)

Results of headform impact simulations

The contact interactions resulting from testing of selected cases were analysed, and the resulting dynamic

amplification models are summarised in Table 2. Note that the base stiffness functions are not presented here.

Table 2.
Dynamic amplification used to model the interaction in each case

Case	Dynamic amplification factor	Constants
H021-86	$c_1 + c_2 v + c_3v^2 + c_4 v ^3 + c_5v^4$	$c_1 = 1.0$ $c_2 = 0.25$ $c_3 = 0$ $c_4 = 0$ $c_5 = 0$
H029-89	$c_1 + c_2 v + c_3v^2 + c_4 v ^3 + c_5v^4$	$c_1 = 1.0$ $c_2 = 0.25$ $c_3 = 0$ $c_4 = 0$ $c_5 = 0$
H032-86	Windscreen: none Dash: $c_1 + c_2 v + c_3v^2 + c_4 v ^3 + c_5v^4$	$c_1 = 1.0$ $c_2 = 1.0$ $c_3 = 0$ $c_4 = 0$ $c_5 = 0$
H070-85	Windscreen: none Dash: $c_1 + c_2(v/c_3)^4$	$c_1 = 0$ $c_2 = 1$ $c_3 = 3$ $c_4 = 0.41$

A comparison between the headform acceleration predicted by each model, and its associated experimental result are shown in Figure 22 to Figure 33.

The magnitude and shape of the acceleration curves are similar in each case showing that the selection of a dynamic amplification model can adequately describe the contact of the headform and bonnet over the velocity range of the impact tests. The second part of the impact in the simulation of the headform tests for Case H070-85 shows that some refinement of the dynamic amplification model may be required. However, the principle of using such a model is demonstrated by the satisfactory simulation of the 12 impact tests performed for this study.

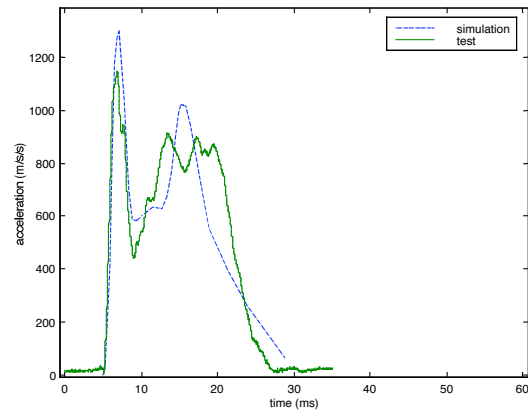


Figure 25. Headform acceleration estimated from the simulation, and the acceleration recorded in the impact test (Case H029-89, impact velocity = 11.14 m/s)

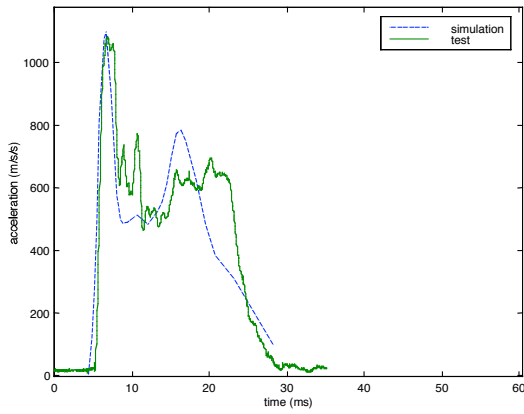


Figure 26. Headform acceleration estimated from the simulation, and the acceleration recorded in the impact test (Case H029-89, impact velocity = 9.97 m/s)

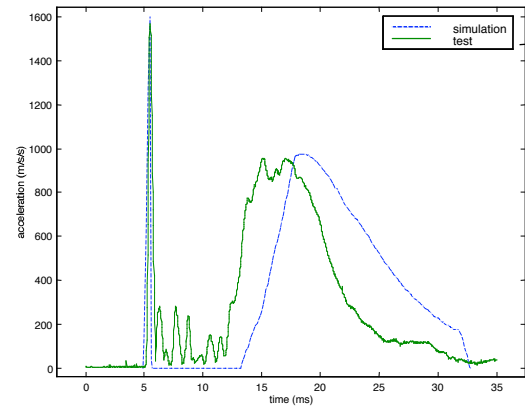


Figure 29. Headform acceleration estimated from the simulation, and the acceleration recorded in the impact test (Case H032-86 impact velocity = 11.71 m/s)

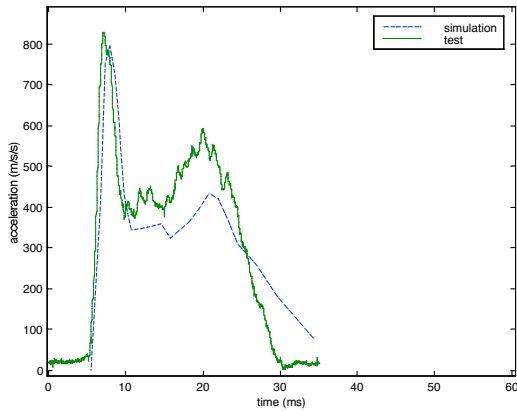


Figure 27. Headform acceleration estimated from the simulation, and the acceleration recorded in the impact test (Case H029-89, impact velocity = 8.08 m/s)

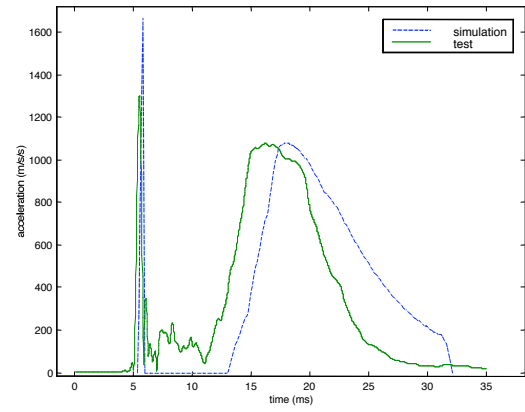


Figure 30. Headform acceleration estimated from the simulation, and the acceleration recorded in the impact test (Case H032-86, impact velocity = 12.46 m/s)

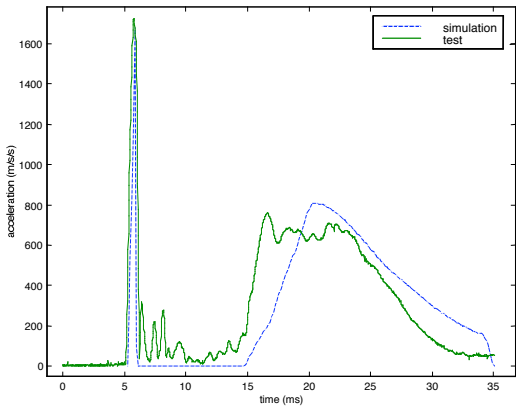


Figure 28. Headform acceleration estimated from the simulation, and the acceleration recorded in the impact test (Case H032-86, impact velocity = 10.24 m/s)

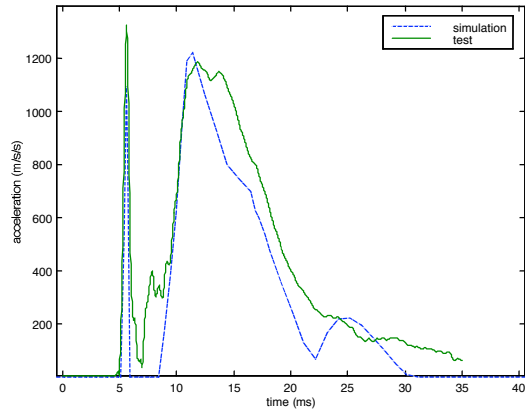


Figure 31. Headform acceleration estimated from the simulation, and the acceleration recorded in the impact test (Case H070-85, impact velocity = 11.1 m/s)

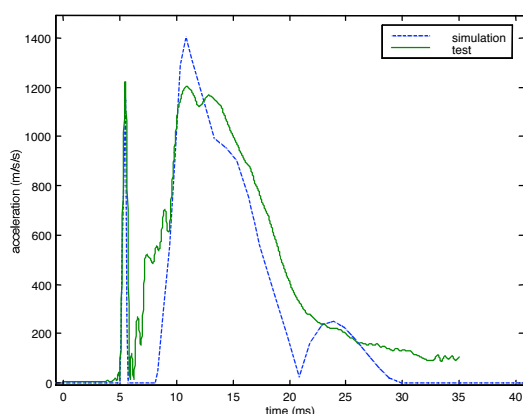


Figure 32. Headform acceleration estimated from the simulation, and the acceleration recorded in the impact test (Case H070-85, impact velocity = 12.56 m/s)

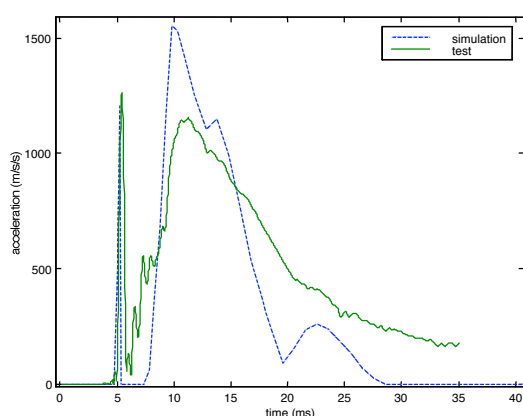


Figure 33. Headform acceleration estimated from the simulation, and the acceleration recorded in the impact test (Case H070-85, impact velocity = 14.37 m/s)

HEAD IMPACT SEVERITY ESTIMATES FROM REVISED MADYMO MODELS

The previous section of this paper described the derivation of contact characteristics for each case. The

contact characteristics appear to be valid over the range of head impact speeds used in the associated impact tests. By extension, we will assume that the contact characteristics are also a valid representation of the stiffness of the head impact over the range of likely head impact velocities in the crashes themselves. The simulations of the crashes can be used to estimate head impact severity by applying the derived contact characteristic to the head-vehicle contact in the MADYMO model of the crash.

Each variant of the case simulation was rerun with the new contact characteristic. The peak linear acceleration, the angular acceleration and the HIC value were estimated in each simulation. The results of these simulations are given in Table 3. The head injuries noted in each case are also given in this table.

Further analysis of the solution space is possible: Figure 34 shows a contour plot of peak linear acceleration values, estimated for Case H021-86. This plot shows the variation in head impact severity over the solution space defined by the range of the dependent variables Gait Position and Vehicle Speed. Gait positions around position 3 (also refer to Figure 2) produce the lowest head impact severity, whereas higher severity estimates are found about gait position 6. As might be expected, higher impact speeds lead to higher estimates of impact severity. Table 3 and Figure 34 show that the variation in the estimate of head impact severity may be considerable.

DISCUSSION

In previous reconstruction studies using our MADYMO pedestrian model, we have limited the use of the model to estimating the impact velocity of the head. We have preferred to estimate impact severity by a physical test using a free flight headform on a vehicle of the same make and model as the vehicle involved in the accident. This is because the use of arbitrary values for - or point-estimates of - the impact stiffness will lead to unreliable estimates of head impact severity. For our purposes, the use of complex and valid finite element models (which might overcome some of the objections to using simulation for estimating head impact severity) is not practicable.

Table 3.

Mean values and standard deviations for head impact severity estimated from the 18 variants of the MADYMO model of each crash, using the experimentally derived stiffness values

Case	Mean estimated HIC (std dev. in parenthesis)	Mean estimated peak acceleration (g) (std dev. in parenthesis)	Mean estimated peak angular acceleration (krad/s ²) (std dev. in parenthesis)	Head and C0 injuries (may not be the fatal injury)
H021-86	1141 (793)	213 (80)	40.8 (8.9)	Fracture of right temporal base of skull and patchy subarachnoid haemorrhage
H032-86	612 (344)	108 (41)	22.9 (6.5)	Subarachnoid haemorrhage
H029-89	1175 (486)	176 (45)	27.2 (9.2)	Fracture/dislocation of the atlanto-occipital joint with spinal cord laceration and lacerations to the head
H070-85	1121 (840)	205 (46)	27.0 (6.0)	Fractured skull base, subdural haematoma, contusion to left frontal lobe, cerebral laceration.

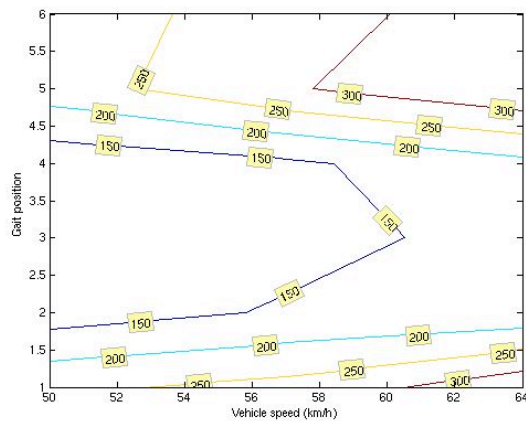


Figure 34. Contour plot of peak acceleration (g) by gait position and impact speed, Case H021-86.

We have developed a multi-body modelling technique that can use a range of estimates for input parameters that are not known precisely, without compromising the validity of the head-vehicle contact interaction model. If the contact interaction model is valid over the range of one or several simulation parameters (such as impact speed of the vehicle or pedestrian posture), then the model may be used to explore the solution space that is bounded by the limits of the simulation parameters over their range.

The mean estimated HIC values and acceleration values reflect not only the choice of the range of each parameter, but also all model parameters. Therefore, the estimates of head injury severity would be likely to change if other aspects of the model were altered.

Figure 34 is an example of the distribution of estimates that this kind of analysis can produce. By checking the kinematics of the simulation and comparing these to the physical evidence left after the collision, the range of each of the dependent variables may be reduced further by, for example, ruling out certain postures as being unlikely in the collision. This may reduce the variance in the estimates of the head impact severity.

CONCLUSIONS

This paper has demonstrated that multi-body techniques can be successfully used to reconstruct and simulate crashes where certain dependent variables are not known precisely. Design-of-experiment type analyses may be applied readily and efficiently to multi-body techniques, and non-linearities in contact interactions may be empirically derived using a combination of simulation and impact testing.

This technique was applied in the reconstruction of four car-to-pedestrian collisions. The results showed that the use of a dynamic amplification model within model could adequately describe the non-linearity in the head impact. The range in the estimate of the head impact severity provides both bounds on the impact dynamics in the actual crash, and demonstrates the sensitivity of the estimate to chosen initial conditions.

REFERENCES

- Anderson, R. W. G. and A. J. McLean (2001) "Australia's involvement in the International Harmonised Research Activities Pedestrian Safety Expert Group", Road Safety, Education and Policing Conference, Melbourne.
- Anderson, R. W. G., A. J. McLean, et al. (2002) "Severity and type of pedestrian injuries related to vehicle impact locations and results of impact reconstructions", 2002 International IRCOBI Conference on the Biomechanics of Impact, Munich (Germany), International Research Council on the Biomechanics of Impact.
- Anderson, R. W. G., L. Streeter, et al. (2003) "Pedestrian subsystem head impact results reflect the severity of pedestrian head injuries", International Journal of Vehicle Design 31 (1/2): 1-15.
- Baughman, L. (1983) "Development of an Interactive Program to Produce Body Description Data", US Air Force Aerospace Medical Research Laboratory.
- Dokko, Y., R. W. G. Anderson, et al. (2003) "Validation of the human FE model against pedestrian accident and its tentative application to the examination of the existing tolerance curve", 18th International Technical Conference on Enhanced Safety of Vehicles, Nagoya, Japan, National Highway Traffic Safety Administration.
- Garrett, M. (1996) "Head impact modelling using computer accident simulation based on cadaver records", 24th International workshop on human subjects for biomechanical research, Albuquerque, New Mexico, US Department of Transportation. National Highways Traffic Safety Administration.
- Garrett, M. (1998) "Head impact modelling using MADYMO simulations of documented pedestrian accidents", Conference on Pedestrian Safety, Melbourne, Victoria, VicRoads, RACV, Federal Office of Road Safety, Australian Hotels Association.
- Ishikawa, H., J. Kajzer, et al. (1993) "Computer simulation of impact response of the human body in car-pedestrian accidents", 37th Stapp Car Crash Conference, Society of Automotive Engineers (SAE), Warrendale PA.
- Prasad, P. and Padgaonkar, A.J., (1981) "Static-to-dynamic amplification factors for use in lumped mass vehicle crash models", SAE paper no. 810475

VALIDATION OF THE CERVICAL SPINE MODEL IN THUMS

A Chawla
S Mukherjee
D Mohan
S Jain

Department of Mechanical Engineering,
Indian Institute of Technology, New Delhi-110016, India.
Paper No: 05-2005

ABSTRACT

THUMS (Total human model for safety) [Watanabe et al¹] is a finite element model of human body developed to study various injury mechanisms and for use as a substitute for crash test dummies. The development team of Toyota Central R&D Labs (TCRDL) has validated different parts of this model against experimental data available in literature. Neck response data for different impact conditions is available in Mertz and Patrick^{2,3} and McElhaney et.al^{4,5}. A preliminary validation of the neck model in Thums, against some of these tests, has been presented by the TCRDL group [Oshita et.al⁶] but no extensive validation has been reported for the variety of test conditions reported in literature. Typically, frontal and rear end impacts are of interest and these cause bending, axial as well as torsional loading on the cervical spine. A computational model can be expected to validate against multiple boundary conditions and initial conditions. Therefore, validation of a computational model (THUMS) in varying test conditions is of significance. Thus the objective of the current work is to independently investigate the fidelity of the neck model of THUMS under varying impact conditions.

From the initial seating position the Thums model has been modified to match the initial position in the tests. The impact test conditions used in the experiments have been then recreated in PAMCRASHTM and simulations have been carried out to validate the neck model. The models and the material properties have then been iterated and the performance of the Thums model has been investigated vis-à-vis the experimental results.

INTRODUCTION

Injuries to the neck, or cervical region, are very important since there is a potential risk of damage to the spinal cord. High-speed transportation have increased the number of serious neck injuries and made

us increasingly aware of its consequences. The incidence data from the injury surveillance program at the Swedish National Board of Health and Welfare, [Karrin⁷] is indicative of this..

The lower cervical spine is the most frequently observed location for spinal trauma. It has been shown that cervical spine injuries are more often connected with spinal cord injuries than the lower spinal regions, Pintar and Narayan⁸. There is also a strong association between head and face trauma and neck injuries. Hence a neck injury in automobile crashes is a problem that needs to be addressed with new preventive strategies.

FE Models of the human body are now being developed to aid in development of new protection devices for vehicles. These models include realistic anatomical geometry of the human body and their physical properties, to predict kinematics, kinetics, and internal stresses and strains inside the human body. THUMS is one such human body model¹.

The THUMS model represents a 50 percentile American male in seating position. The model has been developed by Toyota Central R&D Labs. Inc, Toyota System Research Inc., and Toyota Motor Company in conjunctions with the Wayne State University^{1,9,10}. The model contains about 60,000 nodes and 80,000 elements. Each bone consists of cancellous zone modeled using solid elements and cortical zone modeled using shell elements. In the joints of THUMS model, ligaments that connect the bones are modeled using shell / beam elements and sliding interfaces are defined on the contacting surfaces of these bones. Skin and muscles that cover the bone are modeled with solid elements.

The purpose of THUMS is to simulate responses of human body sustaining impact loads. However these FE models need to be validated before they can be used effectively. Various studies for the validation of different parts of the THUMS model have been reported by the Toyota group (6, 9, 10 to name a few).

In the present work Human Cervical Spine (Neck) Model of THUMS has been validated for different impact conditions (Frontal, Rear and Torsion). Simulations have been developed for these impact configurations and compared against experimental data already available in literature. We first briefly mention the experimental data used in this work and then describe our simulations and comparisons.

EXPERIMENTAL DATA

Considerable work has been done in the area of measurement of the response and tolerance of the human neck in impact environment. Some of these papers include the information of the actual test condition and boundary condition imposed on human cadavers and volunteers. In this section we describe some of this data that we have used for validations.

Mertz and Patrick², conducted several tests on cadavers for investigating the kinematics and kinetics of whiplash. The work also proposes mathematical modeling of dynamics of human head for different impacts. Later, Mertz and Patrick³ conducted test for neck response envelopes for the extension and flexion of the neck. They report motion of the head relative to the torso in the sagittal plane and the static and dynamic strength of the neck in flexion and extension.

McElhaney et al⁴ investigated the lateral, anterior and posterior passive bending responses of the human cervical spine from cadavers. Results include moment angle curves, relaxation moduli and the effect of cyclic conditioning on bending stiffness of cervical spine. Later, McElhaney et al⁵ have investigated the responses of the unembalmed cadaver cervical spine to axial rotations of the head about a vertical axis. Thunnissen and Philippon¹¹ investigated the head-neck response; the neck loads and the sustained injuries obtained from human cadaver experiments in the frontal, lateral and rear-end collisions. Ono and Koji¹² analyzed the motion of the cervical vertebrae under varying conditions. They investigated head and neck responses in low speed rear-end impact conditions and have focused on the head kinematics using sled tests with post mortem human subjects. Rizzetti et al.¹³ reported skull, brain and cervical spine injuries through direct head impacts. Fourteen head impacts (frontal, lateral or occipital) with cadavers were performed.

Panjabi et al.¹⁴ reported the current understanding of the injury tolerance of the human cervical spine and characterization of the mechanical properties and injury criterion of the cervical spine. They also documented the state-of-the-art by which surrogate

devices and models may be used to mimic the mechanical behavior of the human neck.

In this work we present validation of the Thums model against frontal impact tests of Mertz et al^{2,3}, rear end impact tests of Ono et al¹² and torsion tests of Myers et al¹⁵.

VALIDATION METHODOLOGY AND MODEL DEVELOPMENT

The nominal posture of the Thums model is a sitting position. In order to validate the neck model of Thums we had first modified the FE mesh of THUMS, to bring its position identical to that used in the experiments. This turned out to be a non-trivial exercise for human body models. The dummy had been positioned in the correct posture by running successive simulations for altering the dummy position. The deformed / positioned dummy obtained from these simulations were used as an input mesh in the next stage, and iteratively the initial condition for the meshes is obtained.

The following sub-sections describe how the model has been developed for the three tests simulated in this work.

Simulation model for frontal impact

While conducting test on human cadavers for dynamic hyper-flexion, the subjects were restrained on a rigid chair mounted on an impact sled³. The sled is accelerated pneumatically over a distance of 6 ft to the prescribed velocity. The head position was set to a vertical, upright position and backrest at 15 degree from the vertical. The sled was then brought to rest rapidly by a hydraulic cylinder to generate the deceleration pulse. The model of sled in PAM-GENERIS using shell elements, defined as rigid is shown in Figure 1

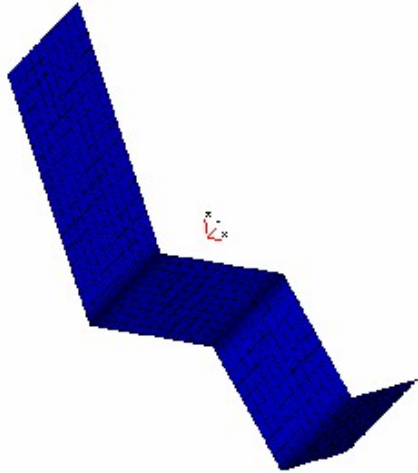


Figure 1. Sled Model using Shell Element

The THUMS model had then been brought into a sitting position on the sled i.e. in the same position as the human subjects were at the time of the experiment. This was achieved by dynamically simulating the sitting process in Pamcrash by successive single axis rotations. The initial and the final position of the THUMS model have been shown in the Figure 2 and Figure 3 respectively.

The restraint system used in the experiment consisted of a lap belt and two individual shoulder harnesses that crossed at the mid-sternum. In addition, the subject's feet were fastened to the foot support.

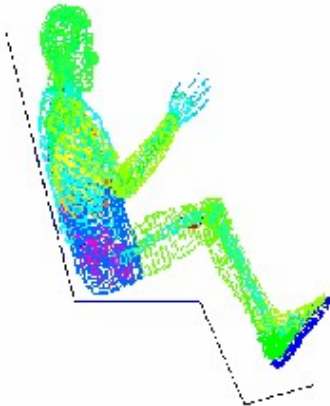


Figure 2. Initial Position of THUMS.

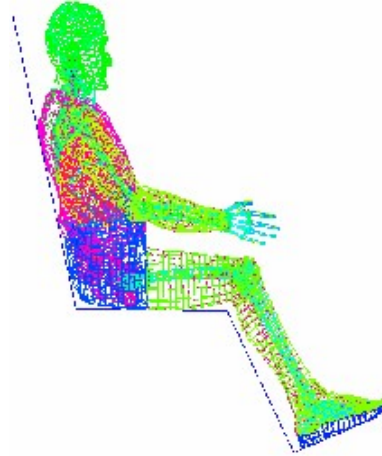


Figure 3. Final Sitting Position of THUMS for frontal Impact.

Belts have been modeled using multiple beam elements, and are assigned a material model 205 in PAM GENERIS™ which is a non-linear tension-only bar element meant for modeling of seat belts.

Simulation models for low speed rear impact simulations

The experimental responses for low speed rear impact has been reported by Ono et al¹². In these tests, the head position was set in a vertical upright position, backrest is at 20 degree from the vertical and sitting base is at 10 degree from the horizontal. The sled has been modeled in PAM-GENERIS using shell elements and has been designated as a rigid body.

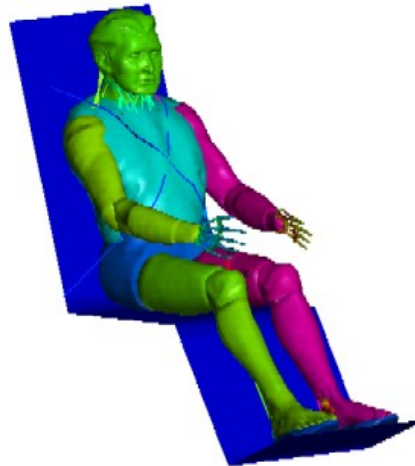


Figure 4. THUMS with chest restraint system

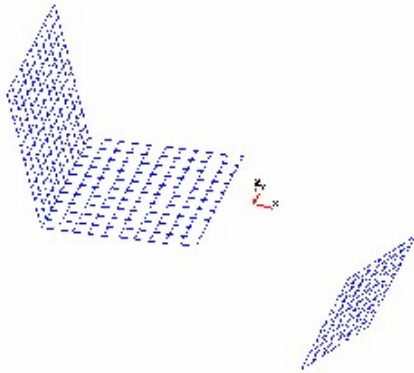


Figure 5. Modeled Sled for rear impact

THUMS mode had been modified so as to have the same initial position as reported in Ono et al¹² (Figure 6).

Simulation models for the neck in torsion

Myers et al¹⁵ reported experimental response for the cervical spine in torsion. The experimental cervical spine specimen included the base of the skull, approximately two centimeters around the foramen magnum and the first thoracic vertebrae at the caudal end, with all the ligaments structures kept intact. It is found after experimentation that all failures were confined to the atlanto-axial joint. A similar model of neck has been prepared for simulation by eliminating the structures other than C2 to T1.

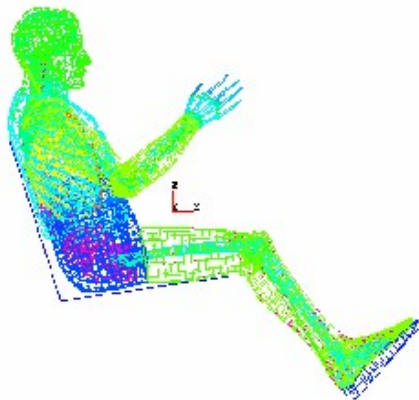


Figure 6. Final sitting position of THUMS for low speed rear impact simulations

The thoracic vertebra was kept fixed and the axis was given various input rotational velocities. Specimens were cast into aluminum cups so that the ends were parallel. The axial movement of the neck has been permitted. Same boundary conditions have been incorporated in the simulation models shown in Figure 7.

Models for the three test conditions, viz, frontal impact, rear impact and torsion, had thus been duplicated to reproduce the geometry and end-fixity conditions. Subsequently the THUMS neck muscle material model and the associated material properties were tuned to match with the experimental results available. Hill material Model was implemented in all the neck muscles, and its properties have been iterated to match the results. The next section describes the results of the simulations and their comparisons with experimental data.

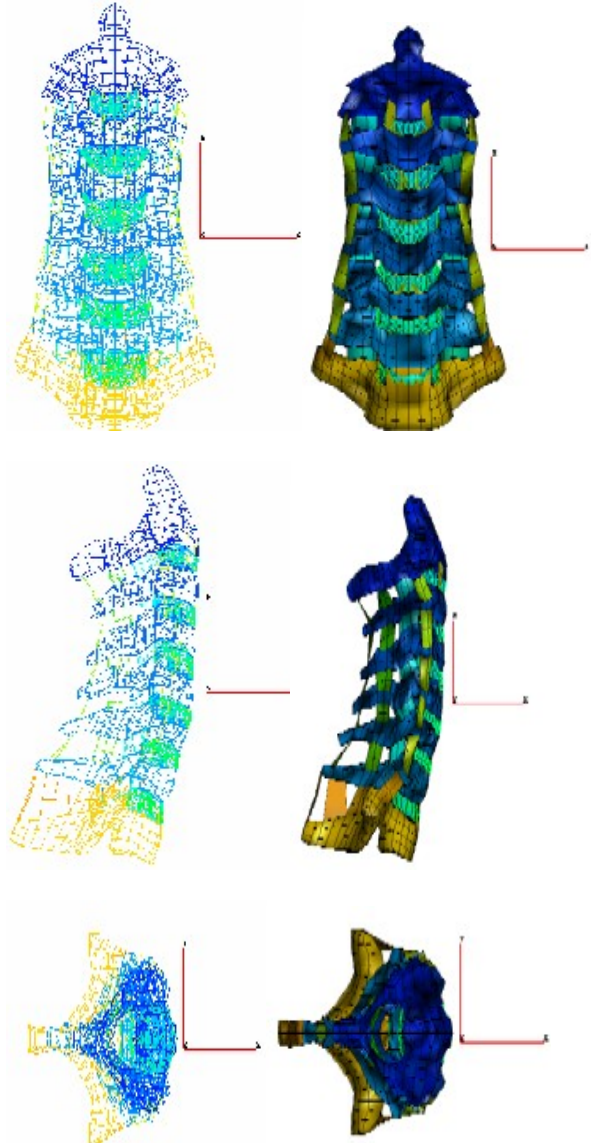


Figure 7. Front, side and Top view of the neck model prepared for simulating Human cervical spine to torsion.

RESULTS AND VALIDATIONS

Results of frontal impact, rear impact and torsion response of THUMS neck are now discussed in this section.

Validation for frontal sled impact test

For the frontal sled impact simulation using THUMS conditions corresponding to cadaver 1538³ have been simulated. Additional weight of 1.36 kg has been put at the center of gravity of head of cadaver, and an initial velocity of 5.88 m/s has been given. The sled has been made to stop within a distance of 0.254 m with a deceleration pulse (Figure 8) having a plateau deceleration of 66.7 m/s^2 .

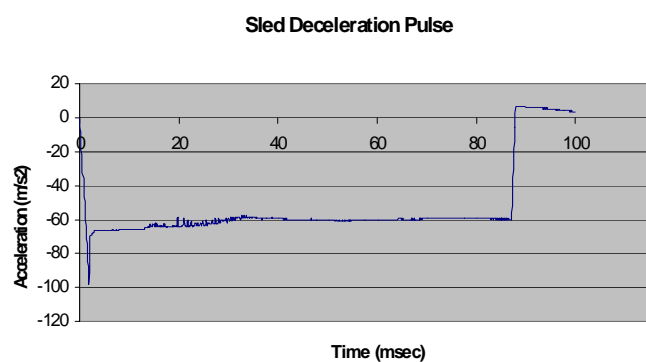


Figure 8. Deceleration pulse used in Rum 200 with cadaver 1538

With the test conditions as stated above, is the model was simulated for 100 msec termination time.. Figure 9 shows the movements in THUMS after 0.025, 0.05, 0.075 and 0.092 msec.

Figure 11 plots the equivalent moment about the occipital condyles as a function of angular rotation of head relative to torso, for experiment and simulation using unmodified, elastic and Hills model for muscles. This curve is of primary interest for validating THUMS neck behavior.

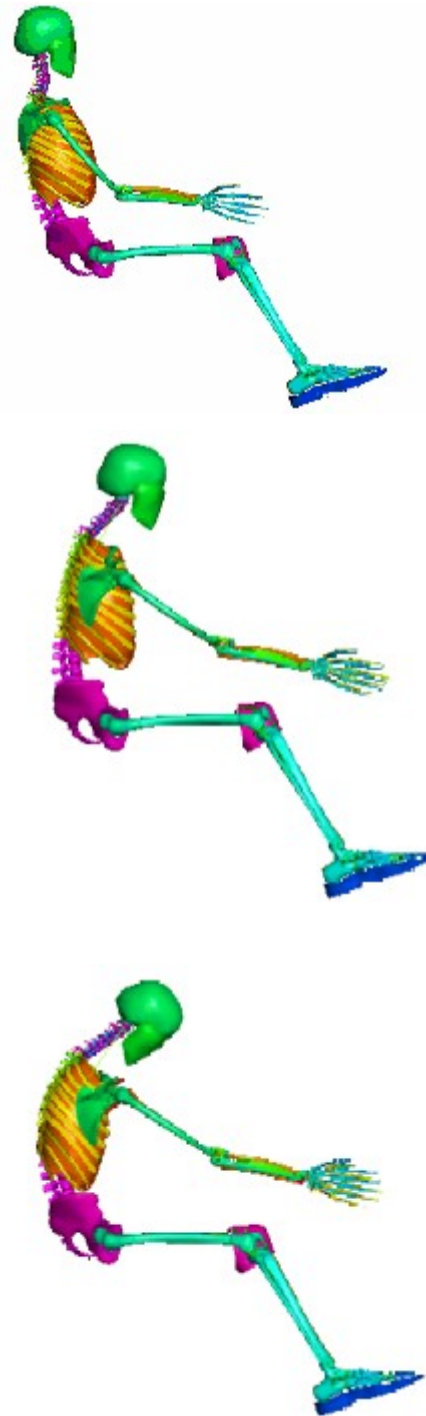




Figure 9. Movements in THUMS after 0.025, 0.05, 0.075 and 0.092 msec.

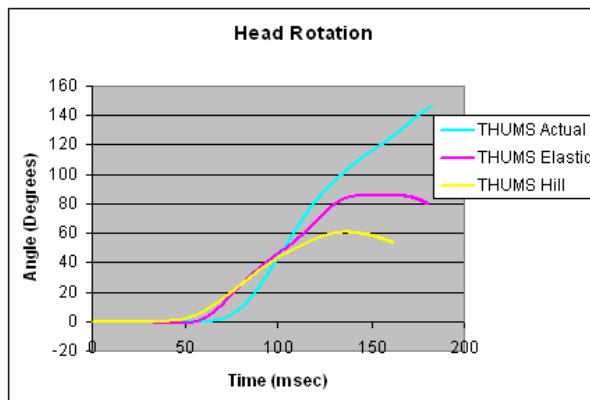


Figure 10. Angular rotation of Head with Torso from simulation.

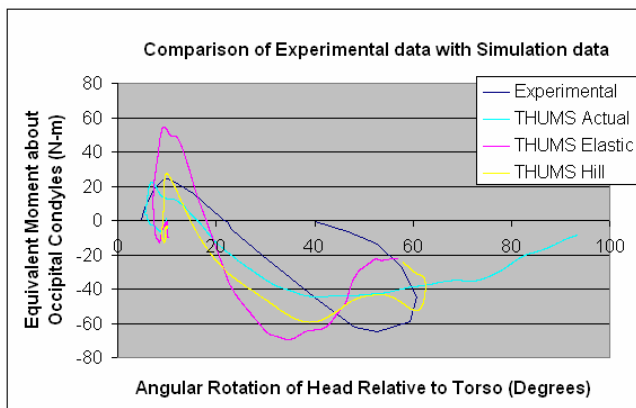


Figure 11. Moment as a function of the angular position of head, under hyper flexion.

Figure 10 shows that the THUMS model had larger relative head angulations, 140 deg as compared to 73

for cadaver 1538. This large difference can be due to difference in neck stiffness and muscular behavior.

For cadaver experiment, maximum equivalent moment of 27 Nm was observed at relative head rotation of 20 deg. For THUMS this was 40 Nm at 19 degree relative head rotation. Peak resisting moment for cadaver was 62 Nm at 50 deg of relative head rotation. For THUMS this was 60 Nm at 50-60 deg of relative head rotation which is similar to the experiment.

After the peak of resisting equivalent moment is achieved, THUMS head was not coming back to its initial position due to inadequate muscular forces and chin chest reactions. Rather the angular rotation of head increased unto 140 deg of relative head rotation. This could be because of cadaver 1538 having a neck stiffer than the neck of THUMS. This magnitude of relative head rotation was observed in cadaver 1404 neck response which had the most flexible neck among the cadavers, with maximum relative head rotation of 100 deg for same test conditions.

The result showed considerable improvements in the model behavior when Hill material model was incorporated in the neck muscles of THUMS. The nature of the overall equivalent moment with head rotation response of the model shows a good agreement with the experimental corridor. Peak values matched but the area under the response curve deviated from the corridor.

The peak value of head rotation had improved to be 60 degree which is as reported by Mertz et al (1971). The head also whipped back after reaching a rotation limit

Low speed rear impact simulation

Speed selected for simulating test conditions was 4 km/h which was the same as in the experiments.

The parameters that had been tracked in simulation were sled acceleration, head acceleration; thoracic spine acceleration, frontal chest acceleration and cervical vertebrae motion analysis. The motions of entire cervical vertebrae were represented by the changes in the relative rotational angle and translation of the third cervical vertebra from the sixth cervical vertebra.

The deceleration pulse given as an input to the sled was generated based on the experimental response data reported by Ono et al¹² (Figure 12).

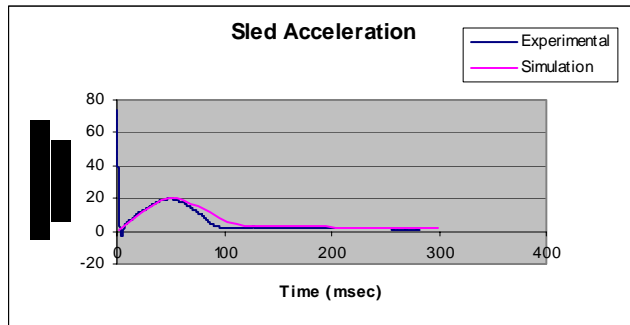


Figure 12. Acceleration Pulse given to the sled from low speed rear impact simulation, Koshiro Ono (1997).

With the test conditions above, THUMS was simulated for 300 msec termination time. Sixty stages have been created at increment of 5 msec per stage. Figure 13 shows the movements in THUMS after 0, 100, 150, 200, 250 msec respectively.

The head rotation curve shown in Figure 16 indicates that THUMS underwent larger relative head angulations, 32 deg as compared to 20 deg for cadaver. After the peak of head rotation is attained, in THUMS the head is not restored to its initial position but angular rotation of head kept on increasing unto 40 deg of relative head rotation. This could be because of less stiff neck of THUMS or improper muscle model in the neck.

In Figure, the time history of equivalent moment for THUMS and that from the experiments has been compared. The peak values of both positive and resisting moments are much higher than the experimental data. For experimental run, maximum equivalent moment of 8 Nm is observed while for THUMS this is coming out to be 25 Nm. Peak resisting moment in experimental data is 3 Nm and for THUMS this is 14 Nm.

In Figure 14, acceleration response of head of THUMS has been compared with that of experimental data.. Peak experimental value achieved is 22m/sec² whereas from simulation this is coming out to be 28 m/sec². Rotational angle of C3 in crash condition has been compared for experimental and simulation results in Figure 16. In general, large variations can be seen between the experimental and simulation results. One of the main reasons for this, we feel, is that the neck muscles have not been modeled completely in Thums.

From the head rotation curve obtained for THUMS™ with Hill model, the peak value of head rotation is 17 degree, which is close to the value of 22 degree for

volunteers. Another significant change that can be observed from the head rotation curve is the coming back of head after attaining the peak value of 17 degree.

Comparison has been made in head acceleration experimental data and simulation data. Nature of the both the curves are same and the peaks values are quiet same with 24 m/sec² for THUMS and 23 m/sec² for volunteers.

The time history of equivalent moment for THUMS and that from the experiments has been compared. The peak value of positive moment is 7.5 N-m for experimental data and 9 N-m for THUMS. The peak resisting neck moment value for THUMS neck is 4 N-m whereas for volunteer it is 2 N-m. The nature of the curve is same as that of experimental data.

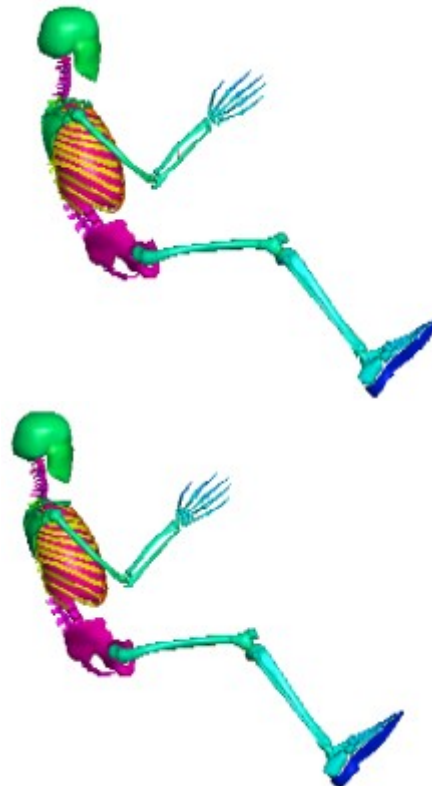




Figure 13. Movements in THUMS after 0 msec, 100 msec, 150 msec, 200 msec and 250 msec respectively.

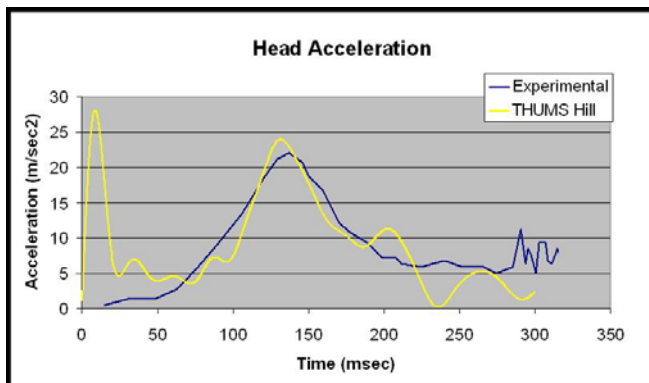


Figure 14. Acceleration response of head of THUMS from simulation.

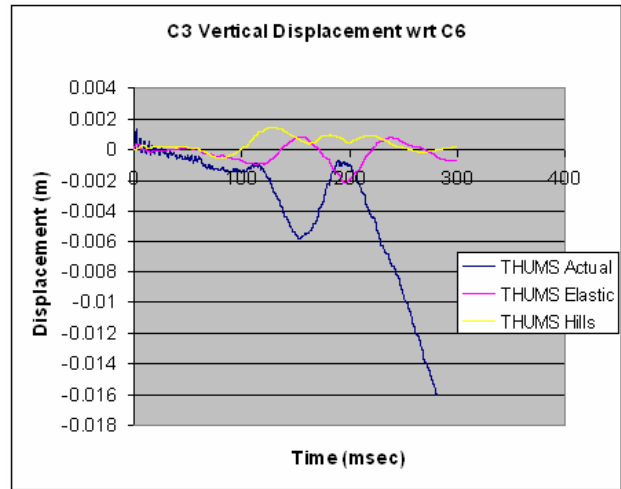


Figure 15. C3 motion relative to C6 – Vertical translation.

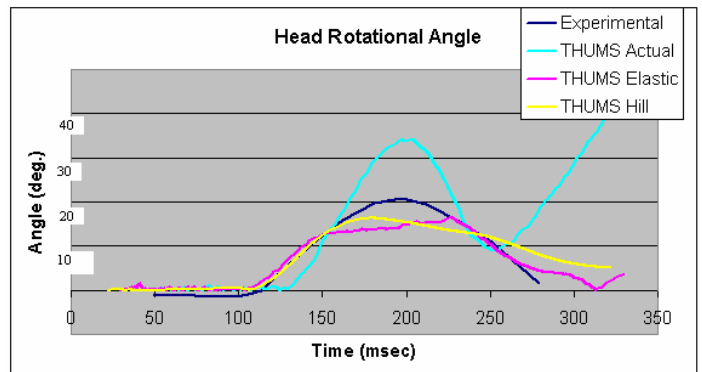


Figure 16. C3 motion relative to C6 – Rotational angle.

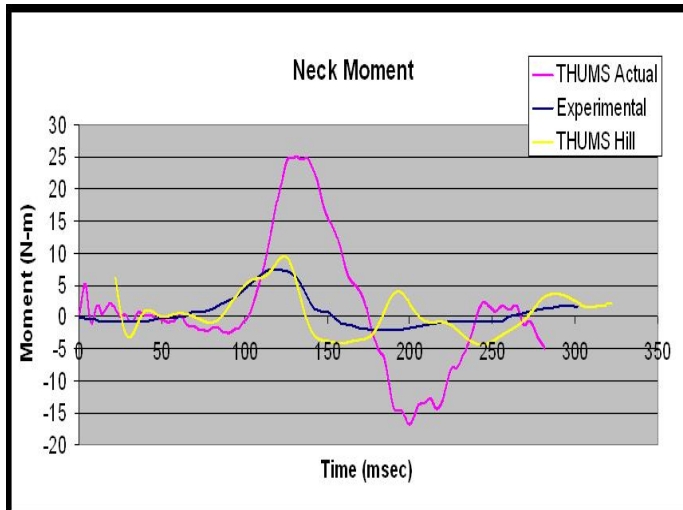


Figure17. Time history of neck moment.

Simulation for the neck in torsion

Simulations have been done for the torsion tests conducted by Myers et al¹⁵. These include visco-elastic tests using relaxation and constant strain rate conditions. The specimen is loaded to failure by applying a ramp and hold at 500 degrees/sec. Relaxation tests use ramp and hold signals with 0.25-second rise times. The deflection is then held constant for next 150 seconds. Myers et al¹⁵ also report a failure test, which has been categorized as high velocity failure tests using ramp to failure velocity displacements. The purpose of these tests was to provide a database representing the lower bound (No muscle action) of the stiffness of the human neck in rotation.

Figure shows the load to failure response of the experiments conducted on 3 human cervical spines reported by Myers and McElhaney¹⁵ and the simulation response of THUMS neck. The results show a fair degree of correspondence.

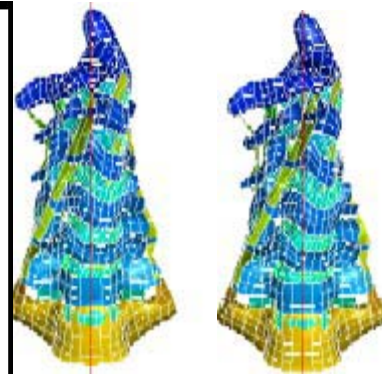
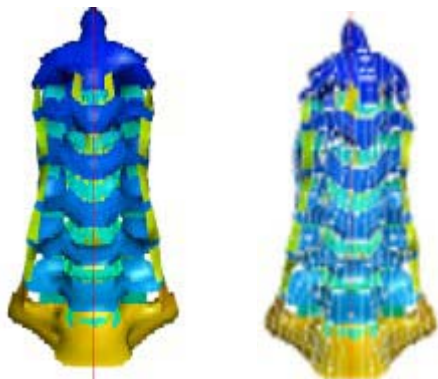


Figure 18. Movements in THUMS neck after 0 sec, 100msec, 200 msec and 300 msec respectively.

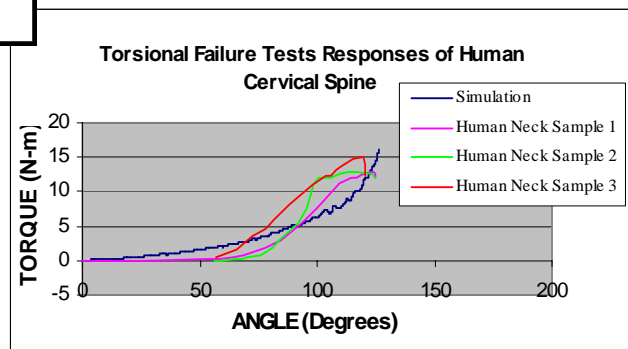


Figure 19. Torsion Failure Test Responses of Human Cervical Spine.

DISCUSSION

In frontal impact simulations, the nature of the overall equivalent moment with head rotation response of the model shows a good agreement with the experimental corridor. But primarily the positive moment path of the model response is deviating from the corridor. In the neck model of THUMS this has been observed that many muscles have been modeled using bars elements, which have been assigned a null material model. This doesn't incorporate the forces coming either in tension or compression on the model. Because of the absence of these forces there is no effect of these muscles on the movement of neck. As a consequence of this the head of THUMS is not whipping back even after a relative head rotation with respect to the torso of more than 140 deg, (Figure 11).

This can be concluded that initially THUMS neck had a very less stiffness value and because of this actual THUMS had a 150-degree of Head rotation. The main cause for this looseness of THUMS neck was identified to be the improper material model used for modeling its neck muscles. There is no contribution of the muscle forces in actual THUMS. By changing the material model of neck muscles to elastic and then to

Hill material model, THUMS neck response has improves considerably.

In the low speed rear impacts, the sled acceleration, head acceleration and cervical spine motion have been compared between the experiment and the simulations. The compressive vertical motion plays an important role in minor neck injuries. In the rear impact simulations, downward and rearward extension motion of the C3 compared to the C6 has been observed, resulting in the cervical spine getting compressed in early stage of the impact Figure 15. Similar behavior was also observed in the experiments.

The motion of C3 in terms of rotational angle (Figure 16) and vertical translation as compared to C6 (Figure 15) reveals that the rotational angle of C3 increases over the time and reaches its peak around 150 ms after impact. After a drop of 10 deg in next 50 msec, it starts increasing again. The vertical translation of C3 wrt C6, on the other hand, reaches its first peak at 150msec after the impact and after a drop in its value for next 50 msec it starts rising again. This variation is however, missing in the experiments. This is primarily because neck muscles have not been modeled completely in the Thums neck model.

In the simulations that have been run for the failure tests in torsion on THUMS neck model; primary goal was the duplication of the in vivo kinematics and dynamics at the computer simulation level, as all the future work is based onto it. The centre of rotation is one such parameter which has been successfully identified in the THUMS neck model based upon the minimum energy method theorem(Myers and McElhaney¹⁵). The neck moment results obtained from THUMS show a good conformity with experimental results. The mean value of THUMS neck stiffness lies in the range of 0.472 Nm/degree in the high stiffness region.

These simulations have given us a good insight into the THUMS neck model and also requirements needed from human body FE models in general. The cervical neck is an extremely complicated joint, and its FE modeling is an arduous task. We have run numerous simulations to study the importance various aspects of these simulations. On the basis of these we are now able to highlight various aspects of these models, which need further attention for a closer validation under different conditions.

THUMS neck needs to be modeled in greater detail, especially with greater care for the muscles and tendons. Also, appropriate pre-tensioning needs to be included for these elements.

No failure model is defined for any of the parts involved in available model of THUMS, though inclusion of failure model for ligaments has been reported in later versions of the THUMS model of some other body parts. In the current model, elements continue to stretch endlessly under load, without failure / rupture.

Similarly, the material model of the soft tissues as well as that of ligaments is found to be critical. Variations in geometry as well as properties from cadaver to cadaver, repeatability of the experiments and establishing appropriate corridors in these experiments are other issues, which need to be addressed. The simulation results suggest that the properties of ligaments and muscles need to be verified and implemented with greater care. This is particularly important as ligament injuries are of considerable interest in most situations.

Neck muscles can alter the head and neck kinematics during frontal and rear end impact. Reflex time, activation level, co-contraction and the initial activation of the muscles can influence the head and neck motion. Additionally, initial seating posture and head restraint position influence the global and local head neck response in a rear end impact as was observed in the simulation results. Therefore, for accurate THUMS validation exact information on muscle activation, seating posture and position of seat and head restraint is essential.

To summarize, in this paper we have verified the THUMS cervical spine model against three sets of experimental data available in literature. The model validates well in some cases but is found lacking in some others. The reasons for the same have been discussed and possible directions for improvement have been suggested. These include better material models for soft tissues, better muscle model, better failure / rupture models, better contact interfaces and inclusion of more details in the neck model, to name a few. We are currently investigating most of these issues and would have more suggestions in these areas in the months to come.

ACKNOWLEDGEMENT

This study has been possible because of supports available from the Toyota Central R&D Labs and the Volvo Research Foundation.

References

1. Watanabe I., et al.; '*Development of practical and simplified human whole body FEM model*', JSAE spring convention, 2000 (In Japanese)
2. Mertz HJ and Patrick LM, 1967, Investigations in the kinematics and kinetics of whiplash, Proceedings of the STAPP Car crash conference, Paper 670919.
3. Mertz HJ and Patrick LM, 1971, Strength and response of human neck, Proceedings of the STAPP Car crash conference, Paper 710855.
4. McElhaney J.H., Jecquellne G.P, Myers B.M and Linda Grey, 1988, combined axial and bending loading responses of the human cervical spine, Proceedings of the STAPP Car crash conference, Paper 881709.
5. McElhaney J.H., Jecquellne G.P, Myers B.M and Linda Grey, 1989, Responses of the human cervical spine to torsion, Proceedings of the STAPP Car crash conference, Paper 892437.
6. Oshita Fuminori, Kiyoshi Mori et.al, 2002, Development of Finite Element Model of the human body, 7th International LS-Dyna Users conference, Japan Automobile Research Institute and Toyota Central R&D Labs, Nagoya Japan.
7. Brolin Karin, 2002, "Cervical Spine Injuries - Numerical Analyses and Statistical Survey" Doctoral Thesis Report, Department of Aeronautics, Division of Neuronic Engineering, Royal Institute of Technology, Stockholm, Sweden
8. Pintar and Narayan 1998, Pinter Frank A., Narayan Yoganandan, Voo L.M. et al., "Mechanism of Hyper flexion Cervical Spine." Session III (Neck Injuries), IRCOBI Proceedings, p-253, 1998.
9. M. Iwamoto, Y. Kisanuki, I. Watanabe, K. Furusu, K. Miki, J. Hasegawa, 2002, "Development of a Finite Element Model of the Total Human Model for Safety (THUMS) and Application to Injury Reconstruction", Toyota Central R&D Labs, - Toyota Motor Corporation (Japan)
10. Katsuya Furusu, Isao Watanabe, Chiharu Kato, Kazuo Miki, Junji Hasegawa, 2000, "Fundamental study of side impact analysis using the finite element model of the human thorax" Bio Mechanics Laboratory, Toyota Central R&D Labs, Japan Vehicle Engineering Div and Toyota Motor Corporation (Japan)
11. Thunnissen and Philipppines, 1996, Jan Thunnissen, Philipppens Mat"Cervical Human Spine Load During traumatic mechanical Investigation" Session II (Biomechanics of spinal injuries and rear impact protection), IRCOBI Proceedings, 1996
12. Ono and Koji, 1997. Koshiro Ono and Koji Kaneoka, "Motion Analysis Of Human Cervical Vertebrae During Low Speed Rear Impacts By The Simulated Sled." Session Iv (Head And Neck Protection), IRCOBI Proceedings, 1997
13. Rizette et al, 2001, A. Rizzetti, D. Kallieris, P. chiemann, R. Mattern, 1997, "Response And Injury Severity Of-The Head-Neck Unit During A Low Velocity Head Impact." Session IV (Head and Neck Protection), IRCOBI Proceedings.
14. Panjabi etal, 1998 Panjabi Manohar M., Barry S. Myers, 1998, "Cervical Spine Protection Report Prepared for NOCSAE", Biomechanics Laboratory, Yale University School of Medicine Department of Orthopedics & Rehabilitation.
15. Myers Barry S., McElhaney James H. et al, 1989, " Responses of the Human Cervical Spine to Torsion." Proceedings of the STAPP Car crash conference, Paper 892437.

Elderly human thoracic FE model development and validation

Atsutaka Tamura

Isao Watanabe

Kazuo Miki

Toyota Central R&D Labs., Inc.

Japan

Paper Number: 05-0229

ABSTRACT

Blunt impact to the anterior chest during frontal crash often causes sternum and rib fractures. In particular, several studies have reported that elderly people are susceptible to the complications following bony fractures mainly in the thoracic region, thereby, leading to high mortality and morbidity rates. These fractures are attributable to the reduced bone strength due to age-related osteoporosis. In this study, the authors developed a human thoracic FE model of the elderly occupant based on the 50th percentile male model, THUMS[®] (Total HUMAN Model for Safety) and the dynamic chest responses were validated during compression against experimental test data using post-mortem human subject (PMHS) specimens under realistic loading conditions that would be experienced by vehicular occupants restrained by an air bag and a seat belt.

INTRODUCTION

Highly energetic, trauma-like traffic accidents result in a high rate of morbidity and mortality. In particular, fractures of the bony thorax are the most frequent lesions in traumatic thoracic injury, while respiratory diseases such as pneumonia, flail chest, and pneumo/hemothorax are regarded as the leading complications associated with sternum and multiple rib fractures. Moreover, elderly people have a decreased injury tolerance due to the deteriorated bone strength related to osteoporosis and have been found to have a higher risk of fatal outcomes (AIS 3+). Thus, chest trauma, to the elderly people which involves bony fractures of the thoracic region, is associated with life-threatening complications despite its lower AIS value, which is an index of threat-to-life due to a specific injury (Bergeron et al., 2003; Bulger et al., 2000; Mayberry et al., 1997; Morris et al., 2002; Segers et al., 2001; Ziegler et al., 1994).

In industrialized countries, it is expected that by the year 2025 approximately 22% of the population will comprise people aged 60 years and above. For

instance, the population aged 65 years and older has been increasing in the U.S., and it is expected to make up more than 20% of the total U.S. population by the year 2030 (Dejeammes et al., 1996; Stutts et al., 1989). On the basis of computed crash rates using an estimate of annual mileage (i.e., crash rates per estimated million vehicle miles), the involvement of older drivers in crashes is greater than that of the overall population, although the percentage increases in the older age group are not as great as in the total licensed driver population (Stutts et al., 1989). Similarly, Shimamura et al. (2003) reported that in Japan, the percentage of elderly people aged 65 years and above reached 17.3% of the total population in the year 2000. They also analyzed the relationship between age groups and chest injury severity using a database of 246 belted occupants that were collected from 1993 to 2000 by ITARDA (Institute for Traffic Accident Research and Data Analysis) in Japan, and clarified that the injury severity in the elderly is closely related with the occurrence of multiple rib fractures. As described above, concerns about the growing transportation needs of the elderly and the necessity to make the traffic environment safer for older drivers arise from the potential risk of high injury rates related to motor vehicle accidents (Dellinger et al., 2002; Sjögren et al., 1993). These concerns are of importance particularly in light of the increase in life expectancy and rise in the proportion of elderly people in the population.

Meanwhile, Cesari et al. (1994) loaded the chests of volunteers, Hybrid III dummies, and human cadavers using a diagonal belt and found out that the location of maximum chest deflection was observed at points other than the mid-sternum. Furthermore, Morgan et al. (1996) investigated separate injury criteria for localized (*belt-like*) and distributed (*bag-like*) loading categories based on the normalized chest deflection and maximum chest acceleration and stated that the belt-only restraint system generally had a higher thoracic injury rate than the air bag-only restraint system. Recently, King (2000) reviewed previous studies on human tolerance to blunt impact and summarized the biomechanical knowledge of traumatic head, neck, and thorax injury. In this review article, King cited that the current injury

criterion prescribed in FMVSS 208 on chest compression of 76 mm is based on a recommendation by Neathery et al. (1973), who analyzed Kroell's data (1994) on blunt impact to the human thorax with a cylindrical rigid impactor to develop the thoracic response corridor. However, when the thorax was subjected to such a blunt impact and the force-deflection relationship was measured at the impacted area, a large inertial force would have been measured prior to the occurrence of the significant deformation of thorax observed. As a result, the characteristics of the thoracic response might be severely dominated by the inertial effect as noted by Kent et al. (2003b). Additionally, as stated earlier, vehicular occupants today are more likely to be restrained by a 3-point belt and air bags; therefore, the injury pattern during frontal crashes has altered due to the increased availability of safety devices. This raises the question of whether it is possible to evaluate the thoracic injury under any realistic loading condition using the injury risk function with this deflection-dependent criterion alone. In response to this, Kent et al. (2003b) designed a series of chest compression tests using human cadaveric specimens to study the effective stiffness of the thorax at a realistic loading rate under four loading conditions. They elucidated that the highest effective thoracic stiffness was measured with a distributed loading, followed by a double diagonal (4-point) belt, diagonal belt, and rigid hub depending on the difference in the loaded area and the interaction with the clavicles.

The purpose of the present study is to develop a thoracic FE model for elderly occupants and investigate the validity of its responses and potential injury patterns under realistic loading environments in a frontal crash.

METHODS

Small specimen test

First, material properties of the cortical rib in an elderly male were determined based on experimental test data obtained by Stitzel et al. (2003) at Virginia Technical University. They performed a dynamic 3-point bending test using small cortical bone samples obtained from the exterior surface of the ribs of human cadaver subjects whose ages ranged between 61 and 67 years (2 males). A total of 23 specimens were procured (6 specimens from the anterior part, 10 specimens from the lateral part, and 7 specimens from the posterior part) per cadaver, and each specimen was subjected to a 3-point bending load dynamically at the rate of ~5 strain/s. Specifically, as shown in Figure 1, a small specimen (24.0 mm in length \times 7.0 mm in

width \times 0.6 mm in thickness) was simply supported at both ends, and the impactor was prescribed to move at 365 mm/s to compress the middle point of a small specimen as per the ASTM Standard D790-00. The bending load for all specimens was applied in an exterior to interior direction relative to the in situ anatomy of the rib. This setup was considered to be a realistic loading condition produced by the seat belt and air bag, with the exception of the lateral part of the rib specimens, which was assumed to be bent from the interior to the exterior direction with compressive load from the anterior chest. According to their report, the strength and stiffness of the cortical rib greatly varied depending on the location and rib level in the human rib cage, and the anterior segment of the cortical rib was found to be weaker than the posterior segment, which is also weaker than that of the lateral rib. In the present study, however, the rib section was simply divided into 3 parts – anterior part, lateral part, and posterior part – and the material strength of the cortical rib was given by averaging the experimental test data obtained from each rib segment so that the difference in the material property of the cortical rib can be clearly considered in the simulation model.

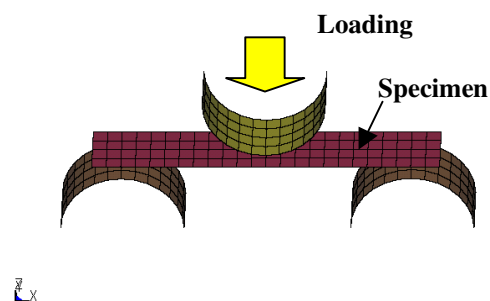


Figure 1: Dynamic 3-point bending test simulation for a small cortical rib specimen

Chest compression test

Second, model responses to the dynamic chest compression were validated against the experimental test data obtained by Kent et al. (2003b) at the University of Virginia (UVA). The human cadavers used in the test were aged between 75 and 79 years. They performed a series of chest compression tests with PMHS specimens positioned with their spine on a rigid table and the slave cylinder was prescribed to translate into a step rise time of 50 ms at a displacement rate of ~1.0 m/s (Figure 2a, b). This is similar to the chest deflection rate of the occupants restrained by a seat belt in a frontal crash while traveling at 48 km/h. In the experimental test setup, the chest deflection was measured anteriorly at the mid-sternum point, while the reaction force was measured posteriorly using the load cell placed behind each subject's back. In reality, however, this type of

loading condition cannot be expected for vehicular occupants since their back is normally free in the compartment, and no reaction force is generated in the posteroanterior direction in a frontal crash. In the present study, data from three elderly cadaver subjects who had undergone dynamic chest compression was compared with the simulation results using distributed, hub, diagonal belt, and 4-point belt loading conditions as shown in Figures 3a–d. Specifically, a 20.3 cm wide band was used to compress the area between the second and seventh ribs for distributed loading, while a 15.2 cm diameter circular plate was used for hub loading to mimic the loading surface described by

Kroell et al. (1994). In addition, a 5.0 cm wide belt was used to pass over the shoulder to the lower ribs of the PMHS specimens for diagonal belt and 4-point belt loading. In these simulations, only gravity was applied for an initial 120 ms prior to dynamic compression of the thorax so that the stable condition would be obtained for determining a zero point in force-deflection curves. It should be noted that in this series of experimental tests, the generation of bone fracture was not attempted by impacting the thoracic region. Finally, we conducted an injury analysis up to the bone fracture level by compressing the thoracic region at a rate of 0.6 m/s.

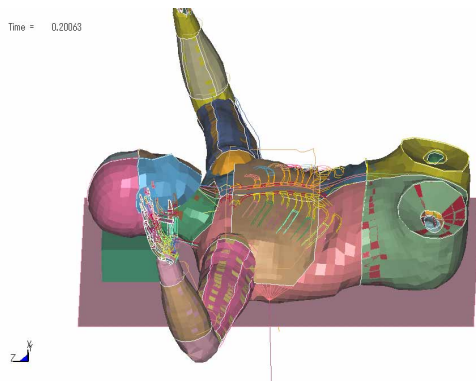


Figure 2a: Simulation setup[#]
[[#]Chest is compressed by distributed loading.]

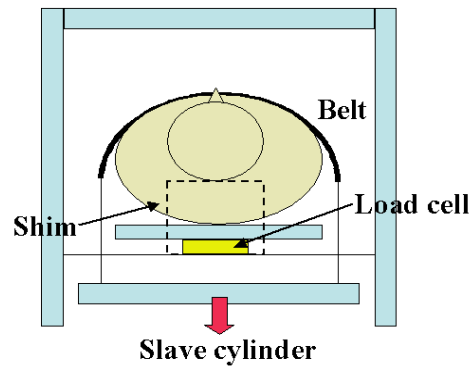


Figure 2b: Test setup for dynamic chest compression via loading cable conducted at UVA

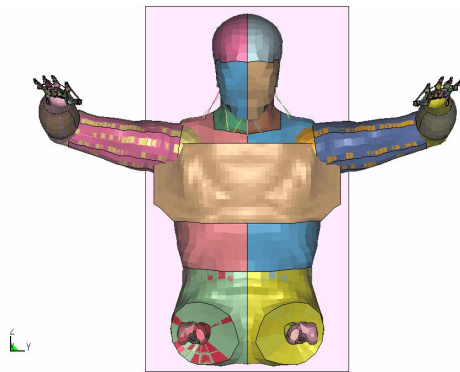


Figure 3a: Initial condition for distributed loading

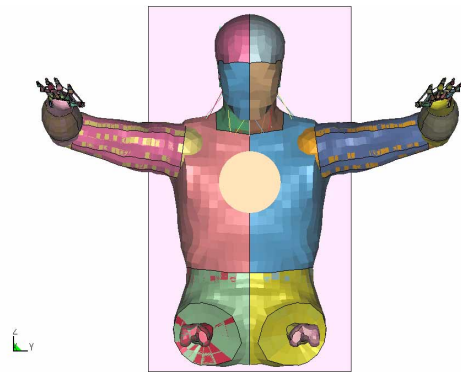


Figure 3b: Initial condition for hub loading

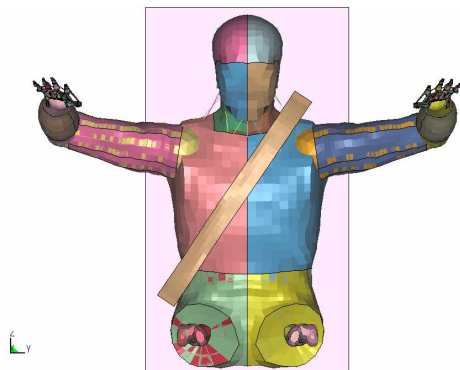


Figure 3c: Initial condition for diagonal belt loading

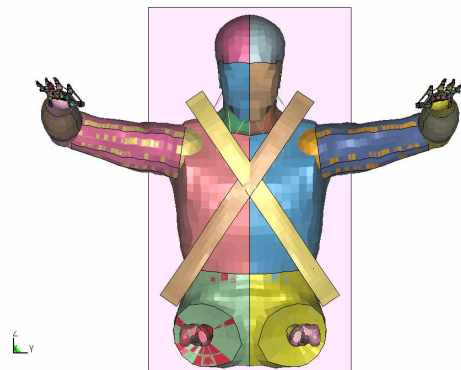


Figure 3d: Initial condition for 4-point belt loading

RESULTS

Small specimen test

First, on the basis of the experimental test results (Stitzel et al., 2003), the material property of the cortical rib in an elderly male was determined as summarized in Table 1 by means of the elastic beam theory, while simulation results using small specimens were compared with those of the experimental tests as shown in Figure 4. In this section, the yield point was defined by averaging the real yield points in each

force-deflection plot by 0.1% offset strain strength. Since the force-deflection responses in cortical rib bending tests were greatly dispersed, material coefficients such as the Young's modulus and plastic tangent modulus were also determined by averaging the experimental test data so that the calculated results would exist within the force-deflection responses. In addition, the ultimate tensile strain was defined as 0.020 (2.0%) in view of the reduced bone strength with aging (Lindahl et al., 1967; McCalden et al., 1993).

Table 1: Material property of the cortical rib in an elderly male[†]

	σ_y (MPa)	ϵ_y	YM (GPa)	Etan (GPa)	ϵ_p	ϵ_{max}
Anterior part	121.6	0.0145	8.394	3.792	0.0055	0.020
Lateral part	135.3	0.0111	12.211	4.610	0.0089	0.020
Posterior part	112.9	0.0103	10.998	6.332	0.0097	0.020

[[†] σ_y : yield stress, ϵ_y : yield strain, YM: Young's modulus, Etan: plastic hardening modulus, ϵ_p : plastic strain, ϵ_{max} : ultimate strain]

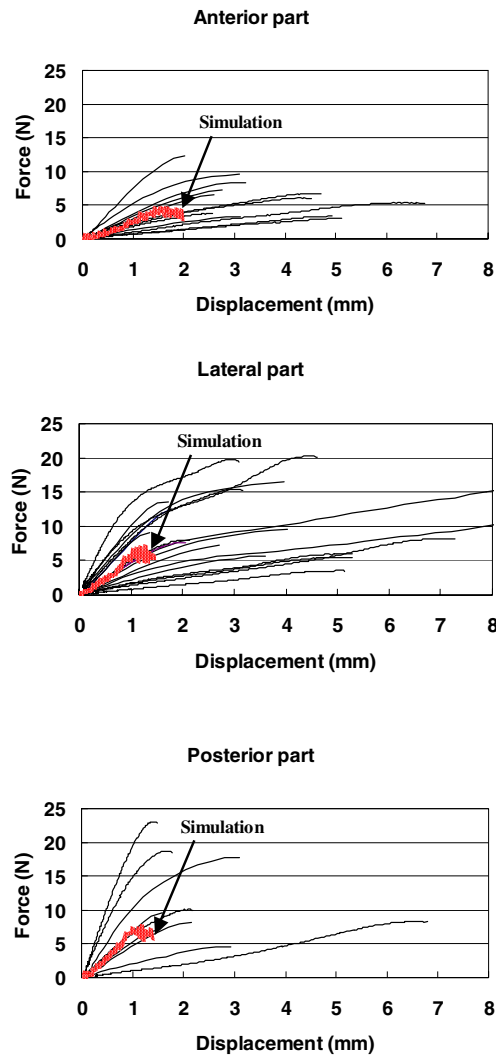


Figure 4: 3-point bending test results using rib cortical specimens

Chest compression test

Second, the calculated result with respect to the thoracic part was validated against laboratory test data obtained by Kent et al. (2003b) using human cadaver subjects. As demonstrated in Figure 5, the calculated thoracic responses to dynamic chest compression are almost identical with the experimental results, and thoracic stiffness was found to be greatly dependent on

the interaction between the clavicles and the 1st ribs as well as the magnitude of the loaded area due to compressing devices. Additionally, as it can be seen in a frontal crash with air bag deployment, stress concentration was observed at the lateral part of the rib cage under distributed loading condition (Crandall et al., 2000; Yoganandan et al., 1996). Meanwhile, for hub loading, stress concentration was only observed at the sternum level.

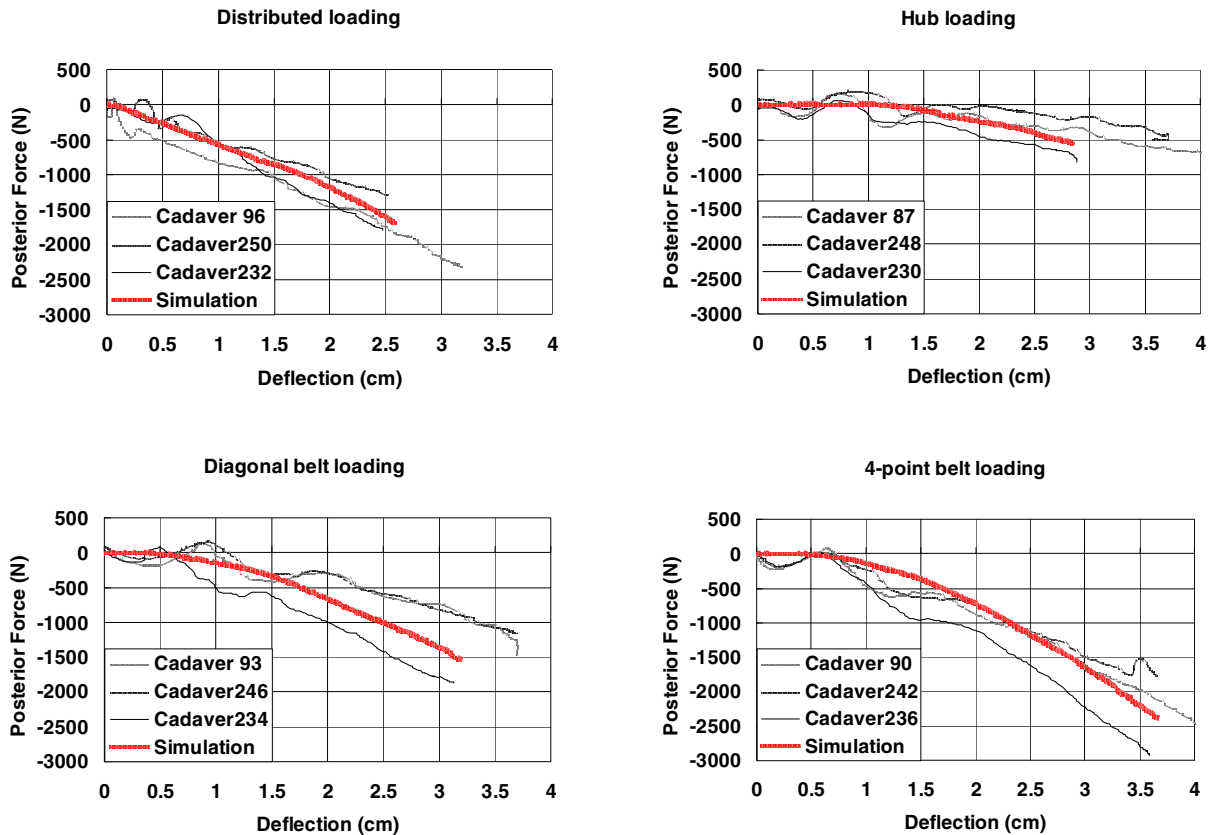
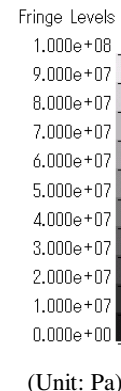


Figure 5: Force-deflection responses in chest compression under four loading environments

Injury analysis

Finally, we investigated thoracic hard tissue failure patterns due to excessive anterior chest compression. The same test setups were used as those employed in the previous section. Hence, a series of FE simulations were subsequently conducted, and the element elimination technique was used to assess the bone fractures of the sternum and the rib cortical bone. As illustrated in Figures 6a–d, multiple hard tissue failures and various fracture patterns were predicted around compressing devices except for the 4-point belt and fracture timing was also tracked (Figures 7a–d). Although no bone fracture was observed against 4-point belt loading, as stated earlier, considerable stress concentrations were observed at several locations in the

clavicles and the lateral part of the rib cage, as shown in Figure 6d.



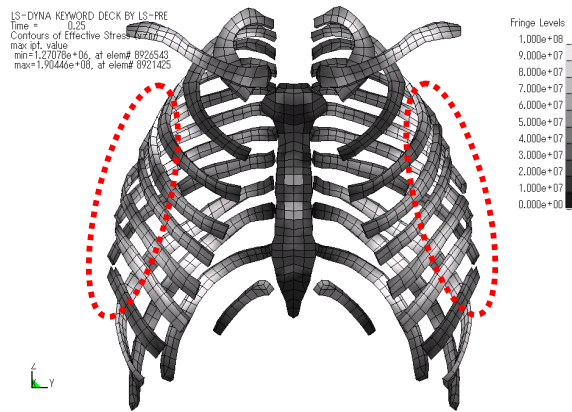


Figure 6a: Equivalent stress distribution by distributed loading (at 120 ms)*

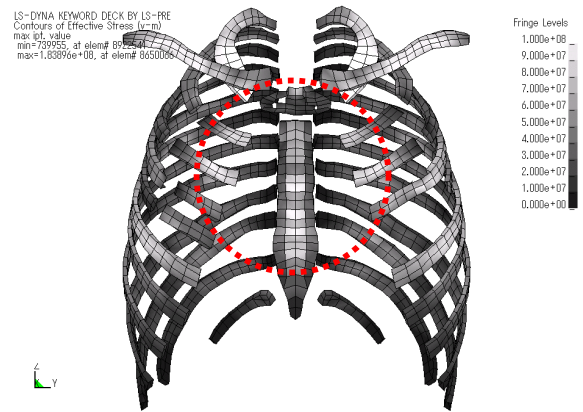


Figure 6b: Equivalent stress distribution by hub loading (at 157 ms)*

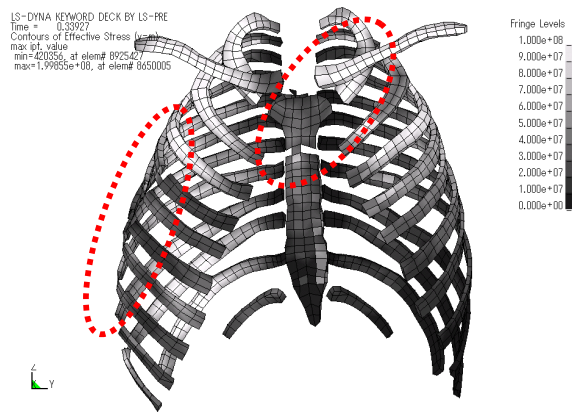


Figure 6c: Equivalent stress distribution by diagonal belt loading (at 210 ms)*

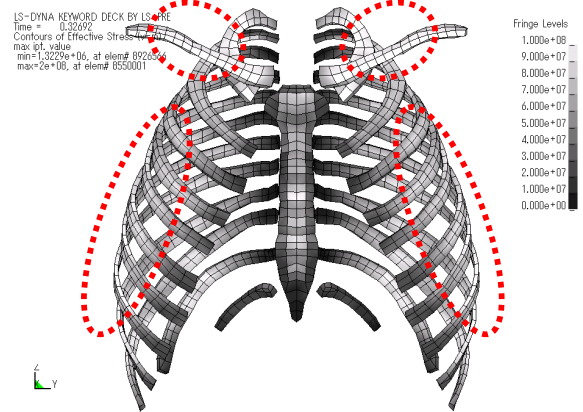


Figure 6d: Equivalent stress distribution by 4-point belt loading (at 197 ms)*

[*Enclosed area with dotted line corresponds to the area of stress concentration.]

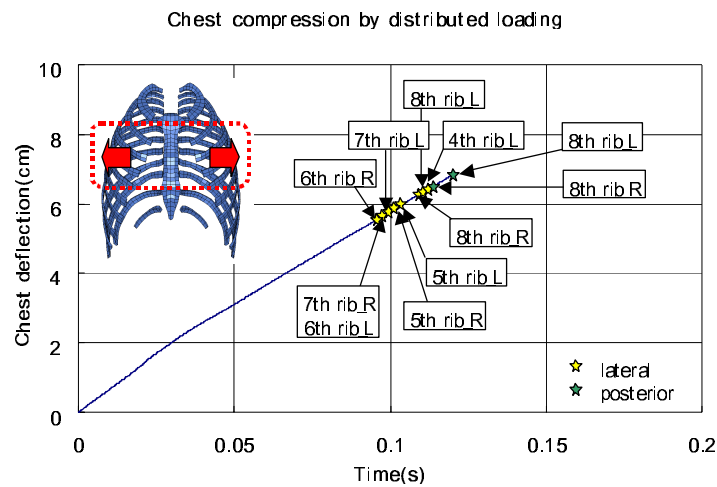


Figure 7a: Time history of chest deflection and fracture timing due to distributed loading*

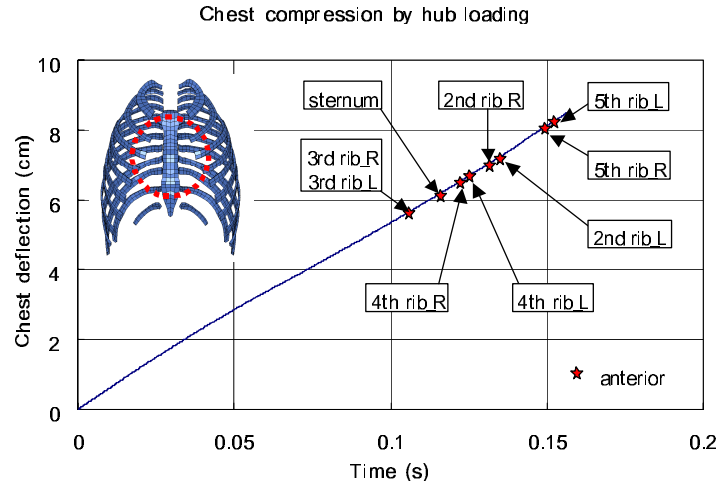


Figure 7b: Time history of chest deflection and fracture timing due to hub loading[‡]

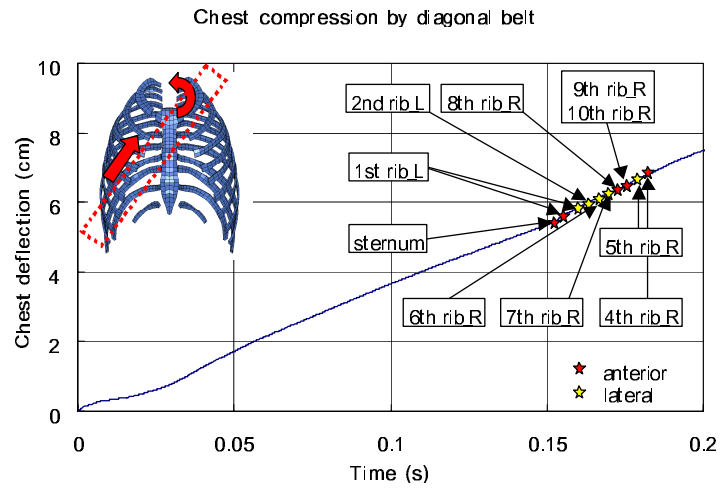


Figure 7c: Time history of chest deflection and fracture timing due to diagonal belt loading[‡]

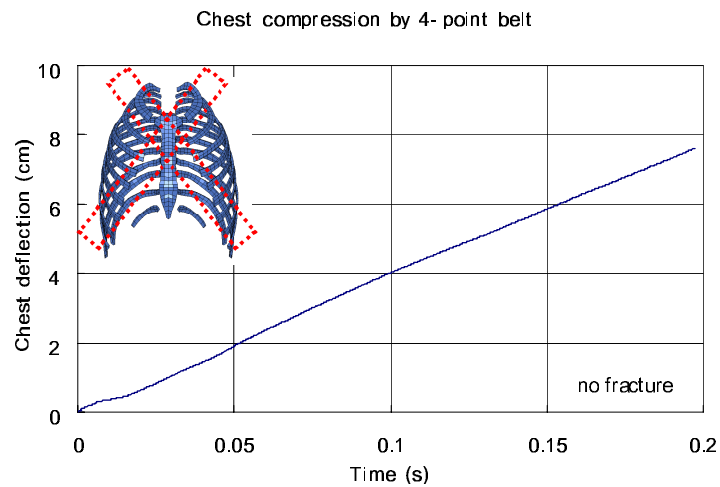


Figure 7d: Time history of chest deflection and fracture timing due to 4-point belt loading[‡]
[‡][[‡]R indicates right ribs, and L indicates left ribs.]

DISCUSSION

Small specimen test

The mechanical property of the cortical rib was determined based on the experimental test results. In general, the ultimate tensile strain as an index of bone strength is considered to gradually reduce with aging. In other words, the mechanical property of cortical bones in the elderly is believed to be relatively close to that of a brittle material rather than an elasto-plastic material. Whereas, by dynamically conducting a 3-point bending test, Stitzel et al. (2003) found that the plastic region of the cortical rib in the elderly is much greater than expected, although material property varies considerably depending on its location and rib level. According to their results, some of the small specimens subjected to a dynamic bending load demonstrated a large tensile strain in excess of 0.080 (8.0%) on the lower surface of the specimens. In the present study, however, ultimate strain was determined as 0.020 (2.0%). This was based on previous studies in which the material property of the cortical bone was experimentally investigated using humeral and femoral coupons in pure tension (Lindahl et al., 1967; McCalden et al., 1993) so that the effect of reduced bone strength with aging can be clearly taken into account. When the elastic beam theory is employed to derive the mechanical property of the cortical rib, the relationship between stress and strain can be calculated based on the assumption that its distribution in the loaded section is ideally symmetrical with respect to the neutral axis. However, this assumption may not be acceptable for large deflections occurring due to excessive bending load, and the behavior post-yield point can no longer be estimated correctly. Nevertheless, the authors will support their test method at this stage because of the difficulty in the existing experimental measuring technique. Further, we believe that the 3-point bending test is still one of the best ways to obtain the mechanical property of the cortical rib against such a high speed impact. This is because such a bending load is regarded to be a dominant factor in causing hard tissue failure of the thorax in a restrained vehicular occupant in frontal crashes.

Chest compression test

The model was then validated against the dynamic thoracic compression tests under four realistic loading conditions. It may be difficult to compare the results obtained here to Kroell's test results (1994) using a rigid impactor, which might be dominated by the inertial effect, because PMHS specimens in this study

were laid along the spine position on a rigid table, and the reaction force was measured posteriorly to derive the effective thoracic stiffness. Therefore, as stated earlier, the authors initially applied only gravity on the model lying on a rigid table in order to obtain a stable condition prior to dynamically compressing the anterior chest. In addition, the material property of the deformable solid elements used as a substitute for internal organs inside the thoracic cavity was adjusted so that it would respond against impacting load in a manner similar to a pressurized lung by means of the preliminary test results obtained at our laboratory (Hayamizu et al., 2003) since Kent et al. (2003b) also pressurized the pulmonary system to model the in vivo condition as much as practically possible before conducting a series of chest compression tests. Although we had paid careful attention to reconstruct the boundary conditions of the experimental test setup, the difference observed in force-deflection responses between simulation and experimental test results might be responsible for a mismatch in its boundary condition or the effect of the internal organ, which are not included in the current THUMS model (Oshita et al., 2001). Nonetheless, we believe that our results showed reasonable responses compared to the experimental test results in view of the general trend observed when subjected to realistic dynamic chest compression. Further, this model can be applied for practical problems such as a frontal crash simulation. However, since rib fracture is suspected to lacerate the internal organs and its injury mechanism remains unknown, we need to develop and integrate a detailed internal organ model so that visceral injury as well as thoracic bony failures can be predicted.

Injury analysis

In this section, the rib cortical bone was subjected to a severe bending load from the anterior chest at a relatively slow loading rate, as mentioned earlier. However, the authors are concerned about the possible overestimation of the magnitude of its ultimate stress strength in the model due to the theoretical approach of the elastic beam theory employed in the present study. Additionally, material property of flesh (soft tissue) remains unclear, although it is believed to be crucial for estimating the probability of chest injury since flesh tissue is considered to be effectively distributing the load from the anterior chest (Kent et al., 2001).

In summary, we have found the following results under these four loading environments:

- 1) **Distributed loading:** Bone fracture was predicted to propagate from the lateral side to the posterior

side as such a fracture pattern could be expected for typical air bag loading.

- 2) **Hub loading:** Bone fracture was only predicted around the anterior chest due to the excessive bending load on the anterior surface of the thorax.
- 3) **Diagonal belt loading:** Bone fracture was predicted in the inferior to superior direction along the path of a diagonal belt. It was also observed that the anterior part of the thorax failed due to sternum torsion and the interaction between the clavicle and the 1st rib.
- 4) **4-point belt loading:** Although bone fracture was not predicted in this case, considerable stress concentrations were observed at several locations for both the clavicles and the lateral part of the rib cage. Since the rate of compression was set to be relatively moderate in comparison with a real loading environment, intrinsic symmetry stemming from such a 4-point belt appears to sufficiently distribute the total load over the rib cage.

In the present study, the chest deflection of 70 mm corresponds to the thoracic compressive ratio of 32.5% for the current chest depth of THUMS. According to the analytical results reported by Kent et al. (2003a), the probability of injury risk for $fx. > 6$ (greater than six rib fractures) can be estimated to be over 50% for elderly people aged 70 years old with the ratio of 32.5% chest compression. Although four types of restraint conditions were employed in this section, the onset of fracture timing was almost similar except in the case of 4-point belt loading. Specifically, the fracture onset was observed at a magnitude of 50 mm chest deflection, and multiple bone fractures ($fx. > 6$) were observed at a magnitude of 70 mm chest deflection. However, most of the stress concentration was observed along the path of the diagonal belt line as well as the lateral part of the rib cage due to excessive bending load from the anterior chest. In particular, stress concentration was observed at the lower part of the rib cage rather than at the mid-sternum level. Despite the fact that the magnitude of chest deflection is evaluated at the mid-sternum level for the current crash test dummy, it is inconclusive as yet whether maximum chest compression (C_{max}) is always suitable for chest injury prediction. Thus, the possibility that the current chest compression criterion based on the mid-sternum level alone would be a sufficient index for predicting injury risk is still open to discussion as suggested by the previous studies (Cesari et al., 1994; Morgan et al., 1996). Future studies should integrate this thoracic model for the elderly with THUMS and apply it for frontal crash simulation in combination with a seat belt and air bag loading to investigate the

effect on the protection and safety of the occupant as shown in Figure 8.

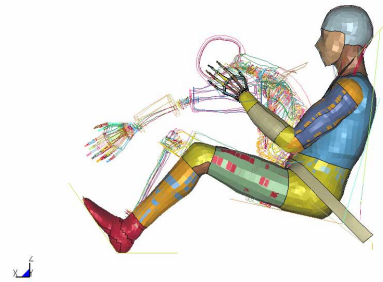


Figure 8: Sled test model with a belted occupant

CONCLUSION

Thoracic part of the elderly male occupant was developed based on Total HUMAN Model for Safety (THUMS®) so that it would be applied for predicting thoracic hard tissue injury by taking into account the decreased bone strength due to aging. Now we hope that the thoracic characteristics of an elderly occupant obtained from the present study will be applied to more realistic cases in order to advance the safety protection performance of the current restraint system.

ACKNOWLEDGMENTS

The authors greatly acknowledge the contribution of Wayne State University for the development of the head and thorax part of THUMS. We also wish to thank the University of Virginia and Virginia Technical University for their sincere support and assistance under the contract of collaborative research program with Toyota Motor Corporation (2002-2003). In addition, the authors thank Mr. Junji Hasegawa and Mr. Fumio Matsuoka of Toyota Motor Corporation who have provided us with a valuable advice and comments to complete this study.

REFERENCES

- Bergeron, E., Lavoie, A., Clas, D., Moore L., Ratte, S., Tetreault, S., Lemaire, J., Martin, M. (2003); "Elderly trauma patients with rib fractures are at greater risk of death and pneumonia", J. Trauma, Vol. 54, pp. 478-485.
- Bulger, E. M., Arneson, M. A., Mock, C. N., Jurkovich, G. J. (2000); "Rib fractures in the elderly", J. Trauma, Vol. 48, pp. 1040-1047.
- Cesari, D., Bouquet, R. (1994); "Comparison of hybrid III and human cadaver thorax deformations loaded by

- a thoracic belt", In Proc. of 38th Stapp Car Crash Conf., pp. 65-76, SAE# 942209.
- Crandall, J. R., Kent, R., Patrie, J., Fertile, J., Martin, P. (2000); "Rib fracture patterns and radiologic detection – A restraint-based comparison", In Proc. of Annual Proceedings of 44th Association for the Advancement of Automotive Medicine, pp. 235-259.
- Dejeammes, M., Ramet, M. (1996); "Aging process and safety enhancement of car occupants", In Proc. of 15th International Technical Conf. on Enhanced Safety Vehicles, pp. 1189-1196.
- Dellinger, A. M., Langlois, J. A., Li, G. (2002); "Fatal crashes among older drivers: Decomposition of rates into contributing factors", American Journal of Epidemiology, Vol. 155, pp. 234-241.
- Hayamizu, N., Watanabe, I., Ishihara, T., Miki, K. (2003); "Measurement of impact response of pig lung", In Proc. of JSME Tokai Branch Conf., pp. 94-95. (in Japanese)
- Kent, R., Crandall, J. R., Bolton, J., Prasad, P., Nusholtz, G., Mertz, H. J. (2001); "The influence of superficial soft tissues and restraint condition on thoracic skeletal injury prediction", Stapp Car Crash Journal, Vol. 45, pp. 183-204.
- Kent, R., Patrie, J., Poteau, F., Matsuoka, F., Mullen, C. (2003a); "Development of an age-dependent thoracic injury criterion for frontal impact restraint loading", In Proc. of 18th International Technical Conf. on Enhanced Safety of Vehicles.
- Kent, R., Sherwood, C., Lessley, D., Overby, B., Matsuoka, F. (2003b); "Age-related changes in the effective stiffness of the human thorax using four loading conditions", In Proc. of International Research Council on the Biomechanics of Impact.
- King, A. I. (2000); "Fundamentals of impact biomechanics Part 1 --- Biomechanics of the head, neck and thorax", Annu. Rev. Biomed. Eng., Vol. 2, pp. 55-81.
- Kroell, C. K. (1994); "Thoracic response to blunt frontal loading", In Biomechanics of impact injury and injury tolerances of the thorax-shoulder complex (Backaitis, S.H., ed.), pp. 51-79, SAE, Inc.
- Lindahl, O., Lindgren, Å. G. H. (1967); "Cortical bone in man II. Variation in tensile strength with age and sex", Acta Orthop. Scandinav., Vol. 38, pp. 141-147.
- Mayberry, J. C., Trunkey, D. D. (1997); "The fractured rib in chest wall trauma", Chest Surg. Clin. N. Am., Vol. 7, pp. 239-261.
- McCalden, R. W., McGeough, J. A., Barker, M. B., Cout-Brown, C. M. (1993); "Age-related changes in the tensile properties of cortical bone", J. Bone Joint Surg., Vol. 75, pp. 1193-1275.
- Morgan, R. M., Eppinger, R. H., Kuppa, S. M., Taylor, L. M. (1996); "Thoracic trauma assessment for the hybrid III dummy in simulated frontal crashes", In Proc. of 15th International Technical Conf. on Enhanced Safety Vehicles, pp. 1605-1621.
- Morris, A., Welsh, R., Frampton, R., Charlton, J., Fildes, B. (2002); "An overview of requirements for the crash protection of older drivers", In Proc. of Annual Proceedings of 46th Association for the Advancement of Automotive Medicine.
- Neathery, R. F., Lobdell, T. E. (1973); "Mechanical simulation of human thorax under impact", SAE Technical Paper, pp. 451-466, SAE# 730982.
- Oshita, F., Omori, K., Nakahira, Y., Miki, K. (2001); "Development of a finite element model of the human body", In Proc. of 7th Int. LS-Dyna Users Conf.
- Segers, P., Van Schil, P., Jorens, Ph., Van Den Brande, F. (2001); "Thoracic trauma: an analysis of 187 patients", Acta. Chir. Belg., Vol. 101, pp. 272-282.
- Shimamura, M., Ohhashi, H., Yamazaki, M. (2003); "The effects of occupant age on patterns of rib fractures to belt-restrained drivers and front passengers in frontal crashes in Japan", Stapp Car Crash Journal, Vol. 47, pp. 349-365.
- Sjögren, H., Björnstig, U., Eriksson, A., Sonntag-Öström, E., Öström, M. (1993); "Elderly in the traffic environment: Analysis of fatal crashes in northern Sweden", Accid. Anal. & Prev., Vol. 25, pp. 177-188.
- Stitzel, J. D., Cormier, J. M., Barretta, J. T., Kennedy, E. A., Smith, E. P., Rath, A. L., Duma, S. M., Matsuoka, F. (2003); "Defining regional variation in the material properties of human rib cortical bone and its effect on fracture prediction", Stapp Car Crash Journal, Vol. 47, pp. 243-265.
- Stutts, J. C., Waller P. F., Martell, C. (1989); "Older driver population and crash involvement trends, 1974-1986", In Proc. of 33rd Annual Proceedings of Association for the Advancement of Automotive Medicine, pp. 137-152.
- Yoganandan, N., Morgan, R. M., Eppinger, R. H., Pintar, F. A., Sances, A. Jr., Williams, A. (1996); "Mechanisms of thoracic injury in frontal impact", J. Biomechanical Eng., Vol. 118, pp. 595-597.
- Ziegler, D. W., Agarwal, N. N. (1994); "The morbidity and mortality of rib fractures", J. Trauma, Vol. 37, pp. 975-979.

PELVIS BONE FRACTURE MODELING IN LATERAL IMPACT

Eric Song

Laurent Fontaine

Xavier Trosseille

Hervé Guillemot

LAB PSA Peugeot-Citroën Renault

France

Paper Number 05-0247

ABSTRACT

This paper presents personalized simulations of eleven isolated pelvic bones under lateral impact and a generic 50th percentile male pelvic bone model based on these simulations. Eleven pelvises were solicited by metallic spheres in the acetabulum, which were impacted by a falling mass of 3.68 kg at a speed of 4 m/s. Each pelvis test was then modeled individually, taking into account its proper geometry and mass. Damageable material law was used to simulate the bone stiffness and fracture. For each pelvis test were determined equivalent elastic modulus, yielding stress and damage plastic strain representing combined contributions of material properties and cortical bone thickness to pelvis bone resistance. Based on these personalized simulations a generic 50th percentile male pelvic bone model was defined and integrated into a full body model to simulate cadaver tests on pelvis where bone fractures were documented. Three material laws were then identified and associated with this model, representing respectively a fragile, a medium and a resistant pelvis bone. The mechanical behavior of this pelvis model was also compared to experimental data on cadavers. It showed that the pelvis model developed is globally relevant with respect to experiments in terms of pelvis loading prediction, this for a large range of impact energy from 130 to 1150 Joules. This paper provides new data and insights for pelvis bone fracture modeling in lateral impact. The resulted model is consistent with available impactor test data on pelvis and constitutes a useful tool for lateral impact injury research.

INTRODUCTION

Side impacts represent 15 to 20% of the automotive collisions in which at least one of the occupants was injured but are the cause of 25 to 30% of serious and fatal injuries encountered in all car accidents. Protection of occupants in side impact remains a big challenge despite of progress made in the past years. In fact the very limited space between car door and occupant make very difficult to dissipate the engaged impact energy in a smooth manner. In order to optimize protection

strategy and to improve protection equipments more biomechanical knowledge is needed on pelvis tolerance of different population groups, for example, a vulnerable 50th percentile male.

The pioneer work of Césari *et al.* [1980, 1982] led the basis for pelvis loading based injury criterion definition. 55 cadaver tests on 22 subjects were performed by impacting the great trochanter with a spherical rigid impactor. Césari concluded that the value of tolerance in terms of impact force is close to 10 kN for a time period of 3ms for the 50th percentile male subjects and close to 4 kN for the 5th percentile female. However it is to be noted that less than 30% of subjects tested have mass included between 77±10kg. Moreover, average age of subjects tested rises to 70 years.

More impactor tests on pelvis have been performed and published ever since. Viano [1989] performed 10 cadaver tests with a circular but flat impactor of 23.4 kg. Subjects tested were relatively younger than those of Césari. Tolerance in terms of impact force revealed to be higher. Bouquet *et al.* [1994] performed cadaver tests also with an impactor of 23.4 kg. The impact surface was nevertheless a rectangular rigid plate of 200x100 mm². They showed a lower tolerance level in terms of impact force: around 8 kN. Bouquet *et al.* [1998] performed more cadaver tests but with a larger impact surface (200x200 mm) in order to include the contribution of iliac wing. Impactor mass and impactor velocity were designed in such a way so that they can examine which one, between mass and velocity, is dominant for a given energy level. In fact they found that to represent car crashes, the impacting masses should be lower than the famous 23.4 kg impactor, and considered essential to know the pelvis behavior in new impact conditions. Based on their new cadaver tests, they concluded that for a given impactor energy, neither its mass nor velocity seemed to be dominant.

Side impact dummies were evaluated with respect to some configurations of above cadaver tests. Both SID and EuroSID were demonstrated to have a too stiff pelvis with respect to cadaver responses. WorldSID shows more close responses. However its load path showed big difference with

respect to EuroSID when comparing symphysis contribution to total loading sustained by pelvis. It is important to understand the mechanism of force path and to determine the consequence of these differences when dummies are used to develop protection systems.

Also to define injury criteria thresholds, it is usual to normalize cadaver test responses while keeping always the same injury outcome. No elements were showed to support such an approach.

A mathematical model of the pelvis, capable of injury prediction, should constitute a valuable tool to address the different problems listed above.

Numerous models of pelvis can be found in the literature. Many of them were developed to simulate the pelvis behavior during the walk cycle or to study the interaction of the pelvic bone with hip prosthesis [Goel *et al.* 1978; Oonishi *et al.* 1983; Dalstra *et al.* 1993, 1995]. Models dealing with pelvis behavior and injuries under car related impact conditions remain a minority.

Chamouvard *et al.* [1993] developed a spring-mass model of pelvis for lateral impact. However, it was limited to give only a global response in terms of force, displacement, or acceleration, in mono-axial conditions. Renaudin *et al.* [1993] developed a finite element model of pelvis. Considering that the trabecular bone had a low influence in terms of overall stiffness of the pelvis [Dalstra *et al.* 1993], they represented pelvis bone by only shell elements, corresponding to the external surface of the structure. The model was designed from a metallic model of the 50th percentile of Reynolds. Moreover, thickness from 1 to 4 millimeters, measured on experimented pelvis, were attributed to the shell elements. Nodal masses were distributed to correspond to the global characteristics of a pelvis. The Young's modulus in this model was low, around 3000 MPa. Static tests [Guillemot *et al.* 1995] were first conducted under side loading conditions, in order to validate this model. Besnault *et al.* [1998] improved this model by adding geometrical parameters to adapt it to different tested bones, using a kriging technique. Plummer *et al.* [1996] proposed a modified version of a model of Bidez, built from CT scan slices, which aimed at the study of pelvis fracture etiology, in the context of automotive side impact conditions. Nevertheless, this model did not represent a whole pelvis: a coxal bone was modeled, but the sacrum and the contralateral ilium were not taken into account. Finally the acetabulum was fitted with a hip prosthesis. Dawson *et al.* [1998] proposed a model, also dedicated to lateral impacts in the field of car accidents. The model was created from 74 CT scan slices, and distorted by scale factors to correspond

to the 50^e percentile of Reynolds. The two coxal bones and the sacrum were built by 8-node elements, and connected to each other by 32 springs for the sacro-iliac joints and 8 springs for the pubic symphysis. Joint properties were established from the literature [Fung 1965; Mak 1986]. Bone characteristics were given element by element, from CT scan density levels, and range from 250 to 1500 MPa for the trabecular bone Young's modulus. The meshing included 1511 8-node elements and 3769 nodes. The complete model was validated by using a modal analysis. However, the pelvis mass (0,534 kg) is lower than a real one.

In spite of numerous models reviewed above, there is still a need of a pelvis model, capable of simulating pelvis bone fracture in lateral pelvis impact, relevant with respect to currently available cadaver impactor test data, and sufficiently validated to represent human pelvis behavior and its variation versus different groups of car occupant population.

This paper intends to develop such a model. Based on the work performed by Besnault *et al.* [1998], where was developed a kriging technique and allows taking into account particular geometry of each pelvis simulated, 11 impactor tests on isolated pelvis bone have been individually simulated and corresponding mechanical properties and its range of variation determined. Then a generic model of pelvis was constructed and integrated to a whole human body model [Lizée *et al.* 1998]. With this model, impactor tests on cadavers presented above were simulated and material laws derived to represent different levels of resistance due to individual variation. Finally model responses were evaluated with respect to impactor test data.

MODEL DEVELOPMENT

Geometry

The reference FE mesh of pelvis bone (See Figure 1 represents the shape of a 50th percentile male.

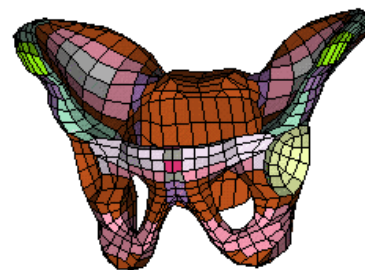


Figure 1. Reference FE mesh of pelvis bone representing the shape of a 50th percentile male.

This shape was based on the data of Reynolds *et al.* [1981]: their statistical study concerning 3000 pelvic bones of north Americans has allowed the design of a pelvis casting corresponding to the 50th percentile male. This pelvis casting was digitalized and then meshed by shell elements to represent cortical bone. Trabecular bone was not taken into account in reason of its low influence on overall stiffness of pelvis. The two acetabula, missing in the casting, were included by two spherical segments positioned at each hip centre.

Stiffness and fracture of pelvis bone are conditioned by thickness of its cortical bone. Examination of five pelvis bone [Guillemot 1992] showed considerable variation of thickness from one location to another: it passes from several tenths millimeter in the centre of iliac wing to nearly 4 mm for the iliac spine. This variation clearly suggests that it is not relevant to use a uniform thickness repartition through pelvis bone, in particular when cortical bone fracture simulation is aimed at, since yielding and rupture occurrence of a plate is directly linked to its thickness for a given local loading. To take into account this variation of thickness through pelvis bone, each element was attributed a thickness according to its position based on data obtained from these five pelvises.

Mechanical properties

Few experimental data are available on pelvic bone. Only data found were given by Kuhn and Goldstein [1989] on iliac crest, with an elastic modulus varying between 3.0 and 5.3 GPa. In this study our objective was to develop a pelvis model with bone fracture simulation. To do this, an elastoplastic law with damage was attributed to cortical bone. As showed by Figure 2, the parameters of this law are the elastic modulus, the elastic threshold, the maximum stress and the damage plastic strain.

Due to the lack of experimental data on these parameters for pelvis cortical bone, Guillemot tests on isolated pelvis [1997] were used: the simulation

of these tests should allow estimating these parameters.

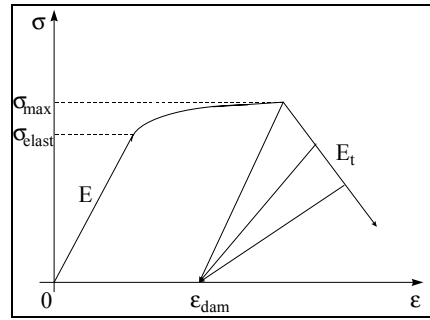


Figure 2. Elastoplastic material law with damage (Radio-Mecalog).

However we know that pelvis bone stiffness and fracture are conditioned by thickness of pelvis bone. So it is no use focusing on real material parameters for simulating an individual pelvis while the thickness and its repartition are unknown.

The following approach was adopted for the definition of mechanical properties: thickness and its repartition remain constant from one pelvis to another while the elastic modulus, the elastic threshold, the maximum stress and damage plastic strain vary to present dispersion of pelvis bone across occupant population. It means that these mechanical parameters should be considered as equivalent ones which assume, together with cortical bone thickness, similitude between the model and corresponding pelvis simulated in terms of dynamic responses and injury outcome for considered configuration.

Although few experimental data are available on pelvis bone, many experiments have been done on long bone, in particular on femur and tibia. Review of these experiments by Viano [1986] showed that cortical bone can undergo yielding up to 3-4% before ultimate failure and elongation above 0.5% strain generally causes microstructure damage in the material and inelastic behaviour. Table 1 is an example of experimental data obtained by Burstein *et al.* [1976] for tibia tensile properties, and indicates that: 1) the ratio σ_y/E is around 0.5%; 2) the difference $\sigma_u - \sigma_y$ is around 28 MPa

Table 1.
Tensile properties of tibia for different age groups according to experiments of Burstein *et al.*

Age (yrs)	E (MPa)	σ_y (MPa)	σ_u (MPa)	σ_y/E	$\sigma_u - \sigma_y$ (MPa)
20-29	18900	126	161	0,0067	35
30-39	27000	129	154	0,0048	25
40-49	28800	140	170	0,0049	30
50-59	23100	133	164	0,0058	31
60-69	19900	124	147	0,0062	23
70-79	19900	120	145	0,0060	25
80-89	29200	131	156	0,0045	25
Moyen	23829	129	157	0,0054	28

Based on these literature data, further specifications were added to the target material law of cortical bone of pelvis:

$$\begin{aligned}\sigma_y &= 0.005 \cdot E \\ \sigma_u - \sigma_y &= 30 \text{ MPa} \\ \epsilon_p &= 3\%\end{aligned}$$

In order to determine the magnitude of these mechanical parameters, simulations of experiments on isolated pelvis bone were performed, giving thus a first estimation of E , σ_y , σ_u and ϵ_p .

Simulations of tests on isolated pelvis bone

Guillemot *et al.* [1997] performed dynamic tests on isolated pelvis bone. 11 pelvis bones were extracted from fresh cadavers. A drop tower was used to impact these bones. It consisted of a falling mass guided between two rails which enables impact speeds up to 4 m/s. Each pelvis was fixed up to the external edge of the left ischial turosity. A falling mass of 3.68 kg impacted a metallic ball

fitted into the right acetabulum which distributes the load all around the joint surface.

Besnault *et al.* [1998] developed an automatic procedure in order to adapt a unique reference FE mesh to different morphologies. This procedure was based on the Kriging technique and a study on pelvis geometry with determination of characteristic dimensions. With this procedure, the reference FE mesh was transformed into the morphology of each pelvis bone tested while thickness and its repartition were kept unchanged between different pelvises. The mass density was adjusted in order to get the mass of the simulated pelvis bone. The model was loaded by imposing the displacement of the ball, according to experiment recording. The reaction force of the pelvis bone was compared to the experimental measurement to determine the appropriate parameters.

Figure 3 shows an example of simulation for the test 9707.

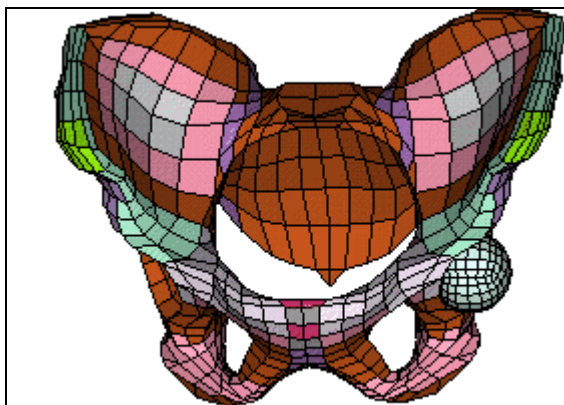


Figure 3a. Simulation of test 9707 : 0 ms.

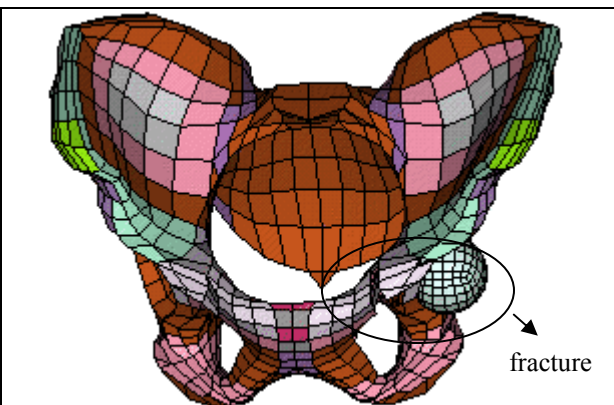


Figure 3b. Simulation of test 9707 : 5 ms.

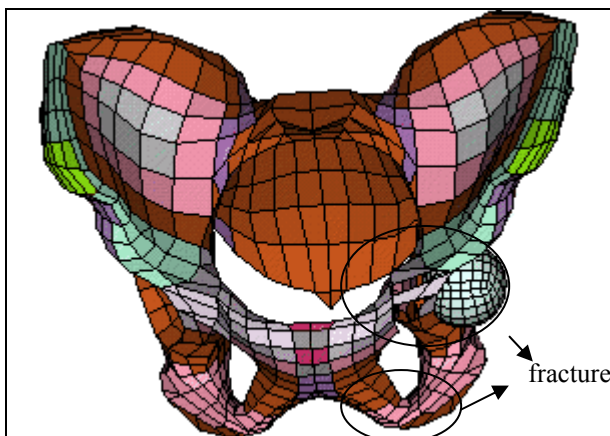


Figure 3c. Simulation of test 9707 : 8 ms.

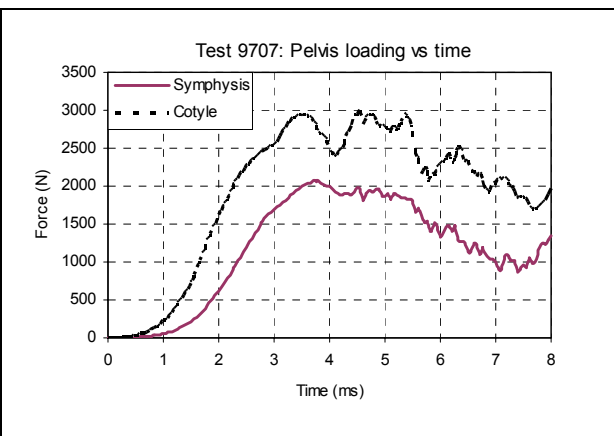


Figure 3d. Cotyle force and symphysis force.

Table 2 summarizes material laws determined by simulating the isolated pelvis tests. Figures in the appendix give a comparison of model responses

with experiments. Table 3 summarizes injury outcome of experiments and injury reproduced by models.

Table 2.
Mechanical parameters determined for 11 isolated pelvis bone tested

Tests	E	σ_y	σ_{max}	ϵ_p
9603	11500	57.5	87.5	3%
9604	10000	100	100	3%
9605	50000	250	280	3%
9607	20000	100	130	3%
9701	15000	75	105	3%
9702	29000	145	175	3%
9703	3000	60	60	3%
9704	25000	125	150	0.5%
9705	12000	60	90	3%
9706	30000	150	180	3%
9707	22000	110	140	3%

Table 3.
Injury outcome of experiments and simulation results

	9603	9604	9605	9607
Experiment	Bone fracture	Bone fracture	No bone fracture	Bone fracture
Simulation	Bone fracture	Bone fracture	No bone fracture	Bone fracture
	9701	9702	9703	9704
Experiment	Bone fracture	No bone fracture	Bone fracture	Bone fracture
Simulation	Bone fracture	Bone fracture	Bone fracture	Bone fracture
	9705	9706	9607	
Experiment	Bone fracture	Bone fracture	Bone fracture	
Simulation	Bone fracture	Bone fracture	Bone fracture	

For a total of eleven tests, nine have been successfully simulated with material laws where:

$$\sigma_y = 0.005 \cdot E$$

$$\sigma_u - \sigma_y = 30 \text{ MPa}$$

$$\epsilon_p = 3\%$$

Material laws determined for tests N9604 and N9703 do not satisfy the relation $\sigma_y = 0.005 \cdot E$ while one test urged an ϵ_p of 0.5%.

Globally we can see that a damageable elastoplastic law with $\sigma_y = 0.005 \cdot E$, $\sigma_u - \sigma_y = 30 \text{ MPa}$, $\epsilon_p = 3\%$ allows representing the majority of pelvis bone tested by Guillemot et al.

Establishing relationship between material law and injury risk

Guillemot tests on isolated pelvis bone and its simulation have permitted to have a first estimation of different mechanical parameters. But alone, they

do not allow establishing relationship between material laws and probability of pelvic fracture occurrence. One way to achieve this objective is to simulate impactor tests on cadavers. In fact data from this type of tests are the most abundant and cover largely configurations with and without pelvis injuries. Furthermore the test set-up is easy to be duplicated by model, thus avoiding confusion due to error on boundary conditions. Following is a brief description of the most commonly used impactor test configurations on pelvis.

Césari tests – Césari *et al.* [1980, 1982] performed 55 tests on pelvis, using 22 fresh human cadavers. The impactor is 17.3 kg and the impacting system is the portion of a sphere ($r = 600 \text{ mm}$, $R = 175 \text{ mm}$). The impact speed was increased progressively in order to reach the pelvic fracture at a level as close as possible to the tolerance. However 5 cadavers were fractured at the first impact. Subjects were seated in a low friction surface. The impactor was guided in its impact direction.

Bouquet tests – Bouquet *et al.* [1994, 1998] performed 20 tests on pelvis, using 10 fresh human cadavers. The impactor was 23.4 kg and the impacting system was a flat, rectangular rigid plate ($200 \times 100 \text{ mm}^2$). Each cadaver was impacted firstly at a low speed (around 3.5 m/s) and then at a higher speed (around 6.7 m/s). The subjects were seated in a low friction surface. The impactor was guided in its impact direction.

Iso-energy tests – Bouquet *et al.* [1998] performed 11 new cadaver tests on pelvis, using 11 fresh human cadavers. But this time the impactor was a flat, rectangular rigid plate of a larger size ($200 \times 200 \text{ mm}^2$). Furthermore the impactor mass (12 and 16 kg) and impact speed (from 9.5 to 13.7 m/s) were designed in such a way to know the respective role of impactor mass and its velocity for a given level of energy.

Viano tests – Viano [1989] performed 14 cadaver tests on pelvis, using 8 unembalmed human cadavers. Impact was realized by a 150 mm flat 23.4 kg pendulum. Impact speeds varied from 3.98 to 10.1 m/s. The cadaver was suspended upright with hands and arms over head.

Injury risk curve in terms of impact force were drawn (see Figure 4) respectively for Césari tests and Bouquet tests. No injury curve was drawn for Viano tests since the number of cases with injury (only 2 cases) are too low. Iso-energy tests contain only 2 cases without injury, too low also to calculate injury risk curve. It can be observed that Césari tests and Bouquet tests lead to very close risk curve.

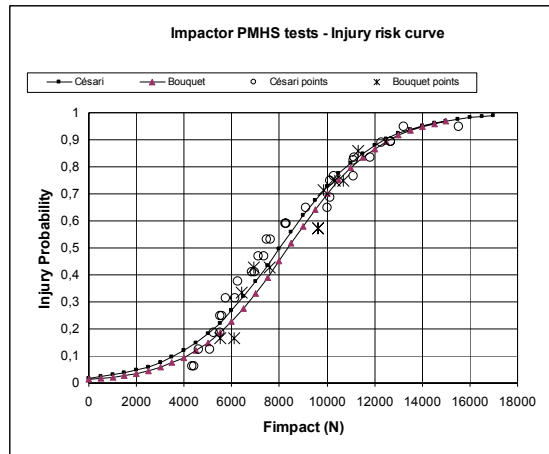


Figure 4. Risk curves on pelvis in terms of impact force according to Césari tests and Bouquet tests.

From these data we can see that:

- 20% of the subjects are exposed to injuries under an impact of 5250 N.
- 50% of the subjects are exposed to injuries under an impact of 8000 N
- 80% of the subjects are exposed to injury under an impact force of 10800.

By simulating Césari tests and Bouquet tests, material laws corresponding respectively to these three levels of tolerance can be determined.

In order to simulate these impactor tests, a human body model was used [Lizée *et al.* 1998]. The pelvis model developed above was integrated to this whole body model. Material laws for pelvis bone were expected to be determined in the variation range of laws given by simulations of Guillemot tests. Figure 5 shows the model set-up for simulation of Césari test configuration.

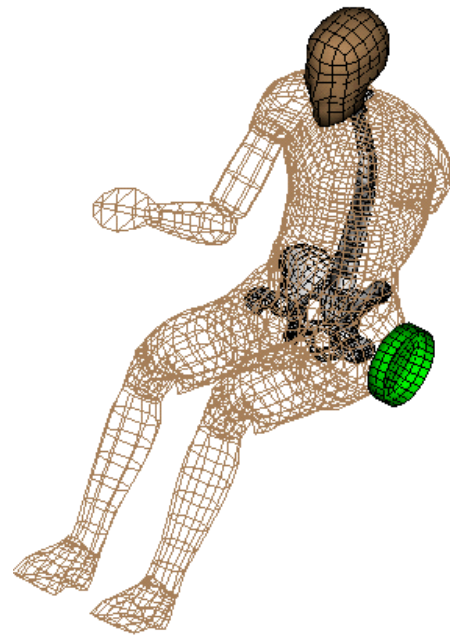


Figure 5. Model set-up for Césari test configuration.

Figure 6 shows results of simulations corresponding to these three levels of loading on pelvis. For each loading level two simulations are presented, one leading to pelvis bone fracture and another not. Table 4 shows material laws used for these simulations. For example no bone fracture was observed with material law Medium-U for an pelvis loading of 8000 N. With a material law slightly less resistant (Medium-L) bone fracture was observed. So we can fix a threshold material law situated between laws Medium-U and Medium-L to represent population with medium resistance. In same way threshold material laws can be defined to represent more fragile and more resistant groups of population. Table 5 gives threshold material laws representing these three groups of population.

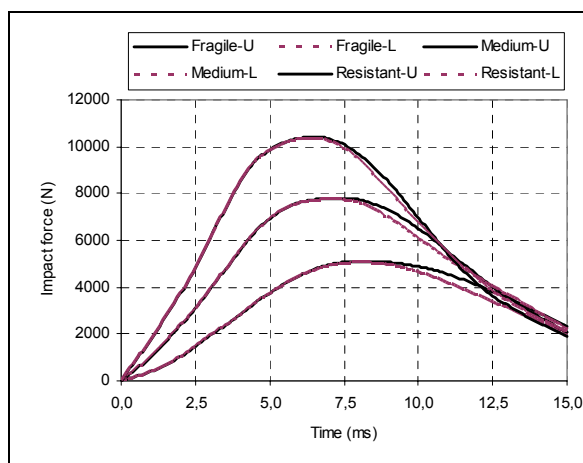


Figure 6a. Impact force time history.

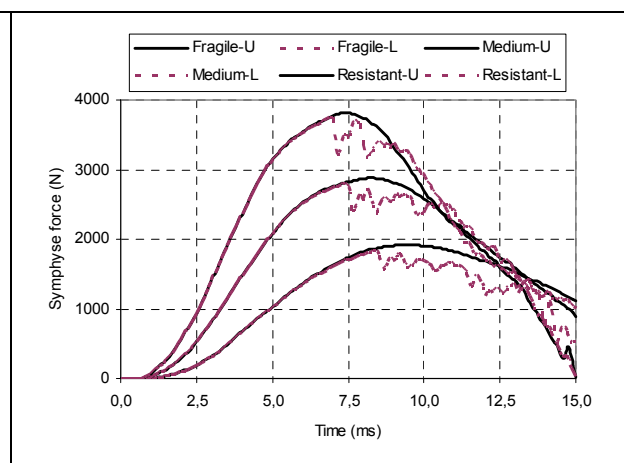


Figure 6b. Symphysis force time history.

Table 4.
Material laws used to identify threshold for each population group (fragile, medium and resistant)

	E	σ_y	σ_{max}	ϵ_p	Fracture
Fragile-L	18000	90	120	3%	Y
Fragile-U	19600	98	128	3%	N
Medium-L	29000	145	175	3%	Y
Medium-U	30000	150	180	3%	N
Resistant-L	40000	200	230	3%	Y
Resistant-U	41000	205	235	3%	N

Table 5.
Material laws representing three population groups (fragile, medium and resistant)

	E	σ_y	σ_{max}	ϵ_p
Fragile	19000	95	125	3%
Medium	29500	147	177	3%
Resistant	40500	202	232	3%

DISCUSSION

It is important to evaluate the relevance of pelvis model to predict forces applied to the pelvis at different impact energy levels. To do this it is essential to select adequate experimental data. One factor to consider is the mass of impacted subject due to its importance for dynamic test, especially when impact velocity is high. Model developed in this study representing a 50th percentile male, it would be misleading to compare it with data affected by the use of cadavers too different from a 50th percentile male in terms of body mass. No

evidence showing relevance of existing techniques of normalization, it is preferable to use raw data while eliminating tests performed with subjects too light or too heavy (i.e. not included between 77±10 kg). Age is another influent factor since it is correlated globally with the mechanical resistance of cadaver.

Figure 7 shows characteristics of cadavers used in the experiments listed in the precedent sections.

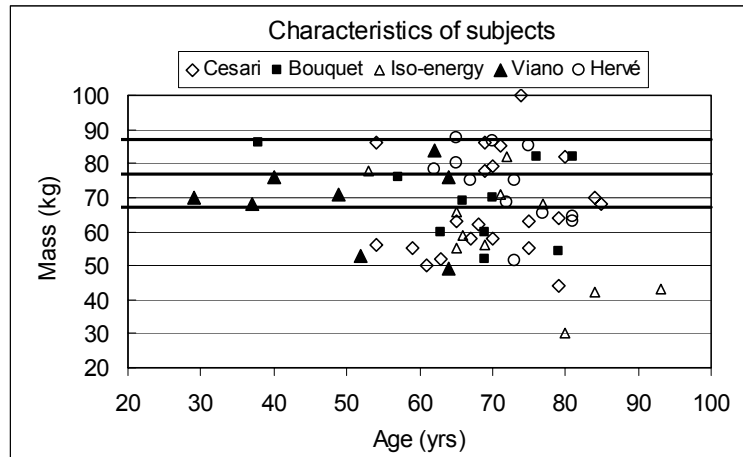


Figure 7. Characteristics of subjects used in different impactor tests.

It can be observed that:

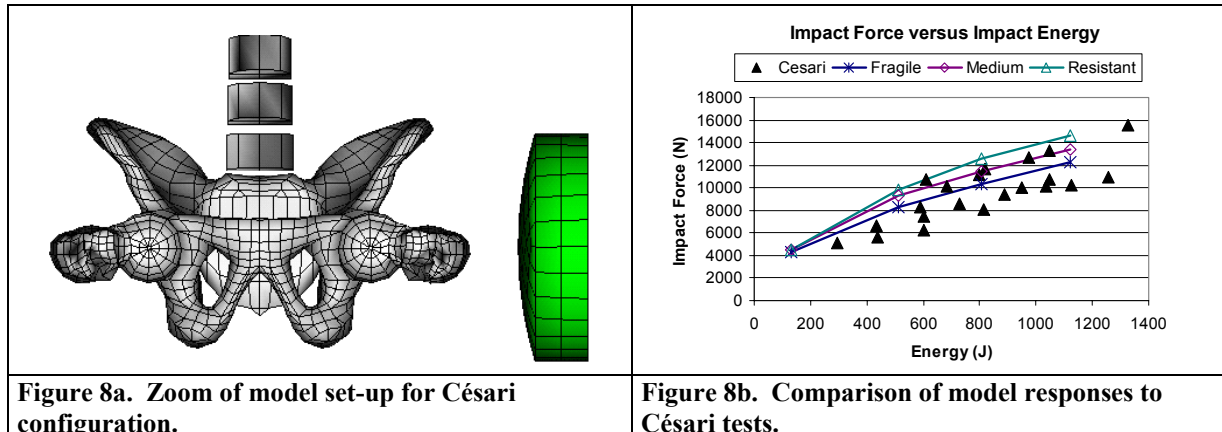
- Among 20 cadavers used in Césari tests, only 7 had a mass between 77kg±10kg. They were only 4 over 11 for iso-energy tests. Subjects used in Bouquet tests and Viano tests were generally closer to the mass of the 50th percentile male.
- Most of subjects tested are old, concentrated between 60 and 80 years.

In the following section, the model responses in terms of pelvis loading and bone fracture are compared to experiments. Only tests performed with subjects with mass between 77kg±10kg were used.

Césari tests - Figure 8 compares impact force between model and experiments. The three material laws used correspond to respectively a fragile bone,

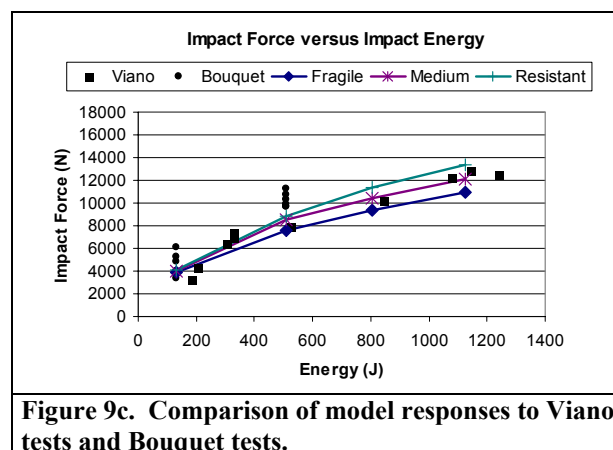
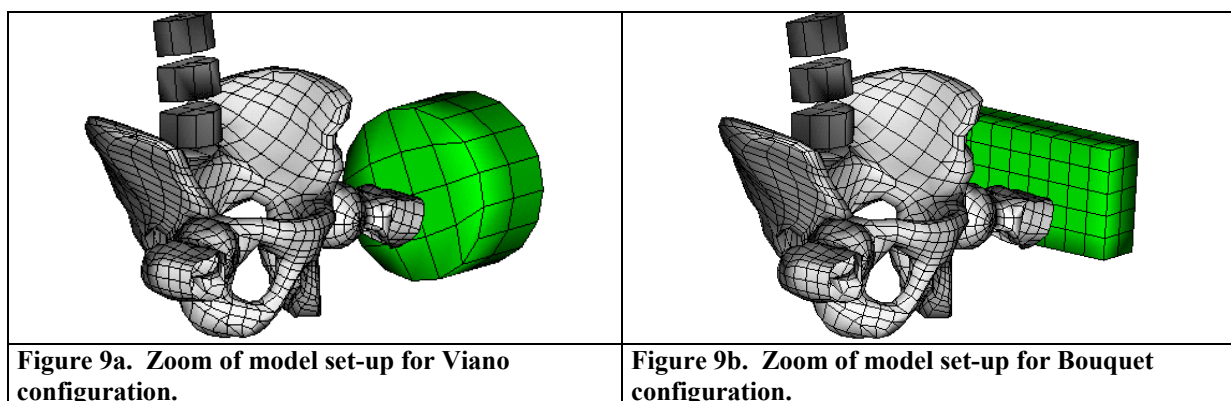
a medium bone and a resistant bone. One can observe that model responses are situated on the

upper limit of impact force distribution given by experiments.



Bouquet tests and Viano tests - Since all these tests used an impactor of 23,4 kg, they were combined and examined together. Figure 9 compares impact force between model and experiments. The three material laws used correspond to respectively a fragile bone, a medium bone and a resistant bone. One can observe that

pelvis model matches well with Viano tests. However Viano tests showed no injuries for all impact energy while pelvis model fractured even with resistant material law at an impact energy of 1150 J. With respect to Bouquet tests, pelvis model responses are situated in the lower limit of experimental data.



Iso-energy tests - Figure 10 compares impact force between model and experiments. The three material

laws used correspond to respectively a fragile bone, a medium bone and a resistant bone.

One can see that pelvis model shows good responses for high energy. In terms of injury

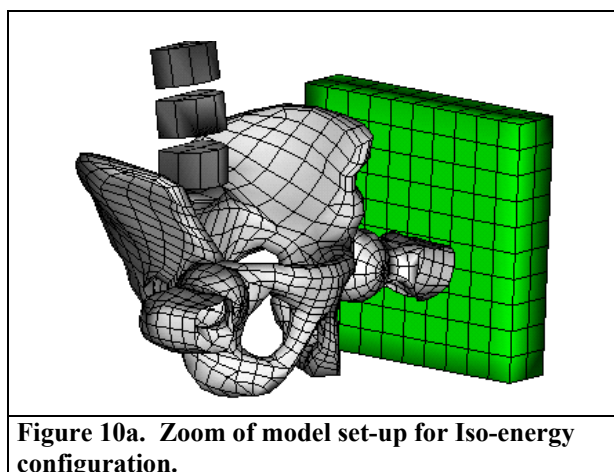


Figure 10a. Zoom of model set-up for Iso-energy configuration.

Elements presented above show that pelvis model is globally relevant with respect to experiments in terms of pelvis loading prediction, this for a large range of impact energy from 130 to 1150 Joules.

Many experiments on pelvis were also performed under sled configurations. Simulation of these tests is much more difficult than that of impactor tests since test set-up is generally more complex and there are more risks of confusion due to error on boundary conditions. Before undertaking simulations of this type of experiments it is necessary to identify tests with reasonable clarity on boundary conditions and adequate measurements allowing comparison with results of simulations.

CONCLUSIONS

Eleven experiments on isolated pelvis bone under lateral impact have been simulated individually by taking into account proper geometry of each pelvis. These simulations showed that by keeping a constant pelvis cortical bone thickness distribution for all pelvis bones tested and by using a damageable elastoplastic material law, the behavior of these eleven pelvis bones in terms of stiffness and bone fracture can be reproduced by defining an equivalent elastic modulus, a yielding stress and a damage plastic strain. Based on impactor tests on cadavers, a generic pelvis model for a 50th male was defined. Three material laws were associated with this model, representing respectively a fragile, a medium and a resistant pelvis bone. The mechanical behavior of this pelvis model was compared to experimental data of impactor tests on cadaver pelvises. It showed that pelvis model is globally relevant with respect to experiments in terms of pelvis loading prediction,

outcome, pelvis model fractured as its experimental counterpart.

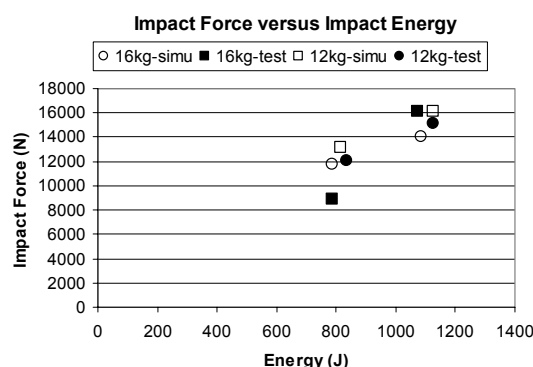


Figure 10b. Comparison of model responses to Iso-energy tests.

this for a large range of impact energy from 130 to 1150 Joules.

REFERENCES

1. Besnault B., Guillemot H., Robin S., Lavaste F., Le Coz J.Y. (1998) A parametric finite element model of the human pelvis. 42nd Stapp Car Crash Conference. 1998.
2. Bouquet R., Ramet M. (1994) Thoracic and pelvis human responses to impact. Proceeding of ESV1994 Munich.
3. Bouquet R., Ramet M., Bermond F., Caire Y., Talantikite Y., Robin S. and Voiglio E. (1998) Pelvis human responses to lateral impact. Proceeding of ESV1998.
4. Burstein AH et al. (1976) Aging of bone tissue : mechanical properties. J Bone Joint Surg 58(A):82.
5. Césari D. and Ramet M. (1982) Pelvic tolerance and protection criteria in side impact. Proceeding of the 26th Stapp Car Crash Conference, Society of Automotive Engineers, Warrendale, PA.
6. Chamouard F., Bouchard L., Brun-Cassan F., Le Coz JY., Guillon F (1993) Simulation of the human behavior in lateral impact. Proceeding of IRCOB 1993, Eindhoven, the Netherlands.
7. Dalstra M., Huiskes R., Odgaard A., Van Erning L.(1993) Mechanical and textural properties of the pelvic trabecular bone. Journal of Biomechanics. 1993 ; 26(4-5). 523-535.
8. Dalstra M. and Huiskes, R. (1995) Load transfer across the pelvic bone, Journal of biomechanics, 28(6), pp. 715-724, 1995
9. Dalstra M., Huiskes, R. and Van Erning, L. (1995) Development and validation of a three dimensional finite element model of the pelvic bone, Journal of biomechanical engineering, 117, pp. 272-278, 1995
10. Dawson J.M., Khmelniker B.V., McAndrew M.P. (1999) Analysis of the structural behavior of

the pelvis during lateral impact using finite element method. Accident Analysis and Prevention. 1999;(31). 109-119.

11. Fung Y.C., Biomechanics - Mechanical properties of living tissues. 1965 ; Bone and cartilage. Springer-Verlag.

12. Goel V.K., Valliapan S., Svensson N.L.(1978) Stresses in the normal pelvis. Comp. Biol. Med. 1978 ; 8 91-104.

13. Guillemot H. (1992) Etude du comportement statique du bassin osseux soumis à des efforts latéraux, Mémoire DEA, ENSAM de Paris.

14. Guillemot H., Skalli, W., Lavaste, F., Got, C. and Le Coz, J.Y. (1995) Static behavior of the pelvic bone under side loading conditions, PLEI Conference, Washington, 1995

15. Guillemot H., Besnault, B., Robin, S., Got, C., Le Coz, J.Y., Lavaste, F. and Lassau, J.P. (1997) Pelvic injuries in side impact collisions : an accidental analysis and dynamic tests on isolated pelvic bones, 41th Stapp Car Crash Conference, 1997

16. Krige D.G. : A statistical approach to some basic mine valuation problems on the Witwatersrand, J. Chem. Metall. Min. Soc. S. Afr., 52, pp. 119-139

17. Kuhn J.L., Goldstein S.A., Choi K., London M., Feldkamp L.A. and Matthews L.S. (1989) Comparison of the trabecular and cortical tissue moduli from iliac crests, Journal of orthopaedic research, 7(6), pp. 876-884, 1989

18. Lizee E., Robin S., Song E., Bertholon N., Le Coz J.Y., Besnault B., Lavaste F. (1998) Development of a 3D finite element model of the

human body. 42nd Stapp Car Crash Conference. 1998 ; 115 p.

19. Mak A.F. (1986) The apparent visco-elastic behavior of articular cartilage - The contributions from the intrinsic matrix visco-elasticity and interstitial fluid flows. Journal of biomechanical engineering. 1986.

20. Oonishi H., Isha H., Hasegawa T. (1983) Mechanical analysis of the human pelvis and its application to the artificial hip joint-by means of the three dimensional finite element method. Journal of Biomechanics. 1983 ; 16(6). 427-444.

21. Plummer J.W., Bidez M.W., Alonso J. (1996) Parametric Finite Element Studies of the Human Pelvis : the Influence of Load Magnitude and Duration on Pelvic Tolerance during Side Impact. STAPP 96. 1996 ; 17 p.

22. Renaudin F., Guillemot H., Lavaste, F. and Skalli, W. (1993) A 3D finite element model of pelvis in side impact, 37th Stapp Car Crash Conference, 1993

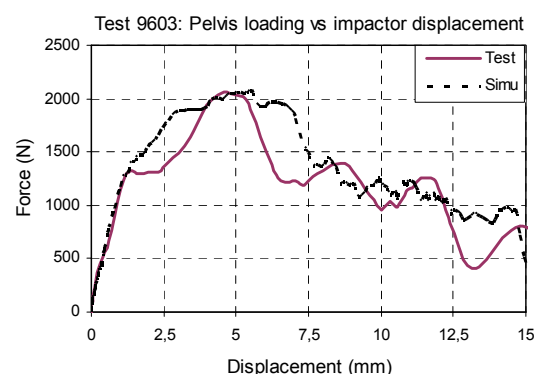
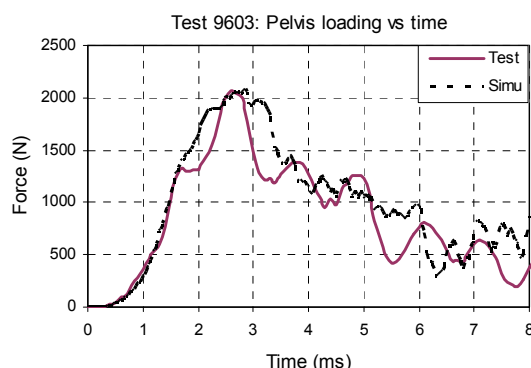
23. Reynolds, H., Snow, C. and Young, J. (1981) Spatial geometry of the human pelvis. Memorandum report No AAC-119-81-5

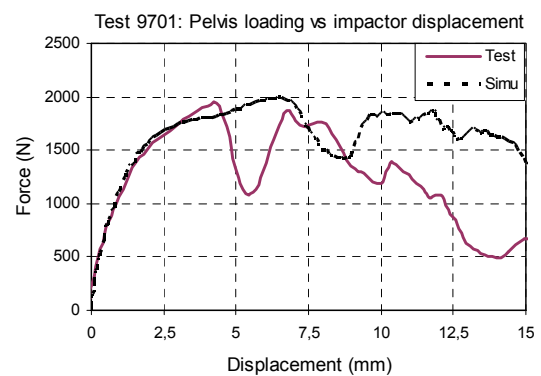
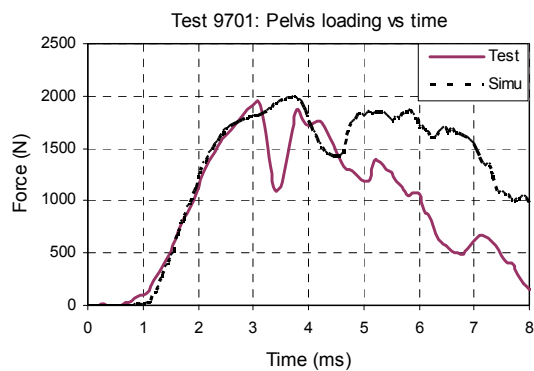
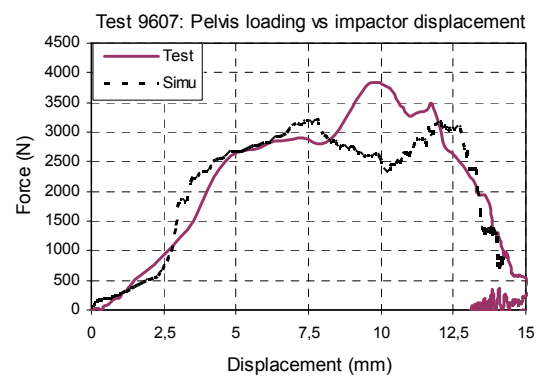
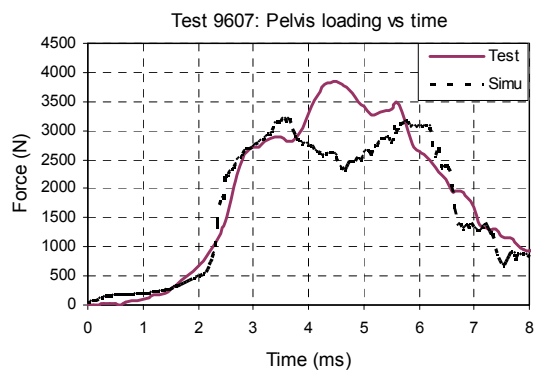
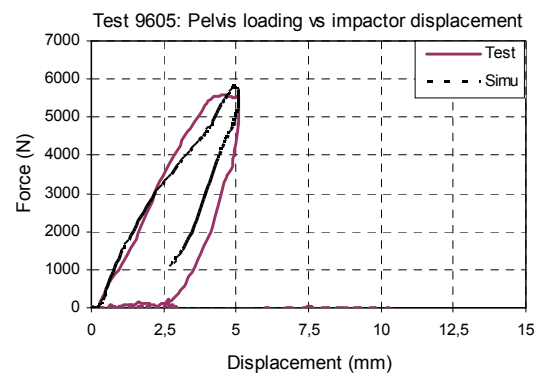
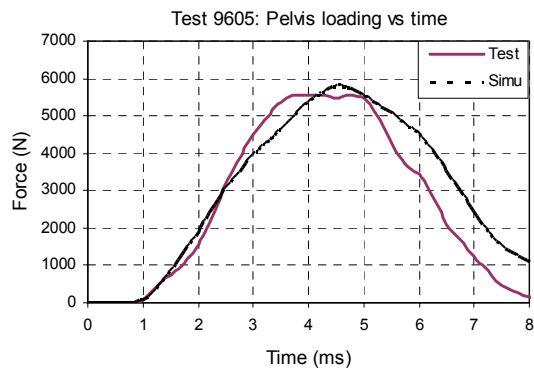
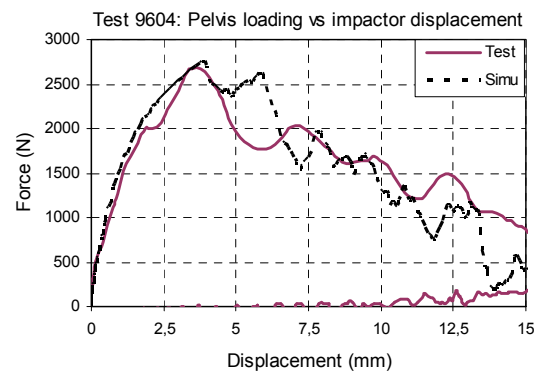
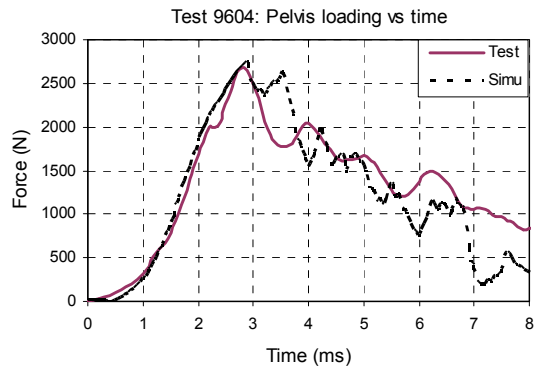
24. Viano D. (1986) Biomechanics of bone and tissue: a review of material properties and failure characteristics. Proceeding of the 30th Stapp Car Crash Conference, pp.33-63, Society of Automotive Engineers, Warrendale, PA

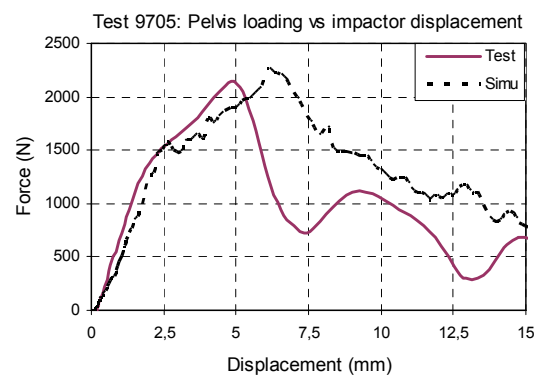
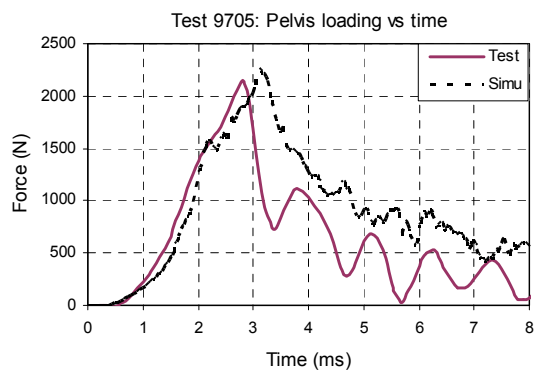
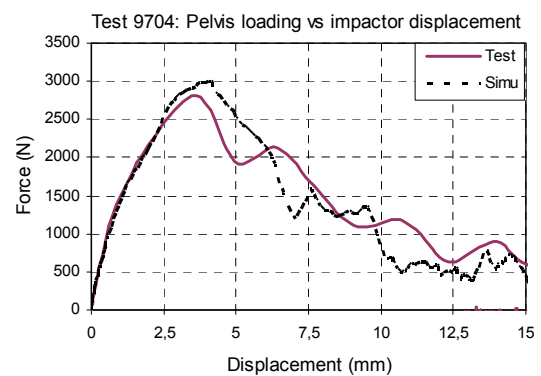
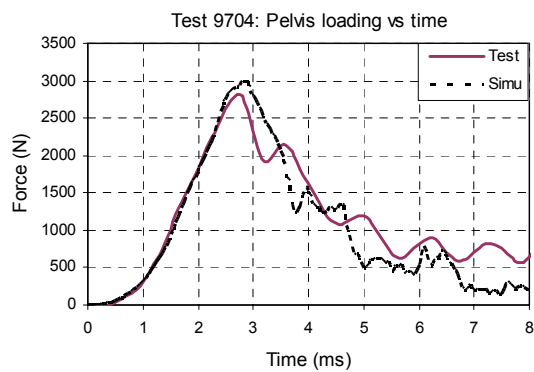
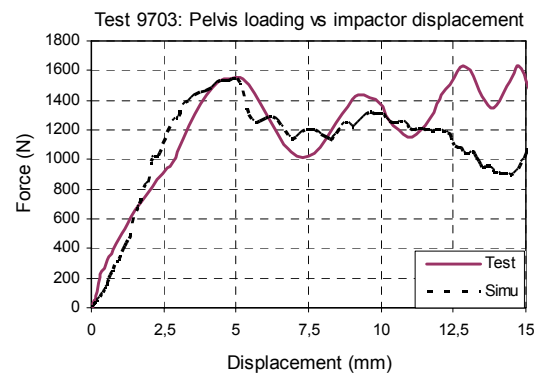
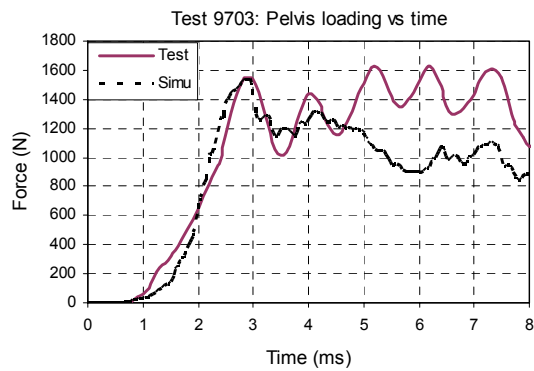
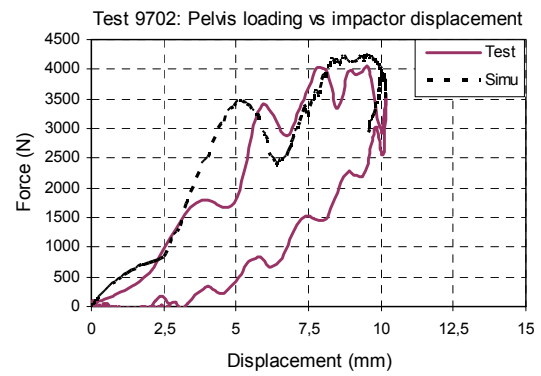
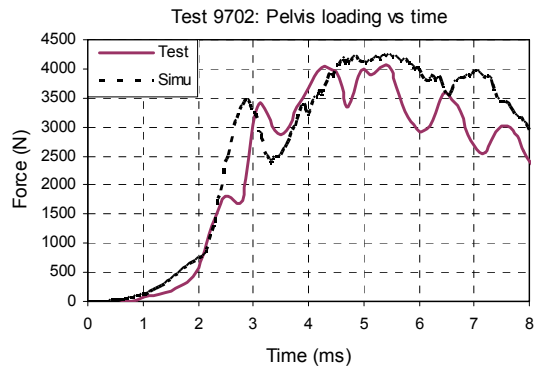
25. Viano D. (1989) Biomechanical responses and injuries in blunt lateral impact. Proceeding of the 33th Stapp Car Crash Conference, pp.113-141, Society of Automotive Engineers, Warrendale, P.

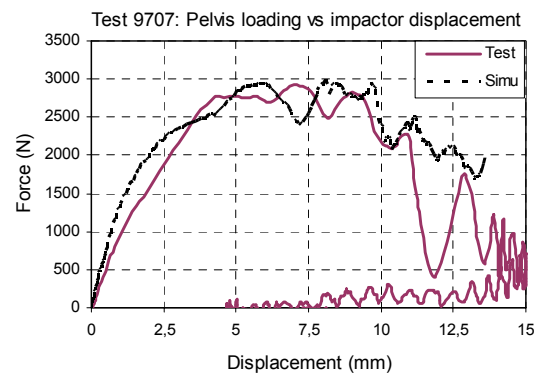
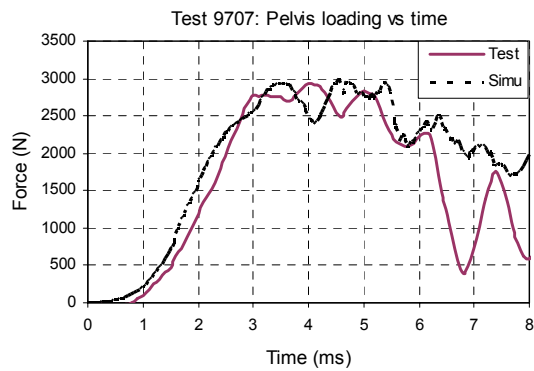
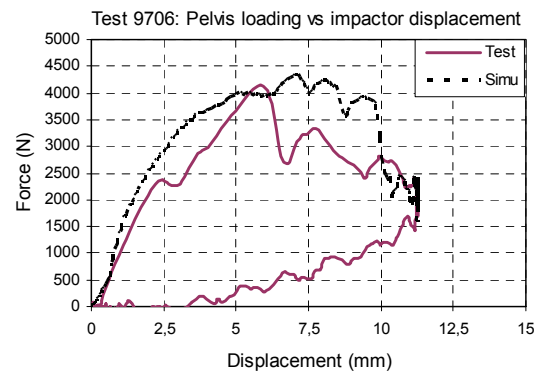
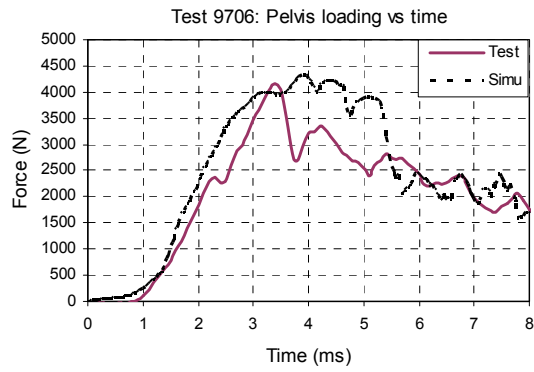
APPENDIX

Model responses compared to isolated pelvis bone tests









BIOFIDELITY EVALUATION FOR THE KNEE AND LEG OF THE POLAR PEDESTRIAN DUMMY

Yukou Takahashi

Honda R&D Americas, Inc.

United States

Yuji Kikuchi

Masayoshi Okamoto

Akihiko Akiyama

Honda R&D Co., Ltd.

Japan

Johan Ivarsson

Dipan Bose

Damien Subit

JaeHo Shin

Jeff Crandall

University of Virginia

United States

Paper Number 05-0280

ABSTRACT

Biofidelity of the Polar-II pedestrian dummy lower extremity was assessed in a series of dynamic bending tests relative to published PMHS (Post Mortem Human Subject) response corridors. Dynamic 4-point lateral bending tests of the knee joint and dynamic 3-point lateral bending tests of the leg from the original version of the Polar-II dummy were performed under identical test conditions to the published PMHS tests that simulated car-pedestrian lower limb impact at 40 km/h. Although the force-deflection and moment-deflection responses of the leg were found to be biofidelic, the knee joint test results showed that the stiffness in lateral bending needed to be increased. Based on the test results, a modified version of the knee joint was designed and fabricated with increased lateral bending stiffness to improve response biofidelity. The modified knee joint was evaluated in the dynamic 4-point lateral bending test, and the test results were compared with the same human response corridors. It was found that the moment-angle response of the modified knee joint in valgus bending was significantly closer to those of human subjects compared to the original version.

INTRODUCTION

Lower limb injuries account for a major part of non-fatal injuries to pedestrians. Ashton et al. [1] investigated 1560 pedestrians struck by the fronts of cars and light goods vehicles in England from 1972 to 1976, and found that more than 60% of pedestrians sustaining non-minor (AIS 2-3) injuries sustained lower limb injuries. Laumon et al. [2] investigated all the road crash victims in the department du Rhone,

France, from 1995, and found that approximately one out of five pedestrian victim sustained AIS2+ lower limb injuries. Stutts et al. [3] collected patient data from eight hospital emergency rooms across the U.S., and found that approximately half of the pedestrians admitted to the emergency rooms were treated for lower limb injuries. Harruff et al. [4] examined 217 fatal pedestrian accidents in Washington State from 1990 to 1995, and identified pelvic and lower limb fractures in 66 % of the cases. Jarrett et al. [5] looked at both the Pedestrian Injury Causation Study (PICS) and the Pedestrian Crash Data Study (PCDS) databases collected by the National Highway Traffic Safety Administration (NHTSA), and the body region injury distribution showed that the lower extremity represented the most frequently injured body region in both databases. Matsui et al. [6] analyzed the pedestrian accident data collected by the Institute for Traffic Accident Research and Data Analysis (ITARDA) in Japan in 1997, and concluded that lower limb injuries accounted for 40% of all severe injuries in non-fatal accidents.

A number of past studies have focused on the development of anthropomorphic test devices for pedestrian lower limbs. Those devices can be classified into two categories – impactors for subsystem tests that represent only one single lower limb of a pedestrian, and dummies for full-scale tests that represent a whole body of a pedestrian.

The European Enhanced Vehicle-safety Committee (EEVC) Working Group 17 has specified a test procedure for legform to bumper test [7]. Based on the requirement from the EEVC Working Group 17, the Transport Research Laboratory (TRL) has developed a legform impactor [8]. Although the TRL legform impactor is one of the most widely used test devices for

assessing performance of a car front with respect to pedestrian lower limb protection, the biofidelity of its knee joint response has not been directly validated. In terms of scientific background for the knee joint stiffness requirement in static lateral bending specified in the EEVC report [7], the preceding EEVC Working Group 10 Report stated that the knee joint stiffness from the specification corridor seemed much stiffer relative to the PMHS test results by Cesari and his co-workers [9]. However, it was believed that the lower impact speed relative to the specification at which the PMHS tests were run as well as the lack of muscle force in the PMHS tests justified the higher stiffness in the specification corridor. Matsui et al. [10] validated the biofidelity of the TRL legform impactor against the impact force time history corridors developed based on the PMHS studies by Kajzer et al. [11][12]. They also used another legform impactor developed by the Japan Automobile Research Institute (JARI), and the JARI impactor was tested with two different pairs of steel knee bars in bending (one with standard 450 Nm maximum moment and the other with 100 Nm maximum moment). The impact force time history comparison showed that the 4.5 times difference in knee joint stiffness did not make a significant difference in impact force time history. This suggests that the impact force time histories obtained from Kajzer et al. are primarily determined by the inertial effects and stiffness of the impact surface rather than the stiffness of the knee joint. In order to validate the bending response of a knee joint in impact effectively, the knee joint response of a test device needed to be validated against test results using isolated PMHS knees. More recently, Konosu et al. [13][14] developed a new legform impactor called Flex-PLI that features flexible thigh and leg as well as four separate knee ligaments. They validated the dynamic response of the thigh, leg, and knee components separately by running similar tests to the PMHS component tests performed by Kerrigan et al. [15]-[17] and Bose et al. [18]. The response of each component was compared with the response corridors developed based on the PMHS tests by Ivarsson et al. [19]. Using the same test set-ups as those employed in the PMHS tests, it was confirmed that the Flex-PLI components had a reasonable level of biofidelity. It was also found from the results of their tests and other studies that the knee joint of the TRL legform was much stiffer relative to the human knee response tested at the same loading rate [13][14][19][20].

Although Konosu et al. has succeeded in developing a legform impactor for which biofidelity was validated at the component level, some of the past studies have found that the lack of upper body weight can lead to non-biofidelic responses of an impactor, particularly when a bumper hits the impactor above the

knee joint level [21][22]. Thus, there is still a need for test tools that incorporate the upper body weight such as a full body pedestrian dummy. In addition, it is difficult to obtain an overall picture of the whole body kinematics using subsystem impactors, and thus a full-scale dummy is needed to investigate the effect of changes to vehicle front components on the whole body kinematics [23]. Based on this understanding, Honda R&D Co., Ltd. has developed a full-scale pedestrian dummy in collaboration with GESAC Inc. and JARI [23]-[26]. The primary goal of the development was to match the head trajectory and resultant velocity with the PMHS corridors developed based on Ishikawa et al. [27] at impact speeds of 32 km/h and 40 km/h. The latest version of the dummy, known as Polar-II, incorporates essential anthropomorphic features of a knee joint as well as a deformable tibia not only for more biofidelic head kinematics but for the biofidelity of the lower limb itself [26]. The flexible tibia was validated in quasi-static and dynamic 3-point tests. However, for the knee joint validation, Artis et al. [26] used the impact test results from Kajzer et al. [28][29], where a very similar test set-up was employed to that used for their older test series at lower impact speeds [11][12]. As noted above, it was anticipated that the contribution from the knee joint stiffness to the impact force time history was relatively small compared to the contribution from inertial properties and the stiffness of the impact surface. In order to ensure biofidelity of the knee joint bending response, some component tests using an isolated knee joint need to be performed and the results need to be validated against recently performed PMHS component tests.

In this study, the knee and leg components were taken from the Polar-II pedestrian dummy and were tested in 4-point lateral bending and 3-point lateral bending, respectively. For both tests, exactly the same test conditions were employed as those used in the PMHS component tests recently performed by Kerrigan et al. [15]-[17] and Bose et al. [18]. The test results were compared with the PMHS response corridors developed by Ivarsson et al. [19] based on the results from Kerrigan et al. [15]-[17] and Bose et al. [18]. Since the original knee joint was found to be less stiff relative to the PMHS response corridor, a modified version of the knee joint was designed and fabricated, and was subjected to the same 4-point lateral bending test.

METHODOLOGY

A series of component tests were performed at the University of Virginia Center for Applied Biomechanics using the knee joint and leg taken from the Polar-II pedestrian dummy. The tests employed the

same set-ups as those used in the PMHS tests performed by Kerrigan et al. [15]-[17] and Bose et al. [18]. Since the knee joint originally designed for the Polar-II dummy was found to be less stiff relative to the PMHS response corridors from Ivarsson et al. [19], a modified version of the knee joint with increased bending stiffness was designed, fabricated, and tested under the same test conditions.

Test Specimens

Knee Joint

The original version of the Polar-II dummy knee joint (denoted as 'original knee' hereafter) consists of the distal femur with femoral condyles and four casings for ligament springs, the tibial plateau with meniscus, four steel wire cables representing knee ligaments, and four springs providing stiffness that represents the tensile properties of the four major knee ligaments (anterior and posterior cruciate ligaments, medial and lateral collateral ligaments). The geometry of the femoral condyles and tibial plateau was based on a surgical human knee model, and was simplified with left and right symmetry. The meniscus was made thicker than the human meniscus to provide durability during impact testing. The ligament path and attachment points were also based on the surgical human knee model, and the two collateral ligaments were made symmetric with the same stiffness for simplicity. The two cruciate ligaments have the same stiffness to each other but different from that of the collateral ligaments. Figure 1 shows the anterior and lateral view of the left original knee assembly. The disassembled state of the left original knee is illustrated in Figure 2. Design details of the original knee were provided by Artis et al. [26].

The test results for the original knee in 4-point bending showed that the stiffness of the knee joint was not sufficient relative to the human knees. In order to provide more biofidelic bending response of the knee joint, it was decided to design and fabricate a modified version of the Polar-II dummy knee joint (denoted as 'modified knee' hereafter). The anterior and lateral views of the right modified knee assembly and the disassembled state of the right modified knee are shown in Figure 3 and 4, respectively. The basic structure and geometry are exactly the same as those of the original knee except that the diameter of the knee ligament springs were increased and the length of the springs were made shorter to provide stiffer bending response than that of the original knee. Aluminum spacers were placed below the springs in order to accommodate the shorter springs in the spring housings.

Leg

The tibia shaft consists of a nylon/kevlar rod surrounded by a hard urethane hollow rod. The

proximal and distal ends of the tibia shaft were reinforced by the inner and outer steel rings that were bonded to the tibia to provide an interface with the upper and lower tibia load cell [26]. The stiffness and damping characteristics of the skin and flesh surrounding the tibia shaft were determined from the computer simulations performed by Huang et al. [25]. For the flesh, Confor foam is used for appropriate damping. The shape of the tibia shaft has been reported as tapered at the proximal and distal ends in previous papers [23][26]. However, it was decided after a number of full-scale tests to further modify the shape of the tibia shaft in such a way that the cross section of the shaft along its long axis is uniform in order to provide increased durability. Figure 5 illustrates the tibia shaft and surrounding flesh/skin of the Polar-II

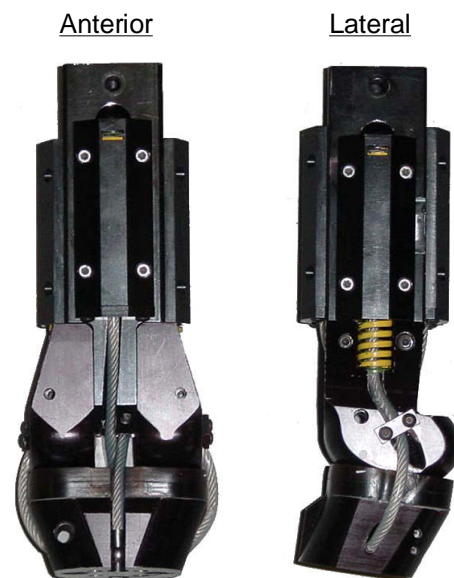


Figure 1. Anterior and lateral view of original knee joint (left knee).

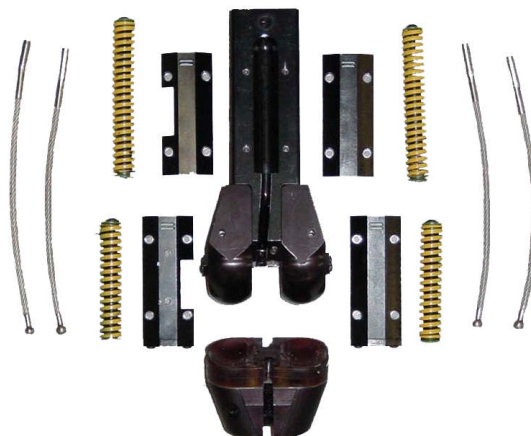


Figure 2. Disassembled original knee joint (left knee).

dummy tested in this study.

Test Conditions

The original and modified versions of the knee joint from the Polar-II pedestrian dummy were subjected to valgus bending with the 4-point bending test set-up used by Bose et al. [18] for their PMHS tests with isolated knee joints. The leg (tibia shaft with surrounding flesh/skin) from the Polar-II dummy was tested in 3-point bending with the test configuration described in Kerrigan et al. [15]-[17].

Knee Joint Test

The 4-point knee bending test configuration used in this study is illustrated in Figure 6. The knee joint was attached to cylindrical aluminum hollow shafts through aluminum adaptors. The aluminum shafts were attached to support pillars through frictionless pin joints that only allow varus-valgus bending of the knee

joint. The support pillar on the tibia side of the knee joint was rigidly fixed to the ground, while the pillar on the femur side was fixed to the ground through a linear bearing that allows translation in the superior-inferior direction of the knee joint in order to achieve simply supported boundary conditions. An impactor fork with two prongs was used to load the aluminum shafts to provide a 4-point bending test configuration. The fork was attached to the actuator of a displacement-controlled servo-hydraulic test machine (Instron 8874) through a frictionless pin joint. The contact surfaces between the prongs of the fork and the aluminum shafts were greased to minimize friction. The knee joint was oriented in such a way that it was subjected to valgus bending, and the initial orientation of the knee joint was set at zero degrees of the flexion-extension, varus-valgus, and axial rotation angles.

The actuator of the test machine was instrumented with a load cell and a displacement transducer to measure applied load and displacement. Three-axis load cells were used to measure reaction forces in the support pillars. A six-axis load cell was mounted between the aluminum shaft and the adaptor on the femur side of the knee joint. A triaxial accelerometer was mounted on the load cell to measure the accelerations necessary for the inertial compensation technique used for estimating the knee joint moment. Magneto-hydrodynamic (MHD) angular rate sensors were mounted on both sides of the knee joint to obtain knee bending angle time histories by time-integrating the MHD signals. A still image of a typical 4-point knee joint bending test configuration is presented in Figure 7.

Two quasi-static and three dynamic tests were run for each of the knee joints tested (original and modified

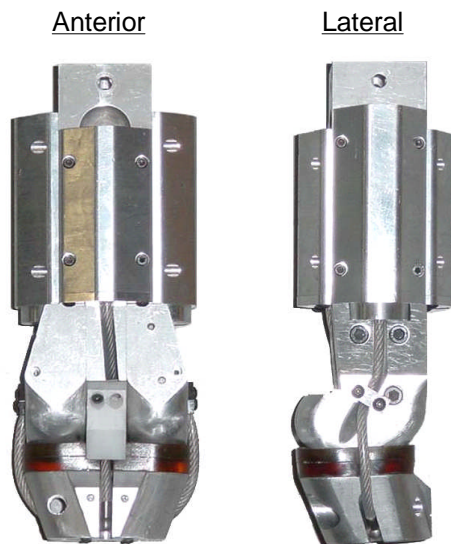


Figure 3. Anterior and lateral view of modified knee joint (right knee).

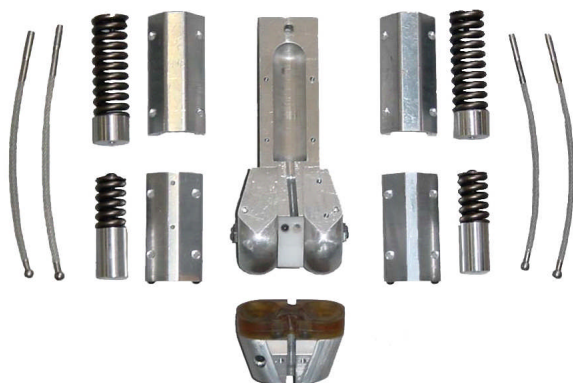


Figure 4. Disassembled modified knee joint (right knee).



Figure 5. Tibia shaft and leg flesh/skin.

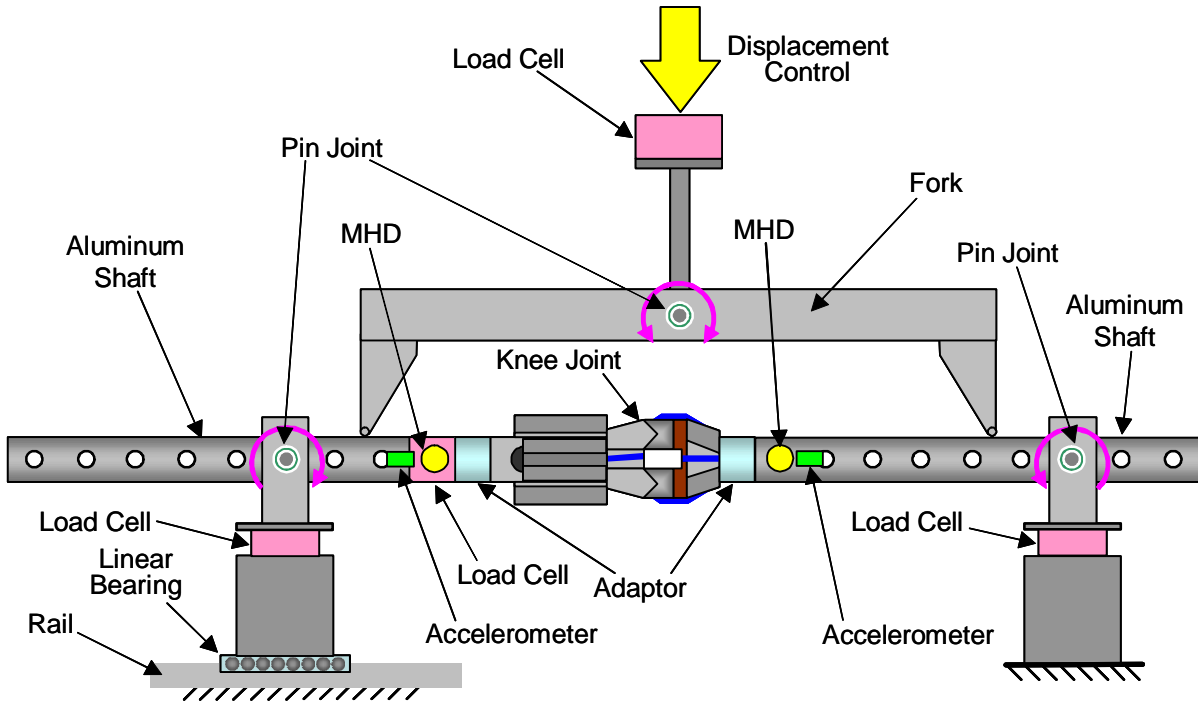


Figure 6. Schematic diagram of 4-point knee bending test configuration.

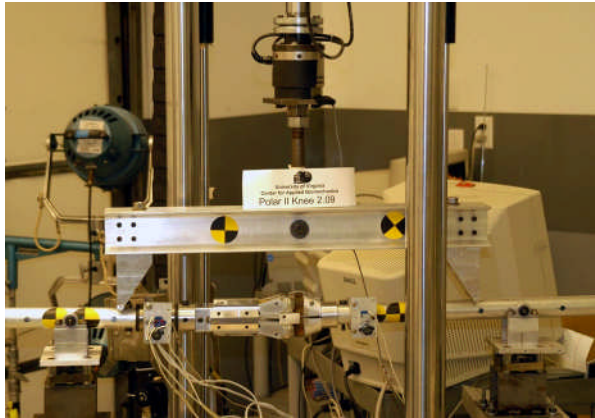


Figure 7. Typical 4-point knee bending test set-up.

knees). Bose et al. [18] investigated previous studies that provided knee bending angle time histories using PMHS lower limbs or legform impactors and found that the bending rate was approximately 1.0 degrees/ms in impacts at 40 km/h. Based on this observation, they decided to use the rate of 1.0 degrees/ms in their dynamic bending tests of isolated PMHS knees. In this study, the same knee bending rate was used in the dynamic tests in order to enable direct comparison with the PMHS test results. The target displacement rate was then determined using a simple geometric analysis. The knee bending rate for the quasi-static tests was approximately 1.0 degrees/s. The maximum knee bending angle was set at 20 degrees for the quasi-static tests and 15 degrees for the dynamic tests in order to

enable comparisons of the test results with the PMHS corridor by Ivarsson et al. [19] up to the maximum bending angle of the average PMHS response.

Leg Test

A schematic of the 3-point leg bending test configuration is shown in Figure 8. Aluminum cylindrical adaptors were rigidly attached to both ends of the deformable tibia shaft. These adaptors were mounted on aluminum disks that were in turn rigidly attached to half-cylindrical solid aluminum rollers. The diameter of the rollers was exactly the same as that of the rollers used in the PMHS tests performed by Kerrigan et al. [15]-[17]. The rollers were placed on the support plates, and the contact surfaces between the rollers and support plates were greased to minimize friction at the contact points. The same test machine as that used for the knee joint test (Instron 8874) was used to load the leg specimen in the lateromedial direction. A rigid impactor that loaded the leg specimen at mid-span had a circular tip and was attached to the actuator of the test machine. The location of the mid-span loading point relative to the tibia shaft was determined in such a way that the point corresponded to the midpoint between the knee joint and the ankle joint in the dummy. In the dummy leg assembly, the tibia shaft is not positioned exactly in the middle of the knee joint and the ankle joint. Therefore, the mid-span loading point defined and used in the current study did not correspond to the mid-shaft of the tibia. This can be confirmed on an example still image of the leg bending test configuration shown in Figure 9 by comparing the

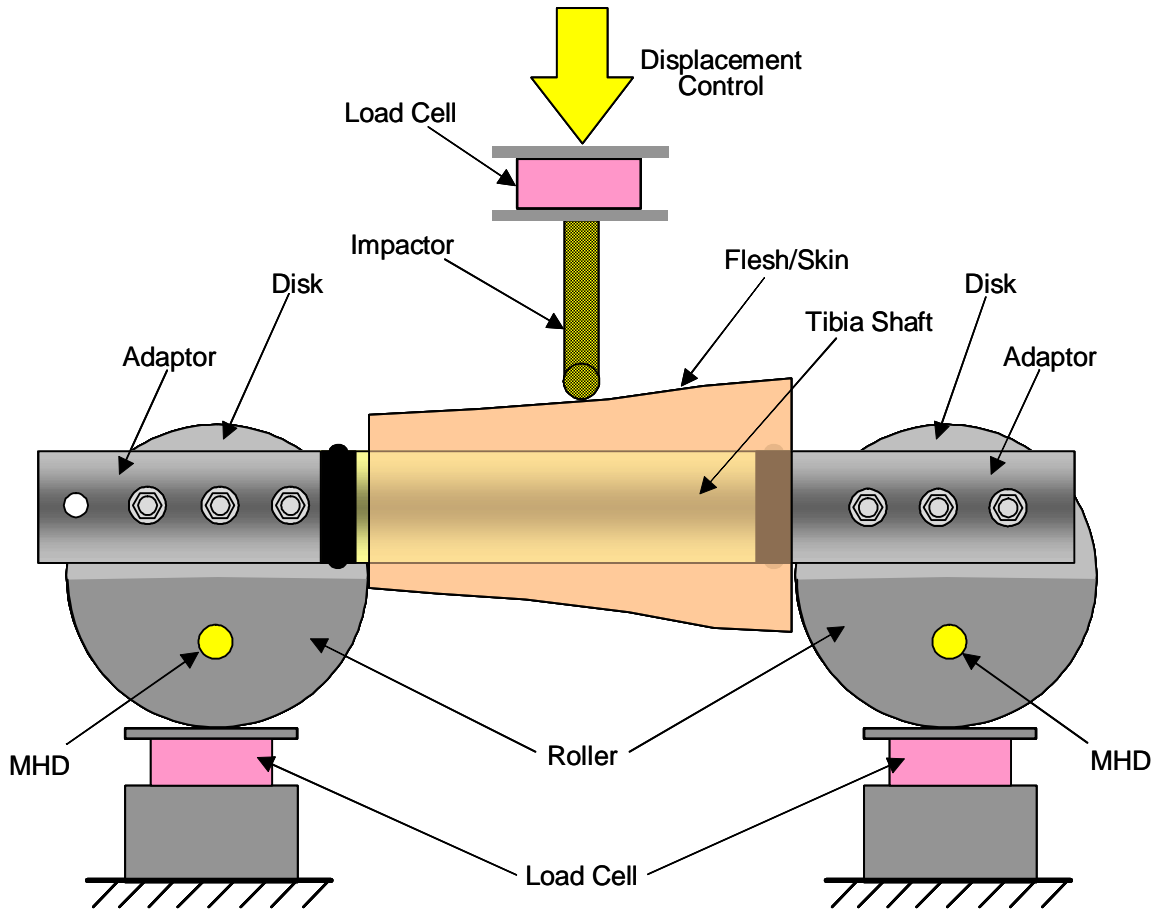


Figure 8. Schematic diagram of 3-point leg bending test configuration.

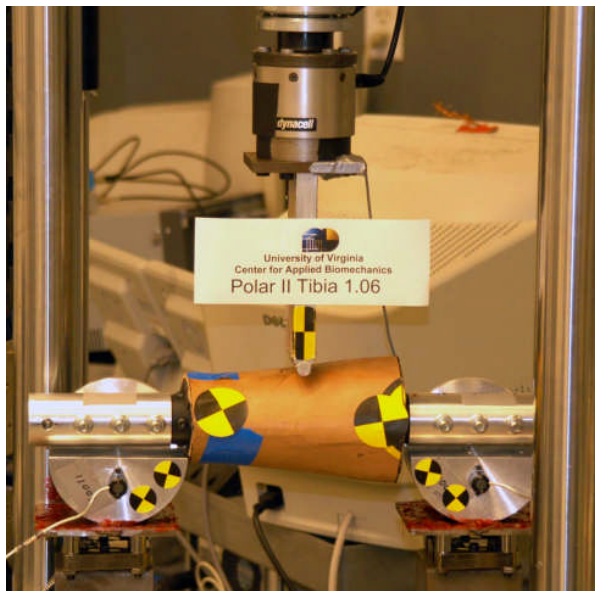


Figure 9. Typical 3-point leg bending test set-up.

position of the steel rings (in black) relative to the rollers (see also Figure 8). The leg flesh/skin for the Polar-II dummy was placed around the tibia shaft in

order to obtain the overall leg bending response. The portion of the leg flesh/skin that corresponds to the superior-inferior range of the tibia shaft in the dummy was cut out from the intact leg flesh/skin assembly in such a way that it fitted between the rollers. The 3-point bending span length was set at 334 mm to which Ivarsson et al. [19] scaled the PMHS test results in order to obtain response corridors scaled to the size of a 50th percentile adult male.

A load cell was mounted between the actuator and the impactor to measure applied load. Three-axis load cells were placed underneath the support plates to obtain reaction forces. Angular velocities of the rollers were measured by the MHD angular rate sensors affixed to the rollers.

Two quasi-static and three dynamic tests were conducted using the tibia shaft of the dummy surrounded by the flesh/skin. For the dynamic tests, the loading rate was set at approximately 1.5 m/s. This loading rate was chosen so that the test results could be directly compared with the PMHS test results by Kerrigan et al. [15]-[17]. The loading rate for the quasi-static tests was approximately 1.0 mm/s.

RESULTS

Ivarsson et al. [19] presented PMHS response corridors for the mid-span 3-point leg bending in the lateromedial direction as well as the 4-point knee valgus bending. The force-deflection and moment-deflection corridors and the moment-angle corridor (all scaled to a 50th percentile adult male anthropometry) were presented for the leg bending and the knee bending, respectively. In order to compare the test results obtained in this study with the PMHS response corridors, the moment-angle response of the knee joint and the force-deflection and moment-deflection responses of the leg were calculated from the signals obtained in the tests.

Knee Joint Test

For the dynamic knee bending tests, Bose et al. [18] estimated forces and moments at the knee joint from the loading environment measured by the load cell installed near the knee joint using an inertial compensation procedure, and the results were used to develop the response corridors by Ivarsson et al. [19]. In this study, the same inertial compensation procedure as that used by Bose et al. [18] was employed to calculate moment at the knee joint. Figure 10 shows a free body diagram of the superior part of the knee joint (proximal knee segment) in the coronal plane. The equations of motion of the knee segment about its center of gravity in tangential (lateromedial) translation and rotation in the coronal plane are given by Equation 1 and 2:

$$M\ddot{u} = V_K - V_F \quad (1)$$

$$I\ddot{\theta} = M_F - M_K + V_F x_F + V_K x_K \quad (2)$$

Since the distal half of the load cell is included in the knee segment, M_F and V_F are given by the load cell signals. Thus, the moment at the knee joint, M_K , can be

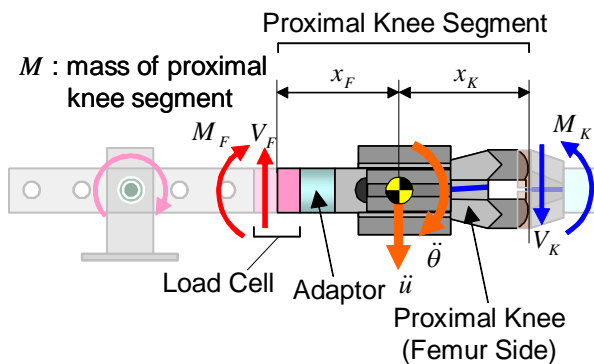


Figure 10. Free body diagram for proximal knee segment.

calculated using Equation 3:

$$M_K = M_F + V_F(x_F + x_K) + M\ddot{u}x_K - I\ddot{\theta} \quad (3)$$

Since the test configuration was intended to provide 4-point bending of the knee joint, V_F was expected to be minimal in the quasi-static tests. However, the test results showed that V_F increases as the knee valgus bending angle goes up. The magnitude of V_F at the knee valgus angle of 15 degrees was approximately 40 N and 70 N for the original knee joint and the modified knee joint, respectively. Since the moment component in Equation 3 generated by those forces corresponded to 17% and 13% of the magnitude of M_F for the original knee joint and the modified knee joint, respectively, it was decided that the effect of V_F on the moment at the knee joint M_K be taken into account, rather than simply using M_F for M_K .

In order to calculate the moment at the knee joint using Equation 3, the moment of inertia and the center of gravity location for the portion between the center of the load cell and the distal end of the femoral condyles of the knee joint (proximal knee segment: Figure 10) were measured using a torsional pendulum (Inertia Dynamic Inc.). Table 1 summarizes the inertial property values measured for the original and modified knee joints. The linear acceleration in Equation 3 was measured by the accelerometer mounted on the load cell. The angular acceleration in Equation 3 was calculated from the accelerometer signal divided by the distance between the support pin joint and the accelerometer.

Figures 11 and 12 plot moment-angle responses at the knee joint calculated using Equation 3 for the original knee joint and the modified knee joint, respectively, in both quasi-static and dynamic valgus bending. In the quasi-static condition, the moment-angle response is fairly linear for both the original knee joint and the stiffer knee joint. However, significant oscillation of moment-angle response is seen in the dynamic condition, particularly for the original knee joint. This oscillation was identified after the dynamic bending tests of the original knee joint. Since the natural frequency estimated using the knee bending stiffness from the quasi-static tests and the inertial

Table 1.
Inertial properties of proximal knee segments.

Knee	Mass (kg)	MOI (kgm ²)	x_F (m)	x_K (m)
Original	2.12	0.01362	0.1238	0.1345
Modified	2.48	0.01397	0.1225	0.1358

(MOI: Moment of Inertia)

properties of the knee and fixtures was much lower than that of the oscillation observed in the moment-angle response, it was assumed before the modified knee joint testing that this oscillation came from the stiffness of the fixtures themselves combined with the stiffness of the connecting portions between the fixtures. Based on this assumption, special attention was paid to increase the rigidity of the connections between the fixtures when setting up for the modified knee joint testing. Since this effort resulted in much lower magnitude of oscillations observed in the moment-angle response of the modified knee joint, it was concluded that the above-mentioned assumption was valid, and that the response of the knee joint itself can be extracted from the oscillated signals by simply eliminating the oscillation. Therefore, the moment-angle response was post-processed in order to eliminate

unfavorable oscillations and compare the results with the published PMHS response corridor.

Two different post-processing procedures were used to try to eliminate the oscillation – filtering and curve-fitting. For filtering, each term of Equation 3 was filtered at CFC 60, and then the moment at the knee joint was calculated using the filtered signals. For curve-fitting, unfiltered signals were used to calculate the moment at the knee joint using Equation 3, and then polynomial regression was applied to the moment-angle curves. Figures 13 and 14 plot the results of filtering and curve-fitting for the moment-angle response of the original knee and the stiffer knee, respectively. The filtered moment-angle curves for the original knee joint presented in Figure 13 show unrealistic bending characteristics such as the initial negative moment and strong nonlinearity. Since the

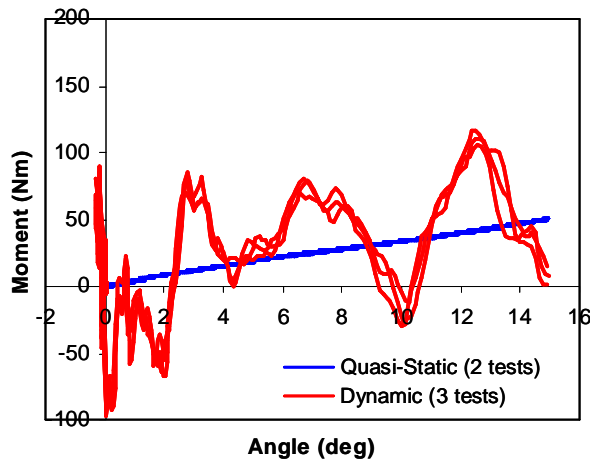


Figure 11. Quasi-static and dynamic moment-angle responses at knee joint for original knee joint.

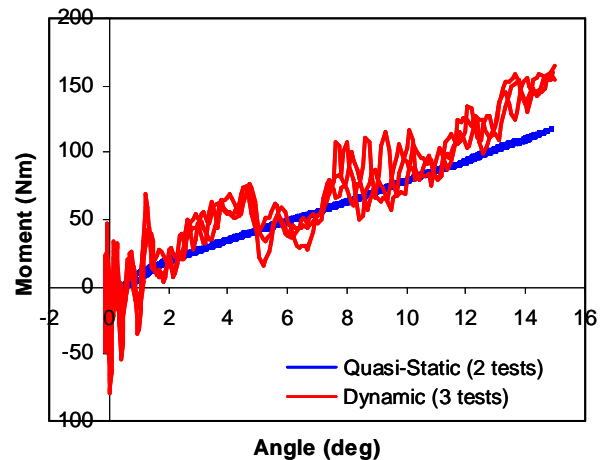


Figure 12. Quasi-static and dynamic moment-angle responses at knee joint for modified knee joint.

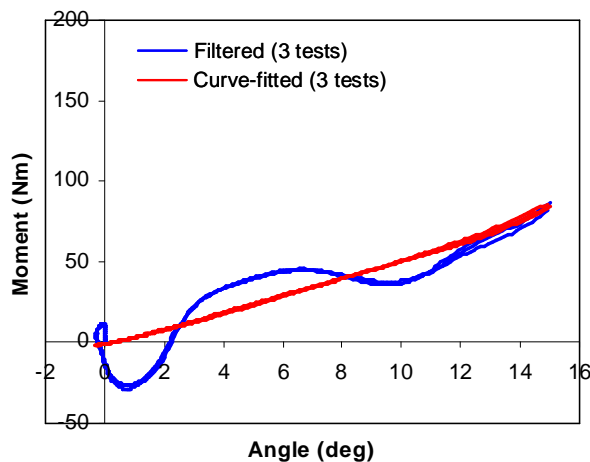


Figure 13. Filtered and curve-fitted dynamic moment-angle responses at knee joint for original knee joint.

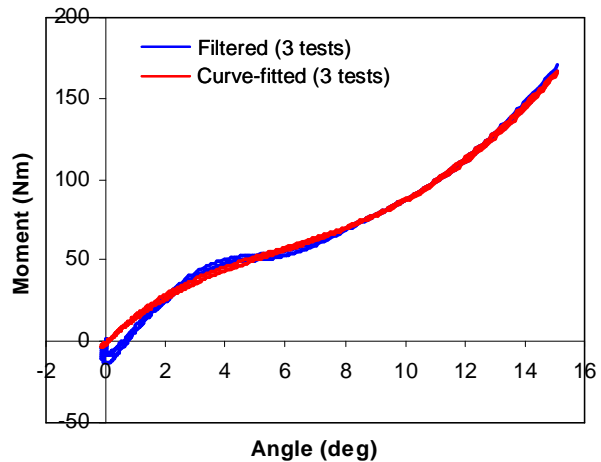


Figure 14. Filtered and curve-fitted dynamic moment-angle responses at knee joint for modified knee joint.

unfiltered moment-angle response for the modified knee joint demonstrates much smaller magnitude of oscillation than that of the original knee joint, the filtered moment-angle curves for the modified knee joint look more realistic (Figure 14). However, the initial negative moment is still seen, although the magnitude is much smaller. Considering the fact that the moment-angle response of both knee joints in quasi-static valgus bending is fairly linear, it can be concluded that the curve-fitting procedure does a better job compared to the CFC 60 filtering to extract characteristics of the knee joint valgus bending response from the oscillated signals.

Leg Test

In order to compare the 3-point bending test results with the PMHS response corridors presented by

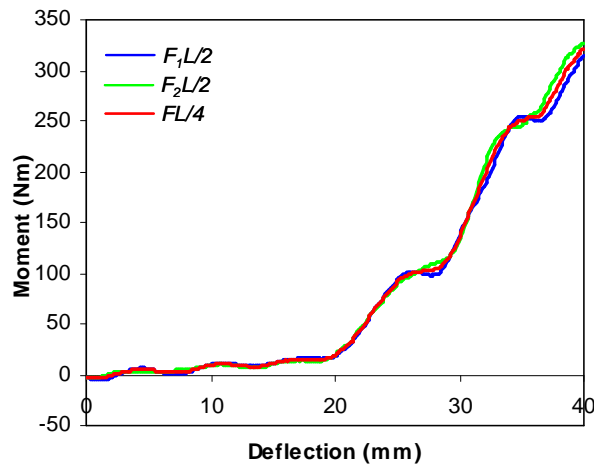


Figure 15. Moment-deflection response from three different methods for moment calculation.

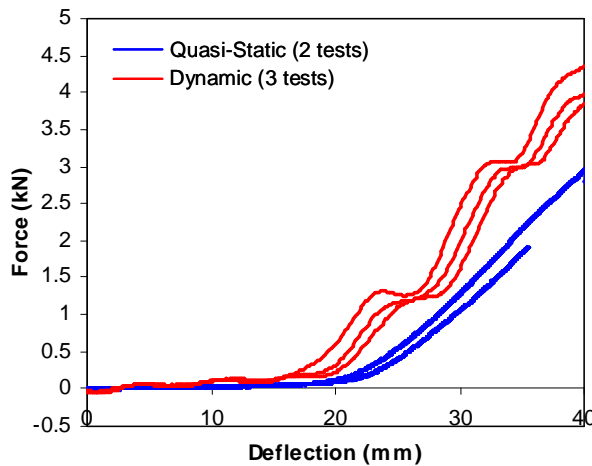


Figure 16. Quasi-static and dynamic force-deflection response of leg.

Ivarsson et al. [19], force-deflection and moment-deflection curves were determined using the signals obtained from the tests. Although the applied force can be measured by the load cell mounted above the impactor, summation of vertical support forces from both support load cells was used to determine the applied force in order to avoid the problem of inertial contribution from mass acceleration. Since the mid-span of the leg specimen was loaded, the moment can be calculated in three ways: $FL/4$, $F_1L/2$, and $F_2L/2$, where F_1 is the vertical component of the reaction force on one support, F_2 is the vertical component of the reaction force on the other support, L is the span length, and $F = F_1 + F_2$. Figure 15 plots the moment-deflection curves from the three different methods for moment calculation for one of the three dynamic 3-point bending tests. In spite of the fact that the mid-span loading configuration defined in this study resulted in asymmetric loading to the tibia shaft, it was found in Figure 15 that the effect of the asymmetry on the moment calculation was so small that the three different methods for moment calculation yielded almost the same moment-deflection curves. Thus, it was decided to use $FL/4$ for moment calculation for simplicity. Figures 16 and 17 show the force-deflection and moment-deflection curves, respectively, obtained from the quasi-static and dynamic 3-point bending tests. The initial toe region with lower stiffness primarily represents the deflection of the flesh/skin surrounding the tibia shaft, and the successive region with higher stiffness corresponds mainly to the bending stiffness of the tibia shaft. For the dynamic tests, some oscillation is observed in the force-deflection and moment-deflection. However, the magnitude of the oscillation is smaller with lower frequency relative to the oscillation seen in the dynamic knee bending tests. Thus, it was decided not

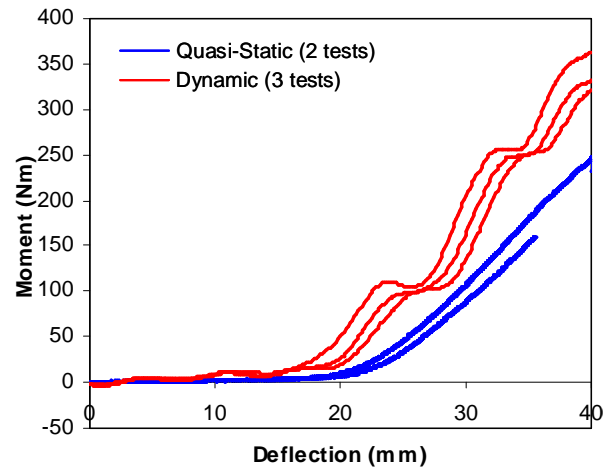


Figure 17. Quasi-static and dynamic moment-deflection response of leg.

to filter or curve-fit the curves for diminishing the oscillation.

DISCUSSION

Since Ivarsson et al. [19] shows scaled PMHS response corridors for the knee and leg test in dynamic condition, only the results from the dynamic tests were compared with the PMHS corridors. Figure 18 compares the moment-angle response at the knee joint between the dummy tests conducted in this study and the PMHS response corridor for a 50th percentile adult male from Ivarsson et al. [19]. Both filtered and curve-fitted response curves were included in the figure. It is obvious that the original knee joint is less stiff than the human knee, with moment-angle curves falling below the lower bound of the PMHS corridor. The curves for the modified knee joint fell almost perfectly within the

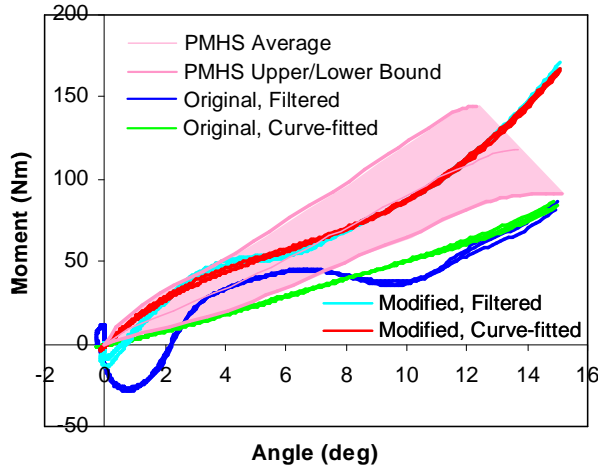


Figure 18. Comparison of moment-angle response of knee between PMHS and dummy.

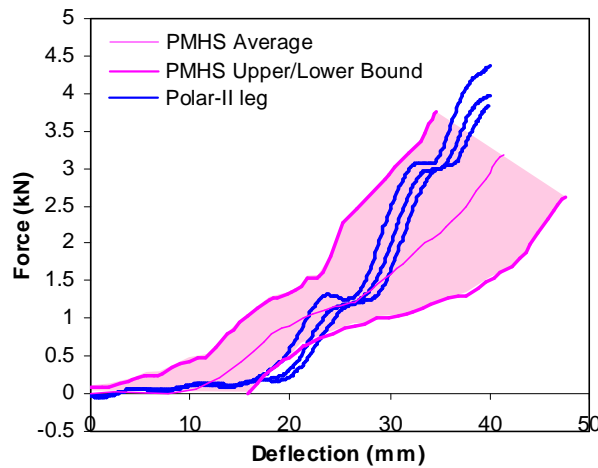


Figure 19. Comparison of force-deflection response of leg between PMHS and dummy.

PMHS corridor except for the artificial initial negative moment in the filtered curves. Figures 19 and 20 compare the force-deflection and moment-deflection responses of the leg, respectively, between the dummy tests and the PMHS corridors. The initial toe region for the dummy leg seems to be longer than that of the PMHS corridors probably due to the difference in thickness of the surrounding flesh between the dummy and PMHS legs. Other than that, all the curves from the dummy leg tests almost fell within the PMHS response corridors.

In order to quantitatively assess the biofidelity of the knee joint and leg of the Polar-II pedestrian dummy tested, the Response Measurement Comparison Value defined by Rhule et al. [30] was calculated for each dynamic test. Figure 21 illustrates the definitions of the Dummy Variance (DV) and Cadaver Variance (CV) presented by Rhule et al. [30]. Although they defined CV and DV for independent variables as functions of time, it was decided to apply this definition directly to the moment-angle curves of the knee joint as well as the force-deflection and moment-deflection curves of the leg since both the PMHS and dummy tests employed the displacement-controlled test machine and thus displacement time histories were prescribed independently from the response of the test specimens. The Dummy Cumulative Variance (DCV), Cadaver Cumulative Variance (CCV), and Response Measurement Comparison Value (R) were then defined by the following formulae:

$$DCV = \sum_{d=0}^n DV(d)^2 \quad (4).$$

$$CCV = \sum_{d=0}^n CV(d)^2 \quad (5).$$

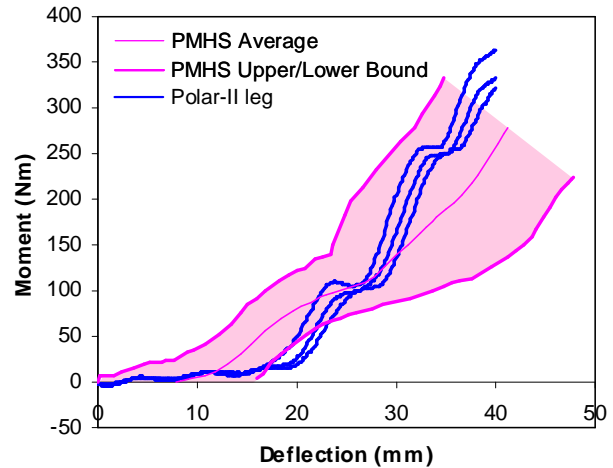


Figure 20. Comparison of moment-deflection response of leg between PMHS and dummy.

$$R = DCV / CCV \quad (6).$$

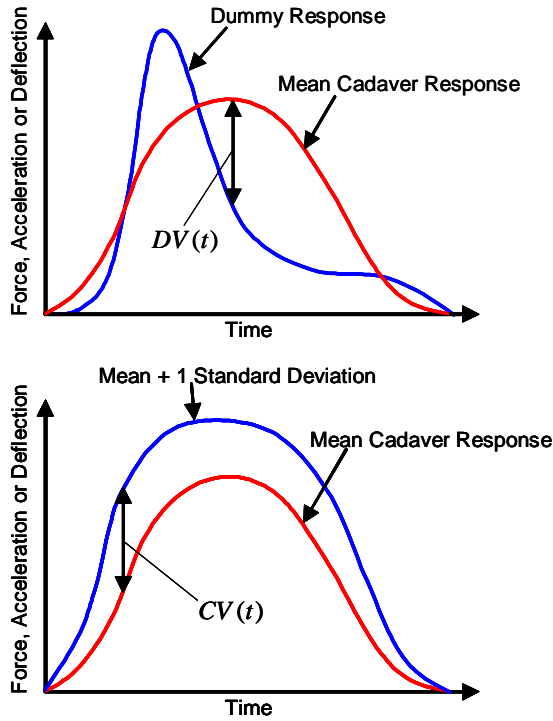


Figure 21. Dummy Variance (DV) and Cadaver Variance (CV) (Rhule et al. [30]).

where d represents either knee bending angle or leg mid-span deflection. Therefore, $R^{1/2}$ represents cumulative dummy variance relative to the mean cadaver response normalized by the cumulative cadaver response variance relative to the mean cadaver response. Thus, if $R^{1/2}$ is less than 1.0, then the cumulative dummy variance is less than the cumulative cadaver variance (both relative to the mean cadaver response) and the biofidelity of the specimen tested can be considered to be very good.

Tables 2 and 3 summarize the results of $R^{1/2}$ calculations for the dynamic knee joint and leg tests, respectively. In terms of the knee joint tests, both filtered and curve-fitted moment-angle curves were subjected to the calculation. The response corridors presented in Ivarsson et al. were developed around the characteristic average response using standard deviation calculations for both the independent and dependent variables [19]. Due to the technique used for the corridor development, the upper and lower bounds do not have the same distance in the vertical direction from the mean response. Thus, both upper and lower bounds were used in calculating CCV , and average CCV was calculated for each response corridor. $R^{1/2}$ for the original knee joint was between one and two for both filtered and curve-fitted moment-angle curves, while the modified knee joint resulted in $R^{1/2}$ values of less than 0.4 for both post-processing methods. $R^{1/2}$ for

Table 2.
 $R^{1/2}$ calculation for bending of original and modified knee with two different signal post-processing methods and two different CCV calculations (upper/lower bound).

Specimen	Test #	Moment-Angle / Filtered			Moment-Angle / Curve-Fitted		
		Upper	Lower	Average	Upper	Lower	Average
Original Knee	1	1.342	1.792	1.567	1.142	1.525	1.333
	2	1.354	1.808	1.581	1.138	1.520	1.329
	3	1.350	1.803	1.576	1.134	1.514	1.324
	Average	1.349	1.801	1.575	1.138	1.520	1.329
Modified Knee	1	0.292	0.390	0.341	0.234	0.312	0.273
	2	0.343	0.458	0.400	0.292	0.391	0.341
	3	0.304	0.406	0.355	0.236	0.315	0.276
	Average	0.313	0.418	0.366	0.254	0.339	0.297

Table 3.
 $R^{1/2}$ calculation for bending of leg with two different signal post-processing methods and two different CCV calculations (upper/lower bound).

Specimen	Test #	Force-Deflection			Moment-Deflection		
		Upper	Lower	Average	Upper	Lower	Average
Leg	1	0.455	0.889	0.672	0.429	0.856	0.642
	2	0.490	0.958	0.724	0.447	0.892	0.669
	3	0.580	1.132	0.856	0.513	1.026	0.769
	Average	0.508	0.993	0.751	0.463	0.925	0.694

the force-deflection and moment-deflection of the leg were less than one. Those results suggest that the biofidelity of the modified knee joint and the leg from the Polar-II dummy in lateral bending is very good at the component level.

Although the modified knee joint and leg of the Polar-II pedestrian dummy were found to be biofidelic, they are not currently designed to fail during impact testing. On the other hand, a human knee and/or leg may fail particularly when a pedestrian is subjected to severe impact conditions. Since the failure to the knee and/or leg may affect the upper body kinematics of a pedestrian in a car-pedestrian impact, future study needs to quantify the effect of the responses of the knee and leg components on the upper body kinematics of the dummy in full-scale testing.

CONCLUSION

In this study, a series of component tests using the original and modified knee joint and the leg from the Polar-II pedestrian dummy were conducted. Based on the results of the tests, the following conclusions were reached.

1. Limited rigidity in the test fixtures resulted in unfavorable oscillation in the moment-angle response of the knee joint.
2. Polynomial regression yielded a better representation of the knee joint bending characteristics from noisy moment-angle curves relative to low-pass filtering.
3. The original knee joint of the Polar-II dummy was found to be less stiff than the human knee in valgus bending ($R^{1/2}=1.33$ with curve-fitted moment-angle response).
4. The modified knee joint of the Polar-II dummy with increased stiffness of the ligament springs exhibited very biofidelic response in valgus bending ($R^{1/2}=0.30$ with curve-fitted moment-angle response).
5. The leg (deformable tibia shaft with flesh/skin) of the Polar-II dummy yielded very biofidelic force-deflection and moment-deflection responses in lateromedial 3-point bending ($R^{1/2}=0.75$ for force-deflection and 0.69 for moment-deflection).
6. Future study needs to quantify the effect of the knee and leg responses on the upper body kinematics of the dummy in full-scale testing.

REFERENCES

[1] Ashton S., Pedder J., Mackay G., "Influence of Vehicle Design on Pedestrian Leg Injuries", Proceedings of the 22nd Annual Conference of the American Association of Automotive Medicine, 1978.

[2] Laumon B., Martin J., Collet P., Chiron M., Vemey M., NDiaye A., Vergnes I., "A French Road Accident Trauma Registry: First Results", Proceedings of the 41st Annual Conference of the American Association of Automotive Medicine, 1997.

[3] Stutts J., "Injuries to Pedestrians and Bicyclists: A Look at Non-Motor Vehicle and Non-Roadway Events", Proceedings of the 41st Annual Conference of the American Association of Automotive Medicine, 1997.

[4] Harruff R., Avery A., Alter-Pandya A., "Analysis of Circumstances and Injuries in 217 Pedestrian Traffic Fatalities", Accident Analysis and Prevention, Vol. 30, No. 1, 1998.

[5] Jarrett K., Saul R., "Pedestrian Injury – Analysis of the PCDS Field Collision Data", 16th ESV Conference, Paper Number 98-S6-O-04, 1998.

[6] Matsui Y., Ishikawa H., Sasaki A., "Pedestrian injuries Induced by the Bonnet Leading Edge in Current Car-Pedestrian Accidents", SAE Paper 1999-01-0713, 1999.

[7] European Enhanced Vehicle-safety Committee, "EEVC Working Group 17 Report; Improved Test Methods to Evaluate Pedestrian Protection Afforded by Passenger Cars", www.eevc.org, 1998.

[8] Laurence G., Hardy B., "Pedestrian Safety Testing Using the EEVC Pedestrian Impactors", 16th ESV Conference, Paper Number 98-S10-O-03, 1998.

[9] European Experimental Vehicles Committee, "EEVC Working Group 10 Report; Proposals for methods to evaluate pedestrian protection for passenger cars", 1994.

[10] Matsui Y., Ishikawa H., Sasaki A., Kajzer J., Schroeder G., "Impact Response and Biofidelity of Pedestrian Legform Impactors", IRCOBI Conference, 1999.

[11] Kajzer J., Cavallero C., Ghanouchi S., Bonnoit J., Ghorbel A., "Response of the Knee Joint in Lateral Impact – Effect of Shearing Loads", IRCOBI Conference, 1990.

[12] Kajzer J., Cavallero C., Bonnoit J., Morjane A., Ghanouchi S., "Response of the Knee Joint in Lateral Impact – Effect of Bending Moment", IRCOBI Conference, 1993.

[13] Konosu A., Tanahashi M., "Development of a Biofidelic Flexible Pedestrian Legform Impactor", Stapp Car Crash Journal, Vol. 47, 2003.

[14] Konosu A., Issiki T., Tanahashi M., "Development of a Biofidelic Flexible Pedestrian Leg-form Impactor (Flex-PLI 2004) and Evaluation of its Biofidelity at the Component Level and at the Assembly Level", SAE Paper Number 05B-161, 2005.

[15] Kerrigan J., Bhalla K., Madeley N., Funk J., Bose D., Crandall J., "Experiments for Establishing Pedestrian-Impact Lower Limb Injury Criteria", SAE Paper Number 2003-01-0895, 2003.

[16] Kerrigan J., Bhalla K., Madeley N., Crandall J.,

- Deng B., "Response Corridors for the Human Leg in 3-point Lateral Bending", The 7th USA National Congress on Computational Mechanics, 2003.
- [17] Kerrigan J., Drinkwater C., Kam C., Murphy D., Ivarsson J., Crandall J., "Tolerance of the Human Leg and Thigh in Dynamic Lateral-Medial 3-point Bending", the 2004 International Crashworthiness Conference, 2004.
- [18] Bose D., Bhalla K., van Rooij L., Millington S., Studley A., Crandall J., "Response of the Knee Joint to the Pedestrian Impact Loading Environment", SAE Paper Number 2004-01-1608, 2004.
- [19] Ivarsson J., Lessley D., Kerrigan J., Bhalla K., Bose D., Crandall J., Kent R., "Dynamic Response Corridors and Injury Thresholds of the Pedestrian Lower Extremities", IRCOBI Conference, 2004.
- [20] Bhalla K., Bose D., Madeley J., Kerrigan J., Crandall J., Longhitano D., Takahashi Y., "Evaluation of the Response of Mechanical Pedestrian Knee Joint Impactors in Bending and Shear Loading", 18th ESV Conference, 2003.
- [21] Cesari D., Alonzo F., Matyjewski M., "Subsystem Test for Pedestrian Lower Leg and Knee Protection", 13th ESV Conference, Paper Number S3-O-08, 1991.
- [22] Takahashi Y., Kikuchi Y., "Biofidelity of Test Devices and Validity of Injury Criteria for Evaluating Knee Injuries to Pedestrians", 17th ESV Conference, Paper Number 373, 2001.
- [23] Akiyama A., Okamoto M., Rangarajan N., "Development and Application of the New Pedestrian Dummy", 17th ESV Conference, Paper Number 463, 2001.
- [24] Akiyama A., Yoshida S., Matsushashi T., Rangarajan N., Shams T., Ishikawa H., Konosu A., "Development of Simulation Model and Pedestrian Dummy", SAE Paper Number 1999-01-0082, 1999.
- [25] Huang T., McDonald J., Artis M., Rangarajan N., Shams T., White Jr. R., Beach D., Campbell Jr. R., Akiyama A., Yoshida S., Ishikawa H., Konosu A., "Development of a Biofidelic Dummy for Car-Pedestrian Accident Studies", IRCOBI Conference, 1999.
- [26] Artis M., McDonald J., White R., Huang T., Shams T., Rangarajan N., Akiyama A., Okamoto M., Yoshizawa R., Ishikawa H., "Development of a New Biofidelic Leg for Use With a Pedestrian Dummy", IRCOBI Conference, 2000.
- [27] Ishikawa H., Kajzer J., Schroeder G., "Computer Simulation of the Impact Response of the Human Body in Car-Pedestrian Accidents", 37th Stapp Car Crash Conference, 1993.
- [28] Kajzer J., Schroeder G., Ishikawa H., Matsui Y., Bosch U., "Shearing and Bending Effects at the Knee Joint at High Speed Lateral Loading", 41st Stapp Car Crash Conference, 1997.
- [29] Kajzer J., Matsui Y., Ishikawa H., Schroeder G., Bosch U., "Shearing and Bending Effects at the Knee Joint at Low Speed Lateral Loading", SAE Paper Number 1999-01-0712, 1999.
- [30] Rhule H., Maltese M., Donnelly B., Eppinger R., "Development of a New Biofidelity Ranking System for Anthropomorphic Test Devices", Stapp Car Crash Journal, Vol. 46, 2002.

A COMPUTATIONAL MODEL OF THE PREGNANT OCCUPANT: EFFECTS OF RESTRAINT USAGE AND OCCUPANT POSITION ON FETAL INJURY RISK

Stefan Duma

Dave Moorcroft

Joel Stitzel

Greg Duma

Virginia Tech – Wake Forest, Center for Injury Biomechanics

United States

Paper Number 05-0367

ABSTRACT

Automobile crashes are the largest single cause of death for pregnant and the leading cause of traumatic fetal injury mortality in the United States. The purpose of this paper is to present a validated model of a 30 week pregnant occupant and to examine the risk of fetal injury in frontal crashes. The pregnant uterine model was imported into MADYMO 6.0 and included in the 5th percentile female human body model using membrane elements to serve as ligaments and facet surfaces for the overlying skin. A simulation matrix of 17 tests was developed to predict fetal outcome and included frontal crash impulses from minor (<24 kph), to moderate (24-48 kph), and severe (>48 kph) crashes for the driver and passenger occupant positions. The test matrix also included various restraint combinations: no restraint, lap belt, 3-point belt, 3-point with airbag, and airbag only. Overall, the highest risk for fetal death was seen in higher speed frontal accidents in the driver position for all restraint conditions. The peak uterine strain was reduced by 26 % to 54 % for the passenger position versus the driver position. This difference was due primarily to driver interaction with the steering wheel. For all impact directions, the maternal injury indices were greatest for the unrestrained occupant. In addition, the possibility of direct fetal brain injury from inertial loading alone appears possible and a component that should be included in further models. The current modeling effort has verified previous experimental findings regarding the importance of proper restraint use for the pregnant occupant.

INTRODUCTION

Automobile crashes are the largest single cause of death for pregnant females [1] and the leading cause of traumatic fetal injury mortality in the United States (US) [22]. Each year, 160 pregnant women are killed in motor-vehicle crashes (MVCs) and an additional 800 to 3200 fetuses are killed when the mother survives [10 & 11] in the US. Unfortunately, fetal injury in motor vehicle crashes is difficult to predict due to the fact that real world crash data is limited and cadaver studies are not feasible.

In the non-pregnant female, the uterus is a muscular organ the size of a lemon located within the abdominal cavity. As the fetus grows during pregnancy, the abdomen stretches to the size of a watermelon. The internal volume increases from 0.005 L to 5 L and as much as 10 L [20]. The uterine wall is uniform prior to delivery, with a thickness of about 1 cm. The uterosacral and round ligaments extend from the uterus to the pelvis and act to support the uterus. The interior of the uterus contains the fetus, which is surrounded by amniotic fluid and the placenta (Figure 1). The placenta is a vascular organ that acts as a permeable membrane that exchanges oxygen, nutrients, and waste products between the mother and fetus via the umbilical cord. It is a flat, roughly circular structure 2 cm thick in the center. Most placentas, as many as 95%, are in the upper half of the uterus [6]. Testing by Fried [6] showed that 31% of the placentas were wholly or partly fundal (at the top of the uterus) and by the 3rd trimester, 40% of the placentas were fundal. The cephalic presentation, in which the fetus is in a head down position, comprises about 75% of pregnancies [6].

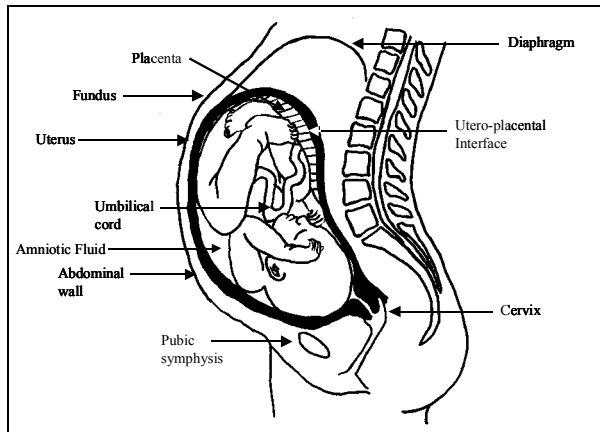


Figure 1. Anatomy of a 40-week pregnant woman (ligaments not shown).

In an effort to reduce the risk of injury to pregnant occupants in car crashes, research was performed on pregnant primates that illustrated the effectiveness of restraint systems in preventing fetal and maternal death [9]. More recently, a pregnant anthropometric test dummy (ATD) has been developed at the University of Michigan Transportation Research Institute [20]. The Maternal Anthropomorphic Measurement Apparatus Version 2B (MAMA-2B) is a second-generation prototype ATD that is a retrofit Hybrid III small female dummy. One of the primary limitations of the pregnant dummy is the lack of injury criteria for the fetus. The MAMA-2B was designed to measure anterior and posterior pressure in the fluid-filled abdomen insert as well as the strain on the perimeter of the insert. However, only the anterior pressure measurements were repeatable [20]. Therefore, it would be beneficial to have an injury criterion for the pregnant dummy that utilizes currently established ATD measurement methods. One leading example would be to measure overall abdominal compression in a similar manner that used to measure chest compression. For example, this could be done by using a string potentiometer as is done in the chest.

The most common cause of fetal death from motor vehicle accidents is placental abruption, which is the premature separation of the placenta from the uterus [11]. Both the pregnant dummy and the pregnant model presented in this study utilize this injury mechanism to predict fetal outcome [14]. However, due to the difficulties in measuring this mechanism in the pregnant dummy, such as tissue strain and pressure, a computational model is desired that can accurately predict fetal injury risk. Therefore, the purpose of this paper is to present a validated model of the pregnant occupant to examine the risk of fetal injury in frontal crashes for a range of restraint configurations in both driver and passenger occupant positions.

METHODOLOGY

Motor vehicle crashes were simulated using the MADYMO (TNO, Netherlands) software package. In order to create the pregnant occupant, the finite element model of a pregnant uterus was inserted into the abdomen of a multibody human model (Figure 2) [14, 15, & 17]. The finite element uterine model is designed to represent an occupant in her 30th week of gestation. The abdomen consists of the uterus, placenta, and amniotic fluid. A fetus was not included because the injury mechanisms that predominantly contribute to fetal loss, as described by [20], are independent of the fetus. The uterus is 27 cm long, 18 cm wide, and 1 cm thick. The placenta is located at the fundus of the uterus and is 2 cm thick. The remainder of the interior of the uterus is filled with the amniotic fluid. The human model is a 5th percentile female (5 ft tall, 110 lbs) and the weight of the pregnant occupant model is 135 lbs. The multibody human model provides biofidelic response of an occupant in a motor vehicle crash, while reducing the computational time compared to a full finite element human model. The anthropometry of a pregnant woman was quantified by Klinich [10]. The abdominal contour of the pregnant model closely matches the Klinich data.

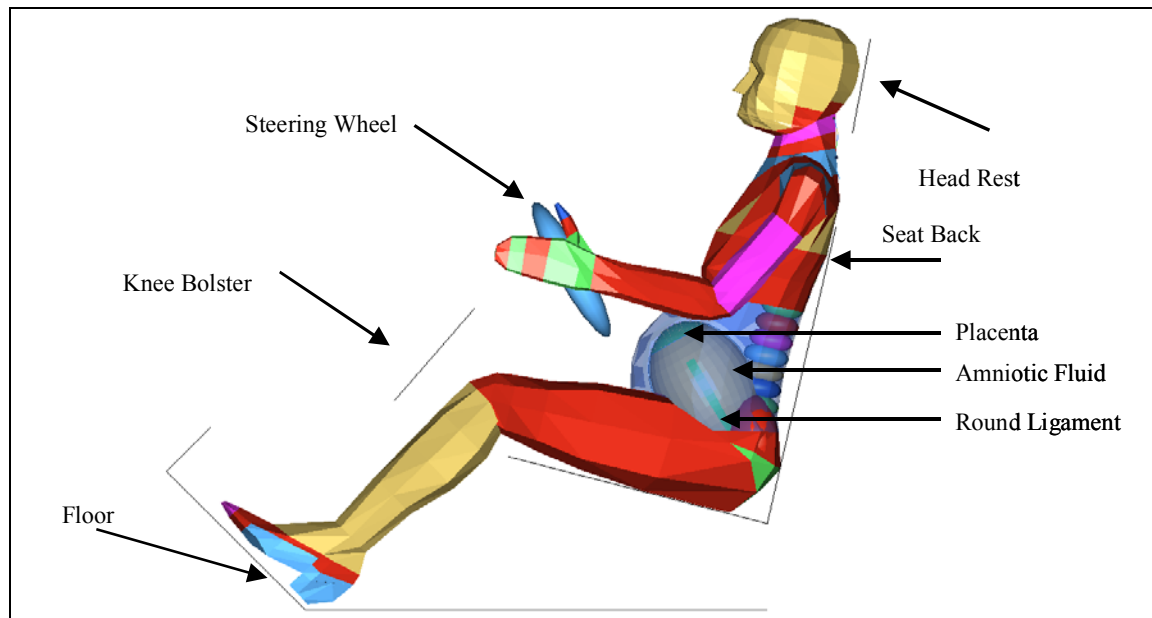


Figure 2. Pregnant occupant in the driver-side interior.

The uterine model is supported to the human model by the uterosacral and round ligaments, as well as the cervix. The bottom four nodes of each ligament are constrained to move with the pelvis for both translation and rotation. The uterine model is also surrounded by fat to represent the boundary conditions involving the spine, abdominal organs, and the pelvis. All uterine bodies were modeled as linear elastic solids. Although the uterus and placenta are considered visco-elastic and anisotropic [2, 13, & 19], sufficient data was not available to accurately apply these material types. The amniotic fluid was modeled as a solid because MADYMO does not utilize fluid elements at the time of model development.

Tension tests on human uterus tissue have been reported by Pearlman [18], Pearsall [19], and Wood [23]. The Young's modulus ranged from 20.3 kPa to 1379 kPa, with an average of 566 kPa. The Poisson's ratio is set to 0.40 since the uterus is a muscular organ and the density is 1052 kg/m³. Pearlman [18] reported the results of five tension tests on placental specimen. The average modulus was 33 kPa, with a high of 63 kPa. Testing was not taken to failure. The highest modulus is used in the pregnant model because it is expected that the placenta is stiffer than the fat. The Poisson's ratio is assumed to be 0.45 because it is muscular tissue ($\nu=0.40$) engorged with blood ($\nu=0.50$). The density of the placenta is 995 kg/m. The amniotic fluid, which is 99% water and therefore incompressible, was assumed to have a negligible Young's modulus and a Poisson's ratio of

0.49. The Young's modulus of 20 kPa is used for the fluid because moduli of lower values produced unstable results. The computational model uses peak von Mises strain in the uterus, near the placenta, as the measure for predicting risk of injury. High risk is associated with the presumed 60% strain tissue limit allowing the prediction of fetal injury based on the strain.

Material properties of the ligaments connecting the uterus to the pelvis were not available in the literature. A brief search of general ligament properties showed that the elastic modulus of ligaments is typically two orders of magnitude greater than the uterus [8, 24, & 25]. Therefore, the elastic modulus of the uterosacral and round ligaments is set to 100 times the modulus of the uterus. The density and Poisson's ratio were also taken from general ligament data [8 & 25]. An isotropic representation of fatty tissue has been used by Todd and Thacker [21] in modeling of the human buttocks. The Young's modulus for a seated female is 47 kPa with a Poisson's ratio of 0.49. This Poisson's ratio represents a nearly incompressible material. Contacts were created such that the fluid interior of the uterus was free to move within the uterus, with contact friction. However, the fluid could not penetrate the uterus or placenta. Default master/slave contact treatments within MADYMO were used for all contacts.

Four techniques were used to validate the pregnant model. First, a global biofidelity response

was evaluated by using a seatbelt to compress dynamically the pregnant abdomen [17]. The force versus compression results were within the published corridors from scaled cadaver tests [7]. Second, a similar validation procedure was performed with a rigid bar [17] and these results were also consistent with previous data [7]. The third technique involved validating the model against real-world crashes in order to investigate the model's ability to predict injury. Using fatal crashes from pregnant occupants [11], the model showed strong correlation ($R^2 = 0.85$) between peak strain at the uterine-placental interface (UPI) as measured in the model compared to risk of fetal demise as reported in the real-world crashes over a range of impact velocities and restraint conditions [14]. The fourth method compared the physiological failure strain from placental tissue tests to the failure strain measured in the model. Tissue tests by Rupp et al. [20] suggested approximately a 60% failure strain for UPI tissues which is in agreement with the model's prediction of 75 % risk of fetal loss at a 60% strain in the UPI. In summary, the global, injury, and tissue level validation techniques all indicate the model is good at predicting injurious events for the pregnant occupant.

The current simulations were chosen to determine the effect of restraint use and occupant position on the response of the pregnant occupant. The test matrix consisted of 17 simulations in two groups. The first group of 15 simulations was performed with occupant position and occupant restraint variations (Table 1). The applied sled pulse is a half-sine wave imposed for duration of 100 ms. Acceleration is defined with respect to time; therefore the area under the curve corresponds to the change of velocity of the crash. Two interiors were used in the simulations; a standard driver-side interior and a passenger-side interior. The driver interior is a typical MADYMO interior made up of rigid planes to represent the seat, vehicle floor, and knee bolster. Positioning of the pregnant occupant was based on the seated anthropometry of a pregnant woman in her 30th week of pregnancy as defined by Klinich [10]. Four parameters were chosen to define the position of the occupant, using the parameter values that correspond to the small female group in the Klinich study (average height: 5 ft, average weight: 134 lb). The abdominal clearance, defined as the distance between the abdomen and the bottom of the steering wheel, is 38 mm. The mean overlap of the uterus to the steering wheel is 12%, where the overlap is defined as the ratio of the vertical height of the uterus above the bottom of the steering wheel to the total vertical height of the uterus. The seatback angle, relative to vertical, is 13 degrees, and the steering

wheel tilt is 29 degrees from vertical. Standard MADYMO finite element belts are used for the three-point restraint condition. For the airbag tests, a MADYMO 600 mm driver airbag (volume = 35 L) is used, with inflation triggered 15 ms into the simulation.

The second group of two simulations was performed to explore the possibility of fetal brain injury due to inertial loading alone. In other words, these simulations were performed to investigate the possibility of fetal brain injury due to an acceleration rather than using the placental separation predictive measure as done in the previous 15 simulations. Therefore, two severe rear impact tests were performed using 100 ms pulse duration and 35 kph and 47 kph crash velocities. This direction was selected in order to generate a pure inertial load without interference from the belts or steering wheel. For these tests, the pelvis acceleration was recorded and a HIC value (15 ms) was determined. It was assumed that in the later part of gestation, the head of the fetus lies firmly in the cervix and is relatively fixed to the pelvis. Therefore, it is assumed that the pelvis acceleration acts as a marker for the fetal head acceleration; however, this assumption will estimate the upper bound of fetal head acceleration given that the coupling to the pelvis is not rigid.

RESULTS

For the pregnant driver occupant, the unrestrained occupant resulted in substantially higher risk of abdominal and head trauma compared to the fully restrained driver in a similar crash (Figure 3). For all simulations both strain in the uterus and maternal responses were considered with respect to fetal outcome (Table 1). Simulations in which the occupant was positioned in the passenger-side interior resulted in lower peak uterine strains measured at the uterine placental interface (UPI) compared to the driver-side interior for all restraints tested. Substantial reductions were seen for the unrestrained and 3-pt belt cases for similar crash speeds. For belted simulations, the peak strain is 26% to 36% less in passenger-side simulations compared to driver-side simulations even though the forward motion of the occupant is roughly equal between simulations with the same restraint. The key difference in the tests is the presence or absence of the steering wheel. In the driver-side configuration, the occupant contacts the steering wheel to some degree in all the configurations tested. A lower peak strain is recorded in the unrestrained cases because the abdomen does not contact the steering wheel, due to the seatbelts in the belted cases and due to the

contact between the head and the windshield in the unrestrained case. For the two belted cases, the occupant does not approach the dashboard and therefore, strain is primarily due to inertial effects.

The main effect of varying the occupant position, therefore, appears to be to alter the abdominal loading pattern from one of contact in the driver-side cases to one of inertia in the passenger-side cases.

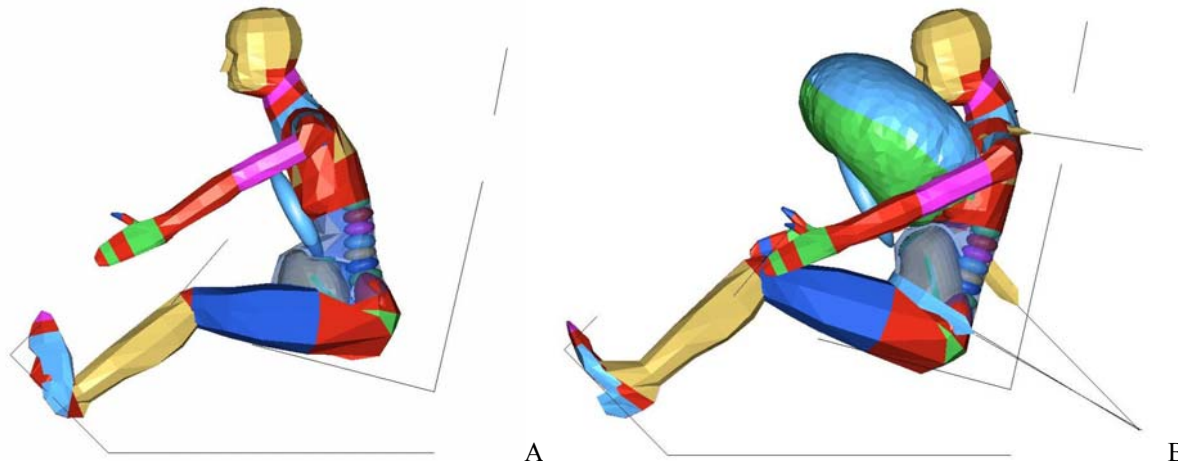


Figure 3. Unrestrained pregnant driver in a simulated 35kph crash (A), and full restrained at 35 kph crash (B).

Table 1.
Pregnant model test parameters and results.

Occupant	Restraint	Crash Speed (kph)	Risk of fetal death (%)	Maximum Strain in the Uterine Wall (%)	HIC	V*C (m/s)	Chest Deflection (mm)
Driver	None	13	44	23.3	1	0.12	38.6
Driver	None	20	65	36.6	13	0.31	39.1
Driver	None	25	77	44.6	41	0.47	39.4
Driver	None	35	100	60.8	156	0.72	39.7
Driver	3-pt Belt	13	32	15.5	4	0.03	43.4
Driver	3-pt Belt	25	51	27.9	62	0.09	47.1
Driver	3-pt Belt	35	89	52.6	185	0.12	52.4
Driver	3-pt Belt	45	99	58.7	211	0.13	54.3
Driver	3-pt Belt	55	100	61.2	310	0.17	58.2
Driver	3-pt Belt + Airbag	25	52	28.1	49	0.22	45.1
Driver	3-pt Belt + Airbag	35	59	33.0	114	0.24	48.2
Driver	3-pt Belt + Airbag	45	80	46.6	173	0.20	49.0
Passenger	None	35	52	28.2	2820	0.33	32.7
Passenger	3-pt Belt	35	60	33.7	181	0.30	51.5
Passenger	3-pt Belt + Airbag	35	46	24.4	140	0.27	47.8

The importance of examining the maternal response is highlighted in the unrestrained passenger-side case. Although this simulation produced a low peak strain, based on the HIC value of 2820, it is reasonable to predict maternal death. This elevated value is the result of severe contact between the occupant's head and the dashboard. HIC scores for the remaining simulations were generally low and consistent between seating position. Thorax response for the unrestrained occupant shows the same trend as for the strain, where the limited contact between the thorax and any vehicle surface reduces the passenger injury risk as compared to the driver response. For the restrained occupant, a slight increase is seen in thorax injury risk with the removal of the steering wheel. This is a result of the contact between the steering wheel and the pregnant abdomen in driver-side simulations reducing the load applied to the shoulder belt as compared to the passenger-side.

In the second group of simulations, the seatback fully supported the occupant thereby resulting in the anticipated pure acceleration field presented to the pregnant abdomen. In the 35 kph crash simulation, the peak fetal head acceleration was estimated as a peak of 73.5 g with a 118 HIC. In the 47 kph crash simulation, the peak fetal head acceleration was 83.7 g with a 215 HIC.

DISCUSSION

Overall, there is a high probability that placental abruption would occur in the driver-side, unrestrained, frontal impact simulation. In the passenger-side simulation, there is a near 100% risk

of life-threatening maternal brain injury in the similarly unrestrained condition, and therefore a high risk for fetal death. The use of a 3-pt. belt, as well as an airbag, reduces the risk to the pregnant women and the fetus. The difference in abdominal clearance between the driver-side and passenger-side simulations played an important role in peak strain in the uterine wall. The strain was 26% to 54% less in passenger side simulations, primarily due to the presence or absence of the steering wheel. Based on the results of this study it is recommended that, when practical, the pregnant woman ride in the passenger seat with a 3-point seatbelt and airbag with the seat positioned as far rearward as possible.

Placental abruption is believed to occur when the strain in the uterine wall exceeds 60%. The risk for placental abruption is largest for high strains that occur near the placenta which can be dramatically influenced by the lap belt position. Simulations have demonstrated that the vertical position of the lap-belt can increase fetal risk by a factor of three (Figure 4) [16]. As the lap-belt approaches the height of the placenta, which is located at the top of the uterus, the observed strain increases for a given crash pulse. Simulations with the lap-belt directly loading the uterus at the placental location, produced the highest recorded strain. Once the lap-belt height is above the placenta, the strain decreases with the strain for the top belt position matching that seen for the recommended belt location. However, it is important to note that there is increased risk to the mother with incorrect lap-belt placement, including elevated head and chest injury response. This is important because the best way to protect the fetus is to protect the mother.

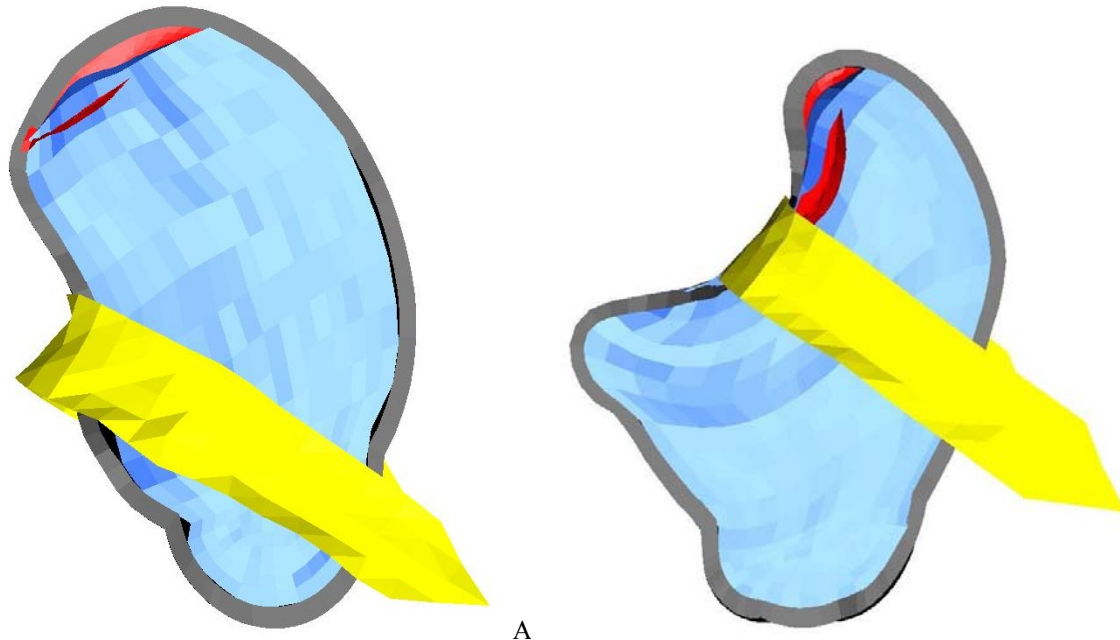


Figure 4. Simulations at 35 kph showing uterine compression for the correctly position belt (A), and the incorrectly positioned belt (B).

Predicting fetal injury from abdominal deflection is loosely analogous to using chest deflection to predict thoracic injury. As a simple comparison, chest deflection for the small female is limited to 52 mm by federal safety standards [4]. A chest deflection of 52 mm is approximately 35% compression which corresponds to approximately 40% risk of an AIS 3 or greater injury [12]. Given the obvious anatomical differences between the thorax and pregnant uterus, it is interesting that 35% compression of the uterus at is also the higher limit of injury [3]. The abdominal deflection could be measured in the same manner as chest deflection, using a string potentiometer, chestband, or through processing of digital video. It is important to note that the measurements need to be taken from a pregnant dummy with the correct anthropometry and abdominal force-deflection response as a pregnant woman.

When examining direct fetal head accelerations, the peak accelerations and HIC values are relatively high and justify additional concern. In order to put these values, which at first seem very low, into

perspective, one can compare the 118 and 215 HIC values to the 390 HIC tolerance level for the 1 year old infant dummy [5]. Moreover, the fetal brain and vasculature is substantially less developed than even the 1 year old brain, and is much more likely to hemorrhage. Therefore, while the injury HIC values for a fetus are unknown, it is clear that they would be much less than the 1 year old.

Like most computer models used in automobile safety, this model of the pregnant female allows for the exploration of advanced restraint systems. For example, the original experimental research performed by King *et.al.* [9] Illustrated that a mesh webbing over the entire abdomen proved to be the best protective measure for the fetus. Therefore, a prototype belt was designed to mimic these properties and attach readily to the standard three-point seatbelt (Figure 5). The type of mesh and attachments can be optimized using this computer model. Moreover, other advanced restraint designs can be readily evaluated for potential risk to the fetus or pregnant occupant.

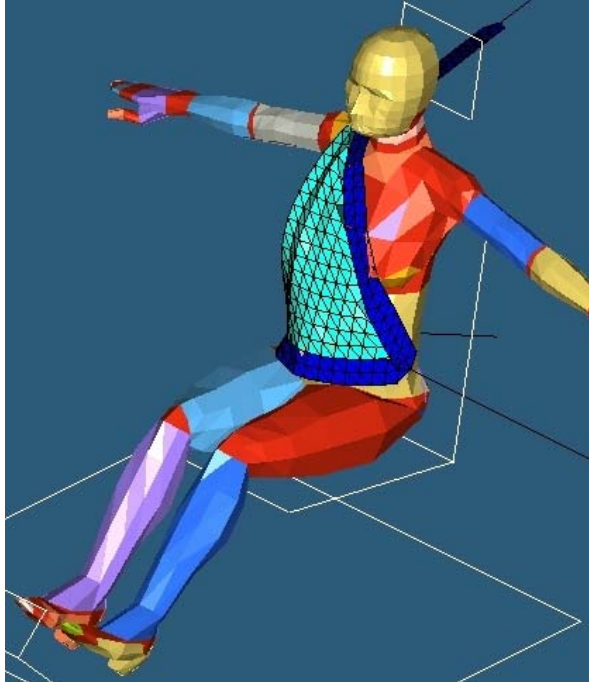


Figure 5. Advanced restraint for the pregnant occupant that can be added to a standard three-point belt.

It is important to note that previous simulations indicate that for all frontal impacts it is safest for the pregnant occupant to ride in the passenger seat while wearing a three-point belt and utilizing the frontal airbag when appropriate [16]. As with all computational models, this model is limited by the accuracy of input and simplifications made. The tissue data, from which the failure strain is derived, is sparse and simplifications are made to use that data as a material model. Additionally, the boundary conditions and geometry can and should be improved in future generations of the model. Furthermore, the model only looks at injury at the UPI. In cases with very large deflections, direct injury to the fetus may occur at injury rates different than those for placental abruption. It is recommended that the methods in this paper be applied to future generations of the pregnant occupant model to provide a continually improving understanding of pregnant occupant injury risk prediction.

CONCLUSIONS

A finite element model of the pregnant abdomen was created to predict fetal outcome following a motor vehicle crash. The model was incorporated into a human body model in a dynamic solver and validated with data from previous studies. The model is sensitive to changes in restraint conditions such as inertial, steering wheel, seatbelt, airbag, and

combined loading. Peak uterine strain was reduced by 30% to 50% in passenger-side simulations vs. driver-side simulations, primarily due to increased distance between the abdomen and the nearest vehicle surface, namely the steering wheel for driver-side tests and the dashboard for passenger-side tests. Simulations results illustrated that the fetal brain may experience direct accelerations that are high enough to cause brain hemorrhaging, and therefore it is suggested that future computer models include the capability of quantifying fetal brain acceleration. Overall, the model has verified previous experimental findings regarding the importance of proper restraint use for the pregnant occupant. The model can be used to run quickly numerous tests and design advanced restraint systems specifically designed for pregnant occupants.

ACKNOWLEDGEMENTS

The authors thank Altair Engineering Inc. for the use of HyperWorks as the pre and post processor, and TNO for the use of MADYMO. The authors would also like to thank Kathy Klinich at the University of Michigan Transportation Research Institute for her assistance in the development of the pregnant model.

REFERENCES

- [1] Attico NB, Smith III RJ, Fitzpatrick MB, Keneally. Automobile safety restraints for pregnant women and children. J Reprod Med, 1986; 31(3):187-92.
- [2] Conrad JT, Kuhn WK, Johnson WL (1966). Stress relaxation in human uterine muscle. American Journal of Obstetrics and Gynecology, 95(2), 254-265.
- [3] Duma SM, Moorcroft DM, Stitzel, JD, Duma, GG, "Evaluating pregnant occupant restraints: the effect of local uterine compression on the risk of fetal injury. Association for the Advancement of Automotive Medicine, October 2004.
- [4] Eppinger R, Sun E, Bandak F, Haffner M, Khaewpong N, Maltese M, Kuppa S, Nguyen T, Takhounts E, Tannous R, Zhang A, Saul R (1999). Development of improved injury criteria for the assessment of advanced automotive restraint systems – II. NHTSA, Docket No. 99-6408-5.
- [5] Eppinger, R., Sun, E., Kuppa, S., Saul, R., "Supplement: Development of Improved Injury Criteria for the Assessment of Advanced Automotive Restrain Systems – II." National Highway Traffic

Safety Administration, Washington DC, 2000.

[6] Fried AM (1978). Distribution of the bulk of the normal placenta. Review and classification of 800 cases by ultrasonography. *American Journal of Obstetrics and Gynecology*, 132(6), 675-680.

[7] Hardy WN, Schneider LW, Rouhana SW (2001). Abdominal impact response to rigid-bar, seatbelt, and airbag loading. *Stapp Car Crash Journal*, 45, 1-32.

[8] Iwamoto M, Miki K, Yang KH, King AI (1999). Development of a finite element model of the human shoulder. AMERI-PAM '99.

[9] King, A.I., Crosby, W.M., Stout, L.C., Eppinger, R.H. (1971) Effects of Lap Belt and Three-Point Restraints on Pregnant Baboons Subjected to Deceleration. *Stapp Car Crash Journal* 15: 68-83. Society of Automotive Engineers 710850

[10] Klinich KD, Schneider LW, Eby B, Rupp J, Pearlman MD (1999a). Seated anthropometry during pregnancy. UMTRI-99-16.

[11] Klinich KD, Schneider LW, Moore JL, Pearlman (1999b). Investigations of crashes involving pregnant occupants. UMTRI-99-29.

[12] Mertz HJ, Horsch JD, Horn G, Lowne RW (1991). Hybrid III sternal deflection associated with thoracic injury severities of occupants restrained with force-limiting shoulder belts. *SAE Technical Paper* 910812, 105-119.

[13] Mizrahi J, Karni Z (1975). A mechanical model for uterine muscle activity during labor and delivery. *Israel Journal of Technology*, 13, 185-191.

[14] Moorcroft DM, Duma SM, Stitzel JD, Duma GG (2003a). Computational Model of the Pregnant Occupant: Predicting the Risk of Injury in Automobile Crashes. *American Journal of Obstetrics and Gynecology* Vol. 189 (2), pp. 540-544, 2003.

[15] Moorcroft DM, Stitzel JD, Duma SM, Duma GG (2003c). The Effects of Uterine Ligaments on the Fetal Injury Risk in Frontal Automobile Crashes. *Journal of Automobile Engineering*, Vol. 217, Part D, pp. 1049-1055.

[16] Moorcroft DM, Duma SM, Stitzel JD, Duma GG (2004). The effect of pregnant occupant position and belt placement on the risk of fetal injury. *SAE Technical Paper*. 2004-01-0324.

[17] Moorcroft DM, Duma SM, Stitzel JD, Duma GG (2003b). A finite element and multi-body model of the pregnant occupant for the analysis of restraint effectiveness. *SAE Technical Paper*. 2003-01-0157.

[18] Pearlman MD, Ashton-Miller JA, Dyer T, Reis P (1999). Data acquisition for development to characterize the uteroplacental interface for the second-generation pregnant abdomen. Submitted to NHTSA.

[19] Pearsall GW, Roberts VL (1978). Passive mechanical properties of uterine muscle (myometrium) tested in vitro. *Journal of Biomechanics*, 11, 167-176.

[20] Rupp JD, Klinich KD, Moss S, Zhou J, Pearlman MD, Schneider LW (2001). Development and testing of a prototype pregnant abdomen for the small-female Hybrid III ATD. *Stapp Car Crash Journal*, 45, 61-78.

[21] Todd BA, Thacker JG (1994). Three-dimensional computer model of the human buttocks, in vivo. *Journal of Rehabilitation Research and Development*, 31(2), 111-119.

[22] Weiss HB, Strotmeyer S. Characteristics of pregnant women in motor vehicle crashes. *Injury Prevention* 2002;8(3):207-214.

[23] Wood C (1964). Physiology of uterine contractions. *British Journal of Obstetrics and Gynecology*, 71, 360-373.

[24] Yamada H (1970). *Strength of biological materials*. Baltimore: The Williams & Wilkins Company.

[25] Zhang L, Yang KH, Dwarampudi R, Omori K, Li T, Chang K, Hardy WN, Khalil TB, King AI (2001). Recent advances in brain injury research: A new human head model development and validation. *Stapp Car Crash Journal*, 45, 369-394.

CONTACT

Stefan M. Duma, Virginia Tech – Wake Forest Center for Injury Biomechanics, Randolph Hall, MC 0238. Blacksburg, VA 24061. duma@vt.edu - www.CIB.vt.edu - (540) 231-3945.